

AD-A176 249

12

TECHNICAL REPORT BRL-TR-2770

A UNIFIED THEORY OF PENETRATION (U)

JAMES T. DEHN

DECEMBER 1986

APPROVED FOR PUBLIC RELEASE; DISTRIBUTION UNLIMITED.

DTIC FILE COPY

DTIC
ELECTE
JAN 29 1987
S E D

87 1 29 053

REPORT DOCUMENTATION PAGE

Form Approved
OMB No. 0704-0188
Exp. Date: Jun 30, 1986

1a. REPORT SECURITY CLASSIFICATION UNCLASSIFIED			1b. RESTRICTIVE MARKINGS None	
2a. SECURITY CLASSIFICATION AUTHORITY N/A			3. DISTRIBUTION / AVAILABILITY OF REPORT Unlimited - Distribution Statement A	
2b. DECLASSIFICATION / DOWNGRADING SCHEDULE N/A				
4. PERFORMING ORGANIZATION REPORT NUMBER(S)			5. MONITORING ORGANIZATION REPORT NUMBER(S)	
6a. NAME OF PERFORMING ORGANIZATION Ballistic Research Laboratory	6b. OFFICE SYMBOL (If applicable) SLC BR-TB-A	7a. NAME OF MONITORING ORGANIZATION N/A		
6c. ADDRESS (City, State, and ZIP Code) Aberdeen Proving Ground, MD 21005-5066		7b. ADDRESS (City, State, and ZIP Code)		
8a. NAME OF FUNDING / SPONSORING ORGANIZATION N/A	8b. OFFICE SYMBOL (If applicable)	9. PROCUREMENT INSTRUMENT IDENTIFICATION NUMBER		
8c. ADDRESS (City, State, and ZIP Code)		10. SOURCE OF FUNDING NUMBERS		
		PROGRAM ELEMENT NO.	PROJECT NO.	TASK NO.
		WORK UNIT ACCESSION NO.		
11. TITLE (Include Security Classification) A Unified Theory of Penetration				
12. PERSONAL AUTHOR(S) Dehn, James T.				
13a. TYPE OF REPORT Technical	13b. TIME COVERED FROM _____ TO _____	14. DATE OF REPORT (Year, Month, Day)	15. PAGE COUNT	
16. SUPPLEMENTARY NOTATION				
17. COSATI CODES			18. SUBJECT TERMS (Continue on reverse if necessary and identify by block number)	
FIELD	GROUP	SUB-GROUP	Penetration mechanics Shaped charge	
			KE Penetrator Theory	
19. ABSTRACT (Continue on reverse if necessary and identify by block number)				
<p>Today's weapons employ compact fragments as well as long rods and shaped charge jets. From the viewpoint of an armor designer, it is desirable to have a method of dealing with all three types of penetrator both in theory and in practice.</p> <p>This report presents an equation of motion which in its most general form describes penetration by a forming, stretching, eroding jet. In various specialized forms, it describes penetration by pre-formed rods and compact projectiles. One specialized form reduces to the classical jet penetration formula according to which penetration in a semi-infinite target is proportional to the square root of the ratio of the jet and target densities. A correction for target hardness is automatically included. The solutions of the various forms of the equation of motion are given explicitly in closed form and are profusely illustrated by numerical examples and comparisons with experimental data.</p> <p>(Cont'd)</p>				
20. DISTRIBUTION / AVAILABILITY OF ABSTRACT <input type="checkbox"/> UNCLASSIFIED/UNLIMITED <input type="checkbox"/> SAME AS RPT. <input type="checkbox"/> DTIC USERS			21. ABSTRACT SECURITY CLASSIFICATION	
22a. NAME OF RESPONSIBLE INDIVIDUAL			22b. TELEPHONE (Include Area Code)	22c. OFFICE SYMBOL

19.

In this report we restrict ourselves to one dimension and to finite or semi-infinite targets made of one material. The chapter on jets is also limited to descriptions of a standard 81mm, 42nd copper cone device. These restrictions will be removed in future reports.

Keywords: Penetration mechanics; Shaped Charge Warheads; Kinetic Energy Projectiles.

Accession For	
NTIS GRA&I	<input checked="" type="checkbox"/>
DTIC TAB	<input type="checkbox"/>
Unannounced	<input type="checkbox"/>
Justification	
By	
Distribution/	
Availability Codes	
Dist	Avail and/or Special
A-1	



TABLE OF CONTENTS

	Page
LIST OF FIGURES	vii
LIST OF TABLES	xii
I. FORMULATION OF THE PROBLEM	1
A. Overview of Penetration Mechanics	1
B. Forces Exerted on the Penetrator	4
C. Pre-formed, Eroding Penetrators	14
D. Jets	17
II. SOLUTIONS	20
A. Solutions without Viscosity	20
1. Constant Mass Projectile	20
2. Eroding Projectile	23
3. A Standard Jet	30
a. Formation	30
b. Stretching	33
c. Fragmentation	36
B. Dimensionless Solutions with Viscosity	37
1. Constant Mass Projectile	37
2. Eroding Projectile	41
3. A Standard Jet	43
III. EXAMPLES OF COMPACT PENETRATORS	46
A. Semi-infinite Targets	46
1. Phenomenology	46
2. Examples	55

TABLE OF CONTENTS (CONT'D)

	Page
a. Hard and Soft Steel Spheres vs. Steel	55
b. A Hard Steel Sphere vs. Two Steels	59
c. Two Sizes of Hard Steel Spheres vs. Steel	61
d. Tungsten Carbide Spheres vs. Copper	64
e. Tungsten Carbide Spheres vs. Lead and Aluminum	64
f. Hard and Soft Steel Spheres vs. Aluminum	68
g. Three Sizes of Hard Steel Spheres vs. Aluminum	70
h. Al/Cu, Cu/Cu and Cu/Al	72
i. Al/Al to 9mm/μs	76
j. Neglect of Erosion and Viscosity	78
B. Finite Targets	79
1. Phenomenology	79
2. Examples	88
a. Steel Spheres vs Three Thicknesses of Aluminum	88
b. Steel Spheres vs Several Thicknesses of Steel	92
c. Steel Spheres vs Titanium Alloy Plates	93
IV. EXAMPLES OF ROD PENETRATORS	97
A. Deformation and Mass Loss	97
B. Calculational Aids	103
C. Semi-infinite Targets	112
1. Examples with Time-dependent Data	112
a. Steel/Magnesium	112
b. Aluminum/Magnesium	119

TABLE OF CONTENTS (CONT'D)

	Page
c. Steel/Aluminum	123
2. Other Examples	127
a. Aluminum/Lead	127
b. Steel/Steel	131
c. Steel/Aluminum	143
d. Aluminum/Steel and Aluminum/Aluminum	150
e. Tungsten versus Steel and Aluminum	159
f. Copper versus Copper, Aluminum and Steel	167
D. Finite Target Examples.	172
1. Steel/Steel	172
2. Tungsten/Steel	188
V. SURVEY OF JET PENETRATION THEORIES	195
VI. AN EXAMPLE OF A JET PENETRATOR	216
A. Device Characteristics	216
B. Penetration by a Train of Rods	224
1. Experimental Data	224
a. Rods with Identical Striking Speeds	224
b. A Train of Jet Fragments	226
2. Models of Penetration by a Fragment Train	229
C. Calculational Aids	234
D. Penetration/Standoff for Armor Steel	236
1. Standoff = $2CD$	236
a. $t_0 \leq t \leq t_1$	238

TABLE OF CONTENTS (CONT'D)

	Page
b. $t_1 \leq t \leq t_2$	239
c. $t_2 \leq t \leq t_E$	240
2. Standoff = 6CD	243
a. $t_0 \leq t \leq t_2$	243
b. $t_2 \leq t \leq t_E$	244
3. Standoff = 10CD	244
4. Standoff = 20CD	244
E. Penetration into Steel and Aluminum Targets of Various Strengths	245
1. Steel Targets	245
2. Aluminum Targets	247
a. $t_0 \leq t \leq t_1$	247
b. $t_1 \leq t \leq t_2$	248
c. $t_2 \leq t \leq t_E$	249
F. Lead Targets	251
1. $t_0 \leq t \leq t_2$	253
2. $t_2 \leq t \leq t_E$	253
G. Finite Targets	254
SUMMARY AND CONCLUSION	256
REFERENCES	257
APPENDIX	270
DISTRIBUTION LIST ,	273

LIST OF FIGURES

<u>Figure</u>		<u>Page</u>
2.1	Dimensionless Solutions for Constant Projectile Mass	40
2.2	Dimensionless Solutions for an Eroding Projectile	44
3.1	Number of Fragments Recovered from a Mild Steel Target versus Speed	47
3.2	Number of Fragments Recovered from Three Steel Targets versus Speed	48
3.3	Shapes of Softened Steel Spheres Recovered from Hard Aluminum Targets	50
3.4	Craters Formed in Steel Targets by Steel Spheres	51
3.5	Craters Formed in Various Targets by Aluminum Spheres	53
3.6	Hardened and Softened Steel Spheres versus Mild Steel	57
3.7	Hardened Steel Sphere versus Two Different Steels	60
3.8	Two Sizes of Hardened Steel Sphere versus Steel	62
3.9	Projectile Shatter Speed versus Target Density for Hardened Steel Spheres	63
3.10	Tungsten Carbide Spheres versus Copper	65
3.11	Tungsten Carbide Spheres versus Lead	66
3.12	Tungsten Carbide Spheres versus Two Different Aluminums	67
3.13	Hardened and Softened Steel Spheres versus Aluminum	69
3.14	Hardened Steel Spheres of Various Sizes versus Aluminum	71
3.15	Copper and Aluminum Spheres versus Copper or Aluminum	73
3.16	Aluminum Spheres versus Two Kinds of Aluminum	77
3.17	Front- and Back-Face Target Effects	81
3.18	Multiple Scabbing in Steel	83
3.19	Limit Thickness versus Semi-inifinite Target Penetration (Steel Spheres vs Aluminum)	84
3.20	Three Ballistic Limit Definitions	85

LIST OF FIGURES (CONT'D)

<u>Figure</u>		<u>Page</u>
3.21	Types of Target Plate Failure	87
3.22	Hard and Soft Steel Spheres versus Three Thicknesses of Aluminum	89
3.23	Flattening of Soft Steel Spheres versus Aluminum	91
3.24	Steel Spheres versus Steel Plates	94
3.25	Steel Spheres versus Titanium Plates	95
4.1	Compact and Long Rod Steel Projectile Deformation after Impacting Steel	98
4.2	Tungsten Rod Deformation while Penetrating Steel	100
4.3	Copper Rod Deformation while Penetrating a Copper Target	101
4.4	Inverted Copper Tube Recovered from Target	102
4.5	Penetration and Length versus Time for a Steel Rod Penetrating Magnesium	114
4.6	Penetration versus Impact Speed for Steel Rods versus Magnesium	115
4.7	X-ray Photographs of Steel Rods Penetrating Magnesium	116
4.8	Craters Made by a Steel Rod Penetrating a Layered Magnesium Target	118
4.9	Penetration and Length versus Time for an Aluminum Rod Penetrating Magnesium	120
4.10	Penetration versus Impact Speed for an Aluminum Rod versus Magnesium	122
4.11	Penetration and Length versus Time for a Steel Rod Penetrating Aluminum	124
4.12	Penetration versus Impact Speed for a Steel Rod versus Aluminum	126
4.13	Aluminum Rods versus Lead	128
4.14	Steel Rods versus Mild Steel	132
4.15	Steel Rods versus Armor Steel	133
4.16	Flattening Factors for Various Aspect Ratios (Steel Rods/Steel)	136

LIST OF FIGURES (CONT'D)

<u>Figure</u>		<u>Page</u>
4.17	Area Ratios (Steel Rods/Steel)	137
4.18	Steel Rods with Various Aspect Ratios Impacting Steel Targets at One Speed	139
4.19	Steel Rods ($L_0/D_0 = 3$)/Steel	140
4.20	Steel Rods versus Aluminum at Three Speeds Target Craters	144
4.21	Steel Rods versus Two Kinds of Aluminum	145
4.22	Steel Rods with Various Aspect Ratios Impacting Aluminum Targets at One Speed	147
4.23	Flattening of Steel Rods against Two Types of Aluminum	149
4.24	Steel and Aluminum Rods versus Steel	151
4.25	Flattening of Aluminum Rods against Steel	152
4.26	Aluminum Rods Recovered after Impacting an Aluminum Target at Various Speeds	154
4.27	Various Aluminum Rods Recovered after Impacting an Aluminum Target at One Speed	156
4.28	Aluminum Rods versus Aluminum Targets	157
4.29	Flattening of Aluminum Rods against Aluminum Targets	158
4.30	Tungsten Rods versus Aluminum, Steel and Tungsten Targets	160
4.31	Flattening of Tungsten Rods against Three Target Materials	161
4.32	Various Aspect Ratio Tungsten Rods versus Armor Steel	163
4.33	Flattening of Various Aspect Ratio Tungsten Rods against Armor Steel	164
4.34	Deformed Tungsten Rods Recovered After Impacting Steel Targets	165
4.35	Two Sizes of Tungsten Rod versus Steel	166
4.36	Deformed Copper Rods Recovered after Impacting Copper Targets	168

LIST OF FIGURES (CONT'D)

<u>Figure</u>		<u>Page</u>
4.37	Deformed Copper Rods Recovered after Impacting a Very Hard Steel Target	170
4.38	Copper Rods versus Aluminum, Steel and Copper	171
4.39	Flattening of Copper Rods against Aluminum, Steel and Copper	173
4.40	Photographs of Steel Rod Perforating a Steel Target Plate	174
4.41	Performance of Steel Rod versus Steel Plate	175
4.42	Residual Speed of Steel Rods after Perforating Steel Plates of Two Thicknesses	177
4.43	Residual Mass of Steel Rods after Perforating Steel Plates of Two Thicknesses	178
4.44	Flattening of Steel Rods against Steel Plates	180
4.45	Residual Speed of Steel Rods of Various Masses after Perforating a Steel Plate	185
4.46	Residual Mass of Steel Rods of Various Masses after Perforating a Steel Plate	186
4.47	Residual Speed of a Tungsten Rod after Perforating a Steel Plate	189
4.48	Residual Mass of a Tungsten Rod after Perforating a Steel Plate	190
4.49	Residual Mass of a Tungsten Rod after Perforating a Steel Plate	191
4.50	Flattening of a Tungsten Rod Perforating a Steel Plate	193
5.1	Jet Velocity and Penetration Velocity versus Time	203
6.1	Cutaway of 81 mm Precision Charge Device	217
6.2	Photographs of a Continuous Jet at Three Times	220
6.3	Penetration versus Standoff for a Semi-infinite Stack of Armor Steel Plates	223
6.4	Cutaway Showing Copper Residue in a Steel Target Billet	227
6.5	Model Hole Profiles at 23CD for a Precision Jet	231

LIST OF FIGURES (CONT'D)

<u>Figure</u>		<u>Page</u>
6.6	Model Hole Profiles at 38CD for a Non-precision Jet	232
6.7	Penetration versus Time versus a Stack of Armor Steel Plates at 2CD	237
6.8	Penetration versus Time for Steel and Aluminum Targets of Various Hardnesss at 2CD	246
6.9	Penetration versus Time for Mild Steel and Lead	252
6.10	Residual Jet Speed after Perforating Various Thicknesses of Armor Steel Plates	255

LIST OF TABLES

<u>Table</u>		<u>Page</u>
1.1	Typical Ranges of Brinell Hardness Numbers and Yield Strengths	6
6.1	Penetration by a Train of Jet Fragments	242

I. FORMULATION OF THE PROBLEM

A. Overview of Penetration Mechanics

Penetrators have been traditionally classified as either kinetic energy (KE) projectiles or chemical energy (CE), that is, explosively-formed jets, rods or pellets. Typical KE projectiles are launched from a gun and arrive at a distant target with a definite striking mass, M_0 , and speed, \dot{S}_0 . Thus, the kinetic energy, $1/2 M_0 \dot{S}_0^2$, is easily found. In contrast, jets are produced at the target by collapsing a metal liner with a hollow explosive charge. Penetration usually begins even before the jet is completely formed. Jet aspect or length-to-diameter (L/D) ratios are typically greater than 100 after formation, with the tip moving about $8 \text{ mm}/\mu\text{s}$ and the rear moving about $1 \text{ mm}/\mu\text{s}$. Long rod aspect ratios are typically less than 20 and each element of the rod moves at the same speed before striking, commonly less than $2 \text{ mm}/\mu\text{s}$. This speed is also typical of fragment penetrators with aspect ratios near unity.

Recently, considerable effort has been devoted to the development of explosively formed penetrators with aspect ratios near unity. These devices tend to blur the traditional distinction between KE and CE weapons by fitting into both categories. They are produced by the explosive collapse of a liner (like a jet), but arrive at a distant target as a single lump of definite striking mass and speed (like a projectile). Such a penetrator is a cross between a jet and a projectile and a cousin to the traditional fragment which is launched and usually produced from a shell filled with explosive.

Because of the differences between jets and KE projectiles, separate theories have been developed. Hydrodynamic theories have been favored for jets, while a variety of theories have been used for bullets and fragments. With the advent of high-speed, long rods, amended jet or bullet theories have been introduced. In this report, we will develop a single theory which describes all types of penetrator from a unified viewpoint.

Two points of view have been used successfully in classical mechanics. The mechanics of particles was systematized by Newton who spoke of "quantity of motion" or momentum as we now call it ^(1.1). Continuum Mechanics followed

Newton's principles. However, instead of describing the time evolution of the coordinates of a particle or system of particles, the goal became a description of the velocity, pressure and density history of every point in space. This view was systematized by Euler ^(1.2) who also showed how the two viewpoints are connected. Especially when they are applied to fluids, we now call these viewpoints Lagrangian and Eulerian, although both forms are due to Euler. Lamb ^(1.3) gives the history and mathematics of both viewpoints.

The choice of one viewpoint or the other is usually governed by considerations of simplicity. If a motion is symmetrical enough to be characterized by one space coordinate, then the Lagrangian view is preferred even in hydrodynamics ^(1.4). The general equation of motion which allows for spatial variation of the dilatational and shear viscosity coefficients reduces to the Navier-Stokes equation when these coefficients are constant and the bulk viscosity vanishes ^(1.5). The usual Eulerian form of the hydrodynamic equation of motion is the inviscid form of the Navier-Stokes equation. If heat conduction is important, it is customary to account for it in the energy rate equation which reduces to Bernoulli's equation in the inviscid, adiabatic case ^(1.6). Usually both heat conduction and viscosity are neglected in hydrodynamics.

In this report, we wish to describe the motion of a solid projectile penetrating a solid target. We limit ourselves to impacts by homogeneous projectiles with zero yaw, striking flat target surfaces at zero obliquity without spin. The targets are assumed to be homogeneous and effectively infinite in lateral extent. The latter description means that there is no detectable distortion of the outermost lateral dimensions of the target. However, the targets may be either finite or semi-infinite in the direction of penetration. The former description means they can be perforated by the projectile speeds and masses available. The latter description means they are thick enough to stop the penetrator without detectable distortion of the rear surface of the target.

Sliding friction forces are present during penetration and can be influential in the final stage of projectile motion. For example, Zaid and co-workers ^(1.7) found that a rod of length greater than the thickness of the target plate might exit from the rear of the plate with almost no residual velocity or, at a slightly lower striking speed, become embedded in the plate, protruding from both the front and rear surfaces. They attributed the defeat

of the slightly less energetic rod to projectile/plate friction. Wingrove (1.8) has also described the increased importance of frictional energy loss near velocity ballistic limits and attributed this to an increase in the coefficient of friction as the projectile velocity is reduced. However, during most of the projectile motion, friction plays a negligible role, at least for metal targets and projectiles, as has been pointed out by Krafft (1.9). In this report we will neglect sliding friction. For similar reasons, penetration by a spinning projectile is negligibly different from penetration by a non-spinning projectile.

For solid targets we may also neglect gravity.

For thin target plates struck by projectiles near velocity ballistic limits, plate bending can play a role. We will confine our attention here to plates which are thick enough that such an effect is negligible. If we are near a ballistic limit, this means that the target thickness is comparable to the projectile diameter.

Various measurements have been made of the manner in which the striking energy of a projectile is eventually partitioned into projectile and target heating and deformation. (1.10 to 1.12). In this report we will be concerned only with the forces at work during a penetration, a process which is complete in tens of hundreds of microseconds. We will not be concerned with the eventual redistribution of the absorbed energy. Electromagnetic radiation, usually a flash of light, accompanies some impacts. Although this occurs in the time frame of interest, it is very brief and involves a negligible amount of energy.

We will treat both projectile and target as approximately incompressible. Some energy is transported by wave motion in both target and projectile in the time frame of interest. For example, the rear of a rod penetrator is slowed when a wave generated at the front reflects at the metal/air interface. Waves also radiate from the target cavity as it is being produced. However, the energies involved are usually negligible. An exception may occur for jets penetrating plastics as will be mentioned later. For very high impact speeds, melting and vaporization may also become important (1.13). In this report we will avoid such cases.

In a previous report (1.14) we concentrated on the case of a constant mass projectile striking a target plate at non-zero obliquity. In that case we found that a force dependent on projectile displacement was essential for

describing ricochet versus embedment versus perforation. However, such a force was found to be negligible in comparison to other forces for zero obliquity impacts. Consequently, in the present report we will neglect forces that depend on displacement. In that report we briefly discussed the case of an eroding rod and transformed the time variable to obtain some interesting solutions to particular cases. Here we will adopt a simpler approach by assuming a particular form for the erosion rate. The previous report also developed a model of projectile breakup which we will use in a future report. Finally, the previous report gave a survey of KE penetrator theories which we will not repeat here. However, in Chapter V below, we will survey jet penetration theories. Selections from parts of the previous report appear in the Sixth Symposium on Ballistics (1.15).

The goal of the present report is to develop a unified theory which includes the essential physics of the problem, yet is simple enough to use in initial design work where insight and ideas for experiment are more important than great precision. Consequently, a number of examples will be given in order to facilitate the use of the theory. It is the author's opinion that the exclusive use of complicated computer codes in penetration mechanics is both premature and inadequate. Our current knowledge of the physics of penetration is still too rudimentary for us to reduce the problem to improvements in numerical methodology. Concentration on this aspect of the problem, while eventually worthwhile, can distract us from learning the physics we need to know. A simple theory should have the advantage that every detail can be understood and modified by the user. It should also enable us to link the specialized field of penetration mechanics to the rest of simple physics where a few mathematical forms can be used to describe a remarkable variety of phenomena (1.16).

B. Forces Exerted on the Penetrator

As outlined above, our problem is sufficiently symmetrical to be characterized by one space coordinate, S , by which we denote the position of the center of mass of the penetrator. Here we will adopt the Lagrangian viewpoint and describe the time evolution of this coordinate or some other coordinate related to it. In the case of a solid projectile penetrating a solid target the penetrator moves in a crater which is usually open at the

rear. In this respect the motion is often simpler than for a solid penetrator in a fluid target where a turbulent wake may exert a drag force on the projectile (1.17). Exceptions can occur as for penetration of a hard, brittle target by a train of fragments as we shall see. If the target cavity is open at the rear of the projectile and is wide enough to justify neglect of sliding friction on the sides of the projectile, then all target forces are exerted on the front of the projectile. This seems to be true for most cases of interest.

Let the mass of the penetrator at any given time be denoted by $M = \rho_p V$, where ρ_p is the density of the penetrator and V is its volume. When it is appropriate to speak of the penetrator length, L , and cross-sectional area, A , then $V = AL$. If the pressure on the front of the penetrator is p and the pressure on its rear and sides is zero, then the pressure gradient along its length is p/L , the force per unit volume. If we multiply this by the volume, AL , we obtain pA for the opposing force due to the strength of the target. Tabor (1.18, 1.19) has shown that the mean pressure exerted by a metal target on a metal penetrator is approximately equal to three times the ultimate yield strength, or elastic limit, Y_t , of the target material as determined in standard tensile tests. He started with the theoretical predictions of Hencky (1.20) and Ishlinsky (1.21) which agreed that the pressure should be a bit less than $3Y_t$. He then measured this pressure for various metals and found it to be quite close to $3Y_t$.

In the appendices of his book (1.19) Tabor noted the proportionality between the ultimate tensile strength and the Brinell hardness number

$$Y_t = C_m (\text{BHN}) \quad (1.1)$$

where C_m is a constant approximately equal to 0.3×10^8 (dyne/cm²)/(kg/mm²) for steel or hard aluminum. For soft aluminum or copper he suggested C_m values about 50% higher with intermediate values for other non-ferrous metals. He also gave hardness values for many metals and a few indenter materials as well as conversions between various hardness numbers. Table 1.1 here gives some typical values.

Table 1.1 Typical range of Brinell hardness numbers, BHN, and yield strengths, Y_t .

<u>Material</u>	<u>BHN (kg/mm²)</u>	<u>Y_t (dyne/cm²)</u>
lead	1	.5 x 10 ⁸
copper	30-130	14-60 "
aluminum	15-150	7-50 "
steel	100-400	30-120 "
diamond	6,000	-

Since the mean pressure to keep bonds breaking and initiate plastic flow in a target is

$$p = 3Y_t \quad (1.2)$$

we can calculate the resistive force of the target due to its hardness as

$$a = pA = 3Y_t A = 3C_m (\text{BHN}) A \quad (1.3)$$

from Eqs. (1.1) and (1.2). Here A is the time average value of the area presented by the projectile to the target during the penetration. Commonly the nose of the projectile deforms during a penetration so that $A > A_0$ where A_0 is the initial cross-sectional area of the projectile before penetration begins. Thus the force a in Eq. (1.3) is a constant in the approximation we are making here. For example, if the target is an armor steel with $\text{BHN} = 300 \text{ kg/mm}^2$, we find $3Y_t = 3(90 \times 10^8) = 2.7 \times 10^{10} \text{ dyne/cm}^2$, and if $A = 1 \text{ cm}^2$ then $a = 2.7 \times 10^{10} \text{ dyne} = .27 \text{ g mm}/\mu \text{ s}^2$. Here we have converted to grams (g), millimeters (mm) and microseconds ($\mu \text{ s}$), the mass, length and time units which seem most appropriate to our problem.

The nose shape of a projectile can affect its penetration, especially as it enters the target, or if the target is thin, and projectile plastic deformation and/or erosion are not important factors (1.22). Shape is not very important in a deep penetration or when projectile deformation and/or erosion are important, since penetrator noses become hemi-spherical mushroom caps. Whenever we discuss non-deforming projectiles in this report, we will restrict ourselves to spheres or rods with hemi-spherical noses so we need not be concerned with other shapes. Even for spheres we should, strictly speaking, use a Hertzian contact surface to account for elastic deformation as described by Goldsmith (1.23). Such precision is not important to our goal of coupled insight and simplicity. Generally speaking, we will be concerned only

with the area presented by a hemi-sphere of diameter somewhat larger than the initial diameter.

A second type of resistance offered by a target is inertial and becomes more important at higher speeds. We approximate this force by

$$\frac{1}{2} \rho_t \dot{P}^2 A = c \dot{P}^2 \quad (1.4)$$

where \dot{P} is the penetration speed and $c = \frac{1}{2} \rho_t A$ is a constant proportional to the target density, ρ_t , and the average projectile presented area, A . In Eq. (1.4), $\frac{1}{2} \rho_t \dot{P}^2$ is the energy of a moving unit volume of target material after its bonds have been broken, assuming it moves with the same speed as the projectile nose. It is also the resistive force per unit area offered by the target because of its mass, so that multiplication by the area gives us the inertial force.

Equations (1.3) and (1.4) give the two main forces we will be concerned with. They require only a knowledge of the target density and hardness as well as an estimate of the area presented by the penetrator. If we add these two forces we have the form proposed by Poncelet 150 years ago. What is new here is the use of $3Y_t$ in Eq. (1.3) so that we can calculate the hardness force term from measured Brinell numbers, instead of treating it as an adjustable parameter. The form for c in Eq. (1.4) is not new, but it also prevents us from treating it as an adjustable parameter. If any adjustment is made, it will be in our estimate of $A \geq A_0$. Whenever possible, we will use experimental information to estimate A , which appears in both a, the hardness force, and c , the inertial coefficient.

A third type of target resistive force which is often considered is a viscous force proportional to the first power of the speed ^{(1.24) to (1.30)}. None of these authors could do more than guess at the magnitude of this effect since they had no experimental measurements of solid viscosity. More recently, Walters ^(1.31) revived interest in solid viscosity by summarizing the available experimental data. Unfortunately, there is more than order of magnitude disagreement between various experimental measurements, with Russian workers tending to favor high values and American workers tending to favor low values. Thus Walters was forced to treat the viscous coefficient as an adjustable parameter (within wide experimental limits) when applying it to penetration mechanics ^(1.32).

The notion of internal friction or viscosity is basically the same for solids and fluids as was pointed out by Thomson over 100 years ago.

This molecular friction in elastic solids may be properly called viscosity of solids, because, as being an internal resistance to change of shape depending on the rapidity of the change, it must be classed with fluid molecular friction, which by general consent is called viscosity of fluids." (1.33)

Somewhat earlier, Maxwell (1.34) made similar observations, pointing out that in a viscous solid the time rate of change of internal stress, $\dot{\sigma}$, is proportional both to the strain rate, $\dot{\epsilon}$, and the stress divided by a relaxation time, τ . That is,

$$\dot{\sigma} = G\dot{\epsilon} - \sigma/\tau \quad (1.5)$$

where G is the rigidity or shear modulus. An integration of Eq. (1.5) for constant $\dot{\epsilon}$ gives

$$\sigma = \eta\dot{\epsilon} + (\sigma_0 - \eta\dot{\epsilon}) \exp(-t/\tau) \quad (1.6)$$

where $\eta = G\tau$ is the coefficient of viscosity. When sufficient time has passed after an initial loading ($t \gg \tau$), $\sigma \rightarrow \eta\dot{\epsilon}$, showing that in this limit the viscosity is the shear stress divided by the strain rate. For simple Newtonian liquids like water τ is very short (10^{-12} s), and considerable effort must be made to observe its relaxation. However, this has been done on a regular basis for some time now (1.35). For non-Newtonian liquids and solids, τ can be much longer.

Hencky (1.36) saw in Maxwell's τ a way to "bridge the gap from solid to liquid continua." By introducing relaxation time or its inverse (frequency), he derived Euler's equations of viscous fluid flow from the deformation of an originally elastic continuum. He showed that the Navier-Stokes equation is the special case of large stress or small relaxation time.

A bit later, de Bruyne (1.37) pointed out that Maxwell's relaxation time could be written in terms of an activation energy, U :

$$\tau = \tau_{\infty} \exp [U/(RT)] \quad (1.7)$$

where R is the gas constant, T is the temperature and τ_{∞} is the high-temperature limit. Multiplying Eq (1.7) by G gives the viscosity η in Maxwell's model which then has the form postulated by Andrade (1.38). He went on to observe that deformation of a solid takes place by "a change of molecular position from one stable state, over an energy barrier, U , to another stable state, and that only those molecules (or groups of molecules) having sufficient energy of thermal agitation to get over the barrier are able to make the change." He let σ_u be the ultimate stress and

$$U = V_M (\sigma_u - \sigma)^2 / (2G) \quad (1.8)$$

since the strain energy per unit volume stored in a solid might be written as $1/2 \sigma^2 / G$. Here V_M is the volume of a mole of material with $V_M = N_0 V_m$, if N_0 is Avogadro's number and V_m is the volume of a molecule. If the velocity is $v = \delta l / dt$ and the strain is $\delta l / dx$, then σ is proportional to the velocity gradient in Eq (1.6) after sufficient time has passed, $t \gg \tau$, that is,

$$\sigma = \eta \dot{\epsilon} = \eta d/dt (\delta l / dx) = \eta dv / dx. \quad (1.9)$$

When $\eta = \sigma / \dot{\epsilon} = G \tau$, Eqs. (1.7) and (1.8) give

$$\eta = G \tau_{\infty} \exp [V_m (\sigma_u - \sigma)^2 / (2GkT)] \quad (1.10)$$

where $k = R/N_0$ is Boltzmann's constant. Eq. (1.10) says that the viscosity decreases as the temperature increases in agreement with observations of condensed matter (liquids and solids). The increase in thermal energy makes it easier for potential barriers to be crossed. However, Eq (1.10) predicts that η will decrease as the stress or pressure is increased toward its ultimate value, $\sigma \rightarrow \sigma_u$, which is contrary to observations. As the pressure applied to condensed matter increases so does the viscosity, since it becomes more difficult to overcome potential barriers.

If τ is large enough in Eq (1.6), then there will be an observable delay in returning to the unstressed state when the material is unloaded. This lagging of the strain behind the stress is a case of mechanical hysteresis

which Zener has dubbed "anelasticity" (1.39). A number of stress-induced mechanisms have been considered such as the inhibition of thermal or particle diffusion or of viscous slip along grain boundaries. $\hat{K}\hat{e}$, a co-worker of Zener, measured the internal friction of both single crystal and polycrystalline aluminum as a function of temperature and found a resonance peak near 500°C in polycrystalline specimens but not in single crystals. He attributed this to viscous slip at grain boundaries and estimated the viscosity of polycrystalline aluminum to vary from 2×10^{16} poise near room temperature to about 2×10^{-1} poise at 660°C, the melting point. (1.40). $\hat{K}\hat{e}$ made similar measurements for a number of other metals. For alpha-iron he found the viscosity to vary from 10^{45} poise near room temperature to 10^{-2} poise at 910°C where a transition to gamma-iron occurs. He found three resonance peaks in alpha-iron. Those centered at 20°C and 225°C he attributed to stress-induced re-distribution of interstitial nitrogen and stress-induced inhibition of nitrogen atom diffusion respectively. The main peak centered at 500°C and extending from 400°C to 600°C he attributed to viscous slip at grain boundaries. He noted that the viscosity decreased from 10^{10} poise at 400°C to 10^3 poise at 600°C, values quite comparable to those of pyrex glass over the same range (1.41). $\hat{K}\hat{e}$ also studied the effects of impurities in aluminum, iron and copper (1.42) as well as the effect of alloying aluminum and copper (1.43). $\hat{K}\hat{e}$'s measurements were carried out at low stress levels and slow speeds, so they may not be transferable to penetration mechanics where high speeds and stresses occur. However, his finding that measurements of the viscosity of solids vary widely with the characteristics of particular specimens may help to account for the large discrepancies between viscosity values reported by various workers for nominally the same materials.

Krausz and Eyring (1.44) have developed these ideas and introduced statistical quantum mechanics via Eyring's absolute reaction rate theory. In the view of these authors a solid can be looked upon as a giant molecule, if it is a perfect crystal. Of course, imperfections and grain structures modify this view and the flow units might be grains rather than molecules in the case of metals. They use their rate theory of plastic deformation to explain a variety of phenomena, including mechanical hysteresis.

In their discussion of viscosity and plastic flow, they develop an expression which relates the strain rate, $\dot{\epsilon}$, to the net number of times per second that a flow unit moves in a direction determined by the stress:

$$\dot{\epsilon} = [1/(2\tau)] [e^z - e^{-z}] = (1/\tau) \sinh z \quad (1.11)$$

where

$$\tau = \lambda_1 / (2 \lambda k^*) \quad (1.12)$$

is the relaxation time,

$$z = (\sigma \lambda_2 \lambda_3 \lambda) / (2kT) = \frac{\sigma V_H}{2kT} \quad (1.13)$$

and

$$k^* = (kT/h) \exp [-\Delta G^*/(kT)] \quad (1.14)$$

Here k^* is the rate constant (sec^{-1}) and involves Boltzmann's constant, k , Planck's constant, h , and Gibb's free energy of activation, ΔG^* , as well as the temperature, T . The parameter z is proportional to the stress, σ , which induces flow units to move from one site to another one an average distance λ_1 away. Here $(\lambda_2 \lambda_3)$ is the cross-sectional area presented by the flow unit to the opposing medium. Consequently, $\sigma(\lambda_2 \lambda_3)$ is the force. In moving to an adjacent site, the flow unit surmounts a potential energy barrier which has a peak located a distance $\lambda/2$ from a valley, so the force does work $\sigma \lambda_2 \lambda_3 \lambda / 2 = \sigma V_H / 2$. This is the numerator of Eq (1.13), the activation energy. The thermal factor, kT , in the denominator has the effect of assisting a passage over the barrier at higher temperatures. The hole volume swept out during the motion is $V_H = \lambda_2 \lambda_3 \lambda$, while the volume of the flow unit is not much different, namely, $V_m = \lambda_1 \lambda_2 \lambda_3$. The exponential terms in Eq (1.11) represent forward and backward motions of flow units. Krausz and Eyring go on to generalize their theory in order to include the motion of more than one type of flow unit, each characterized by its own relaxation time, τ_i , and occupying a fraction, X_i , of the shear surface. They then proceed to apply their theory to a number of solids. However, they do not treat metals to any extent, except to point out the analogy between superplastic flow of metals and the motion of viscous materials like hot glasses. The great elongation which is possible without necking or breaking is familiar to anyone who has observed a demonstration of the glass-maker's art.

Let us recall Maxwell's expression for the viscosity, $\eta = G\tau$. If we use Eq (1.11) for τ ,

$$\eta = [G/(2\dot{\epsilon})] (e^z - e^{-z}) \approx [G/(2\dot{\epsilon})] e^z \quad (1.15)$$

for $z \gg 1$ in Eq (1.13). Near room temperature, the denominator of z is about $2kT \sim 10^{-13}$ erg. For liquids like water composed of small molecules σV_H should be a bit larger than this and z is a bit larger than unity. The second form of Eq (1.15) is essentially the same as Eq (1.10) if τ_∞ corresponds to $1/(2\dot{\epsilon})$, $V_H \sim V_m$, and $(\sigma_u - \sigma)^2/G$ corresponds to σ in Eq (1.13). Thus both equations describe a decrease of viscosity with increasing temperature. However, unlike Eq (1.10), Eq (1.15) correctly describes an exponential increase of viscosity with increasing pressure, σ . For colloidal suspensions, resins and polymers, the flow units and the stresses required to move them become larger, thus increasing z for given T and making the second form in Eq (1.15) an even better approximation. The possible application of Eq (1.15) to polycrystalline metals is unknown at present. However, we note that for $G = .5 \times 10^{10}$ dyne/cm² and $2\dot{\epsilon} = .5 \times 10^{10}$ s⁻¹, $\eta = e^z$ is expressed in poise. If $z = 100$, then $\eta \sim 10^{43}$ poise, a number similar to values reported by K \hat{e} for iron (1.40).

The approximate form of Eq (1.15) has also been given by Frenkel who noted the work of Andrade and Eyring. Frenkel pointed out the necessity of revising classical hydrodynamic theory to incorporate Maxwell's relaxation theory, apparently unaware that Hencky already did this (1.36). In addition, he discussed the need to modify the classical elastic theory of amorphous solids to account for their fluidity (or viscosity) in order to describe the continuous character of the transition from the liquid to the solid state when this transition is not accompanied by crystallization. He devotes most of his attention to the latter modification in order to describe the propagation of transverse waves in fluids. From such a unified viewpoint, diffusion and creep in solids are at one end ($\tau \sim 10^{12}$ s or 30,000 years in geology) of a relaxation time spectrum which extends to the viscous flow of Newtonian liquids ($\tau \sim 10^{-12}$ s for water). As Frenkel remarks, this makes the classification of condensed bodies into solids and liquids a matter of practical convenience rather than something of fundamental importance (1.46).

This rather long digression on the viscosity of solids and liquids is meant to lay the groundwork for future learning about the possible usefulness

of such concepts in penetration mechanics which describes high-pressure, high-shear-rate events. At present we do not have enough quantitative information even to begin an adequate description. Polycrystalline metals are far from perfect crystals, although they are composed of crystallized grains as well as other structures. Only in certain superplastic cases do they flow like liquids in short times. Brittle metals tend to shatter like glasses or ceramics under impact, while glasses can flow like superplastic metals under the proper conditions. Solid plastics are also of interest in penetration mechanics and can flow or shatter depending on conditions. In what follows we will represent the possible effects of viscosity by a simple force term proportional to the first power of the penetration speed, namely.

$$b\dot{P} = 6\pi R\eta\dot{P} = 6\sqrt{\pi A}\eta\dot{P} \quad (1.16)$$

which is Stoke's law for a sphere of cross section $A = \pi R^2$.

In summary then, the target force opposing penetration is

$$F = a + b\dot{P} + c\dot{P}^2 \quad (1.17)$$

where a depends on the target hardness by Eq (1.3), b depends on the target viscosity by Eq (1.16), c depends on the target density by Eq (1.4) and all three depend on the time average area, A , presented to the target by the penetrator nose. To anticipate a bit, we will find both a and c to be indispensable in describing the experimental observations which have been made. However (in spite of our lengthy discussion of viscosity), we will find b to be of negligible importance in describing such observations. This does not mean that viscosity may not turn out to be of some importance in some cases when better observations are made, perhaps in the penetration of very hard targets (high z in Eq (1.13)) like glasses or ceramics for which relatively few fundamental observations have been made. It is clear that a and c are important for solid targets, because bonds must be broken and target material must be moved. We may conjecture that b is unimportant because the process by which the moving target material eventually comes to rest is of no importance in slowing the penetrator, provided there is little or no contact between the moving target material and the penetrator, as in the case of most metal targets. However, if there is considerable contact between moving

target material and penetrator, as there may be in the case of narrow channels in hard, brittle targets, then b may be very important since the sides as well as the nose of a penetrator will be affected by forces exerted by target material. For example, if the narrow penetration channel in a glass target is filled with a mixture of eroded penetrator and target material, both the external friction between this material and the remaining penetrator as well as the internal friction or viscosity of the eroded material might be important. For a long rod penetrator or jet this part of the problem resembles the motion of a solid cylinder inside a flowing "liquid" tube which is in turn contained inside a rigid "pipe" (the undamaged part of the target).

C. Pre-formed Eroding Penetrators

A typical example of this kind of penetrator is a rod of aspect ratio $L_0/D_0 = 10$. Here subscript zero denotes initial value. Except for the deformed nose which presents area $A > A_0$ to the target, most of the rod retains its original cross-sectional area, A_0 . Thus to a good approximation, the remaining mass is proportional to the remaining length, $M = \rho_p A_0 L$. Since neither the penetrator density, ρ_p , nor A_0 change with time, we can write

$$\dot{L} = \dot{M}/(\rho_p A_0) = -\dot{M}_p/(\rho_p A_0) \quad (1.18)$$

where $\dot{M}_p = |\dot{M}|$ (for $\dot{M} < 0$) stands for the mass lost per unit time at the nose which is located at position P (measured from the target surface) and moves with speed \dot{P} , the penetration speed (or growth rate of the crater depth). Let R and \dot{R} be the position and speed of the rear of the penetrator. Just before impact all parts of the penetrator move with the same speed. Just after impact the target resistive force increases from zero to a large value, then starts to decrease. During this brief, transient period (of a few microseconds) the nose speed is decreased to a value $\dot{P}_0 < \dot{R}_0$. Here we are ignoring the details of this transient deceleration of the nose and start our problem just after the resistive force of the target has peaked. The rear of such a rod will begin to decelerate a bit later when pressure waves generated at the nose reach the rear and reflect at the solid-air interface. This deceleration of the rear may occur in several steps. Again we will ignore such details and use average values.

Since S is the position of the center of mass located halfway between the nose and the rear at any time,

$$\dot{P} = \dot{S} + \dot{L}/2 = \dot{S} - \dot{M}_p / (2\rho_p A_o) \quad (1.19)$$

and

$$\dot{R} = \dot{S} - \dot{L}/2 = \dot{S} + \dot{M}_p / (2\rho_p A_o) \quad (1.20)$$

where we have used Eq (1.18). Addition of these equations expresses the fact that the speed of the center of mass is the average of \dot{P} and \dot{R} . Subtraction of these equations expresses the fact that $\dot{R} > \dot{P}$, as expected. In the absence of erosion, $\dot{L} = \dot{M}_p = 0$ and $\dot{P} = \dot{S} = \dot{R}$ with $L = L_o$ and $M = M_o$.

Before proceeding to derive the equation of motion, let us consider an analogous problem formulated by Goddard for rocket motion (1.47). Here we will simplify Goddard's treatment slightly by neglecting the mass of the rocket motor case which has no analog in penetration mechanics. This means setting $k=0$ in Goddard's equation. We will also use the symbol M for the mass remaining at time t instead of writing the difference between the initial mass and the mass expelled (as exhaust) up to time t . The infinitesimal dM represents the mass lost in time dt . During this time the upward (positive) speed of the center of mass of the rocket relative to a stationary observer on the ground is increased from v to $v + dv$. The mass which is lost moves at a constant (exhaust) speed, C_o , relative to the center of mass of the moving rocket in the downward (negative) direction, so $v - C_o$ is the exhaust velocity relative to the ground observer. The change in momentum of the system is equal to the impulse imparted by the force of gravity, G , and the drag force of the atmosphere, D . Thus

$$[(M - dM)(v + dv) + dM(v - C_o)] - Mv = - (G + D)dt \quad (1.21)$$

where Mv is the momentum at the beginning of the time interval dt and the square brackets represents the momentum at the end of this interval.

Initially $v_c = 0$ so $v - C_o < 0$ until enough speed has been attained to reverse the sign. No attempt is made to follow the motion of the exhaust gas after it

has left the rocket. When we pass to the limit, $dt \rightarrow 0$, $dM \rightarrow 0$, $dv \rightarrow 0$, we can neglect the second order term, $dMdv$, in Eq (1.21) and divide by dt to obtain

$$d(Mv)/dt = (v+C_0)(dM/dt) - (G+D) \quad (1.22)$$

This equation states that the time rate of change of momentum is equal to the sum of the forces acting upon the center of mass. In outer space where $G = D = 0$ the mass loss increases the momentum (as it must also do if the rocket is to rise from the earth's surface). The form of Eq (1.22) is that usually set forth in physics texts (1.48, 1.49). Of course Eq (1.22) can be simplified by subtracting $v dM/dt$ from both sides to obtain

$$M dv/dt = C_0 \dot{M} - (G+D) \quad (1.23)$$

which is Goddard's equation with $\dot{M} = dM/dt$. Shortly after ignition $C_0 \dot{M} > (G+D)$ and the rocket rises. At burnout, $C_0 \rightarrow 0$ and $\dot{M} \rightarrow 0$ so $dv/dt < 0$ unless $G + D = 0$ by this time. Thus the rocket will either escape or slow down and fall back to earth. Discussions of Goddard's equation may also be found in some texts (1.50).

In the penetration problem we are describing, mass $dM_p > 0$ is lost at the front instead of the rear where it is wiped off by the target while moving at the nose speed, \dot{P} . The remaining mass, M , is diminished by dM_p , while the speed of the center of mass becomes $\dot{S} + d\dot{S}$. Thus,

$$[(M - dM_p)(\dot{S} + d\dot{S}) + dM_p(\dot{P})] - M\dot{S} = -F dt \quad (1.24)$$

which is the analog of Eq (1.21). In the limit $dt \rightarrow 0$, we can neglect $dM d\dot{S}$ and write a form analogous to Eq (1.22) or go directly to a form analogous to Eq (1.23), namely,

$$M d\dot{S}/dt = (\dot{S} - \dot{P}) \dot{M}_p - F \quad (1.25)$$

If we use Eq (1.19) for $(\dot{S} - \dot{P})$, Eq (1.25) becomes

$$M d\dot{S}/dt = \dot{M}_p^2 / (2\rho A_0) - F \quad (1.26)$$

where F is given by Eq (1.17). In rocketry the force $C_D \dot{M}$ in Eq (1.23) is independent of $(G+D)$ and can be turned on or off. In penetration mechanics the two forces on the right side of Eq (1.26) are connected since the magnitude of the mass loss rate depends on the kind of target being penetrated. In all cases of interest, targets decelerate penetrators, so the right side of Eq (1.26) is negative. This limits \dot{M}_p which achieves its maximum possible value in the extreme case $\dot{P} = 0$ (mud splattering on a hard target). In this case $F=a$ from Eq (1.17) and $\dot{M}_p = 2\rho_p A_0 \dot{S}_0$ from Eq (1.19). the minimum value of \dot{M}_p is zero (no erosion). In this case $\dot{P}=\dot{S}$ in Eq (1.19) and in Eq (1.17) with $M=M_0$. Penetration without erosion occurs for example, when a hard steel ball bearing impacts a typical aluminum target. For moderate striking speeds and soft aluminum, penetration may even occur without deformation of the projectile.

D. Jets

Typical jets stretch and eventually break into fragments because their noses move much faster than their rears. It is possible to make a non-stretching jet (1.51), but this is rarely done in practical devices. Such jets are similar to pre-formed rods if penetration begins after jet formation is complete and Eq (1.26) describes their motion. More generally, penetration begins before formation is complete and stretching must be accounted for as well.

To describe simultaneous addition of mass at the rear of a jet and loss of mass at its front, we can write $\dot{M} = \dot{M}_R - \dot{M}_p$, where $\dot{M}_R > 0$ is the addition rate at its rear, while $\dot{M}_p > 0$ is the addition rate at position P , its front. When formation is complete, $\dot{M}_R \rightarrow 0$ and $\dot{M} = -\dot{M}_p$ as for a pre-formed rod.

For a rod we have been using the symbol A_0 for its cross-sectional area. If the rod is a right circular cylinder, A_0 is its cross-section at every point along its undeformed length. If the rod is tapered slightly front and/or rear or has irregularities like sabot contact grooves along its length, then A_0 is the cross section averaged over the rod length such that its product with the density and length gives the measured mass, $M_0 = \rho_p A_0 L_0$ initially, or $M = \rho_p A_0 L$ at a later time with $L < L_0$. In this approximation any slight

change in A_0 with time is ignored. For the jet we will be considering, such changes cannot be ignored. This jet happens to be tapered (narrower at the front than at the rear). Here we will give A_0 the same meaning, namely, the average cross-section over the jet length at any time, t . However, when the jet stretches like a rubber band or piece of taffy being pulled, A_0 decreases too much to ignore. That is, its time rate of change, $\dot{A}_0 < 0$, is not negligible. Since this stretching occurs even after formation ($\dot{M}_R = 0$) and in free space ($\dot{M}_p = 0$), it is a constant mass process and $\dot{M} = \rho_p (A_0 \dot{L} + \dot{A}_0 L) = 0$, or $\dot{A}_0 = -A_0 \dot{L}/L$ gives us an estimate of this effect. In other words, if we observe a jet in free flight after formation and measure L , \dot{L} and A_0 as time goes on, we can estimate \dot{A}_0 . We then assume that the same process occurs during formation and erosive penetration, making another contribution to the time rate of change of the length, namely, \dot{L} (stretching) $= L|\dot{A}_0|/A_0 > 0$. This can be added to the contributions from mass loss and addition to give a total rate

$$\begin{aligned}\dot{L} &= (\dot{M}_R - \dot{M}_p)/(\rho_p A_0) + (L|\dot{A}_0|/A_0)(\rho_p/\rho_p) \\ &= (\dot{M} + \rho_p L|\dot{A}_0|)/(\rho_p A_0) = (\dot{M} + \dot{\mu})/(\rho_p A_0)\end{aligned}\quad (1.27)$$

where we have introduced the symbol $\dot{\mu} = \rho_p L|\dot{A}_0| > 0$ for the stretching rate, with $\dot{M} = \dot{M}_R - \dot{M}_p$ as before. For a pre-formed ($\dot{M}_R = 0$), non-stretching ($\dot{\mu} = 0$) rod, Eq (1.27) becomes Eq (1.18) above. The form for a non-stretching, still-forming jet ^(1.51) is obvious. Generally speaking, $\dot{M}_R > \dot{M}_p$ as we shall see, so $\dot{M} > 0$ during formation and $\dot{L} > 0$. After formation ($\dot{M}_R = 0$), the sign of \dot{L} will depend on the sign of $(-\dot{M}_p + \dot{\mu})$.

At any instant in time a jet always has a definite mass and length. However, because of jet taper, the center of mass will not be located at the midpoint of its length, but somewhat to the rear of this point. Let C be the geometrical center of the jet length. In a one-dimensional problem such as we are considering any point may be chosen to describe the motion since all forces are exerted through every point along the penetrator length. Consequently, we can write the analogs of Eqs (1.19) and (1.20) as

$$\dot{P} = \dot{C} + \dot{L}/2 = \dot{C} + (\dot{M} + \dot{\mu}) I_0 \quad (1.28)$$

and

$$\dot{R} = \dot{C} - \dot{L}/2 = \dot{C} - (\dot{M} + \dot{\mu}) I_0 \quad (1.29)$$

where

$$I_0 = (2 \rho_p A_0)^{-1} \quad (1.30)$$

Since \dot{L} may well be positive as we have noted, then $\dot{R} < \dot{P}$ is a distinct possibility as is $\dot{R} > \dot{P}$ if formation is complete and erosion is severe. If we have a non-stretching jet ($\dot{\mu} = 0$), then $A = A_0$, $C = S$ and after formation is complete Eqs (1.28) and (1.29) reduce to Eqs (1.19) and (1.20). After formation ($\dot{M}_R = 0$) of a stretching jet, it is possible that $\dot{\mu} = \dot{M}_p$ so $\dot{P} = \dot{C} = \dot{R}$. Usually, however, $\dot{\mu} > \dot{M}_p$ so $\dot{R} < \dot{P}$.

We must also generalize our equation of motion to describe a forming, stretching, eroding jet. The mass added to the rear, dM_R , has speed \dot{R} , and net mass change is $dM = dM_R - dM_p$. Thus

$$[(M + dM_R - dM_p)(\dot{C} + d\dot{C}) + \dot{R}dM_R + \dot{P}dM_p] - M\dot{C} = -Fdt \quad (1.31)$$

Now when we pass to the limit $dt \rightarrow 0$ and neglect $dM_R d\dot{C}$ and $dM_p d\dot{C}$ we find (upon dividing by dt)

$$M d\dot{C}/dt = -(\dot{C} + \dot{R}) \dot{M}_R + (\dot{C} - \dot{P}) \dot{M}_p - F \quad (1.32)$$

We can add \dot{C} to \dot{R} in Eq (1.29) to replace the coefficient of \dot{M}_R in Eq (1.32) and subtract \dot{C} from both sides of Eq (1.28) to replace the coefficient of \dot{M}_p and obtain

$$M d\dot{C}/dt = -[2\dot{C} - (\dot{M} + \dot{\mu}) I_0] \dot{M}_R - (\dot{M} + \dot{\mu}) I_0 \dot{M}_p - F \quad (1.33)$$

where $\dot{M} = \dot{M}_R - \dot{M}_p$. Simplifying leads to

$$M d\dot{C}/dt = I_0 \dot{M} (\dot{M} + \dot{\mu}) - (2\dot{C} \dot{M}_R + F) \quad (1.34)$$

This equation reduces to Eq (1.26) for a non-stretching jet ($\dot{\mu} = 0$, $A = A_0$, $C = S$) which has completed its formation ($\dot{M}_R = 0$). Thus a typical jet differs from a rod in three respects, $\dot{M}_R > 0$, $\dot{\mu} > 0$ and taper.

II. SOLUTIONS

A. Solutions Without Viscosity

1. Constant Mass Projectile

Our method in this report is to begin with the simplest case and add complications as they are needed. Without erosion, $\dot{M}_p = 0$, $M = M_0$, and Eq (1.26) becomes

$$M_0 d\dot{S}/dt = - (a + c\dot{S}^2) \quad (2.1)$$

where we have used Eq (1.17) with $b = 0$, since η is assumed to be unimportant in Eq (1.16), and with $\dot{p} = \dot{S}$ in Eq (1.19). Two integrations of Eq (2.1) with respect to time give us

$$\dot{S} = \sqrt{a/c} \tan [Y_0 - \sqrt{ac} (t - t_0)/M_0] \quad (2.2)$$

and

$$S = S_0 + (M_0/c) \ln \{ \cos [Y_0 - \sqrt{ac} (t - t_0)/M_0] / \cos Y_0 \} \quad (2.3)$$

where

$$Y_0 = \tan^{-1} (\dot{S}_0 / \sqrt{a/c}) \quad (2.4)$$

while t_0 , S_0 and \dot{S}_0 are initial values. In this simple case we can eliminate time between Eqs. (2.2) and (2.3) to obtain the solution in the S, \dot{S} phase plane

$$\dot{S} = \sqrt{a/c} \tan \cos^{-1} \{ (\cos Y_0) \exp [(c/M_0)(S - S_0)] \} \quad (2.5)$$

Thus we can express all three solutions in the \dot{S}, t plane, the S, t plane and the \dot{S}, S plane in terms of a finite combination of classical elementary

functions. This is not usually possible for non-linear equations, as we shall see.

We can also transform Eq (2.1) to the phase plane before we integrate if we divide by $\dot{S} = dS/dt$ to obtain the separated form

$$\dot{S} d\dot{S}/(a+c\dot{S}^2) = -dS/M_0 \quad (2.6)$$

If we have no time-dependent information as is usually the case in penetration mechanics, a solution in the phase plane is all we need. The elimination of the time variable in either the differential or integral form touches on an important characteristic of mechanics. In either classical or quantum mechanics, time is reversible and the equations of motion are invariant with respect to its inversion. Of course this is not true of the world in general as is abundantly illustrated by the applications of irreversible thermodynamics in physics, chemistry and biology (2.1). An integration of Eq (2.6) gives

$$\dot{S} = \sqrt{(a/c) \{ [1 + (\dot{S}_0 \sqrt{a/c})^2] \exp [-(2c/M_0)(S-S_0)] - 1 \}} \quad (2.7)$$

Clearly Eqs (2.5) and (2.7) must be equivalent. This can be shown as follows. Equate the squares of both equations to eliminate \dot{S} , and recall the identity $\tan^2 x = \sec^2 x - 1$, so

$$\begin{aligned} \sec^2 [\cos^{-1} \{ (\cos Y_0) \exp [(c/M_0)(S-S_0)] \}] \\ = [1 + (\dot{S}_0 \sqrt{a/c})^2] \exp [-(2c/M_0)(S-S_0)] \end{aligned} \quad (2.8)$$

after adding 1 to both sides. Now take the square root and recall that $\sec x = 1/\cos x$, so

$$1/[(\cos Y_0) \exp [(c/M_0)(S-S_0)]] = \sqrt{[1 + (\dot{S}_0 \sqrt{a/c})^2]} \exp [-(c/M_0)(S-S_0)] \quad (2.9)$$

Now multiply by $\exp [(c/M_0)(S-S_0)]$, square, and recall the identity $1/\cos^2 x = 1 + \tan^2 x$, so

$$1 + \tan^2 [\tan^{-1}(\dot{S}_0/\sqrt{a/c})] = 1 + (\dot{S}_0/\sqrt{a/c})^2 \quad (2.10)$$

where we have used Eq (2.4) for Y_0 . Since Eq (2.10) is an identity, Eqs (2.5) and (2.7) are equivalent and we can use whichever form seems to be more convenient in our calculations.

A frequent case of interest in penetration mechanics is embedment in a semi-infinite target. The problem ends when the penetrator is brought to rest ($\dot{S} \rightarrow 0$). If we choose the origin of our coordinate system at the target face, then the initial position of the center of mass is $S_0 = -L_0/2$. The final position of the center of mass is S_E (at embedment) and the final position of the nose of the penetrator is $P_E = S_E + L_0/2 = S_E - S_0$. This is also the crater depth. If we let $\dot{S} = 0$ in Eq (2.7), for example, and solve for $(S - S_0)$ with $S = S_E$, we find

$$P_E = (M_0/c) \ln \sqrt{1 + (\dot{S}_0/\sqrt{a/c})^2} \quad (2.11)$$

which gives us the penetration depth as a function of the striking speed, \dot{S}_0 , for given penetrator mass, M_0 . The target hardness appears in the parameter a , given by Eq (1.3) while the target density appears through the parameter $c = 5\rho_t A$ in Eq. (1.4). The average area, A , presented to the target by the penetrator during the penetration does not appear under the square root in Eq (2.11) since $\sqrt{a/c} = \sqrt{6Y_t/\rho_t}$, which depends only on the target strength and density. However, for $M_0 = \rho_p A_0 L_0$, $(M_0/c) = (2L_0)(\rho_p/\rho_t)/(A/A_0)$ with $(A/A_0) \geq 1$, depending on whether or not nose deformation has taken place.

If we take the derivative of Eq (2.11) with respect to \dot{S}_0 , we find the slope,

$$dP_E/d\dot{S}_0 = (M_0/a) \dot{S}_0 / [1 + (\dot{S}_0/\sqrt{a/c})^2], \quad (2.12)$$

which vanishes in both extremes of small striking speed ($\dot{S}_0 \rightarrow 0$) and large striking speed ($\dot{S}_0 \rightarrow \infty$) and has positive values in between. By setting the second derivative with respect to \dot{S}_0 equal to zero, it is easy to show that $\dot{S}_0 = \sqrt{a/c}$ is an inflection point. Thus Eq (2.11) describes a situation in which the penetration depth increases rapidly at first as \dot{S}_0 is increased above

zero, but eventually approaches a situation in which further increase in striking speed has little effect. By contrast, an increase in penetrator mass always increases penetration depth in a linear manner. The advantage of increasing penetrator mass rather than striking speed at high speeds has been known for a long time. For example, it was mentioned by Bethe more than forty years ago (2.2). The law of diminishing returns expressed by Eq (2.11) is sometimes called a sigmoid or lazy -S curve. Of course, we can also set $\dot{S} = 0$ in Eq (2.5) to obtain

$$P_E = -(M_0/c) \ln \cos \tan^{-1} (\dot{S}_0 \sqrt{a/c}) \quad (2.13)$$

which has Eq (2.12) as its slope as well.

Another common case in penetration mechanics is perforation of a finite plate. If T_0 is the plate thickness, then we can find the residual speed by letting $S = T_0$ in Eq (2.7) or Eq (2.5). Alternatively, we could choose another criterion for perforation and let $P = S - S_0 = T_0$. Various criteria for ballistic limits as well as the role of "breakout" effects will be discussed in the next chapter. For example, a ballistic limit might be defined by the simultaneous conditions $\dot{S} = 0$ and $P = T_0$, so letting $P_E = T_0$ in Eqs (2.11) or (2.13) enables us to find the limit speed, \dot{S}_{01} .

2. Eroding Projectile

In other fields ablation or erosion seems to depend on the speed with which the object being ablated moves through the medium responsible for its erosion. The example of a space vehicle re-entering the earth's atmosphere comes to mind. A simple form which expresses such a dependence is

$$\dot{M} = -\mu_0 \dot{P} \quad (2.14)$$

where $\mu_0 > 0$ is constant. As we shall see, this form is not only reasonable (agreeing with trends in other fields), but enables us to describe many observations in penetration mechanics rather closely. In addition, it enables us to give an alternate derivation of the density law which has been used for

so long to describe jet penetration. If there is a nose speed, \dot{P} , below which erosion ceases, then we can set $\mu_0 = 0$ for \dot{P} less than this value, and continue the solution as in the previous sub-section. However, there is no evidence that erosion, once begun, ceases below some speed $\dot{P} > 0$.

An integration of Eq (2.14) gives us

$$M = M_0 - \mu_0 P \quad (2.15)$$

since $P_0 = 0$ in the coordinate system we have chosen.

If we use $\dot{M}_p = |\dot{M}| = \mu_0 \dot{P}$ from Eq (2.14) in Eq (1.19) and solve for \dot{S} , we find

$$\dot{S} = (1 + \mu_0 I_0) \dot{P} = k \dot{P} \quad (2.16)$$

where $I_0 = (2\rho_p A_0)^{-1}$ is a penetrator characteristic. Since the constant, k , in Eq (2.16) is greater than unity for $\mu_0 > 0$, it is clear that the penetration speed, \dot{P} , is less than the projectile center of mass speed, \dot{S} , as we expect when erosion of the projectile nose is taking place. Now let us use Eq (2.15), Eq (2.16) and $\dot{M}_p = \mu_0 \dot{P}$ in Eq (1.26) with $F = a + c\dot{P}^2$ to obtain

$$M_0 [1 - (\mu_0/M_0)P] k d\dot{P}/dt = - (a + \bar{c}\dot{P}^2) = - F \quad (2.17)$$

where

$$\bar{c} = c - I_0 \mu_0^2 \quad (2.18)$$

may be called the reduced inertial coefficient. From Eq (2.18) we see that the effect of erosion ($\mu_0 > 0$) is to reduce the opposing force of the target while reducing the mass of the projectile. Of course in penetration mechanics (by contrast with rocketry) this tendency for a projectile to accelerate as it loses mass is never so great that the net force on the right side of Eq (2.17) turns positive. An extreme case of considerable interest occurs however when $\bar{c} = 0$ and only the target strength opposes the motion. Since $I_0 = (2\rho_p A_0)^{-1}$

and $c = .5\rho_t A$, we can let $\bar{c} = 0$ in Eq (2.18) and solve for μ_0 to find

$$\mu_0(\max) = \sqrt{\rho_p \rho_t A_0 A} \quad (2.19)$$

Eq (2.19) gives us an estimate of the upper limit for the erosion rate constant μ_0 (with zero as its lower limit). The effects of target and projectile hardness on erosion rate appear through $A > A_0$, the nose deformation. Once we have estimated A from a knowledge of A_0 , then the geometric mean of the densities enables us to estimate an upper limit for μ_0 .

If we have no time-dependent data to describe (which is, unfortunately, the usual case in penetration mechanics), then a solution in the phase plane is sufficient, as we have noted. Let us divide Eq (2.17) by $\dot{P} = dP/dt$ and obtain a separated form in the P, \dot{P} plane.

Integration of this equation gives

$$\dot{P} = \sqrt{(a/\bar{c}) \{ [1 + (\bar{c}/a)(\dot{S}_0/k)^2] [1 - (\mu_0/M_0)P]^{2\bar{c}/(\mu_0 k)} - 1 \}} \quad (2.20)$$

where $(\dot{S}_0/k) = \dot{P}_0$ from Eq (2.16). First let us note that Eq (2.20) reduces to Eq (2.7) for $\mu_0 \rightarrow 0$, $k \rightarrow 1$, $\dot{P} \rightarrow \dot{S}$, $\bar{c} \rightarrow c$. This may be seen by letting $w = -(\mu_0/M_0)P$ and noting that

$$\begin{aligned} \lim_{\mu_0 \rightarrow 0} [1 - (\mu_0/M_0)P]^{2\bar{c}/(\mu_0 k)} &= \lim_{w \rightarrow 0} [(1+w)^{1/w}]^{-2\bar{c}P/(kM_0)} \\ &= \exp [-(2c/M_0)P] \end{aligned} \quad (2.21)$$

by definition of the base of the natural logarithm. Use of $P = S - S_0$ and $\dot{P} = \dot{S}$ completes the demonstration.

For a semi-infinite target, embedment occurs and the motion ceases for $\dot{P} \rightarrow 0$ in Eq (2.20), so

$$P_E = (M_0/\mu_0) \{ 1 - [1 + (\bar{c}/a)(\dot{S}_0/k)^2]^{-\mu_0 k/(2\bar{c})} \} \quad (2.22)$$

which reduces to Eq (2.11) for $\mu_0 \rightarrow 0$, $\bar{c} \rightarrow c$, $k \rightarrow 1$. For perforation of a finite target we might let $P = T_0$ to find the residual speed in Eq (2.20) and the residual mass in Eq (2.15). The slope of Eq (2.22) is

$$dP_E/d\dot{S}_0 = [M_0 \dot{S}_0 / (ak)] / [1 + (\dot{S}_0 / k\sqrt{a/c})^2]^{1+\mu_0 k / (2\bar{c})} \quad (2.23)$$

which reduces to Eq (2.12) for $\mu_0 \rightarrow 0$. Again we see that the slope vanishes for very small and very large \dot{S}_0 with an inflection point at

$$\dot{S}_0 = k\sqrt{a/(\bar{c} + \mu_0 k)} \quad (2.24)$$

which reduces to $\dot{S}_0 = \sqrt{a/c}$ for $\mu_0 \rightarrow 0$.

In the special case $\bar{c} = 0$, Eq (2.20) becomes

$$\dot{P} = \sqrt{(\dot{S}_0/k)^2 + [2a/(\mu_0 k)] \ln [1 - (\mu_0/M_0)P]} \quad (2.25)$$

and

$$P_E = (M_0/\mu_0) \{1 - \exp [-(\mu_0 k/2a)(\dot{S}_0/k)^2]\} \quad (2.26)$$

replaces Eq (2.22). If we use $M_0 = \rho_p A_0 L_0$ and Eq (2.19) in Eq (2.26), we find

$$P_E/L_0 = \sqrt{\gamma \rho_p / \rho_t} \{1 - \exp [-(\mu_0 k)/(2a)(\dot{S}_0/k)^2]\} \quad (2.27)$$

where $\gamma = A_0/A \leq 1$. If the target strength is zero ($a = 0$), this is the classical density law which was originally derived to describe penetration by a jet of constant length as we shall see. The exponential correction factor depends on the target strength through the force a . Since $\mu_0/(2k)$ does not differ greatly from unity in most cases of interest, then for large \dot{S}_0 and small a ,

$(\dot{S}_0)^2/a \gg 1$ and the correction factor is negligible. However, for moderate speeds and hard targets it is not negligible as we shall see.

So far we have considered only the solution in the phase plane, Eq (2.20). This equation is easily separated since the right side is a function of P while the left side is dP/dt . An integration gives us

$$D(\epsilon X, X_0) = [(X_0 \sqrt{a/\bar{c}})/(\epsilon M_0/\mu_0)] (t-t_0) \quad (2.28)$$

with

$$D(\epsilon X, X_0) = \int_X^{X_0} x^{\epsilon-1} (x-1)^{-1/2} dx \quad (2.29)$$

and

$$X = [1+(\bar{c}/a)(\dot{S}_0/k)^2] [1-P/(M_0/\mu_0)]^{1/\epsilon} \quad (2.30)$$

Here $\epsilon = (\mu_0 k)/(2\bar{c})$ is the dimensionless erosion rate. Since X depends on P by Eq (2.30) with $X = X_0$ for $P = 0$ initially, then Eq (2.28) is the solution in the P, t plane. However, the relation between t and P cannot be expressed in terms of a finite combination of classical elementary functions except in special cases.. As is usually the case with non-linear differential equations, the solution involves some sort of special integral, at least for ordinary, low-order equations. Here Eq (2.29) gives the special integral we need. By analogy we might call it a generalized, incomplete, confluent hypergeometric function ^(2.3). We will encounter a number of special integrals as we proceed. There is really no need to name them since they have not been tabulated in standard references anyway. We only need to evaluate them by any one of a number of standard methods, provided we need a time-dependent solution. Usually a phase plane solution will do. In the chapters which follow we will give examples of time-dependent solutions together with methods of evaluating the special integrals by simple procedures. With the advent of electronic calculators, there is no need to create tables of integrals. Particular cases can be evaluated as needed by a few operations on a hand-held calculator, by the push of a function button on a slightly larger calculator, or by means of a subroutine if one's calculator is fully programmable. Once $P(t)$ is found, we can use Eq (2.20) to find the solution in the \bar{P}, t plane as well as Eq (2.15) to find $M(t)$.

Alternatively, we can find $[1-(\mu_0/M_0)P]$ from Eq. (2.20) and use it in Eq (2.17) to find

$$dt = - [(kM_0)/(aX_0^{\epsilon})] [1+(\bar{c}/a)\dot{P}^2]^{\epsilon-1} d\dot{P} \quad (2.31)$$

in the \dot{P} , t plane. An integration gives

$$[\mu_0 \sqrt{a/\bar{c}} X_0^{\epsilon} / (\epsilon M_0)] (t-t_0) = D(\epsilon | Z, Z_0) \quad (2.32)$$

where D has the same form as Eq (2.29), but

$$Z = 1 + (\bar{c}/a)\dot{P}^2 \quad (2.33)$$

is the limit instead of X as in Eq (2.30). Of course $X_0 = Z_0$.

For the special case $\bar{c} = 0$, a similar procedure can be used. By integrating Eq (2.25) we find

$$[(\mu_0 \dot{P}_0)/(\epsilon_1 M_0)] (t-t_0) = d = \int_X^1 x^{-1/2} e^{\epsilon_1(x-1)} dx \quad (2.34)$$

with

$$X = 1 + \ln [1 - (\mu_0/M_0)P]^{1/\epsilon_1} \quad (2.35)$$

where $\epsilon_1 = \mu_0 k \dot{P}_0^2 / (2a)$. By using $[1 - (\mu_0/M_0)P]$ from Eq (2.25) in Eq (2.17) with $\bar{c} = 0$, we find

$$[(\mu_0 \dot{P}_0)/(\epsilon_1 M_0)] (t-t_0) = d = \int_Z^1 x^{-1/2} e^{\epsilon_1(x-1)} dx \quad (2.36)$$

with

$$Z = (\dot{P}/\dot{P}_0)^2 \quad (2.37)$$

instead of X as in Eq (2.35). Thus Eqs (2.34) and (2.36) give the solutions in the P , t and \dot{P} , t planes respectively for the special case $\bar{c} = 0$.

Finally, let us note that the projectile mass never vanishes in cases of interest.

First, for relatively small erosion rates, $\bar{c} > 0$ in Eq (2.18), we can

use Eqs (2.15) and (2.16) to write Eq (2.20) as

$$[1+(\bar{c}/a)\dot{P}^2] = [1+(\bar{c}/a)\dot{P}_0^2] (M/M_0)^{2\bar{c}/(\mu_0 k)} \quad (2.38)$$

Clearly even for $\dot{P} \rightarrow 0$, $M = M_E > 0$ at embedment.

Secondly, for $\bar{c} = 0$, Eq (2.25) can be written as

$$\dot{P} = \dot{P}_0 [1+\epsilon_1^{-1} \ln (M/M_0)]^{1/2} \quad (2.39)$$

so for $\dot{P} \rightarrow 0$, $M_E = M_0 \exp (-\epsilon_1) > 0$ for finite ϵ_1 .

Finally, for $\bar{c} < 0$ we can write Eq (2.20) as

$$(|\bar{c}|/a) \dot{P}^2 = 1 - [1-(|\bar{c}|/a)\dot{P}_0^2]/(M/M_0)^{2|\bar{c}|/(\mu_0 k)} \quad (2.40)$$

Now if $(|\bar{c}|/a) \dot{P}_0^2 \gtrless 1$, then $F \lesseqgtr 0$ in Eq (2.17) and $d\dot{P}/dt \gtrless 0$, so the speed increases, stays constant or decreases. The only realistic case in penetration mechanics is given by the lowermost signs. In this case also, then,

$$M_E = M_0 [1-(|\bar{c}|/a)\dot{P}_0^2]^{\mu_0 k/(2|\bar{c}|)} > 0 \quad (2.41)$$

In short, there should be a residual mass in every case of practical interest, although it may be so small that it cannot be observed in practice. The only cases in which the penetrator can be completely eroded involve either no change in speed or an acceleration during penetration. While these cases are mathematically possible, they do not occur. The extreme case of no penetration at all ($\dot{P} = 0$ always, the case of mud splattering on a steel plate) involves no speed change and complete erosion, but is of little practical interest. After noting this case, it is hard to imagine a case in which acceleration could occur.

3. A Standard Jet

a. Formation

The jet we are considering in this report is formed from a 42° copper cone (81 mm base diameter) collapsed by composition B explosive. In chapter VI below we will describe this jet in more detail and note that its formation rate, \dot{M}_R , and its stretching rate are both constants to a good approximation. We will also note that its formation rate is about ten times bigger than its erosion rate even in dense, hard targets like armor steel. Consequently, for penetration during jet formation it is a good approximation to take the mass change rate to be a constant, \dot{M}_O , which is not much smaller than the formation rate, \dot{M}_R :

$$\dot{M} = \dot{M}_R - \dot{M}_p \approx \dot{M}_R \approx \dot{M}_O \quad (2.42)$$

This approximation will be used only for penetration during jet formation, which for a standoff of about two cone diameters might last for only ten microseconds (compared to 300μs for the entire penetration). This approximation is good enough for our purpose and enables us to write explicit solutions at early times. After jet formation is complete ($\dot{M}_R \rightarrow 0$), the mass change rate in Eq (2.42) is $\dot{M} = -\dot{M}_p = -\mu_O \dot{P}$ by Eq (2.14) as for a rod. If we used Eq (2.42) for penetration of a semi-infinite target by either a rod or a jet, we would face a problem near the end of the embedment. With \dot{M}_p a constant in Eq (1.19), \dot{P} and \dot{S} would differ by a constant and could not vanish together at t_E as they do in Eq (2.16). A constant \dot{M}_p would force us to assume that erosion stops before penetration stops so that $\dot{P} \rightarrow \dot{S}$ before $\dot{S} \rightarrow 0$. This would introduce an unobserved discontinuity in \dot{P} . Eq (2.16) also implies a discontinuity in \dot{P} if there is a discontinuity in erosion ($\mu_O \rightarrow 0$ for $t < t_E$), but does not force us to assume that this occurs so that \dot{P} and \dot{S} may vanish together at t_E .

If we integrate Eq (2.42) we find

$$M = M_O + \dot{M}_O (t - t_O) \quad (2.43)$$

If we use Eq (2.42) in Eq (1.28), we find

$$\dot{C} = \dot{P} - (\dot{M}_O + \mu) I_O \quad (2.44)$$

so $d\dot{C}/dt = d\dot{P}/dt$. We can use these relations in Eq (1.34) to find

$$M_0 [1 + (\dot{M}_0/\dot{M}_0)(t-t_0)] d\dot{P}/dt = - (\bar{a}_F + \bar{b}_F \dot{P} + c \dot{P}^2) \quad (2.45)$$

which is separable. The constants during formation are

$$\bar{a}_F = a - \frac{1}{2} (\dot{M}_0/\dot{M}_0) (\dot{M}_0 + 2\dot{M}_R) \quad (2.46)$$

and

$$\bar{b}_F = b + 2\dot{M}_R \quad (2.47)$$

with the inertial coefficient c unchanged. Here the effect of erosion appears in the relation $\dot{M}_0 < \dot{M}_R$ [Eq (2.42)]. Eq (2.46) says that formation and stretching tends to counteract the resistance due to target hardness, and in fact overwhelms it as we shall see ($\bar{a}_F < 0$). However, Eq (2.47) says that formation leads to a resistive term proportional to \dot{P} even when viscosity is negligible ($b = 0$). Thus the net effect of formation modified by erosion and stretching will depend on target and penetrator properties as well as the speed and must be assessed for individual cases.

The solution forms for Eq (2.45) depend on the value of the discriminant

$$\Delta_F = 4\bar{a}_F c - \bar{b}_F^2 \quad (2.48)$$

For $\Delta_F > 0$,

$$\dot{P} = \delta \tan Y - \beta \quad (2.49)$$

$$P = (M_0/c) \exp (\epsilon_F^+ Y_0) J - (\beta M_0/\dot{M}_0) \{ \exp [\epsilon_F^+ (Y_0 - Y)] - 1 \} \quad (2.50)$$

$$Y = \tan^{-1} [(\dot{P} + \beta)/\delta] = Y_0 - \ln [1 + (\dot{M}_0/\dot{M}_0)(t-t_0)]^{1/\epsilon_F^+} \quad (2.51)$$

$$J = \int_Y^{Y_0} \exp(\epsilon_F^+ x) \tan x \, dx \quad (2.52)$$

with $\delta = \sqrt{\Delta_F}/(2c)$, $\beta = \bar{b}_F/(2c)$ and $\epsilon_F^+ = 2\dot{M}_0/\sqrt{\Delta_F}$. The special integral in Eq (2.52) is mentioned by Gradshteyn and Ryzhik who point out that it cannot be expressed as a finite combination of elementary functions (2.4). The first form of Eq (2.51) is simply Eq (2.49) solved for Y . When this is used in Eq (2.50) and Eq (2.52) we have the solution in the P, \dot{P} plane. The second form in Eq (2.51) gives $Y(t)$ and may be used in Eq (2.49) to obtain the solution in the \dot{P}, t plane (which is expressible as a finite combination of elementary functions), or in Eq (2.50) to obtain the solution in the P, t plane.

For $\Delta_F = 0$, $F = \bar{a}_F (1 + \dot{P}/\sqrt{\bar{a}_F}/c)^2$, so

$$\dot{P} = \alpha \{[(F_0/\bar{a}_F)^{-1/2} + Z/\epsilon_F]^{-1} - 1\} \quad (2.53)$$

$$P = (M_0/c)(F_0/\bar{a}_F)^{1/2} E - (\alpha M_0/\dot{M}_0)[\exp(Z) - 1] \quad (2.54)$$

$$Z = \epsilon_F [(F/\bar{a}_F)^{-1/2} - (F_0/\bar{a}_F)^{-1/2}] = \ln [1 + (\dot{M}_0/M_0)(t - t_0)] \quad (2.55)$$

$$E = \int_0^Z x^{-1} \exp(x) \, dx \quad (2.56)$$

with $\alpha = \sqrt{\bar{a}_F}/c$ and $\epsilon_F = \dot{M}_0/\sqrt{\bar{a}_F}c$. The special integral in Eq (2.56) might be called an incomplete exponential integral.

For $\Delta_F < 0$,

$$\dot{P} = (\gamma^+ - \gamma^- G)/(1 - G) \quad (2.57)$$

$$P = (M_0/\sqrt{-\Delta_F}) G^{\epsilon_F} [\gamma^+ B(1 + \epsilon_F) - \gamma^- B(\epsilon_F)] \quad (2.58)$$

$$G = (\dot{P} - \gamma^+)/(\dot{P} - \gamma^-) = G_0 [1 + (\dot{M}_0/M_0)(t - t_0)]^{-1/\epsilon_F} \quad (2.59)$$

$$B(\epsilon_F) = \int_G^{G_0} (1-x)^{-1} x^{-\epsilon_F} dx \quad (2.60)$$

with $\epsilon_{\bar{F}} = \dot{M}_0 / \sqrt{-\Delta_F}$, and

$$\gamma^{\pm} = (-\bar{b}_F \pm \sqrt{-\Delta_F}) / (2c) \quad (2.61)$$

the special integral in Eq (2.60) might be called a generalized incomplete beta function.

b. Stretching

When jet formation is complete ($t = t_1$), $\dot{M}_R = 0$ and $\dot{M} = -\mu_0 \dot{P}$, so

$$M = M_1 - \mu_0 (P - P_1) \quad (2.62)$$

where M_1 and P_1 are the mass and nose position at time t_1 . If we use $\dot{M} = -\mu_0 \dot{P}$ in Eq (1.28), we find

$$\dot{C} = k\dot{P} - I_0 \mu \quad (2.63)$$

so $d\dot{C}/dt = k d\dot{P}/dt$ and Eq (1.34) becomes

$$kM_1 [1 - (\mu_0/M_1)(P - P_1)] \dot{P} d\dot{P}/dP = - (a + \bar{b}\dot{P} + \bar{c}\dot{P}^2) = -F \quad (2.64)$$

after using $d\dot{P}/dt = \dot{P} d\dot{P}/dP$. Now

$$\bar{b} = \bar{b} + I_0 \mu_0 \dot{P} \quad (2.65)$$

and

$$\bar{c} = c - I_0 \mu_0^2 \quad (2.66)$$

with a unchanged. The form of \bar{c} in Eq (2.66) is almost the same as for an eroding rod in Eq (2.18). However, for a stretching jet ($\dot{P} > 0$) Eq (2.65) says that there is a resistive force proportional to \dot{P} , provided erosion takes place, contrary to the case of a non-stretching rod (with negligible viscosity,

$b = 0$). Jet stretching reduces the area A and so increases $I_0 = (2\pi_j A)^{-1}$. One effect of this is to increase $I_0 \mu_0^2$ in Eq (2.66) which tends to make \bar{c} closer to zero, and decrease target resistance. Another effect is to increase \bar{b} . The net effect of erosion and stretching is complicated and must be assessed for individual jet/target combinations. When $\bar{c} \approx 0$ we have a situation close to the classical density law, as we say in Eq (2.27), modified not only by target hardness but also by the interaction between erosion and stretching, expressed by $I_0 \mu_0 \dot{\mu}$ in Eq (2.65). In some cases, the net effect may not depart greatly from the classical density law.

Now the form of the solutions depends on

$$\Delta = 4a\bar{c} - \bar{b}^2. \quad (2.67)$$

If $\Delta > 0$,

$$(P - P_1) = (M_1 / \mu_0) \{1 - (F/F_1)^{\bar{c}k/2} \exp [\bar{c}k\beta^+(Y_1 - Y)]\} \quad (2.68)$$

$$Y = \tan^{-1} \{(\dot{P}/\alpha) + \beta^+\} \quad (2.69)$$

where F is given by Eq (2.64) and subscript 1 means at time t_1 . Here $\bar{c} = \mu_0 / \bar{c}$ is the dimensionless erosion rate, $k = 1 + I_0 \mu_0$ as before, $\beta^+ = \bar{b} / \sqrt{\Delta}$ and $\alpha = \sqrt{\Delta} / (2\bar{c})$. Eqs (2.68) and (2.69) give the solutions in the P, \dot{P} plane as a finite combination of classic elementary functions. We can solve Eq (2.68) for $[1 - (\mu_0 / M_1)(P - P_1)]$ and use it in Eq (2.64) to obtain

$$kM_1 (F/F_1)^{\bar{c}k/2} \exp [\bar{c}k\beta^+(Y_1 - Y)] d\dot{P}/dt = -F \quad (2.70)$$

which is the differential form in the \dot{P}, t plane since Y and F depend on \dot{P} . This equation is separable, and an integration gives us

$$(t - t_1) = kM_1 F_1^{-\bar{c}k/2} \exp [\bar{c}k\beta^+ Y_1] D^+ \quad (2.71)$$

$$D^+ = \int_{\dot{P}}^{\dot{P}_1} F^{\bar{c}k/2 - 1} \exp [-\bar{c}k\beta^+ Y] d\dot{P} \quad (2.72)$$

These equations give the solution in the t, \dot{P} plane. Once we know $\dot{P}(t)$, we also know $F(t)$ and $Y(t)$ and so $P(t)$ from Eq (2.68) as well as $M(t)$ from Eq (2.62).

If $\Delta = 0$, $F = a (1 + \dot{P}/\sqrt{a/\bar{c}})^2$, so

$$(P - P_1) = (M_1/\mu_0) \{1 - (F/F_1)^{\bar{\epsilon}k/2} \exp [\bar{\epsilon}k \{ (F/a)^{-1/2} - (F_1/a)^{-1/2} \}]\} \quad (2.73)$$

again expressing the solution in the P, \dot{P} plane in terms of a finite combination of elementary functions without special integrals as in Eq (2.68).

If we proceed as before, we find

$$(t - t_1) = k M_1 F_1^{-\bar{\epsilon}k/2} \exp [-\bar{\epsilon}k/\sqrt{F_1}] D^0 \quad (2.74)$$

$$D^0 = \int_{\dot{P}}^{\dot{P}_1} F^{\bar{\epsilon}k/2-1} \exp (\bar{\epsilon}k/\sqrt{F}) d\dot{P}. \quad (2.75)$$

As before, we have the complete solution in all three planes, once we know $\dot{P}(t)$.

If $\Delta < 0$,

$$(P - P_1) = (M_1/\mu_0) \{1 - (F/F_1)^{\bar{\epsilon}k/2} (G_1/G)^{\beta^- \bar{\epsilon}k/2}\} \quad (2.76)$$

$$G = (\dot{P} - \gamma^+) / (\dot{P} - \gamma^-) \quad (2.77)$$

$$\gamma^\pm = (-\bar{b} \pm \sqrt{-\Delta}) / (2\bar{c}) \quad (2.78)$$

and $\beta^- = \bar{b}/\sqrt{-\Delta}$. As expected, Eq (2.76) expresses the solution in the P, \dot{P} phase plane as a finite combination of classical elementary functions.

Proceeding as before, we find

$$(t - t_1) = k M_1 F_1^{(\bar{\epsilon}k/2)} G_1^{\beta^- (\bar{\epsilon}k/2)} D^- \quad (2.79)$$

$$D^- = \int_{\dot{P}}^{\dot{P}_1} F^{[(\bar{\epsilon}k/2)-1]} G^{[-(\beta^-)(\bar{\epsilon}k/2)]} d\dot{P} \quad (2.80)$$

If $\Delta < 0$, because $\bar{c} = 0$, $F = a + \bar{b}\dot{P}$, so

$$(P-P_1) = (M_1/\mu_0) \{1-(F_1/F)^{(a/\bar{b})(k\mu_0/\bar{b})} \exp [-(k\mu_0/\bar{b})(\dot{P}_1-\dot{P})]\} \quad (2.81)$$

and

$$(t-t_1) = kM_1F_1^{(a/\bar{b})(k\mu_0/\bar{b})} \exp [-(k\mu_0/\bar{b})\dot{P}_1] D \quad (2.82)$$

$$D = \int_{\dot{P}}^{\dot{P}_1} F^{-[1+(a/\bar{b})(k\mu_0/\bar{b})]} \exp [(k\mu_0/\bar{b})x] dx \quad (2.83)$$

Instead of working with special integrals which involve \dot{P} as a limit, we can of course work with the inverse functions and express \dot{P} symbolically as a function of t , instead of t as a function of \dot{P} . There is no particular advantage to this procedure, however, so we will not adopt it.

For a constant mass change rate, the approximation we are using during jet formation, Eq (2.42), we can express $\dot{P}(t)$ as a finite combination of classical elementary functions, Eqs (2.51), (2.55) and (2.59), while solutions in the \dot{P}, P and P, t planes involve special integrals. For a mass change rate proportional to the nose speed, we can express $P(\dot{P})$ as such a finite combination, while solutions in the $P(t)$ and $\dot{P}(t)$ planes involve special integrals.

c. Fragmentation

As we shall note later, the jet we are considering starts to fragment at the front first (at time t_2) since the front is thinner than the rear (jet taper). The fragmentation process proceeds to the rear so rapidly that for $t > t_2$ the remaining penetration is accomplished by a train of fragments which are approximately identical in size and shape although their striking speeds are smaller the closer they are to the rear of the jet. These fragments tend to yaw and become misaligned as time goes on and may encounter interference from eroded target and/or jet material which enhances their misalignment and/or yaw. Such matters are highly dependent on the original standoff and the properties of the target and jet. Since interference, yaw and misalignment require a three-dimensional treatment, a detailed theory (which ought to be statistical in nature) is beyond the limits we have set for

ourselves in this report. A later report will discuss such matters theoretically. In this report we will adopt a temporary expedient, an efficiency factor, in place of a theory. This will be explained in Chapter VI below. When stretching ceases ($\dot{\mu} = 0$), each jet fragment can be approximately described as a rod, using the theory of section A2 above.

B. Dimensionless Solutions with Viscosity

So far we have not included viscosity in our solutions, except for section A3 above for a jet. This was done in anticipation of the cases studied below where viscosity does not seem to play a significant role. Viscosity was included for a jet in Eqs (2.47) and (2.65), not because we have any evidence that it is more significant for a jet, but because jet formation and stretching factors require us to include a term involving the first power of the speed in any case. Actually, the presence of such factors makes it even more difficult to discern the role of viscosity. In this section we include the viscosity term even for pre-formed, non-stretching penetrators for the sake of completeness and as an aid to possible future use.

Sometimes non-dimensional formulations can be useful, especially if cases with different parameter values can be represented by a single curve. Such formulations are also more general since they require no choice of a system of units. However, the indiscriminate use of dimensionless formulations in reporting experimental data can often mislead rather than clarify, especially if such data are not accompanied by the original dimensional data. For this reason we always use dimensional formulations in our examples below. Finally, the choice of a dimensionless representation is not unique, as we shall illustrate by a few examples.

1. Constant Mass Projectile

If we add $(-b\dot{S})$ to the right side of Eq (2.1), the form of the solutions will depend on the value of the discriminant

$$\Delta = 4ac - b^2 \quad (2.84)$$

Let us introduce the dimensionless time

$$\bar{\tau} = (\sqrt{ac}/M_0)(t-t_0) \quad (2.85)$$

as well as the parameters $\beta^+ = b/\sqrt{\Delta}$ and $\beta^- = b/\sqrt{-\Delta}$.

For $\Delta > 0$, let us choose the dimensionless displacement

$$\sigma = (c/M_0)(S-S_0) = \ln(\cos Y/\cos Y_0) - \beta^+(Y_0-Y) \quad (2.86)$$

$$\text{where } Y = \tan^{-1}(v+\beta^+) = Y_0 - \bar{\tau} \quad (2.87)$$

$$\text{with } v = \dot{S}/[\sqrt{\Delta}/(2c)] \quad (2.88)$$

being our choice of dimensionless speed. In the $v, \bar{\tau}$ -plane the solution is then

$$v = \tan(Y_0 - \bar{\tau}) - \beta^+ \quad (2.89)$$

which is found from Eq (2.86) with $v = -d\sigma/dY = d\sigma/d\bar{\tau}$, or by solving Eq (2.87) for v . Use of the two forms for Y from Eq (2.87) in Eq (2.86) gives the solutions in the σ, v and $\sigma, \bar{\tau}$ planes. For embedment in a semi-infinite target, $\bar{\tau}$ varies from zero to $\bar{\tau}_E = Y_0 - \tan^{-1}(\beta^+)$, while v varies from v_0 to zero and σ varies from zero to σ_E which can be found by using $Y_E = \tan^{-1}(\beta^+)$ in Eq (2.86). If $P = S - S_0 = T_0$, the target thickness, is our perforation criterion, then replacement of $(S - S_0)$ by T_0 in Eq (2.86) gives us Y_p which can be used to find $(Y_0 - \bar{\tau})$ or $\bar{\tau}$ in Eq (2.87) and so v_p in Eq (2.89). Such a choice of dimensionless solutions is not unique, of course. For example, we can use $\bar{\tau}/\bar{\tau}_E$ which varies from zero to one as does σ/σ_E while v/v_0 varies from one to zero for a semi-infinite target, and so on.

Another formulation might use $\alpha = \sqrt{\Delta}/(4ac)$ and

$$\tau = \alpha \bar{\tau} = \sqrt{\Delta}/(4ac) \bar{\tau} = [\sqrt{\Delta}/(2M_0)](t-t_0) \quad (2.90)$$

instead of Eq (2.85), replacing $\bar{\tau}$ by τ/α in Eqs (2.87) and (2.89). Since

$\tau/\tau_E = \bar{\tau}/\bar{\tau}_E$, there is some advantage to using ratios. In another type of problem where $4ac$ is expected to be less important than b^2 , we might use a formulation involving $\sqrt{-\Delta/b^2} = 1/\beta^-$ and dimensionless time $(b/M_0)(t-t_0)$.

For $\Delta = 0$, $b = 2\sqrt{ac}$, $F = a(1+v)^2$, and

$$\sigma = \ln [(1+v_0)/(1+v)] - [(1+v)^{-1} - (1+v_0)^{-1}] \quad (2.91)$$

$$v = [\bar{\tau} + (1+v_0)^{-1}]^{-1} - 1 \quad (2.92)$$

$$\sigma = \ln [1 + (1+v_0)\bar{\tau}] - \bar{\tau} \quad (2.93)$$

where $\bar{\tau}$ is still given by Eq (2.85) but

$$v = \dot{S}/\sqrt{a/c} \quad (2.94)$$

instead of Eq (2.88). For $v = 0$ in Eq (2.91) we find $\bar{\tau}_E = v_0/(1+v_0)$ and σ_E from Eq (2.90), and so on.

For $\Delta < 0$,

$$\sigma = \ln \{ [(1-G)/(1-G_0)] (G_0/G)^{1/2} \} - \beta^- \ln (G_0/G)^{1/2} \quad (2.95)$$

$$G = G_0 \exp (-2\tau) = (v+\beta^- - 1)/(v+\beta^- + 1) \quad (2.96)$$

$$\tau = [\sqrt{-\Delta}/(2M_0)](t-t_0) \quad (2.97)$$

$$v = [(1-\beta^-) + (1+\beta^-)G]/[1-G] \quad (2.98)$$

for $v = \dot{S}/[\sqrt{-\Delta}/(2c)]$ instead of Eq (2.88) or Eq (2.94). In Eq (2.97) we have chosen τ to be like Eq (2.90).

For cases with negligible viscosity, only the case $\Delta > 0$ is of interest since $a > 0$ and $c > 0$. Eqs (2.86) to (2.89) reduce in an obvious way for $\beta^+ = b = 0, \sqrt{\Delta} = 2\sqrt{ac}$ to Eqs (2.2) to (2.5) or (2.7).

Fig. 2.1 shows curves of a particular choice of dimensionless speed

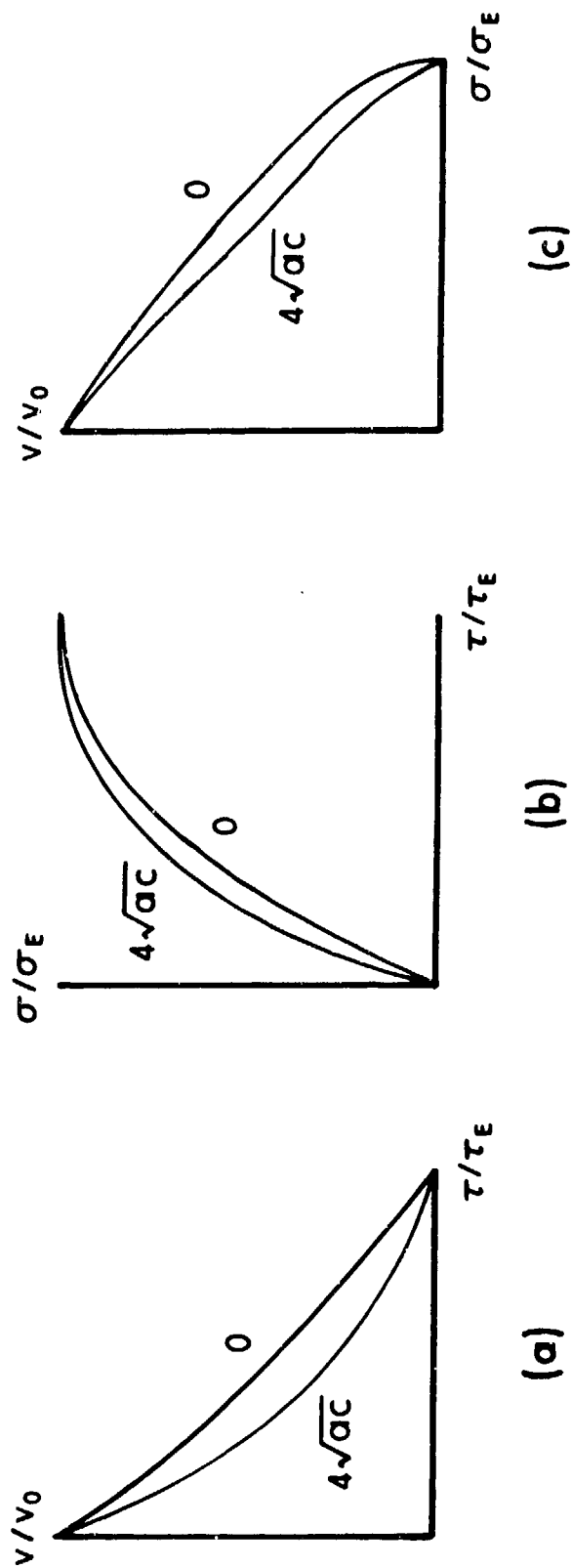


Fig. 2.1. Dimensionless solutions for constant projectile mass with target viscosity, b , as parameter ($b = 0$ and $b = 4\sqrt{ac}$ with $\Delta = (4ac - b^2)$ and $v_0 = 1$).

and displacement versus dimensionless time and each other for two values of b , namely, $b = 0$ ($\Delta > 0$) and $b = 4\sqrt{ac}$ ($\Delta < 0$). The curves for $b = 2\sqrt{ac}$ ($\Delta = 0$) lie between.

2. Eroding Projectile

Since we are adding $(-b\dot{P})$ to the right side of Eq (2.17), the solution forms will depend on

$$\Delta = 4a\bar{c} - b^2 \quad (2.99)$$

where $\bar{c} = c - I_0 u_0^2$ is given by Eq (2.18).

For $\Delta > 0$, let $\alpha^+ = \sqrt{\Delta}/(2\bar{c})$, $\beta^+ = b/\sqrt{\Delta}$, $\bar{\epsilon} = \mu_0/\bar{c}$ and $k = 1 + \mu_0 I_0$, so $\dot{P} = \alpha^+ v$, and

$$\bar{\epsilon} \sigma = (\bar{c}/M_0) P = \{1 - (F/F_0)^{\bar{\epsilon} k/2} \exp [-\beta^+ \bar{\epsilon} k (Y - Y_0)]\} \quad (2.100)$$

$$(F/a) = 1 + (b/a)(\alpha^+ v) + (\bar{c}/a)(\alpha^+ v)^2 \quad (2.101)$$

$$Y = \tan^{-1} (v/\beta^+) \quad (2.102)$$

In this formulation α^+ has the dimensions of speed, although β^+ , $\bar{\epsilon}$ and k are dimensionless as are the variables σ and v . When $b = \beta^+ = 0$, $\alpha^+ \rightarrow \sqrt{a/\bar{c}}$ and Eq (2.100) reduces to Eq (2.20) solved for $P(\dot{P})$. Let

$$\tau = [a/(M_0 \alpha^+)] (t - t_0) = k \exp [\beta^+ \bar{\epsilon} k Y_0] (F_0/a)^{-\bar{\epsilon} k/2} (D^+) \quad (2.103)$$

$$\text{with } D^+ = \int_v^{v_0} (F/a)^{\bar{\epsilon} k/2 - 1} \exp [-\beta^+ \bar{\epsilon} k Y] dv. \quad (2.104)$$

Here τ and D^+ are both dimensionless. When $b = \beta^+ \rightarrow 0$, $\alpha^+ \rightarrow \sqrt{a/\bar{c}}$, Eq (2.103) reduces to Eq (2.32), since $\bar{\epsilon} = (\mu_0 k)/(2\bar{c}) = \bar{\epsilon} k/2$, $X_0 = 1 + v_0^2$ by Eq (2.30) and $(F/a) = 1 + v^2 = x$ from Eqs (2.101) and (2.29), so $D^+ \rightarrow D$.

From Eq (2.15) and Eq (2.100) we can define a dimensionless mass

$$m = M/M_0 = 1 - \bar{\epsilon} \sigma. \quad (2.105)$$

Once we know $v(\tau)$ from Eqs (2.103) and (2.104), we can find $\sigma(v)$ or $\sigma(\tau)$ from Eqs (2.100) to (2.102) and $m(v)$ or $m(\tau)$ from Eq (2.105).

For $\Delta = 0$, let $\dot{P} = \alpha v = \sqrt{a/\bar{c}} v$, so $(F/a) = (1+v)^2$, and

$$\bar{\epsilon} \sigma = 1 - [(1+v)/(1+v_0)]^{\bar{\epsilon} k} \exp [\bar{\epsilon} k \{ (1+v)^{-1} - (1+v_0)^{-1} \}] \quad (2.106)$$

$$\tau = [a/(M_0 \alpha)] (t - t_0) = k(1+v_0)^{-\bar{\epsilon} k} \exp [-\bar{\epsilon} k (1+v_0)^{-1}] D^0 \quad (2.107)$$

$$D^0 = \int_v^{v_0} (1+v)^{\bar{\epsilon} k - 2} \exp [\bar{\epsilon} k (1+v)^{-1}] dv \quad (2.108)$$

Even though Eq (2.106) is somewhat simpler than Eq (2.100), it is still transcendental and cannot be made separable by solving for $\dot{P}(P)$ explicitly. Since $b = 2\sqrt{a\bar{c}} > 0$ for $\Delta = 0$, there is no analog in section A 2 above. The analog of Eqs (2.106) to (2.108) appears in section A3 above in Eqs (2.73) to (2.75). The solution forms are the same. Only the parameters might differ ($\bar{u} \geq 0$, $\bar{b} \geq b$). The same correspondence holds for other values of Δ , so there is no need for a special non-dimensional discussion for jets.

For $\Delta < 0$, let $\alpha^- = \sqrt{-\Delta}/(2\bar{c})$, $\beta^- = b/\sqrt{-\Delta}$, $\dot{P} = \alpha^- v$, so

$$\bar{\epsilon} \sigma = 1 - (F/F_0)^{\bar{\epsilon} k/2} (G_0/G)^{\beta^- \bar{\epsilon} k/2} \quad (2.109)$$

$$(F/a) = 1 + (b/a)(\alpha^- v) + (\bar{c}/a)(\alpha^- v)^2 \quad (2.110)$$

$$G = (\alpha^- v - \gamma^+) / (\alpha^- v - \gamma^-) \quad (2.111)$$

$$\gamma^\pm = (-b \pm \sqrt{-\Delta}) / (2\bar{c}) \quad (2.112)$$

$$\tau = [a/(M_0 \alpha^-)] (t - t_0) = k(F_0/a)^{-\bar{\epsilon} k/2} G_0^{\beta^- \bar{\epsilon} k/2} (D^-) \quad (2.113)$$

$$D^- = \int_v^{v_0} (F/a)^{\bar{\epsilon} k/2 - 1} G^{-\beta^- \bar{\epsilon} k/2} dv \quad (2.114)$$

the analogs of Eqs (2.76) to (2.80). The analogs of Eqs (2.81) to (2.83) are also easily written as are other special cases.

Fig 2.2 illustrates some non-dimensional forms with $\bar{\epsilon}$ as parameter and no target viscosity. The curves with $\bar{\epsilon} = 0$ in Fig. 2.2 are the same as those with $b = 0$ in Fig. 2.1 above. When $\bar{\epsilon} = 1$, ($b = 0$), $v = 1 - \tau$, $\sigma = \tau (1 - .5\tau) = .5 (1 - v^2)$, so the solution forms are particularly simple. For large $\bar{\epsilon} = \mu_0/\bar{c}$, that is, large erosion rate, small \bar{c} , v/v_0 decreases relatively slowly during most of the penetration and very rapidly toward the end. The penetration depth, σ/σ_E , becomes more linear in time as does the remaining mass, M/M_0 , which approaches zero. This behavior is characteristic of high speed rods and jets before fragmentation, although in the latter case it is modified by the fact that $\bar{b} > 0$ even if $b = 0$. However, the square-wave approximation for v/v_0 , indicated by the dashed line in Fig. 2.2 is not observed experimentally as we shall see. Consequently, steady-state theories which assume this approximation are not correct. Neither are quasi-steady state theories which try to keep and yet reject this approximation.

3. Standard Jet

Once formation is complete, the solution forms are identical to those for an eroding projectile in II.B.2 above. We only need to use \bar{b} from Eq (2.65) instead of b .

During formation the solution forms depend on the value of Δ_F in Eq (2.48). Let

$$\tau = (\dot{M}_0/M_0) (t-t_0) \quad . \quad (2.115)$$

For $\Delta_F > 0$, let $\dot{P} = [\sqrt{\Delta_F}/(2c)] v = \delta^+ v$, and $\beta^+ = \bar{b}_F \sqrt{\Delta_F}$, so Eqs (2.49) to (2.52) become

$$\sigma = (c/M_0) P = J \exp (\bar{\epsilon}_F^+ Y_0) - [\bar{b}_F/(2\dot{M}_0)] \{ \exp [\bar{\epsilon}_F^+ (Y_0 - Y)] - 1 \} \quad (2.116)$$

$$Y = \tan^{-1} (v + \beta^+) = Y_0 - \ln (1 + \tau)^{1/\bar{\epsilon}_F^+} \quad (2.117)$$

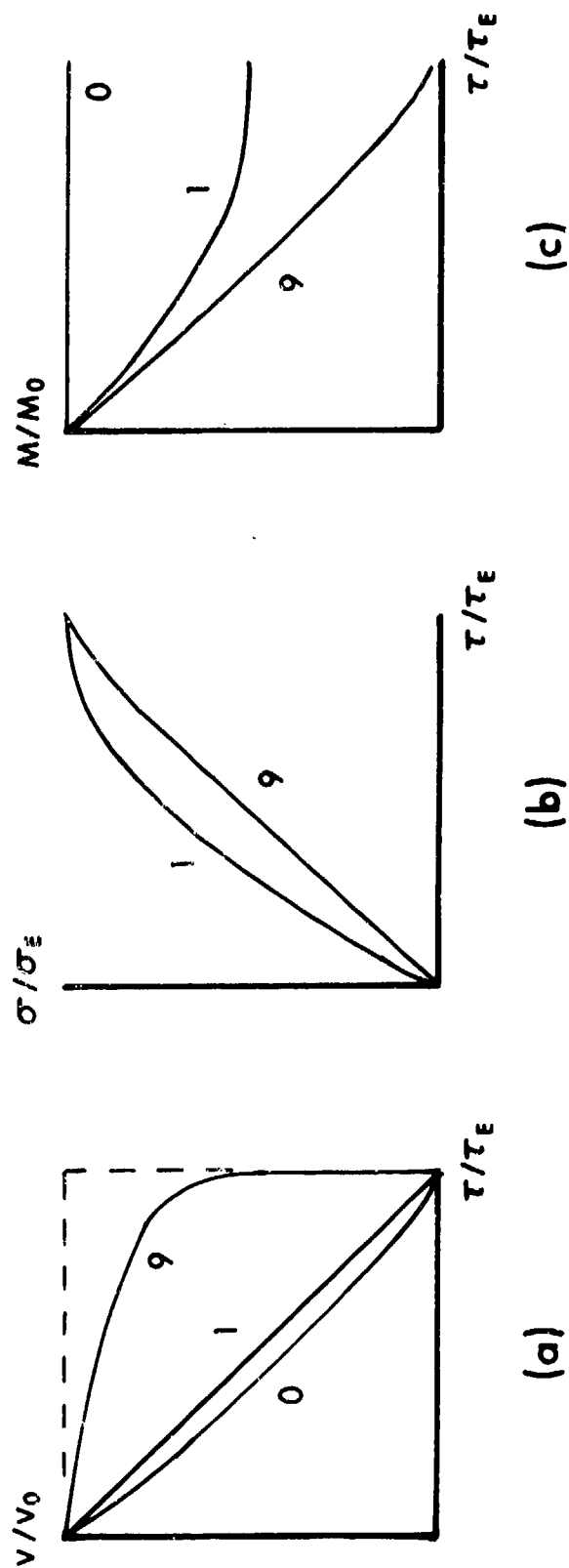


Fig. 2.2. Dimensionless speed (v), displacement (σ) and time (τ) for an eroding projectile penetrating a semi-infinite target with no viscosity. Erosion, $\bar{\epsilon} = \mu_0/\bar{c}$, is the parameter labelling the curve.

with ϵ_F^+ and J as before.

For $\Delta_F = 0$, let $\dot{P} = \sqrt{\bar{a}_F/c} v = \alpha v$, so $(F/\bar{a}_F) = (1+v)^2$, and

$$\sigma = (c/M_0) P = E (1+v) - (\alpha c/\dot{M}_0) [\exp(Z)-1] \quad (2.118)$$

$$Z = \epsilon_F [(1+v)^{-1} - (1+v_0)^{-1}] = \ln(1+\tau) \quad (2.119)$$

with ϵ_F and ϵ as before.

For $\Delta_F < 0$, let $\dot{P} = (\sqrt{-\Delta_F}/c) v = \delta^- v$, $g^\pm = \gamma^\pm/\delta^-$, so

$$\sigma = (c/M_0) P = [g^+ B(1+\epsilon_F^-) - g^- B(\epsilon_F^-)] G^{\epsilon_F^-} \quad (2.120)$$

$$G = (v-g^+)/(v-g^-) = G_0 (1+\tau)^{-1/\epsilon_F^-} \quad (2.121)$$

with ϵ_F and B as before.

III. EXAMPLES OF COMPACT PENETRATORS

A. Semi-infinite Targets

1. Phenomenology

When a brittle sphere strikes a thick target above a certain threshold speed it breaks into pieces and penetrates as a more or less compact collection of fragments. Just below the threshold speed the sphere recovered from the bottom of the crater after target sectioning will appear to be intact. However, there will be cracks, some nearly joined to each other and the projectile surface, such that the removal process may cause the pieces to separate. As the striking speed increases, the number of pieces recovered also increases until a speed is reached at which it is appropriate to speak of projectile shatter. Fig. 3.1 shows the number of pieces recovered as a function of striking speed for two sizes of hard steel spheres impacting a mild steel target. The speed at which breakup begins can be called \dot{S}_{OF} , the striking speed threshold for fracture. The larger (20 mm diameter) sphere breaks into more pieces at a given striking speed than the smaller (12.7 mm diameter) but has about the same threshold speed.

Fig. 3.2 shows the number of pieces ~~recovered~~ for the 20 mm sphere impacting three types of steel target of different hardness values. The lowest curve is the same as in Fig. 3.1. The uppermost curve is for the hardest target. Clearly, target hardness as well as projectile diameter (and hardness) influence the number of fragments produced. However, within the experimental accuracy available, there is almost no influence on the threshold speed, \dot{S}_{OF} . Near $\dot{S}_0 = 1 \text{ mm}/\mu\text{s}$ the rate at which the number of fragments increases with striking speed seems to decrease. One might conjecture that by 1.5 mm/ μs , the projectile is shattered to such an extent that further pulverization will make little difference in the penetration process. More will be said about this below. Figs. 3.1 and 3.2 are taken from a report by Weimann (3.1).

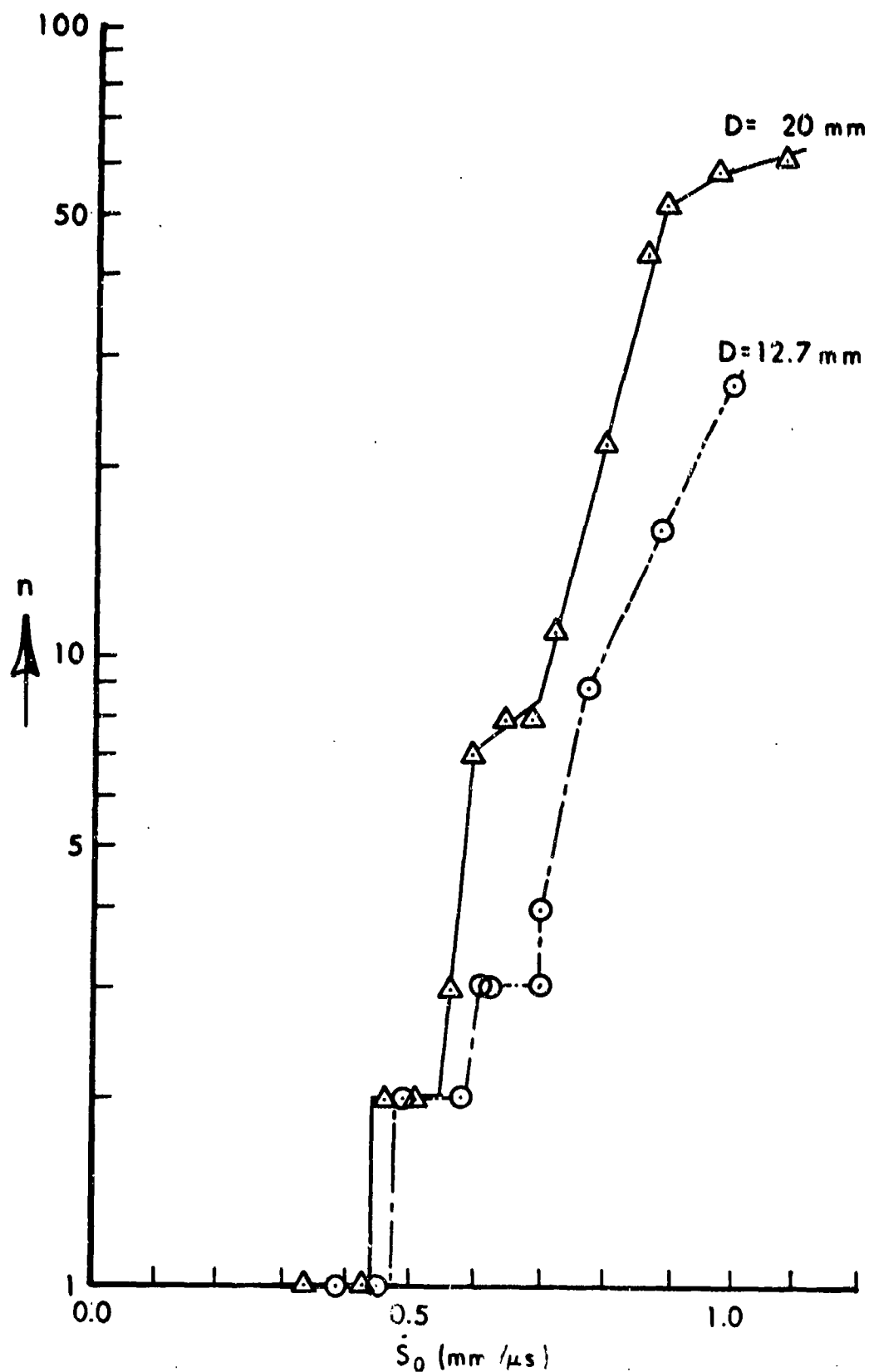


Fig. 3.1. Number of fragments recovered from a mild steel target struck by hard steel spheres of two different diameters at various speeds.

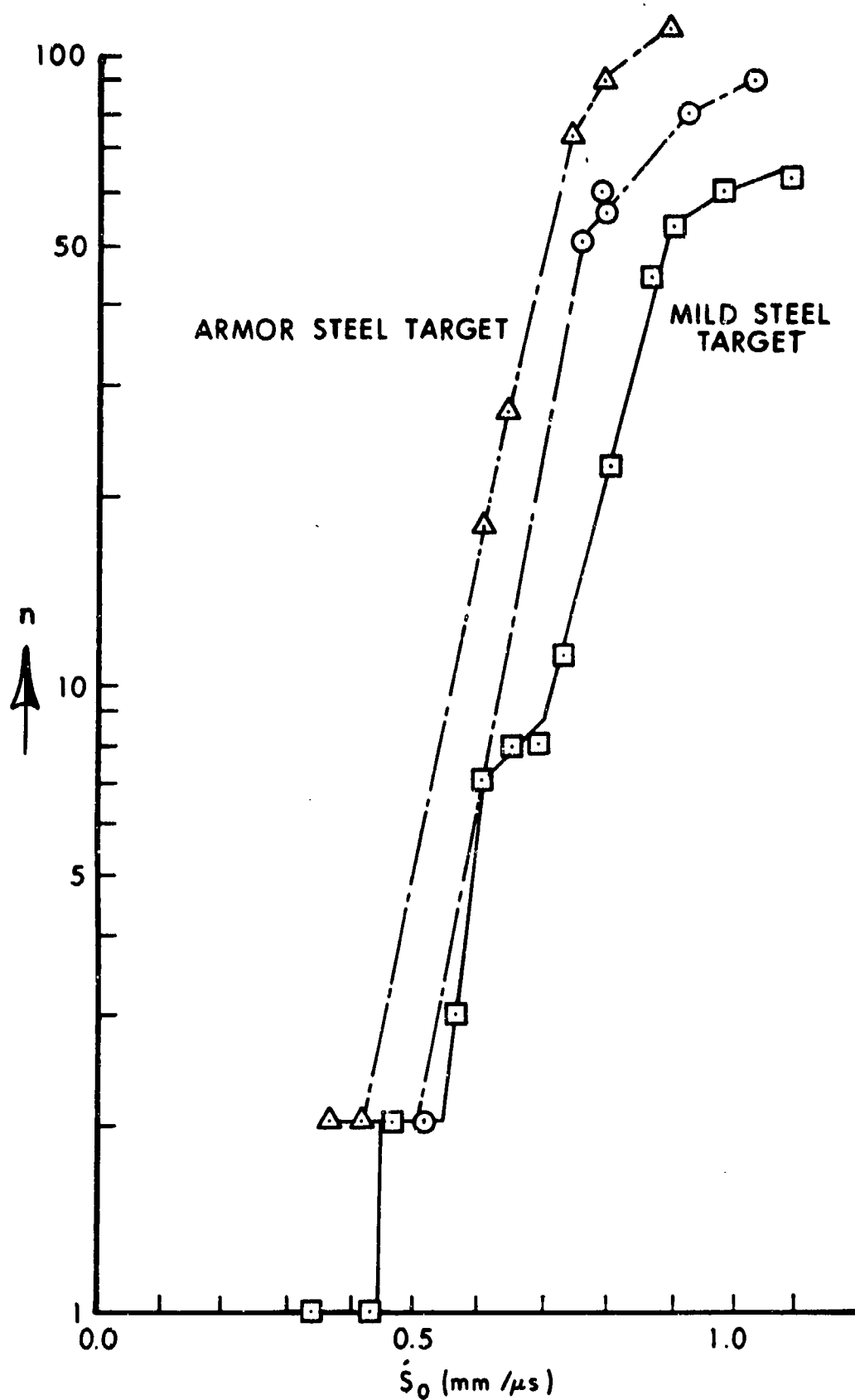


Fig. 3.2. Number of fragments recovered from three steel targets struck by a 20mm hard steel sphere at various speeds.

When a ductile sphere strikes a target, it flattens out, so that its time-average cross-sectional area presented to the target, A , is greater than its initial cross-sectional area, A_0 . This is illustrated in Fig. 3.3 which shows a series of 12.7 mm softened steel spheres recovered from hard aluminum targets (3.2). As the striking speed is increased from 0.7 to 1.6 mm/ μ s, the recovered projectiles are found to be progressively more flattened, but are still unbroken. The radial (D_r) and axial or longitudinal (D_l) diameters given in the Figure measure this effect. The crater depth or deepest position of the projectile nose at embedment, P_E , is also given. For $\dot{S}_0 = .863$ mm/ μ s, P_E is less than the original sphere diameter ($D_0 = 12.7$ mm) but greater than the deformed longitudinal diameter ($D_l = 10.75$ mm). For lower striking speeds the sphere is not yet buried in the target and is easily removed if it has not already rebounded. For higher speeds, some rebound may occur, but friction can keep the projectile from leaving the target. A small air gap may exist between the projectile and the crater bottom at least for hard spheres, so it is necessary to section the target in order to obtain a true measure of P_E (3.3). At still higher speeds this gap disappears and the front of the flattened projectile is found in contact with the crater bottom.

Fig. 3.4b shows a flattened steel sphere at the bottom of a steel target crater after an impact at about 1.5 mm/ μ s. Fig. 3.4a shows progressively larger crater cross sections corresponding to higher striking speeds (1.5 mm/ μ s at the left to 3.75 mm/ μ s at the right). The original sphere is also shown below the last crater for comparison. No mass loss was reported in any case. However, incipient fragmenting of the sphere was indicated by cracks at the higher speeds. The target hardness near the crater wall was also observed to increase from its initial value (its value far from the crater after impact) by about fifty percent (3.4).

Target density as well as target hardness has an effect on flattening or shattering a compact projectile as we shall see. There is some indication of this if we compare Fig. 3.3 (steel vs. aluminum) with Fig. 3.4b (steel vs. steel) for about the same impact speed. In Fig. 3.4b there is already an indication that the projectile is beginning to turn inside out with its final configuration resembling a mushroom cap (without the stem). Even at the highest speed in Fig. 3.3 there is not yet an indication of this shape. However, such a shape will result at still higher impact speeds, if the







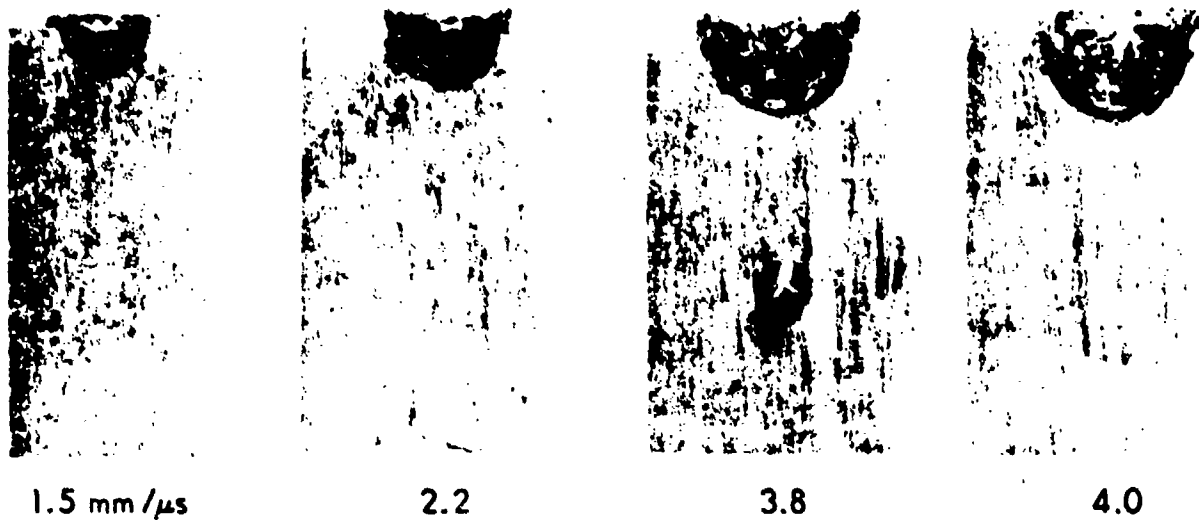
Sphere Shape	\dot{S}_0 (mm/ μ s)	P_E (mm)	D_r (mm)	D_1 (mm)
	0.726	10.4	13.06	11.62
	0.863	11.3	13.67	10.75
	1.073	15.2	14.53	9.45
	1.182	17.6	15.07	8.77
	1.391	19.0	17.80	6.95
	1.637	22.1	19.50	6.16

Fig. 3.3. Shapes of softened steel spheres recovered from hard aluminum targets after impacting at various speeds, \dot{S}_0 .



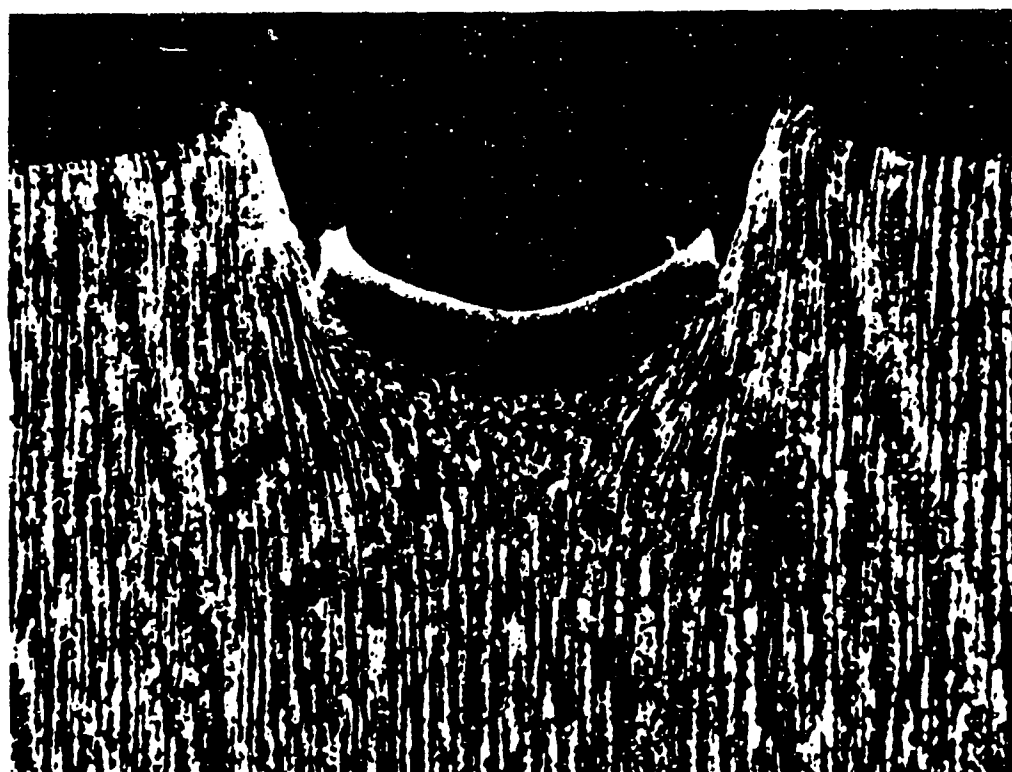
1.5 mm/μs

2.2

3.8

4.0

(a)



1.5 mm/μs

(b)

Fig. 3.4. Craters formed in steel plates by steel spheres.

projectile does not shatter. Of course, after-impact observations such as these do not tell us how the projectile shape changes in time during the penetration. We might conjecture, however, that something close to the final shape is assumed at earlier times for higher impact speeds. Since we have no evidence about time-dependent shapes, we will deal only with the time-average presented area, A , in this report.

Crater shapes are highly dependent on target properties even for spherical projectiles. Fig. 3.5 shows various shapes in different target materials, all produced by the same size aluminum spheres ($D_0 = 6.35$ mm) striking at the same speed ($\dot{S}_0 = 3$ mm/ μ s). The crater in the soft aluminum target is nearly hemi-spherical, except for a large lip at its mouth, indicating extensive plastic flow. Very little target material has been lost and the process is almost pure deformation. The crater in the cast iron target has very irregular walls. There is a slight rise rather than a lip and brittle fracture has caused most of the target material missing from the crater to be ejected. The crater in the titanium target is conical. Various plastic materials (elektron or perspex) exhibit quite different shapes. In spite of their generic name, many polymer plastic solids are quite brittle under impact conditions and undergo extensive cracking in the neighborhood of an irregular crater. This Figure is taken from Smith and co-workers (3.5).

Similar effects concerning the dependence of crater sizes and shapes on target properties have been reported by Pond and Glass (3.6). These authors note that shock loading of single-crystal and polycrystalline specimens result in different fracture phenomena, with craters in single crystals influenced by the orientation of the crystal. Even pre-straining versus annealing polycrystalline specimens can result in significantly different craters produced by nominally the same projectile impacts.

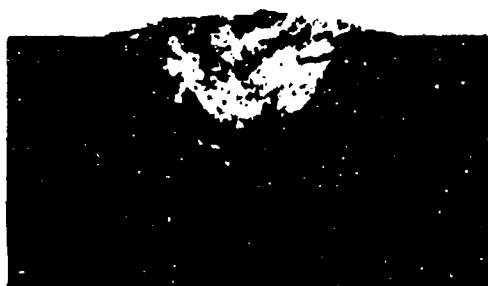
The deformation of solids at slow rates is fairly well understood, although the mathematical descriptions can get rather complicated. The response of solids to high-speed loading is poorly understood, especially when fragmentation caused by the interference of compression and rarefaction waves occurs. Rinehart has published a series of pioneering works on the subject (3.7 to 3.9).



(a) ALUMINUM



(b) ELEKTRON



(c) CAST IRON



(d) TITANIUM



(e) PERSPEX

Fig. 3.5. Typical craters formed in various targets when attacked by 6.35mm Diameter Aluminum Spheres at 3 mm/ μ s.

Much of the variability in penetration mechanics experiments can be attributed to the variability of penetrator and target materials. This is especially true when fragmentation phenomena of any kind occur, since these are usually controlled by unknown defect distributions present in individual specimens which are only nominally the same. Practical interest focuses on the average performance to be expected from various batches of nominally the same materials and various lots of devices manufactured to nominally the same geometrical dimensions. Whether or not we have a basic understanding of the phenomena involved, we eventually desire a statistical formulation of some kind. In previous reports the present author has made some contributions to the subject (3.12 to 3.13). In this report we will not employ such models. Instead, we will use average values of parameters to represent and describe the average performance to be expected.

In this chapter we will give a number of examples of compact projectile penetration, limiting ourselves to spheres as representative of this class. Cubes, discs and pellets of more irregular shapes can exhibit some shape dependence in penetration, at least at lower speeds. The differences are usually minor and are customarily described by a "shape factor" (3.14). Many of the examples we will use in this chapter first appeared in a series of seven symposia on hypervelocity impact which lasted from 1955 to 1965. In the middle of this period, Charters (3.15) wrote an article which described the common interests in penetration shared by two scientific communities, namely, those interested in space exploration which involves protection of space craft from meteorites as well as the study of meteor craters on planets and their satellites, and those interested in military matters such as the attack and defense of armored vehicles and fortifications. The considerable overlap and convergence of these fields was evident then and is again evident in the Strategic Defense Initiative. Some of our examples will also be taken from individual reports, especially some published after 1965.

2. Examples

a. Hard and Soft Steel Spheres versus Steel

Let us begin with an example from Weimann (3.1) who measured crater depth, P_E , versus striking speed, \dot{S}_0 , for 12.7 mm diameter steel spheres impacting a mild steel target. There are two sets of data in Fig. 3.6. The upper set with the sharp break near 0.8 mm/ μ s was obtained with hardened steel spheres, while the lower set was obtained with spheres deliberately softened to make them ductile. The effect of soft sphere flattening from 0.5 to 1.0 mm/ μ s is evident in the lower penetration depth achieved with these spheres compared to the hardened spheres. For the hard, brittle spheres there is a greater increase in penetration with increase in striking speed even beyond the fracture threshold speed. At still higher speeds, P_E at first decreases sharply and then increases again at a lower rate, soon exceeding the local maximum exhibited near 0.8 mm/ μ s. Above 1.5 mm/ μ s the two data sets merge and it seems to make no difference whether a sphere is deformed by shattering or by flattening. The information in Fig. 3.6 should be compared with that in Figs. 3.1, 3.3, and 3.4 above.

It is interesting to note from Fig. 3.1 that the hardened 12.7 mm sphere has already broken into two pieces at 0.5 mm/ μ s. However, the pieces are still together in the original spherical shape after the penetration. By 0.75 mm/ μ s, the sphere has broken into five or six pieces. However, there has not been time during the penetration for the pieces to separate and affect the motion. In the range from 0.8 to 0.95 mm/ μ s, the penetration decreases with increasing speed. Now there are enough pieces that they do not remain interlocked during the penetration. Instead, they spread apart and present a larger cross-sectional area to the target which impedes the penetration. Near 1.0 mm/ μ s this average area is almost as large as the area presented by the softened, flattened sphere, since the penetration is not much greater. Near 1.0 mm/ μ s the final sphere area in Fig. 3.3 has increased about 30% after impacting an aluminum target. As noted in our discussion of Fig. 3.4, we expect the increase to be larger than this against a steel target. Above 1.5 mm/ μ s in Fig. 3.6, the areas of the shattered sphere and the flattened sphere

must be the same, since the penetration depths are indistinguishable. There seems to be no mass loss for either sphere during the penetration, although pieces of the shattered sphere might fall out of the target block if it is oriented to permit this.

For a constant mass projectile, the penetration depth is given by Eq (2.11). We recall from Eq (1.3) that $a = 3Y_t A$ and from Eq (1.4) that $C = .5\rho_t A$, so the inflection point, $\sqrt{a/c} = \sqrt{6Y_t/\rho_t}$, depends only on target properties and is independent of A . Since $A = A_0 (A/A_0)$, then the time average value of the inertial coefficient can be written as $C = C_0 (A/A_0)$ where the initial value is $C_0 = .5\rho_t A_0 = .5\rho_t (\pi/4)D_0^2$. The mass is $M_0 = \rho_p (\pi/6)D_0^3$, so $M_0/C_0 = (4/3)D_0(\rho_p/\rho_t)$. Eq (2.11) becomes

$$P_E = [(M_0/C_0)/(A/A_0)] \ln \sqrt{1 + (\dot{S}_0/\sqrt{6Y_t/\rho_t})^2} \quad (3.1)$$

For the mild steel target used, $BHN \sim 125 \text{ kg/mm}^2$ or $Y_t \sim 40 \times 10^8 \text{ dyne/cm}^2$. Since $\rho_t = 7.85 \text{ g/cm}^3$, we find the inflection point to be $0.55 \text{ mm}/\mu\text{s}$. Since $D_0 = 12.7 \text{ mm}$, $A_0 = 127 \text{ mm}^2 = 1.27 \text{ cm}^2$ and $C_0 = 4.97 \text{ g/cm} = 0.497 \text{ g/mm}$. The mass was reported to be $M_0 = 8.36 \text{ g}$ so $M_0/C_0 = 16.82 \text{ mm}$. Since $\rho_p = \rho_t$ this should be equal to $(4/3)D_0$ which implies that D_0 was actually 12.6 mm and only nominally 12.7 mm .

With these values and $A/A_0 = 1$, we can calculate the uppermost dashed curve in Fig. 3.6. This coincides with the solid curve connecting the hard sphere data points from $\dot{S}_0 = 0$ to $\dot{S}_0 = 0.75 \text{ mm}/\mu\text{s}$. This agrees with the fact that the hard sphere does not change its shape in this range, whether unbroken ($0 < \dot{S}_0 < 0.5 \text{ mm}/\mu\text{s}$) or broken ($0.5 < \dot{S}_0 < 0.75 \text{ mm}/\mu\text{s}$). In contrast, the softened sphere has noticeably flattened by $\dot{S}_0 = 0.4 \text{ mm}/\mu\text{s}$. By $\dot{S}_0 = 0.75 \text{ mm}/\mu\text{s}$, the penetration depth is only about 5 mm instead of 9 mm as for the hard sphere. This implies $(A/A_0) = 9/5 = 1.8$ in Eq (3.1). The lowest dashed curve in Fig. 3.6 is $5/9$ of the uppermost dashed curve. These two curves bound the two data sets. Apparently the softened sphere area does not change much for impacts between $0.6 \text{ mm}/\mu\text{s}$ and $1.1 \text{ mm}/\mu\text{s}$ since the data points lie close to the lowest dashed curve. However, for higher speeds, the time average area during a penetration becomes smaller, because a mushroom cap begins to form as the rim of the flattened sphere flows back and trails behind the center rear. By $\dot{S}_0 = 1.5 \text{ mm}/\mu\text{s}$ the data points for the soft sphere have

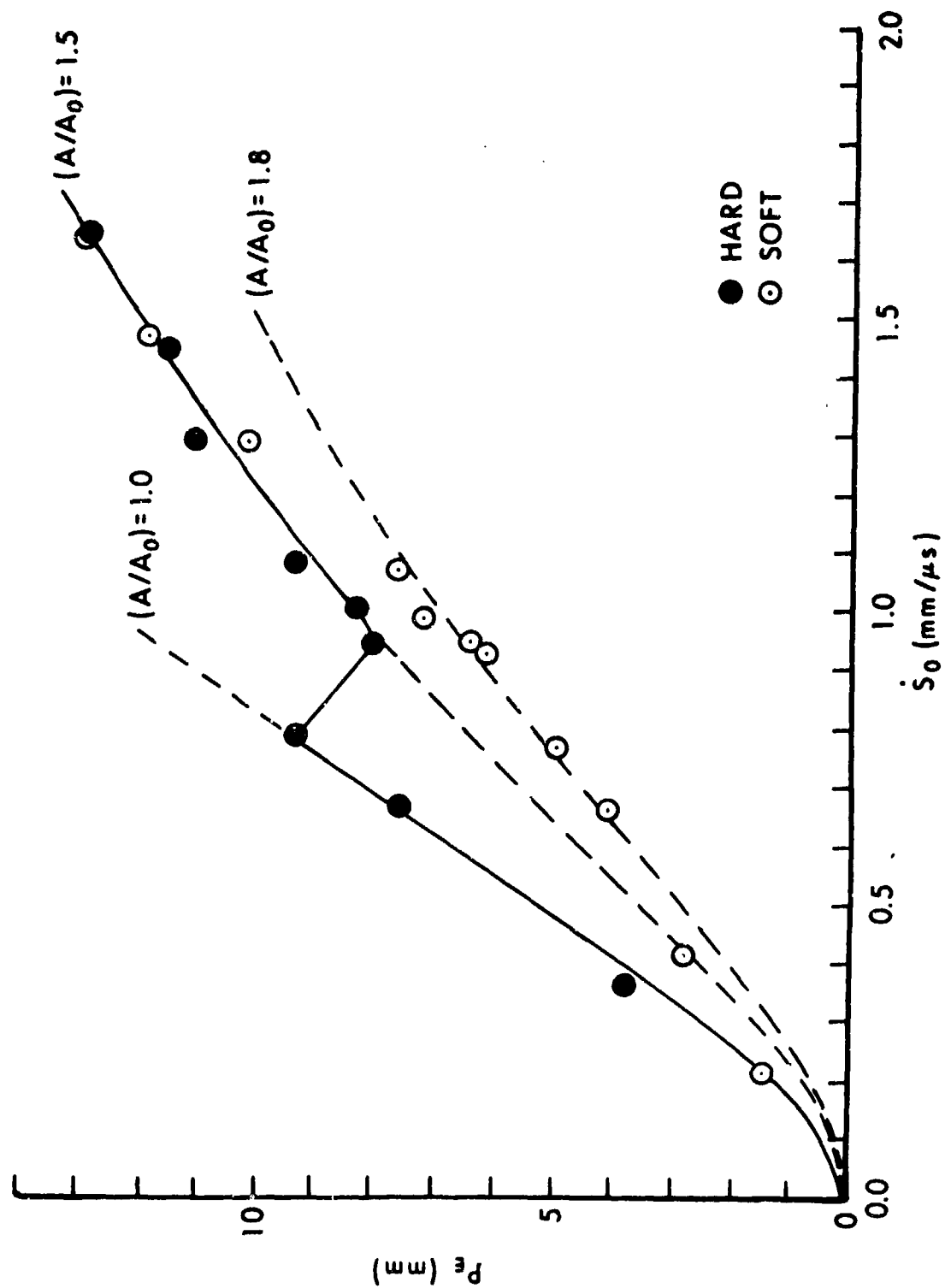


Fig. 3.6. Hardened and softened 12.7mm steel spheres versus a mild steel target.

joined those for the hard sphere and lie on the middle dashed curve for which $(A/A_0) = 3/2 = 1.5$ in Eq. (3.1). This curve coincides with the solid curve which joins the data points above $\dot{S}_0 = 1.0$ mm/ μ s. The fact that it passes through the soft sphere data point near $\dot{S}_0 = 0.4$ mm/ μ s, indicates the amount of flattening that has taken place at this speed. Between 0.75 mm/ μ s and 0.95 mm/ μ s, A has increased from A_0 to $1.5 A_0$ for the hard sphere because of shatter. However, no further increase is indicated for higher impact speeds. This might mean a sharp leveling off in the number of pieces above 1.0 mm/ μ s as for the 20 mm sphere in Fig. 3.1. Further pulverization probably takes place at higher impact speeds. However, once there are enough pieces for the shattered sphere to assume a compact shape, further subdivision does not seem to change this shape.

In this description we have not used Eq (2.22) for an eroding penetrator since no mass loss was observed. In addition we have assumed that viscosity is negligible. Thus, for example, for $\dot{P} = \dot{S} = 1$ mm/ μ s, we have assumed from Eq (1.16) that

$$b = 6\sqrt{\pi A} \eta \ll a + c = .51A \quad (3.2)$$

since $a = .12A$ gmm/ μ s² and $c = .39Ag$ /mm, so $c\dot{S}^2 = .39A$ gmm/ μ s² for A in cm² not much larger than $A_0 = 1.27$ cm². Eq (3.2) then implies $\eta \ll .05$ g/(cm- μ s) = 5×10^4 g/(cm-s) = 5×10^4 poise = 5×10^3 Pa-s. Walters (3.16) quotes values of η both larger and smaller than this for steel, depending somewhat on strain rate, but more on the laboratory making the measurement. For example, investigators in the United States generally find $\eta \sim 10^2$ Pa-s, so that viscosity would be negligible in the present case. If η is indeed as small or smaller than 10^2 Pa-s = 10^3 g/(cm-s), then $b \leq .012$ g/ μ s from Eq (3.2) and $b\dot{S} < a_0 = .15$ gmm/ μ s² < a for $\dot{S} < 12.5$ mm/ μ s. This is far above the speed range covered in Weimann's experiments. Although the uncertainty in measured values of viscosity remains, there is another reason for neglecting it in the present case. If it were a significant factor, then the calculated penetration for undeformed spheres, the uppermost dashed line in Fig. 3.6, would lie below the solid (experimental) curve for $\dot{S}_0 \leq 0.75$ mm/ μ s. Since the agreement between theory and experiment is so good without including viscosity, we are justified in neglecting it.

b. A Hard Steel Sphere versus Two Steels

Next let us consider some data reported by a co-worker of Weimann. Senf (3.17) impacted the same 12.7 mm hardened steel spheres against steel targets of three different hardness values, all harder than the target material used in Fig. 3.6. The two data sets in Fig. 3.7 are for the softest and hardest targets Senf used and even the softest target allows less penetration than in Fig. 3.6. As expected for hardened, brittle spheres, both data sets in Fig. 3.7 exhibit an impact speed range where the penetration declines because of sphere shatter.

The target material used for the upper solid curve in Fig. 3.7 had $\text{BHN} \sim 200 \text{ kg/mm}^2$ which is 1.6 times harder than the target material in Fig. 3.6. Since the target density is unchanged, this shifts the inflection point up by $\sqrt{1.6}$ to 0.7 mm/ μs which replaces 0.55 mm/ μs in Eq (3.1). With this change and for $A/A_0 = 1$, we can calculate the uppermost dashed curve in Fig. 3.7 which agrees closely with the data up to $\dot{S}_0 = 0.8 \text{ mm}/\mu\text{s}$. When we use $A/A_0 = 1.5$, we get the solid curve in Fig. 3.7 which passes through the upper data set above 1.0 mm/ μs .

We have not shown this as a dashed curve below 1.0 mm/ μs to avoid confusion with another dashed curve.

Similarly, the target material used for the lower solid curve in Fig. 3.7 had $\text{BHN} = 367 \text{ kg/mm}^2$. This shifts the inflection point to 0.94 mm/ μs , a value which replaces 0.55 mm/ μs in Eq (3.1). The middle dashed curve in Fig. 3.7 is then obtained by using $A/A_0 = 1$ and agrees with the lower data set below 0.7 mm/ μs . Letting $A/A_0 = 1.5$ gives the lowest dashed curve in Fig. 3.7 which agrees with the lower data set above 0.8 mm/ μs .

From our discussion so far, we see that a rather simple theory, using measured values of target density and hardness as well as projectile mass and size, can describe observed variations in both penetrator and target hardness values. The only parameter which might be considered adjustable is $A \geq A_0$. This has been varied by 80% or less and follows available experimental trends. We note that the shatter threshold speeds in Figs. 3.6 and 3.7 show some variability much like that reported (3.1) when the sphere diameter was varied from 9 to 20 mm against a single target material. We conclude that the shatter threshold for typical steel/steel impacts is about $0.75 \pm 0.05 \text{ mm}/\mu\text{s}$ since fragmentation is involved.

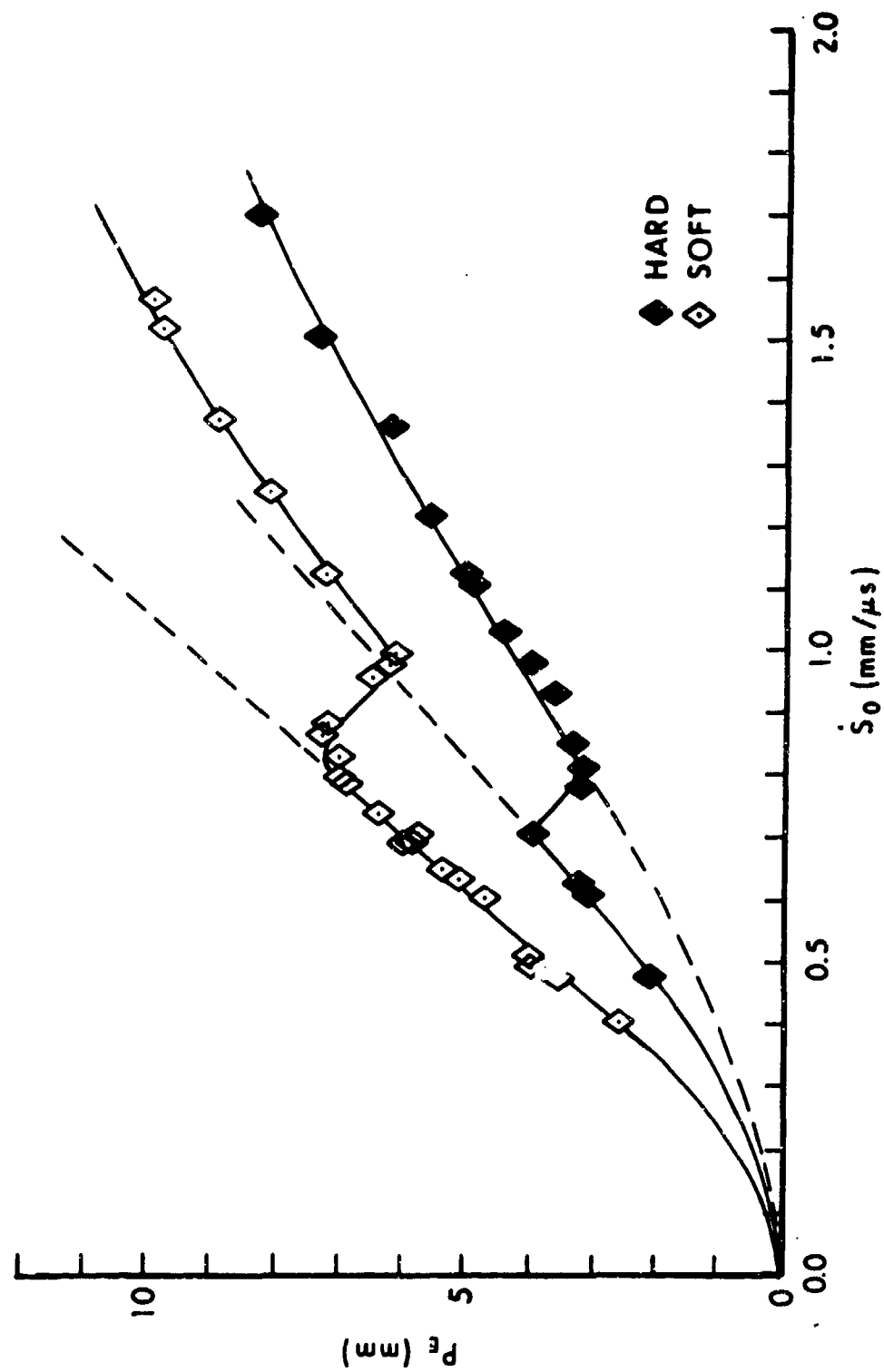


Fig. 3.7. 12.7mm hardened steel sphere versus steel of two different hardness values.

c. Two Sizes of Hard Steel Spheres versus Steel

As mentioned above, Weimann (3.1) also reported data for 8.9 mm and 20 mm hardened steel spheres versus a steel target with $BHN \sim 200 \text{ kg/mm}^2$. The upper curve in Fig. 3.7 lies between the two curves in Fig. 3.8 since it is for a 12.7 mm hardened steel sphere. In Eq (3.1), $M_o \sim D_o^3$ while $C_o \sim D_o^2$ so $M_o/C_o \sim D_o$, while the inflection point remains unchanged if the target material is the same. Thus for $A/A_o = 1$ and $A/A_o = 1.5$ we should be able to obtain the lower and upper branches of the curves in Fig. 3.8 by multiplying the upper solid curve in Fig. 3.7 by an appropriate factor. For the upper solid curve in Fig. 3.8 we used (20/12.7) while for the lower solid curve we used (8.9/12.7). The measured masses of the spheres were 32.62 g and 2.92 g respectively which differ by an order of magnitude. The agreement between theory and experiment is reasonable for $\dot{S}_o > 0.5 \text{ mm}/\mu\text{s}$, but theory lies below experiment for lower impact speeds. The reason for this is not clear. One might conjecture that there were some differences in the hardening of the spheres or targets used. What data there is for low impact speeds in Figs. 3.6 and 3.7 lies close to the theoretical curves.

Palmer and co-workers (3.18) also impacted hard steel spheres on a variety of target materials and noted a systematic decrease in the shatter threshold speed (the onset of penetration decline) with increasing target density. Fig. 3.9 shows their data for seven target materials. For steel they found a value somewhat higher than that observed by Weimann and Senf, perhaps because of a difference in projectile hardness (not reported). Other factors besides target density probably influence the threshold speed for a given projectile.

In the military literature the speed range from the onset of penetration decline to that speed at which penetration again is as deep as it was at the threshold is called the "shatter gap" (3.19). In World War II the British two-pounder projectile failed to perforate armor when fired close to the target, but perforated when fired from farther away (lower striking speed below the gap), or at much higher speed (above the gap).

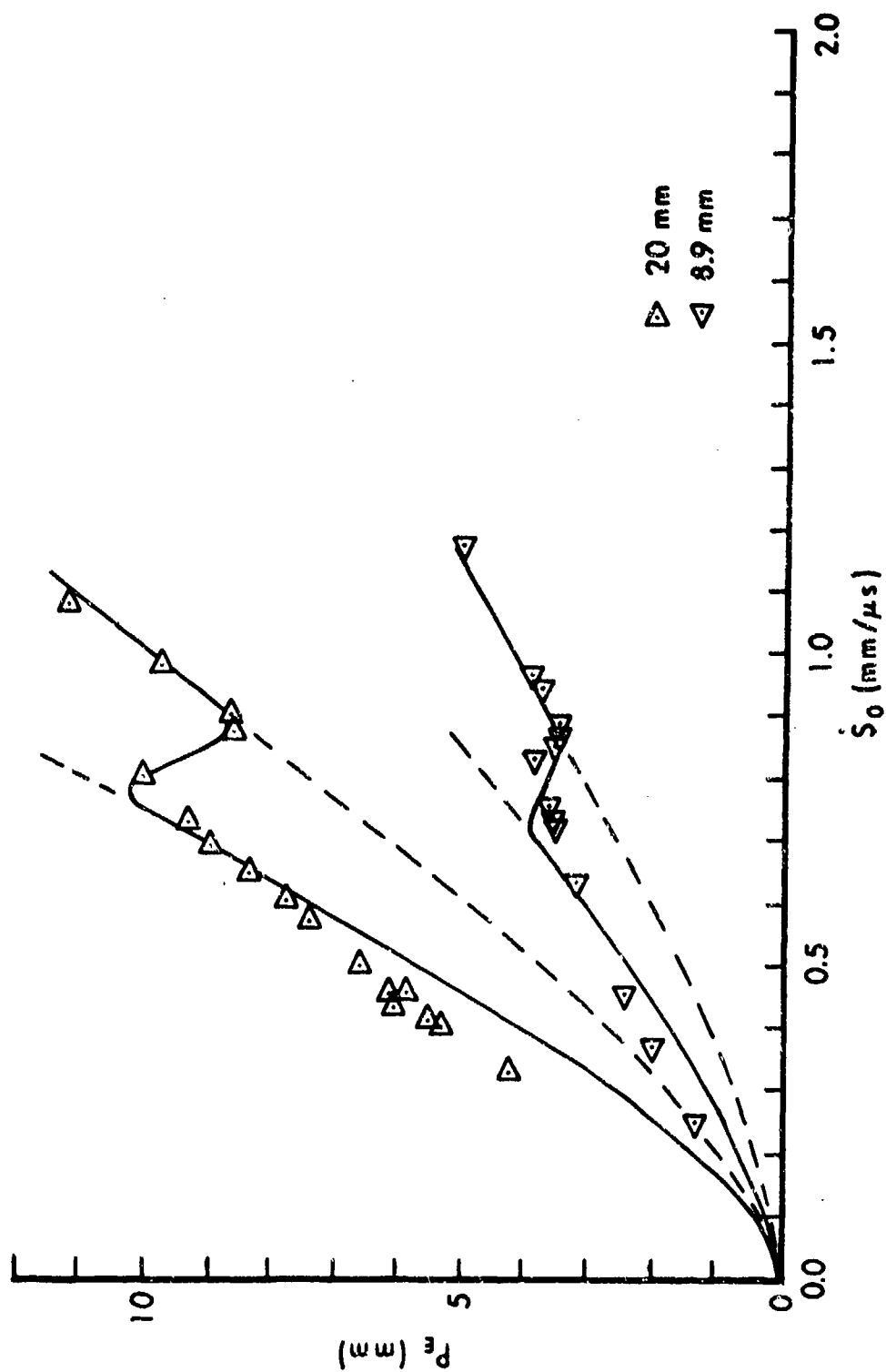


Fig. 3.8. Two sizes of hardened steel spheres versus a steel target.

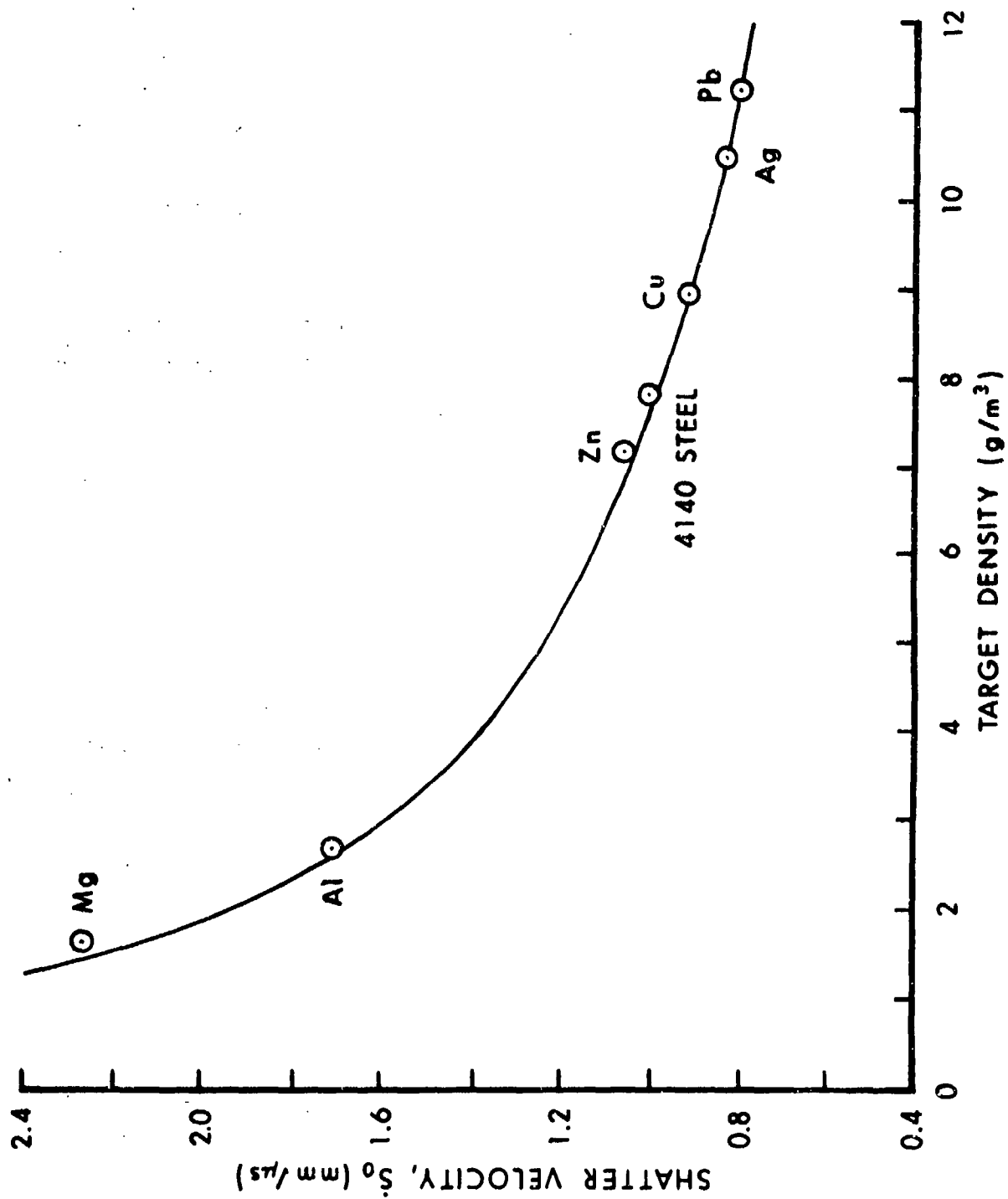


Fig. 3.9. Projectile shatter velocity vs. target density for impact of hardened steel spheres into various targets.

d. Tungsten Carbide Spheres versus Copper

Now let us turn to some other projectile/target material combinations.

Atkins (3.20) gun-launched tungsten carbide spheres against copper targets at speeds up to 3 mm/ μ s. Fig. 3.10 shows his data for two sizes of WC spheres ($D_0 = 12.7$ mm, $M_0 = 16$ g) and ($D_0 = 3.175$ mm, $M_0 = 0.25$ g) so the masses differ by a factor of 64. No strength was reported for the copper target so we have assumed $BHN \sim 60 \text{ kg/mm}^2$ or $Y_t = 18 \times 10^8$, using $C_m = .30 \times 10^8$ (dyne/cm²)/(kg/mm²) in Eq (1.1). Since the density of copper is about 8.9 g/cm³, we find the inflection point to be about 0.33 mm/ μ s. We also find C_0 to be 0.57g/mm and 0.036g/mm for the larger and smaller spheres respectively. This gives us (M_0/C_0) equal to 28.1 mm and 7 mm respectively. Now Eq (3.1) gives us the lower impact speed branches of the two solid curves in Fig. 3.10 when we use $A/A_0 = 1$ and the upper branches when we use $A/A_0 = 1.55$. The agreement with experiment is good even for low impact speeds. Once more an increase in presented area of about 50% seems to account for P_E versus \dot{S}_0 above 2km/s.

e. Tungsten Carbide Spheres versus Lead and Aluminum

Later Atkins (3.21) impacted WC spheres on other target materials.

The solid curve in Fig. 3.11 connects his data points for a 2.0g sphere ($D_0 = 6.35$ mm) impacting a lead target ($\rho_t = 11.3 \text{ g/cm}^3$). If $Y_t = .5 \times 10^8$ dyne/cm² we find the inflection point to be 0.05 mm/ μ s. We find $C_0 = .18 \text{ g/mm}$ and (M_0/C_0) = 11.2 mm in Eq (3.1). For $A/A_0 = 1$ we obtain agreement with the solid curve to 0.5 mm/ μ s, while for $A/A_0 = 1.63$ we obtain agreement for $\dot{S}_0 > 1.5$ mm/ μ s. The "shatter gap" in this case extends from 0.5 mm/ μ s to 3.0 mm/ μ s. The soft lead target seems to allow a bit more spreading of the shattered sphere pieces than the copper target, although its greater density might tend to counteract this trend.

In the same paper he reported data for the same spheres impacting two strengths of aluminum. The upper curve in Fig. 3.12 is for soft 1100-F, while the lower curve is for 2014 ($\rho_t = 2.7 \text{ g/cm}^3$). If we use $Y_t = 10 \times 10^8$ dyne/cm² and 60×10^8 dyne/cm² respectively, we find inflection points of 0.47 mm/ μ s and 1.15 mm/ μ s respectively. Since $C_0 = .043 \text{ g/mm}$, $M_0/C_0 = 46.7$ mm.

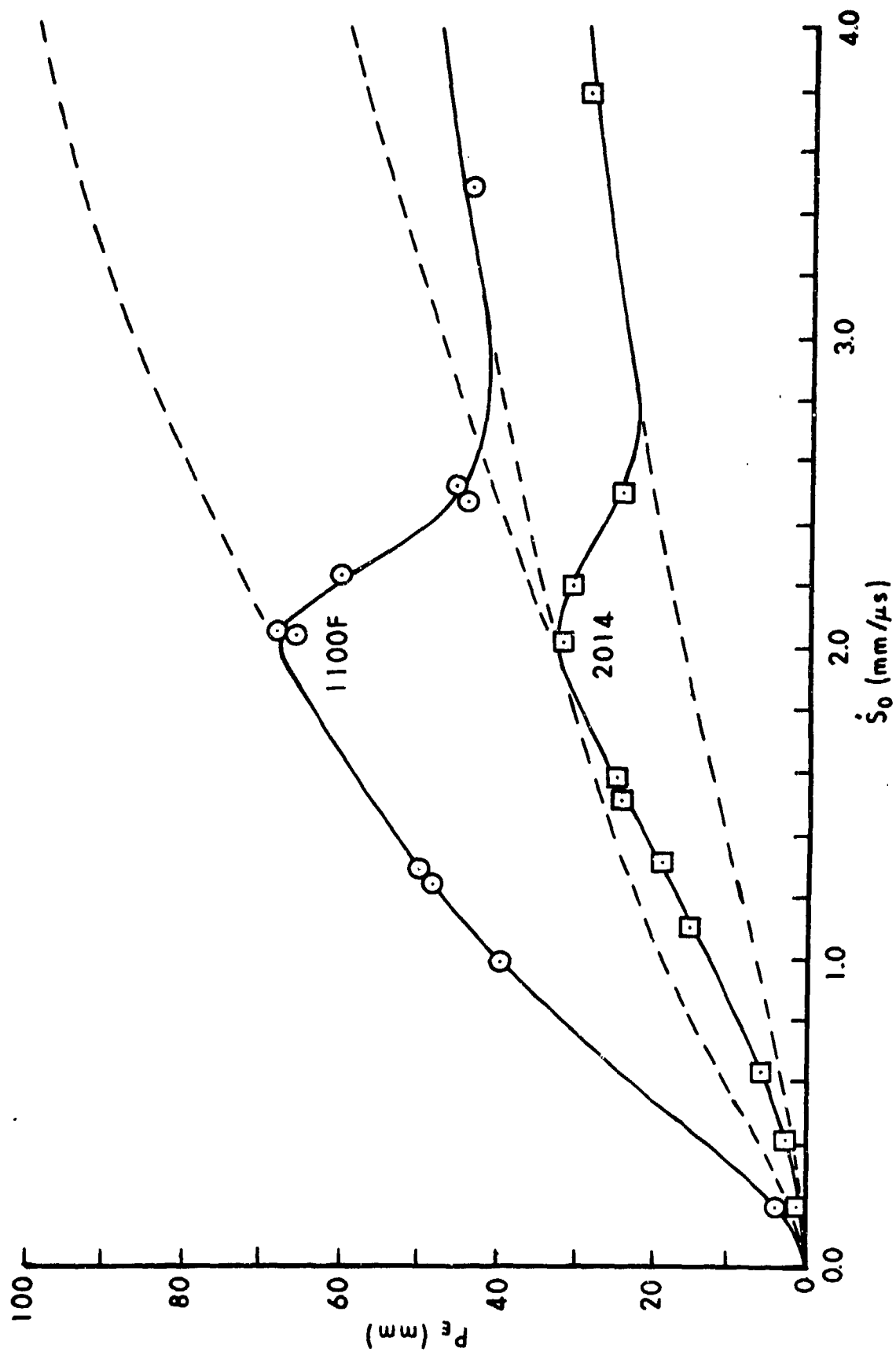


Fig. 3.10. WC spheres/Cu.

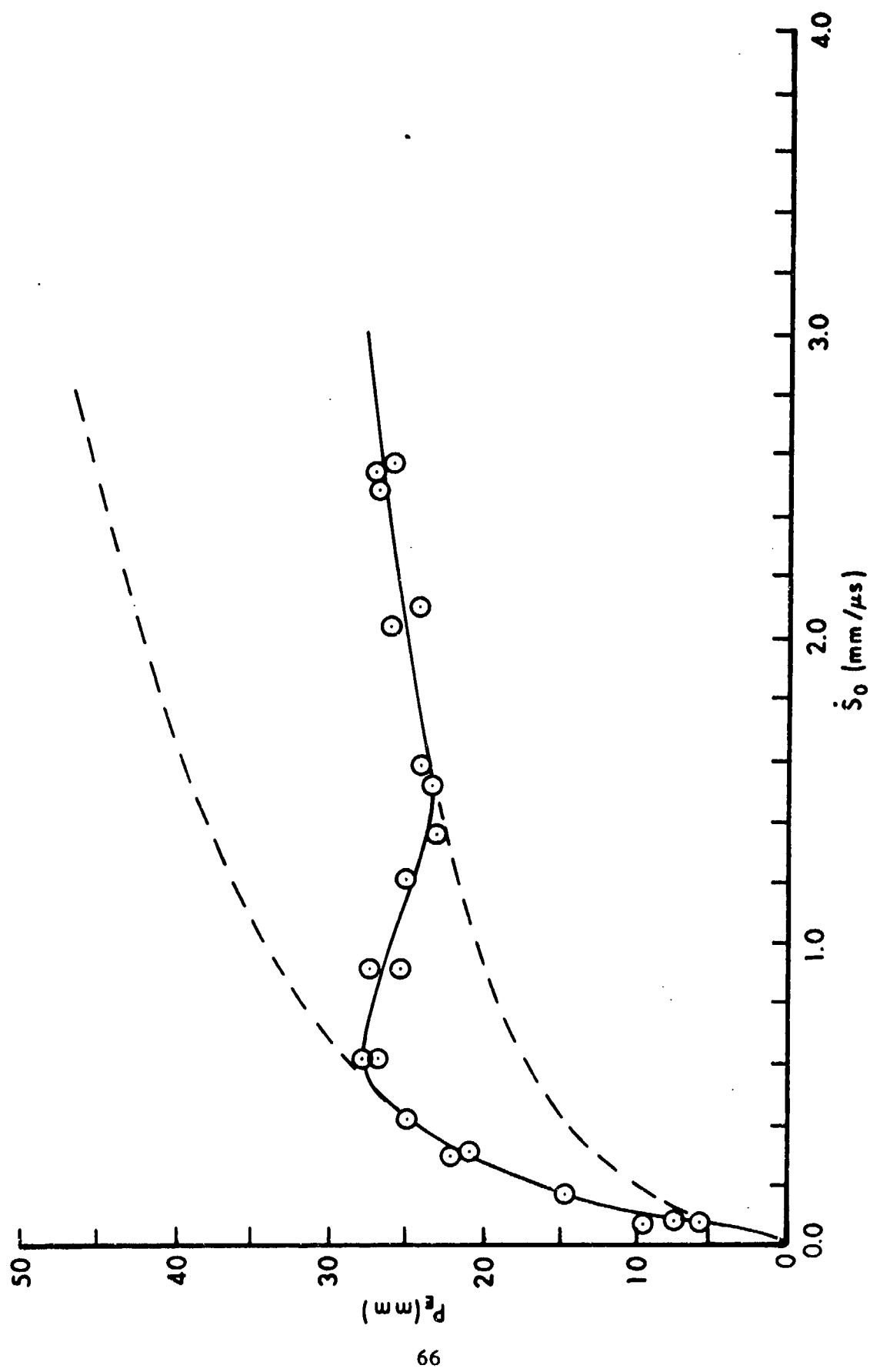


Fig. 3.11. WC sphere/Pb.

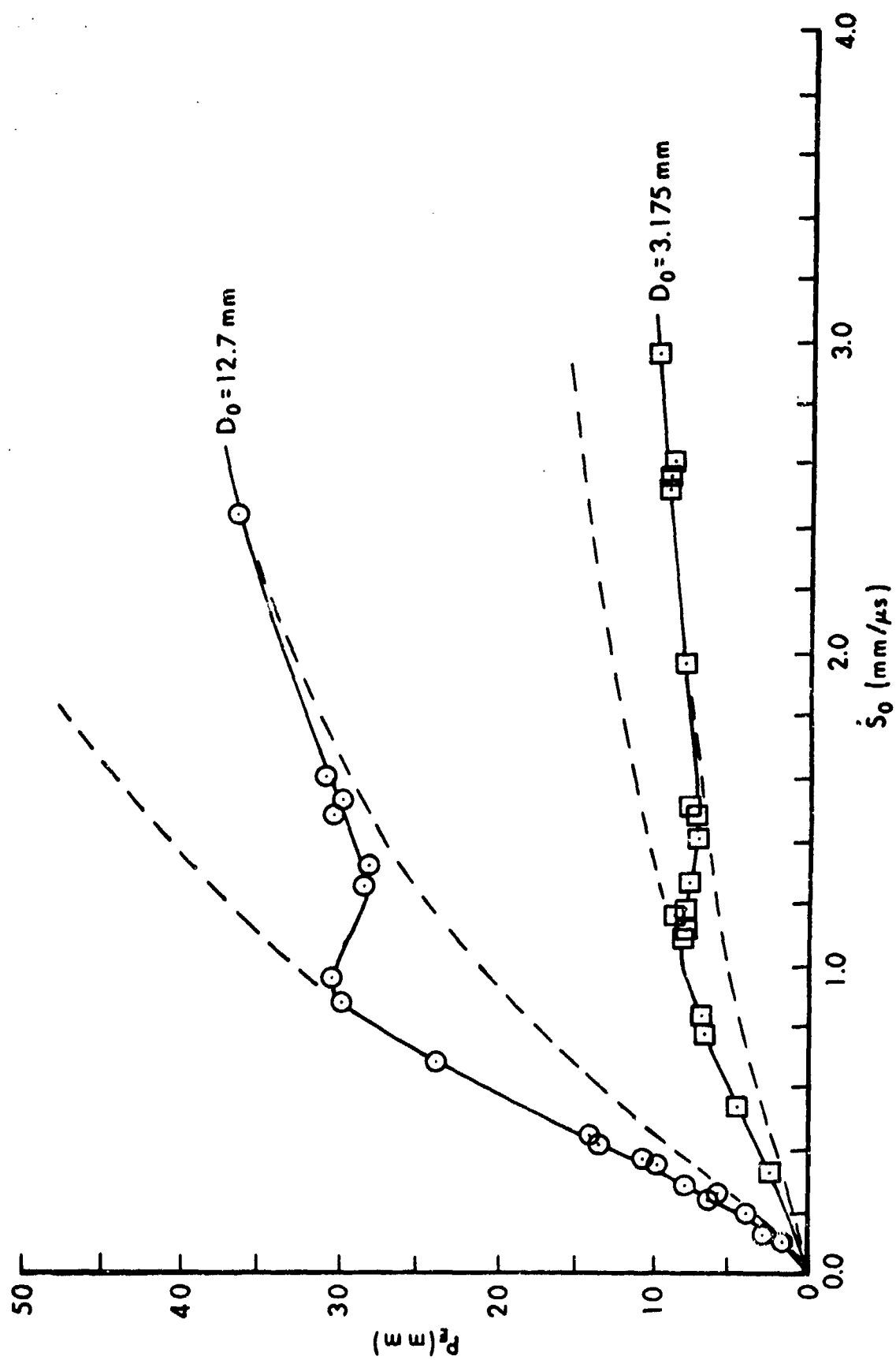


Fig. 3.12. WC spheres/Al.

For $A/A_0 = 1$ in Eq (3.1) we find agreement with both data curves on their low-speed branches (up to 2 mm/μs). If we let $A/A_0 = 2$ we obtain the high-speed branch curves shown. Since there is only one data point on each of these high-speed branches, it is difficult to claim agreement above 3 mm/μs. The greater spreading of the shattered sphere indicated by the large value $A/A_0 = 2$ can be attributed to the lower density of aluminum compared to lead, copper or steel. The higher threshold speed of 2 mm/μs compared to 0.5 mm/μs for lead is comparable to the trend in Fig. 3.9 for steel spheres versus aluminum and lead targets.

f. Hard and Soft Steel Spheres versus Aluminum

In Fig. 3.3 we showed some data from Weimann (3.2) for a softened 12.7 mm steel sphere impacting a hard aluminum target (BHN ~ 125 kg/mm²). His data is plotted as the lower curve in Fig. 3.13. He also used a hardened 12.7 mm steel sphere against the same target and his data points are connected by the upper curve in Fig. 3.13. He noted that the recovered spheres began to break above 1.1 mm/μs. However, there is no evidence of a decline in penetration up to the highest impact speed used near 1.6 mm/μs. This is to be expected in view of Fig. 3.9 which indicates that Weimann stopped just short of the shatter velocity. The inflection point for this aluminum target is $\sqrt{6Y_t/\mu_t} = 0.9$ mm/μs for $Y_t = .37 \times 10^8$ dyne/cm² and $\rho_t = 2.7$ g/cm³, while $C_0 = .5(2.7)(1.27) = 1.71$ g/cm = .171 g/mm, giving $M_0/C_0 = 48.9$ mm for $M_0 = 8.36$ g. With these values in Eq (3.1) we obtain the upper curve in Fig. 3.13 for $A/A_0 = 1$ and the lower curve for $A/A_0 = 1.67$. As in Fig. 3.6, we note a change of the softened sphere data points from the upper curve to the lower curve as the sphere flattens with increasing speed. Presumably if speeds in excess of 2 mm/μs had been used we would observe a shatter gap for the hardened sphere and a convergence of the two data sets at higher speeds as in Fig. 3.6.

The steel targets in Fig. 3.6 and the aluminum targets in Fig. 3.13 all had about the same hardness value (BHN ~ 125 kg/mm²). Presumably the differences in penetration observed are attributable to the fact that aluminum

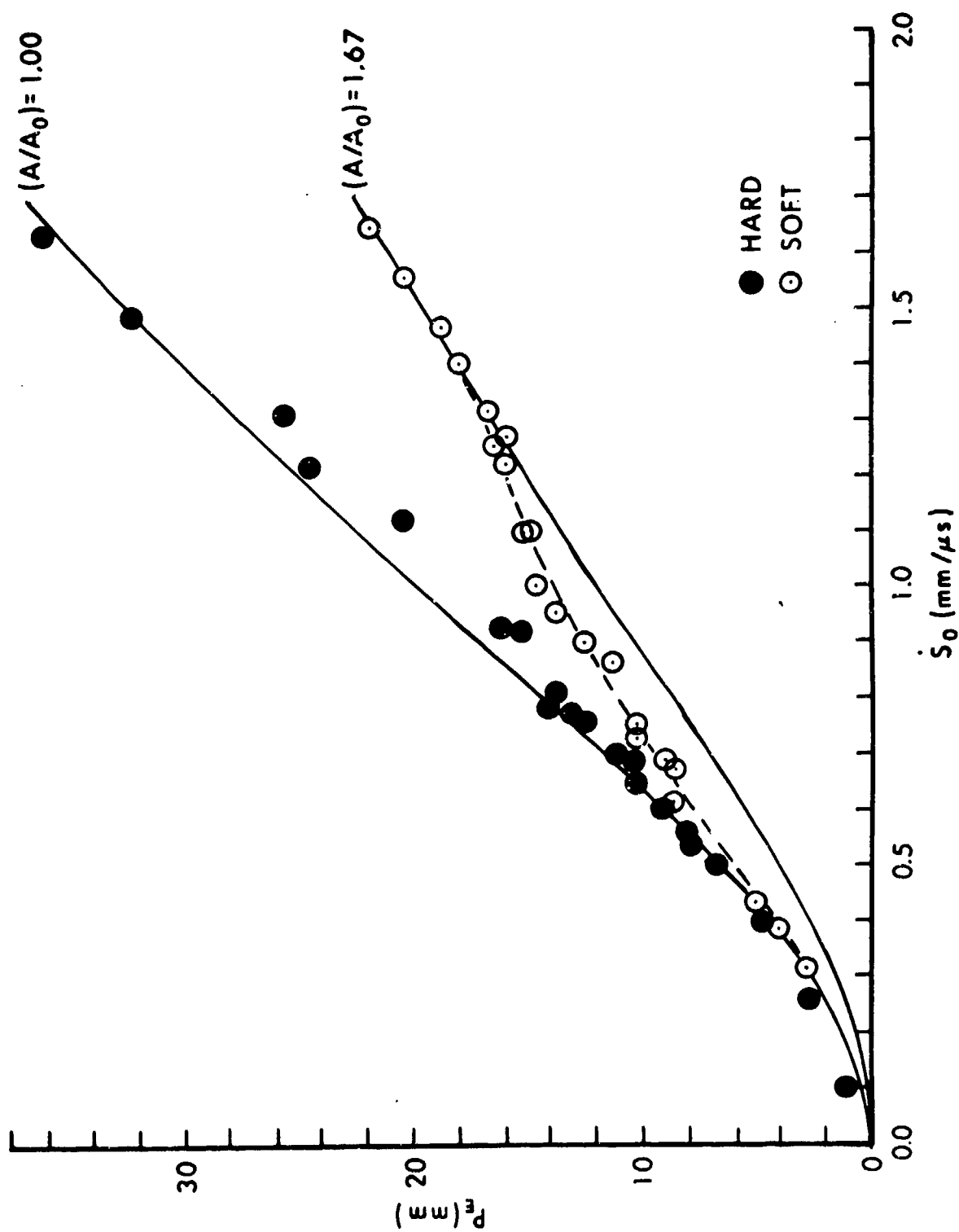


Fig. 3.13. Hardened and softened 12.7mm steel spheres versus aluminum.

is only about one-third as dense as steel. The greater density of steel targets causes more flattening of the same softened steel sphere for a given impact speed ($A/A_0 = 1.8$ versus 1.6 for aluminum). It is also responsible for a lower fracture threshold speed (.05 mm/ μ s versus 1.1 mm/ μ s) and a lower shatter threshold speed (0.8 mm/ μ s versus perhaps 1.7 mm/ μ s) for the same hardened steel sphere.

The three figures for tungsten carbide spheres, Fig. 3.10 to 3.12, were for targets of different densities and hardness values. The shatter threshold speeds decrease as the density increases in agreement with the trend in Fig. 3.9 for steel spheres. The soft aluminum was about as hard as the copper, while the lead target was more than an order of magnitude softer. Target density appears to be the factor which dominates shatter threshold speeds rather than target hardness, provided the projectile is hard enough to shatter rather than flatten. Projectile density may also play a role, although we need more information before we can assert this with any confidence.

g. Three Sizes of Hard Steel Spheres versus Aluminum

Weimann (3.2) also used the same hard aluminum as a target for various size hardened steel spheres. His data for 20 mm, 9 mm and 3 mm spheres appear in Fig. 3.14. The measured masses were 32.64g, 2.92g, and 0.11g, a variation of more than two orders of magnitude. The solid curves in Fig. 3.14 were calculated by using Eq (3.1) with the same target properties as in Fig. 3.13 and with $A/A_0 = 1$, so the penetrations are proportional to the masses at any given impact speed. Obviously the upper curve in Fig. 3.13 lies between the two upper curves in Fig. 3.14. In no case was the shatter threshold speed reached. The deviation between theory and experiment for the 20 mm sphere above 0.8 mm/ μ s is attributable to the fact that the target block used was only 50 mm thick, not thick enough to be a truly semi-infinite target. As Weimann noted, these targets exhibited bulges on their rear faces, a phenomenon which allows a greater penetration depth than a semi-infinite target would allow.

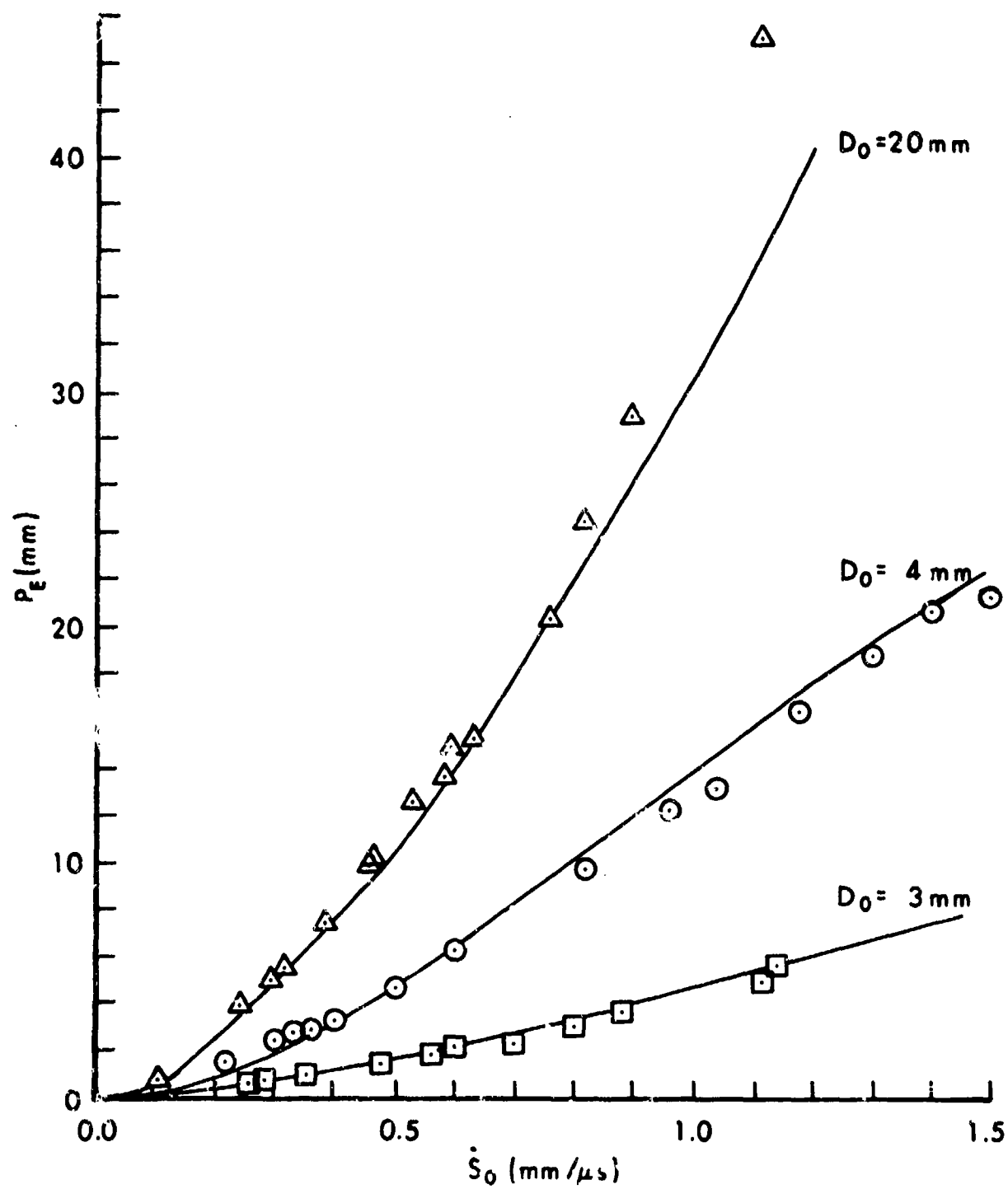


Fig. 3.14. Hardened steel spheres of various diameters vs. Al.

h. Al/Cu, Cu/Cu, and Cu/Al

In this section and the next we will examine combinations of soft aluminum and copper used as projectiles and targets. Since the materials used had about the same hardness values ($\text{BHN} \sim 33 \text{ kg/mm}^2$ or $Y_t = 10^9 \text{ dyne/cm}^2$), a study of projectile/target combinations becomes a study of density effects, provided we compare spherical projectiles of the same diameter. The notation Al/Cu means a spherical aluminum projectile impacting a copper target.

Goodman and Liles (3.22) obtained data for pure aluminum ($\rho = 2.7 \text{ g/cm}^3$) and pure copper ($\rho = 8.8 \text{ g/cm}^3$). Fig. 3.15 shows their data for $D_0 = 4.76 \text{ mm}$ (3/16 inch) spheres with $M_0 = 0.158 \text{ g}$ for aluminum and 0.496 g for copper. These reported masses imply either somewhat different densities or diameters than were actually reported. Their data for Al/Al has been omitted since it is equivalent to the upper data set in Fig. 3.16 and lies close to the Cu/Cu curve as it should, since $M_0/C_0 = (4/3)D_0^3 \rho_p/\rho_t$ for Al/Al and Cu/Cu, so the curves differ only in their inflection points. We expect (A/A_0) to be the same.

Using the reported densities and strengths, we find the inflection points to be about $0.5 \text{ mm}/\mu\text{s}$ for aluminum targets and $0.25 \text{ mm}/\mu\text{s}$ for copper targets.

The two lower curves in Fig. 3.15 differ because of projectile mass or density since $M_0/C_0 = (4/3)D_0^3(\rho_p/\rho_t)$ with D_0 and ρ_t the same. If we use $(A/A_0) = 1.0$, we calculate the lowest solid curve and if we use $(A/A_0) = 1.4$, we calculate the middle solid curve. Letting (A/A_0) vary slightly with \dot{S}_0 would give better agreement but is not justified in view of the approximate nature of our model and the variability of the experiments. It is remarkable that a single value for (A/A_0) can give such good agreement over such a range of impact speeds. The lower value of (A/A_0) for the aluminum sphere implies that the denser copper target not only turns it inside out like a mushroom cap but also keeps its rim from spreading out on average during the penetration any more than the original diameter. That is, $(A/A_0) = (D/D_0)^2 = 1$ implies that the average diameter during the penetration, D , is no greater than the original diameter.

The two upper curves in Fig. 3.15 differ because of target density which appears not only in M_0/C_0 but also in the inflection point. If we use

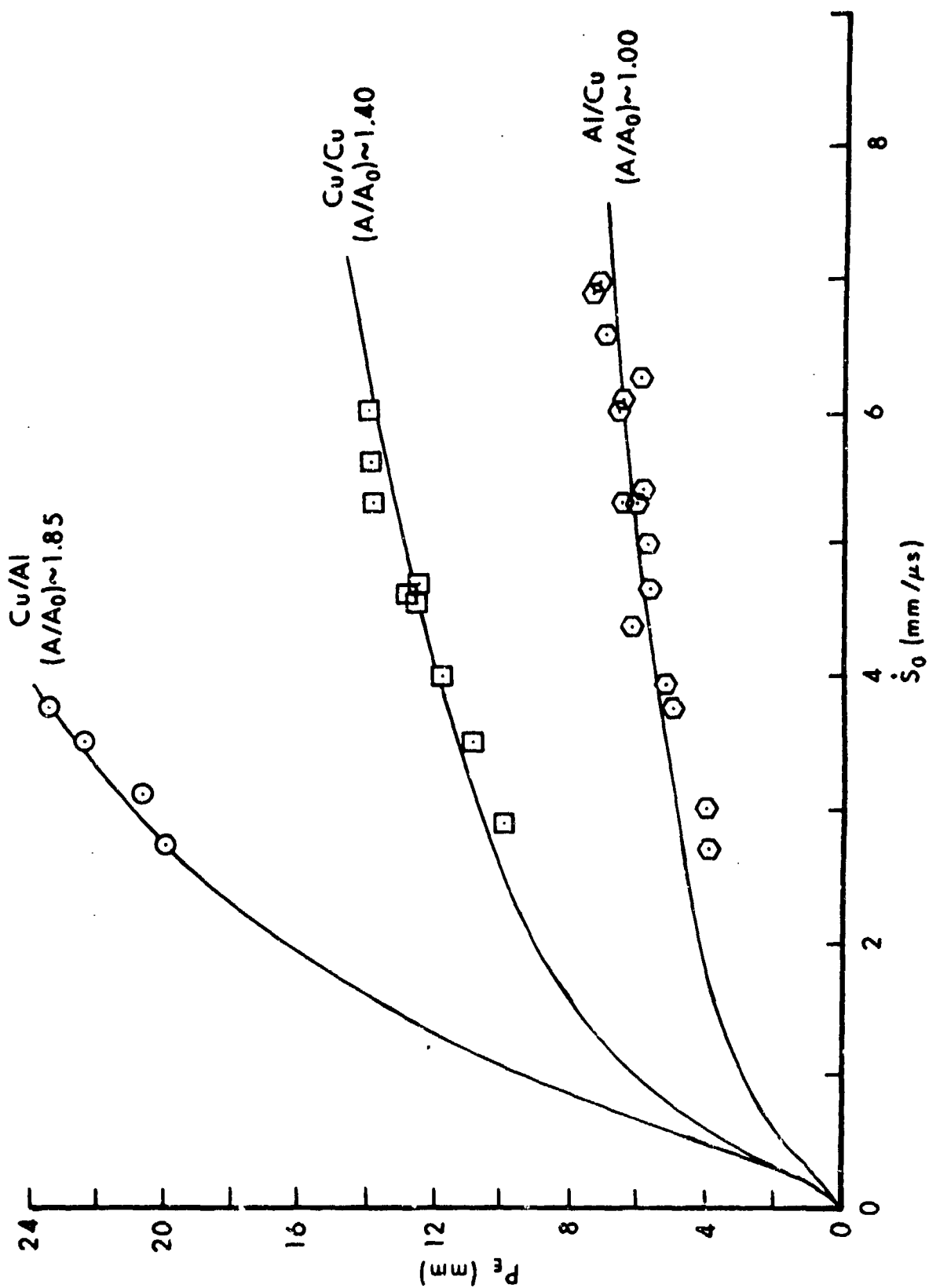


Fig. 3.15. Copper and Aluminum Spheres versus Two Kinds of Aluminum

$(A/A_0) = 1.85$ with the other reported values, we calculate the uppermost curve in Fig. 3.15. This implies that the less dense aluminum target allows the deformed copper sphere to spread out more than copper target does. This does not contradict the trend noted in section f above (Fig. 3.13) where a comparison was made with Fig. 3.6. In those cases impact speeds below 1.6 mm/ μ s were used and the spheres were flattened but not fully deformed and turned inside out. The denser steel targets flattened the soft steel spheres more than the aluminum targets did [$(A/A_0) = 1.8$ versus $(A/A_0) = 1.67$]. However, at higher impact speeds, we might expect the aluminum targets to offer less resistance to lateral spreading of the fully deformed spheres.

This interpretation is compatible with the final crater diameters, D_c , measured at the original target surface and reported by these authors. We can compare the three curves in Fig. 3.15 in the 3 to 4 mm/ μ s range where data was obtained in all cases. For Al/Cu, $D_c/D_0 \sim 3$, for Cu/Cu, $D_c/D_0 \sim 4$ and for Cu/Al, $D_c/D_0 \sim 5$. In other words, as the projectile/target density ratio, ρ_p/ρ_t , increases from 0.3 to 1.0 to 3.3, and D_c/D_0 increases from 3 to 4 to 5, we find A/A_0 increasing from 1.0 to 1.4 to 1.85 or D/D_0 increasing from 1.0 to 1.2 to 1.4. For lack of time-dependent information on projectile shapes, we must be content with noting these trends.

Both the final crater depth, P_E , and final crater diameter at the surface, D_c , increase as \dot{S}_0 increases. For Cu/Cu, P_E/D_c is roughly equal to the hemispherical value of 0.5 over the speed range investigated. However, for Al/Cu this ratio increases from 0.3 to 0.4 over the range investigated, while for Cu/Al it declines from 1.0 to 0.9. Presumably for high enough impact speeds the hemispherical value will be reached. Near $\dot{S}_0 = 3.0$ mm/ μ s, we find that as ρ_p/ρ_t increases from 0.3 to 1.0 to 3.3, P_E/D_c increases from 0.3 to 0.5 to 1.0. Thus the final crater shape changes from oblate (shallow) to hemispherical to prolate (deep) as the projectile/target density ratio increases through unity. A theory of crater shapes must be at least two-dimensional and so is beyond the scope of this report.

Engel (3.23) sectioned and polished some of the target blocks used by Goodman and Liles and measured the thickness of the projectile material remaining in the bottom of the craters. The few thicknesses she reported for 4.76 mm spheres ranged from 0.02 to 0.70 mm and lead to less than 5%

corrections to the crater depths reported by Goodman and Liles. Engels did not report the lateral extent of the sphere residue nor estimate the sphere mass remaining in the crater. For Cu/Cu she reported a thickness $d = 0.18$ mm for $\dot{S}_0 \sim 3.5$ mm/ μ s and $d = 0.10$ for $\dot{S}_0 \sim 4.5$ mm/ μ s. The surface area of the hemisphere is $(\pi/2)D_0^2(1-\cos \theta)$ where θ is the polar angle measured from the center bottom point. If we assume that the entire sphere is still in the crater and is spread uniformly over the center bottom, then the volume of the 4.76 mm sphere, namely 56.5 mm^3 , must be equal to $d(\pi/2)D_0^2(1-\cos \theta)$ where D_0 was reported by Goodman and Liles. In this way we estimate that for $\dot{S}_0 \sim 3.5$ mm/ μ s, $\theta \sim 60^\circ$, while for $\dot{S}_0 \sim 4.5$ mm/ μ s, $\theta \sim 75^\circ$. In neither case did the sphere spread out over the whole crater.

The final diameter of the inverted sphere is $D_0 \sin \theta$ and is about 17 mm at 3.5 mm/ μ s and 21 mm at 4.5 mm/ μ s, that is, 3.5 to 4.5 times D_0 , if all our assumptions are correct. This is much larger than $D = 5.6$ mm, the average value we have estimated during the penetration (almost 20% larger than D_0). We can conjecture that the sphere is initially flattened, achieving a diameter greater than D , then turned inside out, having a diameter about equal to D for most of the penetration, then spreads out to a diameter much greater than D toward the end of the penetration. This conjecture is not the same as another conjecture often found in the literature and called "secondary penetration." The latter conjecture supposes that the sphere residue has somehow "ceased to act" on the target (even though it is still in contact with it) and that the target material continues to flow "by itself," eventually coasting to a stop when target strength dominates inertial flow. There is no evidence for this conjecture. On the contrary, the entire sphere seems to flow with the target material up to the end of the penetration when all motion ceases. In fact, since $\theta < 90^\circ$ for cases which have been examined, each element of the residual projectile must have some forward component of velocity up to the very end. This implies that each element of the sphere continues to deepen (as well as widen) the crater up to the end of the motion. Elements which have spread beyond $\theta = 45^\circ$ near the end of a penetration will contribute more to widening than to deepening the crater, while for those with $\theta < 45^\circ$ the opposite will be true. In any case, target material in contact with sphere material does not flow "by itself," nor does the deformed sphere somehow "cease to act"

before the end of a penetration. Even target material near the lip of a crater which is no longer in contact with penetrator material is pushed up to the end by adjacent target material which is still in contact with penetrator material.

In the next chapter we will examine some cases of ductile rods which develop mushroom caps during penetration and for the most part turn inside out, leaving a hollow tube of penetrator material lining a long, narrow crater. In such cases a rod element ceases to have either a forward or radial component of velocity at some time during the penetration. At this time we can consider this rod element to be "eroded." Since the deformed elements of ductile spheres are never turned back to this extent, they cannot be said to be "eroded." In this sense there is no mass loss and a constant mass model is justified.

i. Al/Al to 9 mm/ μ s

The largest speed range examined for a given projectile/target combination has been reported on by Halperson (3.24 to 3.25). In the first paper a 2024 aluminum sphere was used while in the second paper a 2017 aluminum sphere was used. However, in both cases the sphere diameter was the same, namely, $D_0 = 4.76$ mm so $M_0 = 0.158$ g as in section h above. Earlier studies of Al/Al include a paper by Halperson and Atkins (3.26) and one by Atkins (3.21). The targets were either soft (1100-F) or hard (2014-T6) aluminum. The slightly different types of aluminum used as projectiles seemed to make little difference since data in Halperson's last paper merged smoothly with data from his previous paper. However, from Fig. 3.16 we see that target hardness plays an undiminished role up to 9 mm/ μ s, a speed in excess of typical jet tip speeds. Halperson concludes that hydrodynamic theories which neglect target strength should not be used.

Others have also noted the undiminished importance of target strength for impacts by compact projectiles at the highest speeds attained (3.27 to 3.30).

Since $\rho_p = \rho_t$ we have $M_0/C_0 = (4/3)D_0 = 6.35$ mm in Eq (3.1). For the 1100-F aluminum target we find an inflection point of 6.5 mm/ μ s as in section

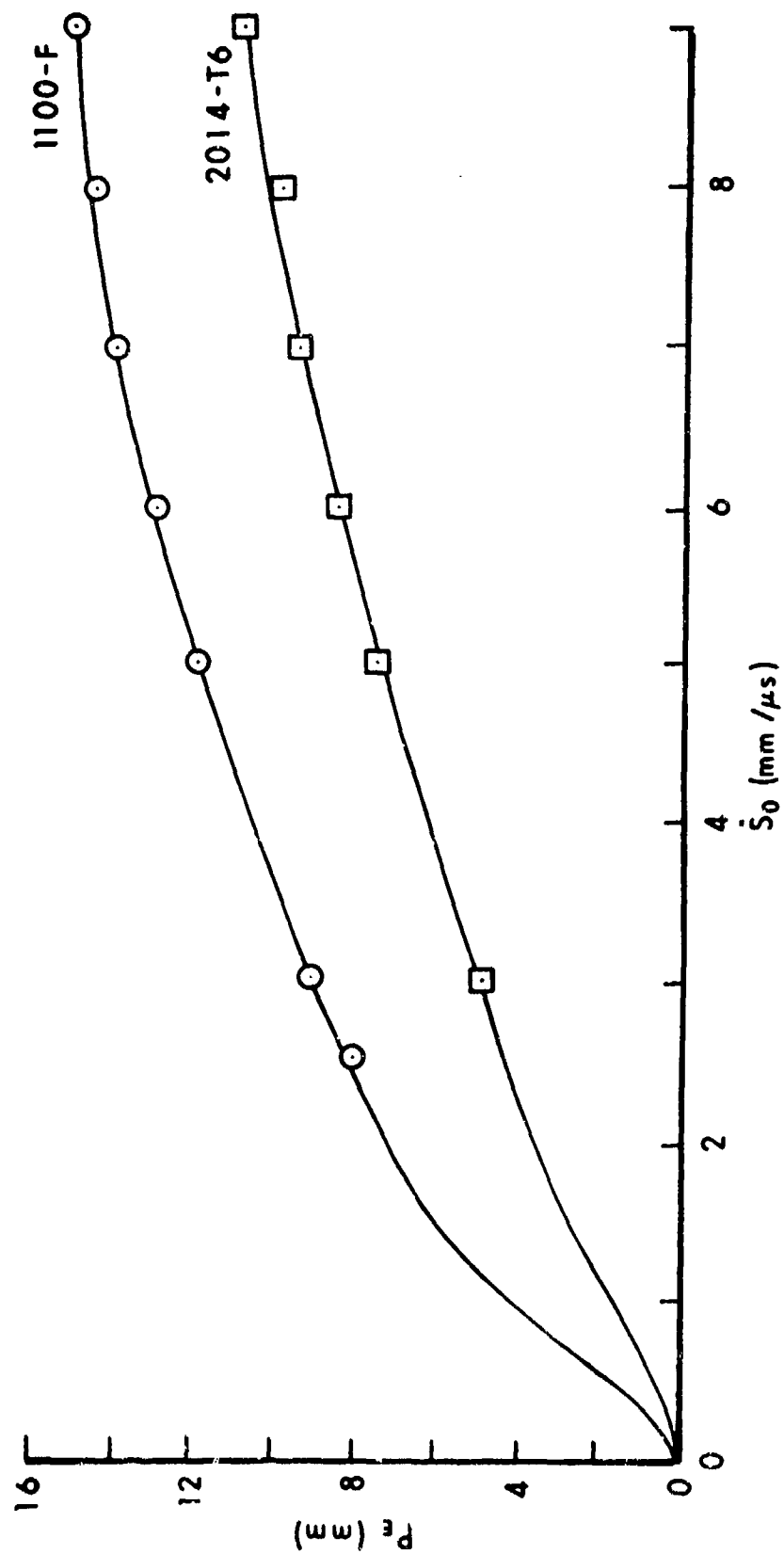


Fig. 3.16. 4.76mm aluminum spheres versus two types of aluminum target.

h above, while for the 2014 aluminum target ($BHN = 200 \text{ kg/mm}^2$ or $Y_t = 60 \times 10^8 \text{ dyne/cm}^2$) we find an inflection point of $1.15 \text{ mm/}\mu\text{s}$. Thus Eq (3.1) differs only in the inflection point of the two target materials, if we use $A/A_0 = 1.3$ for both cases. In this way the solid curves joining the data points for each target were generated. The value of $A/A_0 = 1.3$ is not very different from $A/A_0 = 1.4$ used for Cu/Cu in the previous section. The higher inflection point for soft aluminum ($0.5 \text{ mm/}\mu\text{s}$) compared to that of soft copper ($0.25 \text{ mm/}\mu\text{s}$) makes the upper curve in Fig. 3.16 lie somewhat below the middle curve in Fig. 3.15. The higher inflection point for hard aluminum ($1.15 \text{ mm/}\mu\text{s}$) makes this curve lie well below the upper curve in Fig. 3.16. Halperson (3.25) found approximately hemispherical craters for both types of aluminum target with a slight tendency for the hard target craters to be a bit oblate and the soft target craters to be a bit prolate. Although target hardness has a very significant effect on crater depth, it only seems to have a slight effect on crater shape, which is controlled more by the projectile/target density ratio, as we have seen. Engel (3.23) also examined residual penetrators in the case of Al/Al and found about the same residual thicknesses as for Cu/Cu. This implies the same spreading angles under the assumptions made previously as well as no erosion.

j. Neglect of Erosion and Viscosity

If we add a term ($-b\dot{P}$) to the target force, the penetration will clearly be reduced. In fact this reduction will be larger for larger striking speeds which lead to larger penetration speeds. Since reasonable values of $A/A_0 > 1$ which reflect experimental observations of projectile deformation already lead to rather close agreement between theory and experiment, we do not need such a term.

A similar conclusion is true for erosion. We have already examined some experimental evidence for a lack of erosion in the case of compact projectiles. If we compare Eq (2.11) for a constant mass projectile with Eq (2.22) for an eroding projectile, we find that a non-eroding projectile penetrates more deeply, if all other factors are equal. In fact, as the striking speed increases, so does the advantage of the constant mass

projectile. Numerical comparisons can be made or series expansions used. In the extreme case of near maximum erosion rate, $\bar{c} = 0$, the comparison is especially simple when the projectile and target are made from the same material, so $\rho_p = \rho_t = \rho$ and $Y_p = Y_t = Y$. In this case Eq (2.19) gives $\mu_o = \rho A$ so $M_o/\mu_o = (\rho A_o L_o)/(\rho A) = L_o/(A/A_o)$ for a rod, or $M_o/\mu_o = [\rho(\pi D_o^2/4)(2D_o/3)]/[\rho(\pi D^2/4)] = (2D_o/3)/(A/A_o)$ for a sphere. Thus Eq (2.26) can be written as

$$P_E = [L_o/(A/A_o)] \{1 - \exp[-(2/3)x]\} \quad (3.2)$$

where we could use $(2D_o/3)$ instead of L_o . Similarly, $M_o/c = (\rho A_o L_o)/(.5\rho A) = 2L_o/(A/A_o)$ for a rod or $2(2D_o/3)/(A/A_o)$ for a sphere. Since $\ln \sqrt{y} = .5 \ln y$, Eq (2.11) can be written as

$$P_E = [L_o/(A/A_o)] \{\ln(1+x)\} \quad (3.3)$$

where $x = (c/a)\dot{S}_o^2 = [\rho/(6Y)]\dot{S}_o^2$. Eq (3.3) gives a greater P_E than Eq (3.2) for all $x > 0$. For $x = 0$ ($\dot{S}_o = 0$), the penetrations are equal (but zero). For large values of x the curly brackets in Eq (3.2) approach a maximum value of unity, while the curly brackets in Eq (3.3) increase without limit. This agrees with the general observation that a target which erodes a projectile makes a better armor than one which does not.

B. Finite Targets

1. Phenomenology

Target perforation is more complicated than penetration in a semi-infinite target because break-in and break-out effects become more significant.

When a projectile first enters a target its nose shape has an effect as we have mentioned. For example, the area presented by a sphere entering a target increases with penetration depth, P , according to the formula $A = \pi P(D_o - P)$, so A increases from zero for $P = 0$ to $(\pi/4)D_o^2$ as $P \rightarrow (D_o/2)$. If the target thickness is of the same magnitude as the projectile diameter,

$T_0 \sim D_0$, then this variation in A and the variation in target resistance it implies are significant. However, if $T_0 \gg D_0$, they are not. Analogous formulas and considerations hold for conical, ogival or other nose shapes. Only a flat-nose projectile immediately presents its maximum area. In section I. B. above we mentioned the work of Osborn and Woodward (1.22). A well-known effect which they studied is the formation of a "cap" of target material which is punched out and rides on the nose of a blunt projectile. Even Newton discussed such an effect (3.31). When projectile deformation takes place, the effects of nose shape are reduced. Under the right conditions, all projectiles assume the most compact (hemi-spherical) nose shape. Lip formation or other types of front-face target deformation also affect penetration to some degree and may be included under break-in effects.

More attention is usually paid to back-face target deformation or break-out effects like petalling, spalling or scabbing. For semi-infinite targets these effects do not occur by definition. However, even bulging at the back face can lead to greater penetration than would otherwise occur as we saw in Fig. 3.14. Fig. 3.17 shows a sketch of front-face (break-in) and back-face (break-out) effects in an aluminum target perforated by a hard steel sphere (3.32). The diameter of the hole in the target is uneven but not much larger than the diameter of the sphere which is not permanently deformed. Exceptions occur at the front face where a lip has been formed and at the back face where a shallow crater has been formed. The depth of this crater diminishes the original target thickness, T_0 , to the value T shown in the figure. As reported by Zook et al. (3.3), (T/T_0) is about 3/4.

As the striking speed increases so do the amplitude and speed of the pressure pulse which travels ahead of the projectile and reflects as a tensile wave from the rear surface of the plate. Interference between the incident compression wave and reflected tensile wave causes the plate to scab if the amplitude exceeds the fracture threshold of the target material. Rinehart (3.33 to 3.34) estimates this threshold to be about 10^{10} dyne/cm² for 24S-T4 aluminum and about three times this value for 4130 steel. If the wave amplitude is more than twice the threshold stress, multiple scabbing will occur. An example of multiple scabbing in steel given by Rinehart is shown in Fig. 3.18. When the first scab forms, it leaves a new metal-metal interface

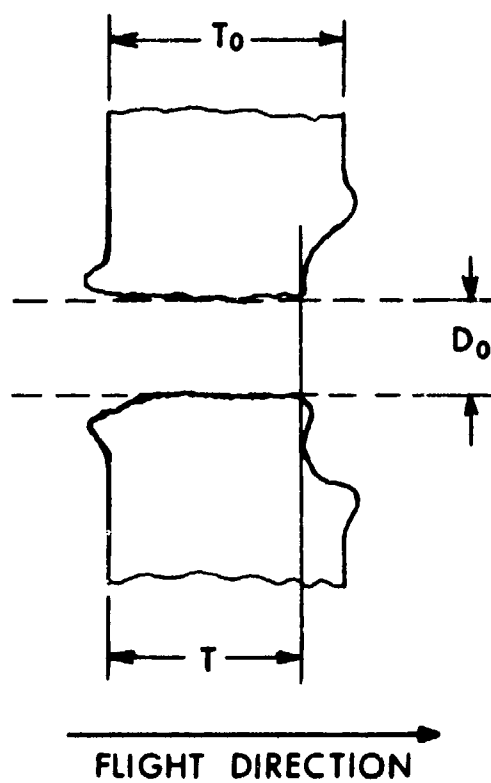


Fig. 3.17. Front-face and back-face target effects (hard aluminum perforated by a hard steel sphere).

inside the target. The trailing part of the incident pressure pulse then reflects from this interface and interferes with itself, forming a second scab, and so on, until the resultant amplitude drops below the threshold value.

Let us assume that the peak amplitude of a pressure pulse caused by a projectile impact is proportional to the impact energy per unit volume of projectile, namely $(.5\rho_p\dot{S}_0^2)$. For a steel projectile with $\dot{S}_0 = 1 \text{ mm}/\mu\text{s}$ this is about $4 \times 10^{10} \text{ dyne/cm}^2$ (or erg/cm^3), which is above Rinehart's estimate of the threshold for steel of $3 \times 10^{10} \text{ dyne/cm}^2$. As we have seen, hard steel spheres exhibit significant fracture effects at impact speeds above $0.7 \text{ mm}/\mu\text{s}$. For an aluminum target to fracture we need a pulse greater than $10^{10} \text{ dyne/cm}^2$ according to Rinehart, or twice this value for two scabs to form. If the impact speed is great enough to produce one scab but not great enough to produce two, then the depth of the back face crater, namely, $(T_0 - T)$ might not increase as \dot{S}_0 increases. This depth might even decrease because of an increase in pulse speed, leading to earlier interference closer to the back surface. Little is known about the detailed effects of pulse shape and speed as a function of geometry and material properties of projectile and target. At present we must rely on the observation of experimental trends in order to form any conclusions.

The ballistic limit thickness of a finite target, T_1 , is the minimum thickness needed to prevent perforation according to some criterion. Clearly $T_1 > T_0$ in Fig. 3.17. It is also true that $T_1 > P_E$, the depth of the crater in a semi-infinite target under otherwise identical conditions. Senf and Weimann^(3.35) impacted 12.7 mm hard steel spheres on finite hard aluminum target plates and obtained the curves shown in Fig. 3.19. The curve labelled P_E is the same as the upper curve in Fig. 3.13. The curve marked T_1 lies higher than that marked P_E over the speed range investigated, with $P_E/T_1 \sim 3/4$. Of course the amount by which T_1 exceed P_E depends on one's criterion for perforation. In this matter there is no universal standard. Fig. 3.20 from Backman and Goldsmith^(3.36) illustrates the Army limit (any pinhole in the rear of the target), the Navy limit (projectile emerges with zero residual speed and falls under the action of gravity), and the protection limit (spall just fails to perforate a witness plate of prescribed material and thickness at a given distance behind the target plate). The ratio T_1/P_E can vary from about 1.1 to 3.0, depending on one's definition of ballistic limit for particular projectile/target combinations. For theoretical simplicity the Navy limit is



Fig. 3.18. Multiple scabbing in steel subjected to explosive attack.

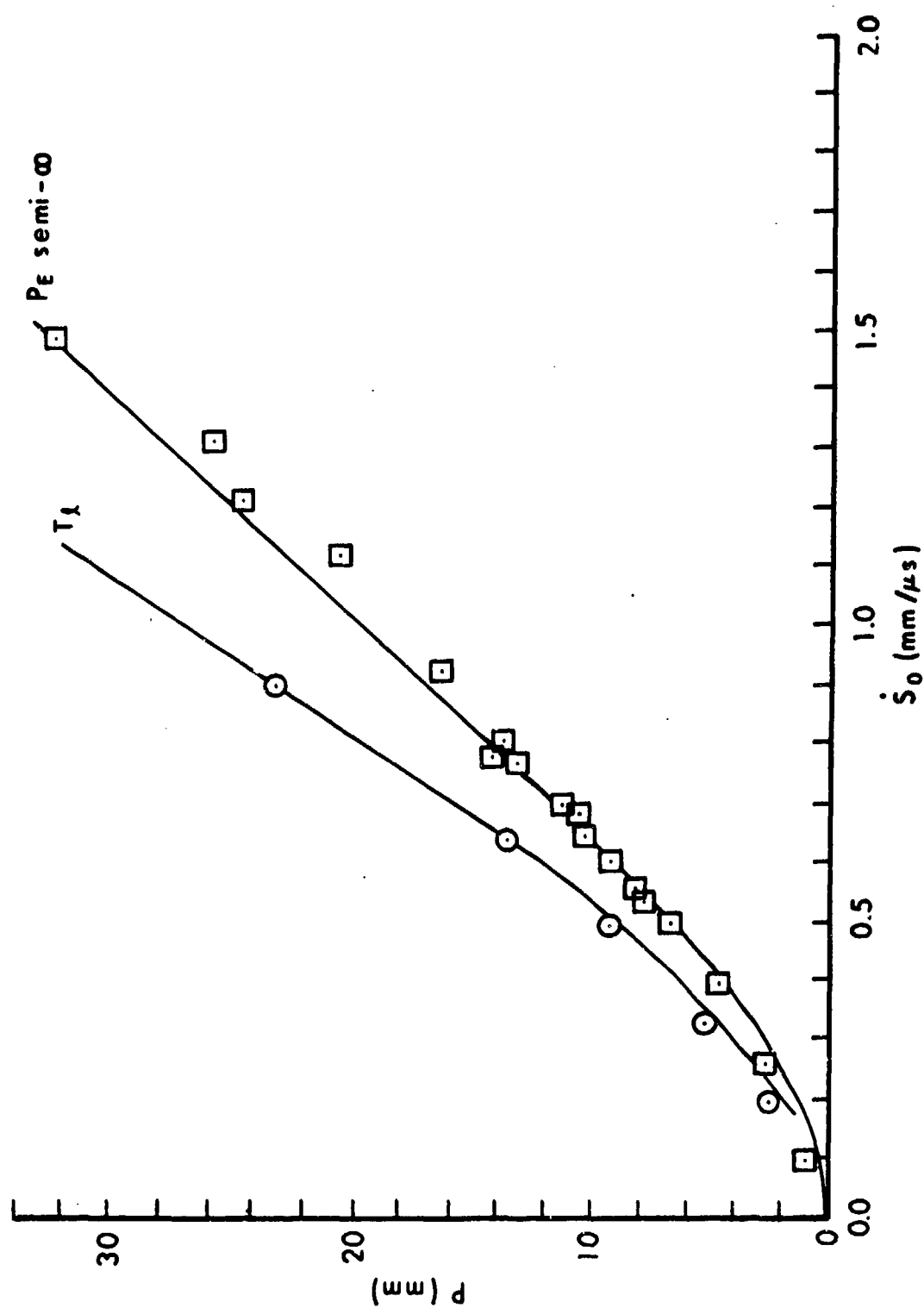


Fig. 3.19. Limit Thickness versus Semi-infinite Target Penetration (Steel Spheres vs Aluminum)

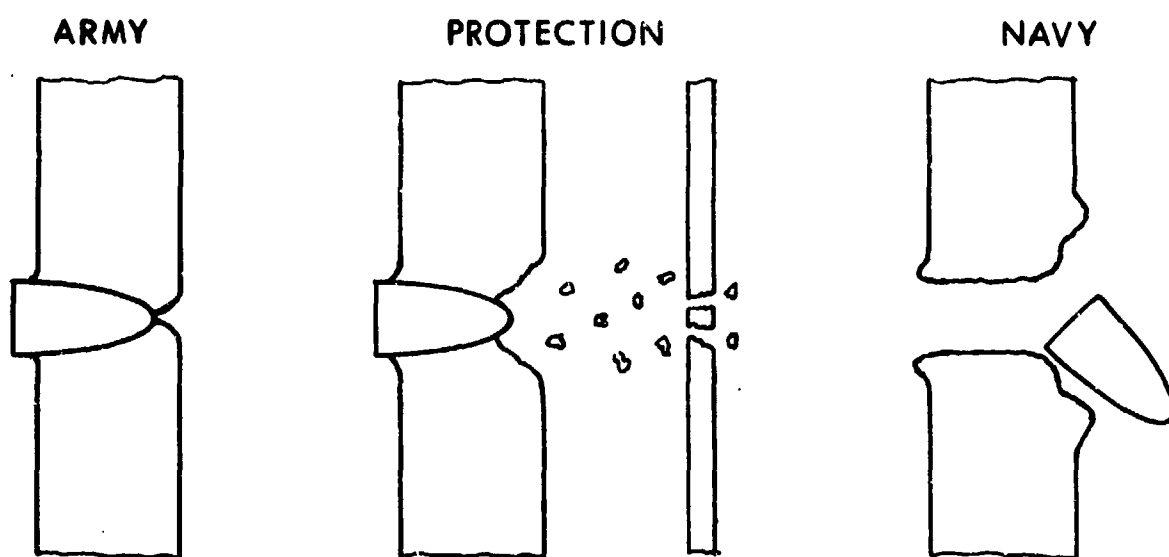


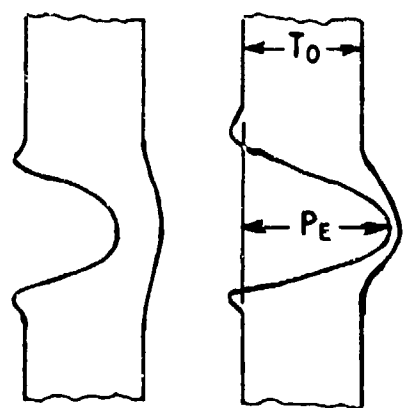
Fig. 3.20. Three Ballistic Limits

preferable and will be used in this report. Considerations of engineering safety margins might lead us to adopt more conservative limits, however.

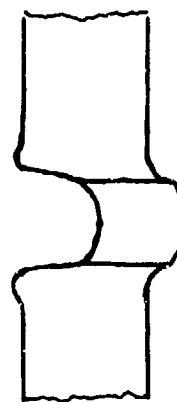
If we have a soft, ductile target, its behavior near a ballistic limit can be quite different from that of a hard, brittle target. Fig. 3.21a shows two sketches of bulges in such a target made by the impact of a sphere. The second sketch shows an extreme case in which the crater depth, P_E , is greater than the original thickness of the target, T_0 . Clearly, the limit thickness is greater than T_0 , $T_1 > T_0$. It is also greater than P_E for a semi-infinite target in known cases. Thin, ductile targets often fail by petalling at the rear. Targets of intermediate strength will often fail by having a plug of target material sheared out by the impact of a sphere. Fig. 3.21b is a sketch of such a plug partially punched out of such a target. In this case the plug is a "cap" which rides in front of the projectile, as mentioned above. Further details on the phenomenology of target plate failure have been given by Backman and Finnegan (3.37).

From our discussion so far we see the truth of the assertion we made in the beginning of this section, namely, perforation is a more complicated phenomenon than penetration in a semi-infinite target. Theories of thin target perforation are legion and generally address one or another type of failure process. There does not seem to be a detailed unified theory which can be specialized to particular cases by letting certain parameters vanish. The state of the art of both theory and experiment has been recently summarized and advanced by Goldsmith and co-workers (3.38 to 3.42).

In this report we wish to remain as simple as possible so that our unified theory will be useful as well as informative. For this reason we have been avoiding detailed physical descriptions in order to concentrate on a few main points. We will continue to do so in the next section by once more introducing an average parameter, T , which we will call the target thickness at the moment of failure. As we see from Fig. 3.17, T can be given a definite, if approximate, experimental meaning. It is similar to the average presented area, A , which we have already used extensively and will use again. This sort of procedure is certainly not completely satisfactory. However, it is presently necessary because of our lack of knowledge and perhaps even desirable as a working tool.



(a) DUCTILE YIELDING



(b) SHEAR PLUGGING

Fig. 3.21

2. Examples

a. Steel Spheres vs Three Thicknesses of Aluminum

The data shown in Fig. 3.22 for 12.7 mm steel spheres impacting hard aluminum plates of three different thicknesses were also reported by Semf and Weimann (3.35). For $T_0 = 10 \text{ mm} < D_0$ they reported no differences between impacts by hardened and softened spheres. However, for $T_0 = 15 \text{ mm} > D_0$, the residual speed after perforation, \dot{S}_R , was greater for the hardened sphere (open circles) than for the softened sphere (open squares), because of flattening. The curves tend to merge and are experimentally indistinguishable near the velocity ballistic limit, $\dot{S}_{01} = 0.67 \text{ mm}/\mu\text{s}$. The differences are even greater for the thickest target ($T_0 \sim 2D_0$) and even the ballistic limits are experimentally distinguishable, being about $0.95 \text{ mm}/\mu\text{s}$ for the hard spheres (solid circles) and $1.0 \text{ mm}/\mu\text{s}$ for the soft spheres (solid squares). If there were no target present ($T_0 = 0$), then $\dot{S}_R = \dot{S}_0$ for any \dot{S}_0 , the straight line in the figure.

In order to calculate the residual speed, \dot{S}_R , as a function of striking speed, \dot{S}_0 , let us once more assume that there is no erosion and that viscosity is negligible. Then we can use Eq (2.7) which is the same equation which led to Eq (2.11) for semi-infinite targets. A semi-infinite target was defined to be one with a thickness, T_0 , sufficiently greater than the final depth of penetration, P_E , that not even a bulge appears on the back face. If T_0 is small enough to permit a bulge, then a further reduction in T_0 versus a particular threat projectile will result in plate failure, reducing T_0 to T as in Fig. 3.17 for a hard target, and turning a target victory into a defeat. The value $T_0 = T_1 > P_E$ semi-infinite as in Fig 3.19 will just gain the victory for the target. For 12.7 mm steel spheres versus hard aluminum, we recall that the ratio $P_E/T_1 \sim 3/4$. This seems to be approximately equal to the observed average value of T/T_0 in Fig. 3.17. This is probably a coincidence, although it would be nice if it were a more general relation. Additional experiments are needed to clarify this point.

The argument of the exponential function in Eq (2.7) involves the penetration depth $P = S - S_0$. At the moment of perforation, when target

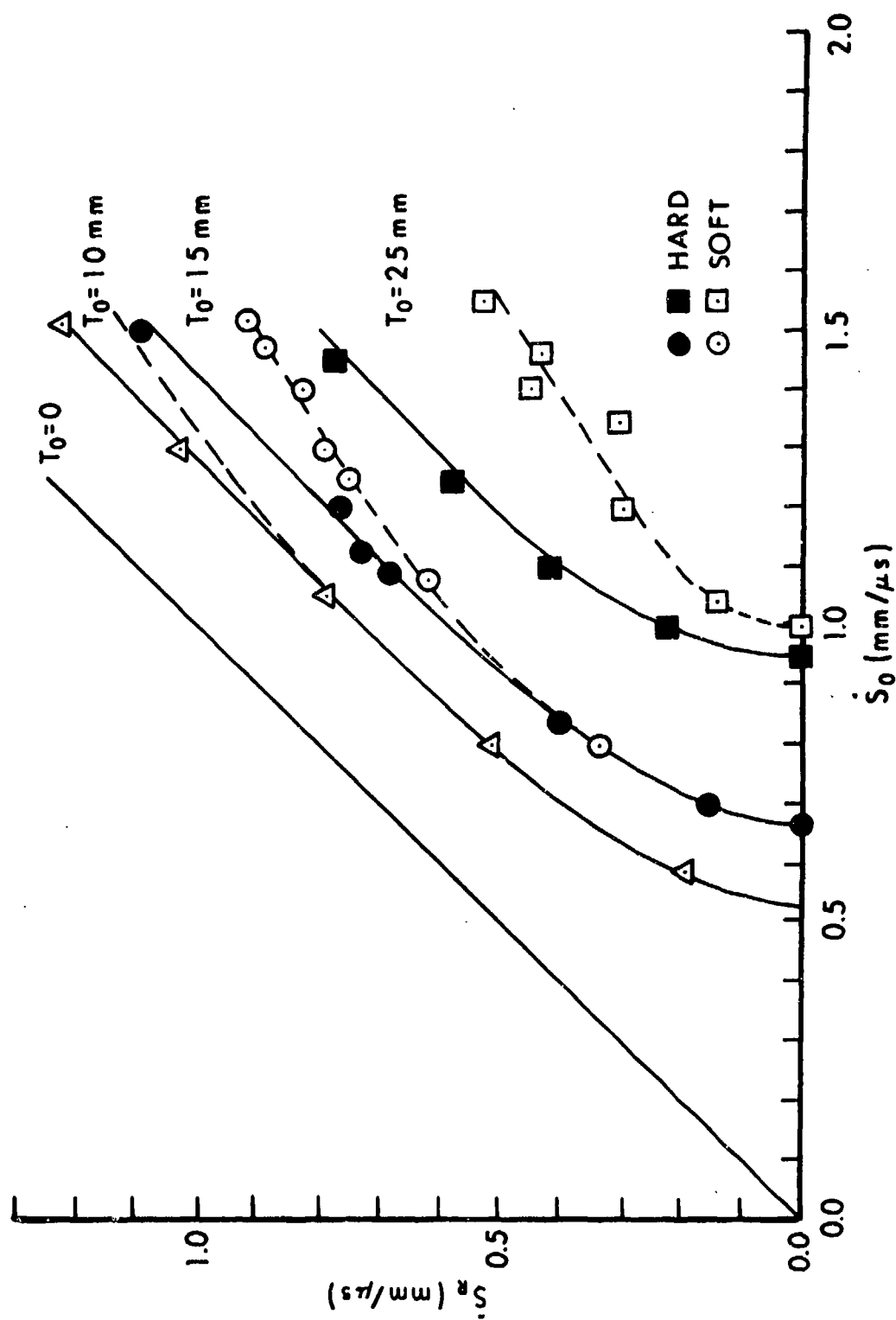


Fig. 3.22. 12.7mm steel spheres versus three thicknesses of aluminum S_R (mm/μs).

failure occurs, $P = T = T_0(T/T_0)$, introducing the ratio (T/T_0) . Since $C = C_0(A/A_0)$ as before, we can re-write the argument as

$$[2T_0/(M_0/C_0)][(A/A_0)(T/T_0)] = [2T_0/(M_0/C_0)]\phi \quad (3.4)$$

where ϕ denotes the product of our two average parameters in ratio form. When P reaches the value T , \dot{S} is the residual speed, \dot{S}_R , and Eq (2.7) becomes

$$\dot{S}_R = \sqrt{a/c} \{ [1 + (\dot{S}_0/\sqrt{a/c})^2] \exp[-2\phi T_0/(M_0/C_0)] - 1 \}^{1/2} \quad (3.5)$$

First let us apply Eq (3.5) by calculating the solid curves in Fig. 3.22. Obviously, if $T_0 = 0$ (no target), $\dot{S}_R = \dot{S}_0$, the straight line in Fig. 3.22. From section III.A.2.f above, we recall that $\sqrt{a/c} = 0.9 \text{ mm}/\mu\text{s}$ is the inflection point for a hard aluminum target, while $M_0/C_0 = 48.9 \text{ mm}$ for a 12.7 mm steel sphere versus an aluminum target. For a hard steel sphere we also recall that $(A/A_0) = 1$, so $\phi = (T/T_0) = 3/4 = P_E/T_L$ on average. Thus, Eq (3.4) becomes $.04\phi T_0 = .03T_0$, and Eq (3.5) becomes

$$\dot{S}_R = 0.9 \sqrt{[1 + (\dot{S}_0/0.9)^2] \exp(-.03T_0) - 1} \quad (3.6)$$

for the solid curves in Fig. 3.22 with $T_0 = 0, 10, 15$ and 25 mm . Close agreement with experiment supports the use of a single average value for $P/T_1 = T/T_0 = 3/4$ for the ranges of \dot{S}_0 and T_0 covered.

Second, let us apply Eq (3.5) by calculating the dashed curves in Fig. 3.22 for the soft steel spheres. We recall from Fig. 3.13 that these spheres progressively flattened as \dot{S}_0 increased above $0.4 \text{ mm}/\mu\text{s}$. The dashed line in Fig. 3.13 indicates the transition from $(A/A_0) = 1$ to $(A/A_0) = 1.67$ near $1.3 \text{ mm}/\mu\text{s}$. This variation is plotted as the upper solid curve in Fig. 3.23 which we have extended above $1.6 \text{ mm}/\mu\text{s}$ with a dashed line, indicating an expected decrease in (A/A_0) as suggested by Fig. 3.6 (for steel targets). As was mentioned, semi-infinite targets provide enough lateral confinement to turn spheres into mushroom caps at high enough impact speeds, reducing A/A_0 after such an inversion. Tapering of the crater diameter may be evidence of this. The lower solid curves give the values of (A/A_0) vs \dot{S}_0 used in Eq (3.5) for the three dashed curves in Fig. 3.22. The agreement with experiment for $T_0 = 15 \text{ mm}$ is rather good. The theory predicts an observable difference for

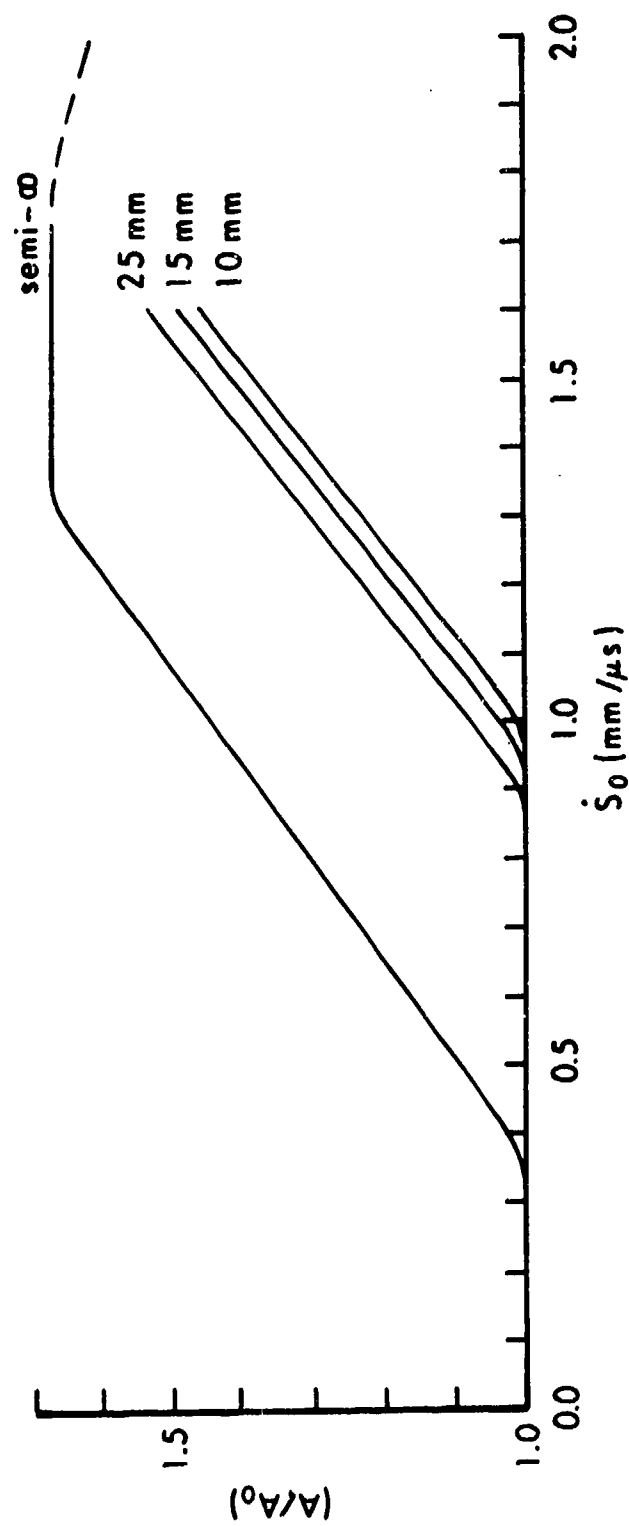


Fig. 3.23. Flattening of 12.7mm soft steel spheres versus various thicknesses of hard aluminum vs. impact speed.

$T_0 = 10$ mm plates near $\dot{S}_0 = 1.5$ mm/ μ s. Apparently only hard spheres were used against this plate thickness. The data available for $T_0 = 25$ mm plates is somewhat scattered, but the agreement between theory and experiment is reasonable.

Fig. 3.23 indicates that finite targets flatten soft steel spheres less than semi-infinite targets do, with thicker target plate effects approaching those of a semi-infinite target. Presumably as the target thickness approaches zero, these curves approach the value $(A/A_0) = 1$, independent of \dot{S}_0 (the \dot{S}_0 axis in the figure). We have not extended the finite plate curves above $\dot{S}_0 = 1.6$ mm/ μ s. However, we can speculate that they will not level off in the manner of the semi- ∞ curve, since the break-out crater at the rear of finite plates relieves the lateral confinement needed to convert a sphere to a mushroom cap. We have no direct evidence for any of these curves. Their postulated shape assumes a constant value of $(T/T_0) = 0.75$, and the combination of these two assumptions is supported indirectly by agreement between soft sphere data and the dashed curves in Fig.

3.22. Other combinations are possible and more experimental information is needed before we can resolve these questions. For example, (T/T_0) may decrease somewhat as \dot{S}_0 increases, requiring higher values of (A/A_0) for the same $\phi = (T/T_0)(A/A_0)$. We might expect a decrease in (T/T_0) if flatter spheres produce wider, shallower breakout craters. If multiple-scabbing occurs, we might even expect a sudden decrease in (T/T_0) above some impact speed.

Before leaving this example, let us recall Fig. 3.14 where a larger 20mm hard sphere showed a penetration at higher impact speeds greater than that calculated. For example, at $\dot{S}_0 = 1.1$ mm/ μ s we calculated $P_E = 36$ mm and attributed the difference to the reported back face bulging. If $T_1/P_E = 4/3$ and $P_E = 36$ mm, then $T_1 = 48$ mm, which is almost equal to the 50 mm thickness of the target block used. This is consistent with the observed bulging.

b. Steel Spheres versus Several Thicknesses of Steel

Fig. 3.24 gives data for steel spheres impacting steel plates reported by Backman and Finnegan (3.37).

Curve (1) shows residual speeds of a hard steel sphere ($D_o = 6.35$ mm) perforating a mild steel target ($T_o = 1.47$ mm $= 0.23D_o$). If we assume BHN = 100kg/mm^2 so $Y_t = 30 \times 10^8$ dyne/cm², then $\sqrt{a/c} = 0.5$ mm/ μs . Since $M_o = 1.05\text{g}$ and $C_o = 0.124\text{g/mm}$, $(M_o/C_o) = 0.47$ mm and $2T_o/(M_o/C_o) = 0.35$. Since $(A/A_o) = 1$ for a hard sphere and $(T/T_o) = 1$ for a ductile target which stretches and petals rather than cratering, we have $\phi = 1$. Eq (3.5) then enables us to calculate curve (1) in reasonable agreement with experiment. A slightly greater target strength might give better agreement.

Curves (2), (3), and (4) show the residual speed of the central fragment of the fragment systems emerging from the back of the targets. These curves are for mild steel spheres impacting armor steel target plates which cratered at the rear. We expect the deformed spheres to be the lead fragment. The spheres were of different sizes ($M_o = 1.15\text{g}$, 1.32g and 0.92g), to obtain integer ratios $D_o/T_o = 4$, 2 and 1 respectively. The target strength was not reported, but if we assume BHN = 300kg/mm^2 , $Y_t = 90 \times 10^8$ dyne/cm², then $\sqrt{a/c} = 0.83$ mm/ μs . We expect $(A/A_o) > 1$ for deforming spheres and $(T/T_o) < 1$ for brittle targets reported to have spall craters at the back face. However, no quantitative information was reported on either ratio. In the absence of such information, we will assume that the product $\phi = (T/T_o)(A/A_o) = 1$ for the speed and target thickness ranges used. Also $2T_o/(M_o/C_o)$ is 0.375 , 0.75 and 1.5 for curves (2), (3), and (4) respectively. The agreement between theory and experiment is remarkable, considering the simple approximations we have been making.

Before leaving this example, let us note that there was apparently some difficulty in determining the ballistic limit for curve (2) as indicated by the two open circles below $\dot{S}_o = 0.5$ mm/ μs . If such a thin target craters in the back, it offers almost no resistance to a projectile and the usual statistical uncertainties involved in determining ballistic limits are compounded when gross fracture dominates the phenomenon.

c. Steel Spheres versus Titanium Alloy Plates

Ricchiuzzi and Brown (3.43) have reported data for hard steel spheres ($Y_t \sim 100 \times 10^8$ dyne/cm², $M_o = 0.13\text{g}$) perforating titanium alloy plates (90Ti/6Al/4V, $\rho_t = 4.43\text{g/cm}^3$, $Y_t = 40 \times 10^8$ dyne/cm², $T_o = 1.32$ mm). This

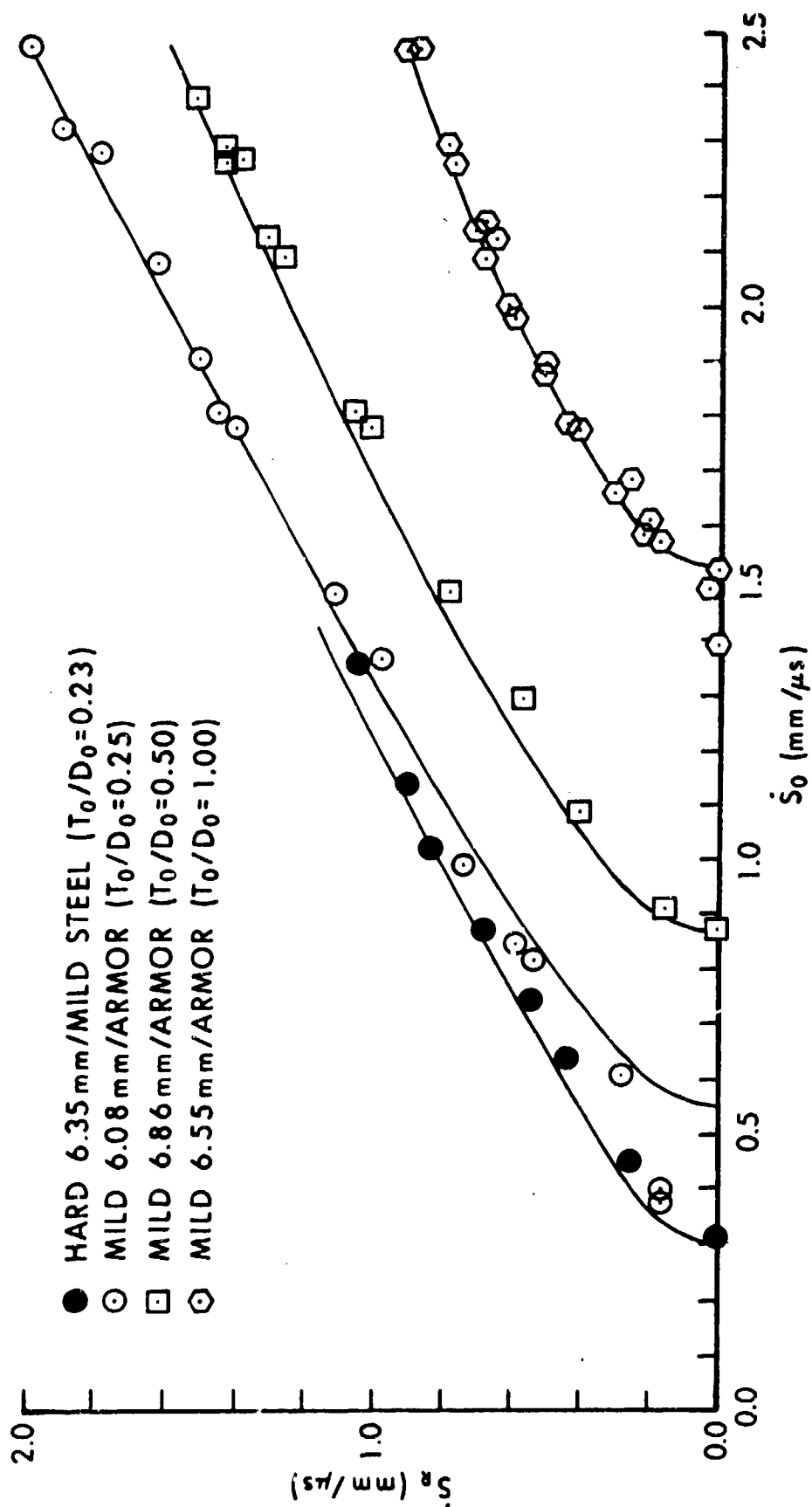


Fig. 3.24. Steel spheres versus steel plates.

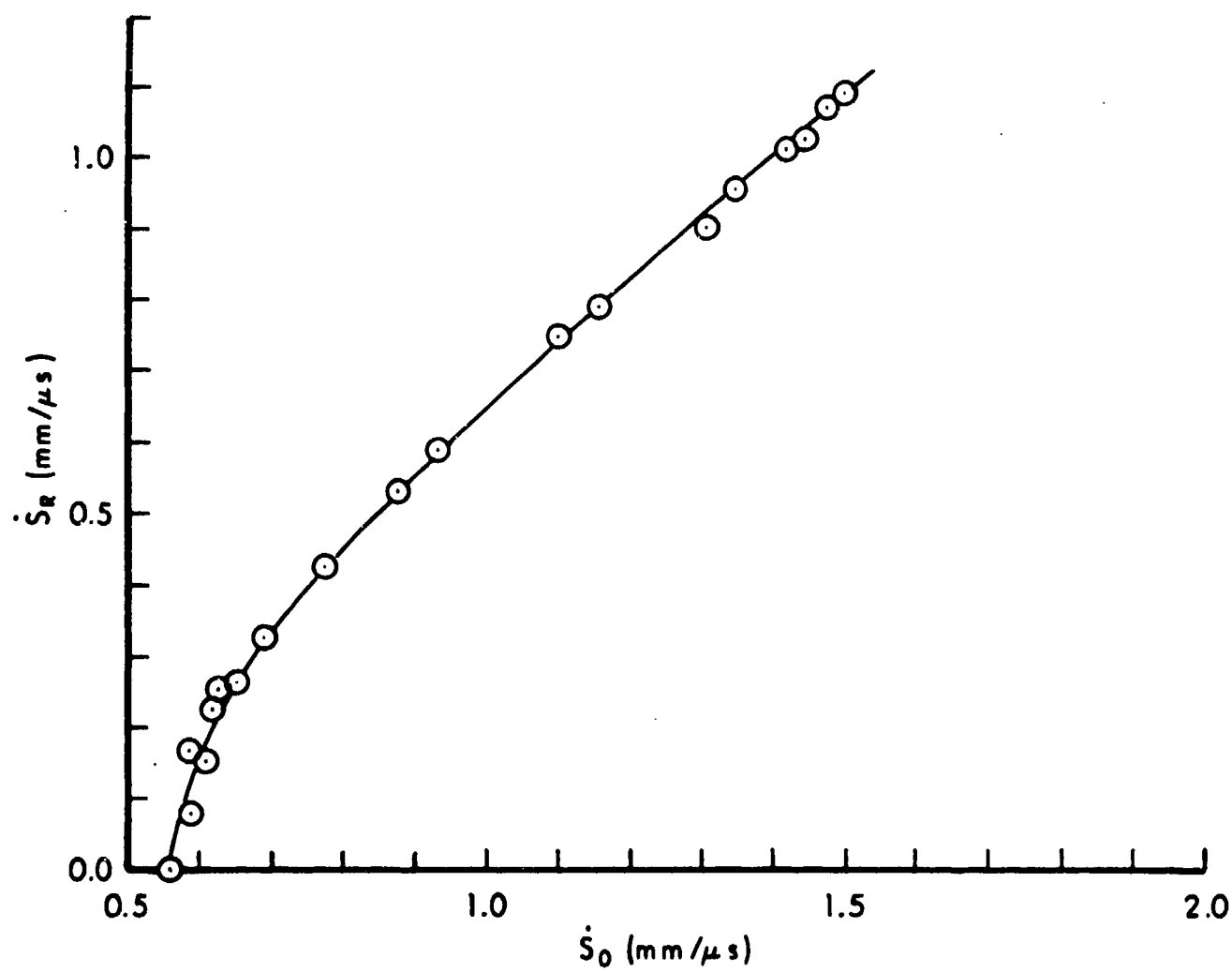


Fig. 3.25. Steel spheres/Ti

steel sphere data was included for comparison with other shapes of tungsten fragments. We find $D_0 = 0.316$ cm, $C_0 = 0.0174$ g/mm, and $M_0/C_0 = 7.5$ mm, so $2T_0/(M_0/C_0) = 0.352$. For lack of detailed information on target or sphere condition, we have assumed $\phi = (T/T_0)(A/A_0) = 1.3$. We also find $\sqrt{a/c} = \sqrt{.54} = .736$ mm/ μ s. With these values in Eq (3.5) we calculate the curve in Fig. 3.25 which agrees closely with the experimental data points. Again it is encouraging that a single value of ϕ can do so well over the range investigated.

IV. EXAMPLES OF ROD PENETRATORS

A. Deformation and Mass Loss

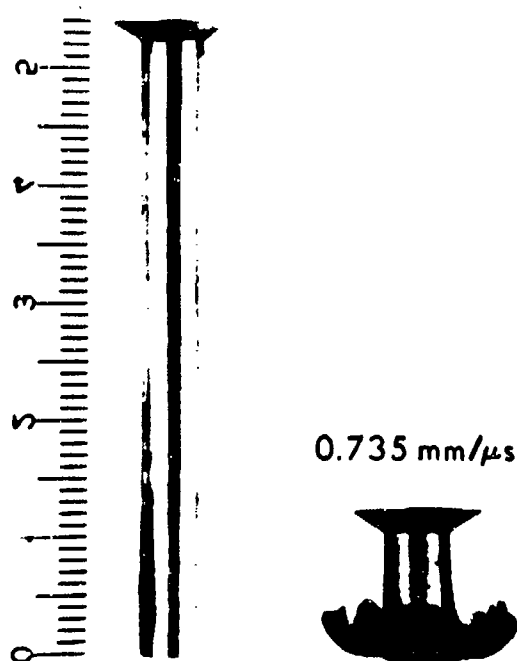
For compact penetrators of spherical shape we saw that severe deformation to a mushroom cap shape or severe shattering can occur at sufficiently high impact speeds. However, there is no evidence that any penetrator mass is lost during a penetration in the sense that no element of mass is without some forward component of velocity right up to the end of the penetration. Very ductile projectiles might be found after a penetration spread in a thin layer over most of the crater. Very brittle projectiles which have been pulverized might be lost because of target orientation. Intermediate cases might yield intermediate results when residual projectile masses are sought after an event. More reporting of the whereabouts of projectile mass after a penetration is surely desirable. In any case, our theory and the available experimental evidence indicate that all of the mass of a compact spherical projectile participates in the cratering process during the entire time of a penetration event.

For compact projectiles of rod shape, that is with L_0/D_0 near unity, the same comments seem to hold. Fig. 4.1a shows a steel rod ($L_0/D_0 = 12 \text{ mm}/12 \text{ mm} = 1$, $M_0 = 10.6 \text{ g}$, $\text{BHN} = 230 \text{ kg/mm}^2$) lifted out of the sectioned crater it made in a steel target ($\text{BHN} = 135 \text{ kg/mm}^2$) after an impact at about $1.0 \text{ mm}/\mu\text{s}$. This figure is similar to Fig. 3.4b for a steel sphere impacting a steel target at a somewhat higher speed (1.5 km/s). The mushroom cap shape is clearer in Fig. 4.1a. Perhaps the distorted rear end of the rod still forms a short stem in the middle of the cap. Fig. 4.1b shows the remains of a long rod ($L_0/D_0 = 54 \text{ mm}/5.4 \text{ mm} = 10$, $M_0 = 9.85 \text{ g}$) made of the same steel after striking a harder steel target ($\text{BHN} \sim 300 \text{ kg/mm}^2$) but at a lower speed ($S_0 = 0.735 \text{ mm}/\mu\text{s}$). For comparison, an original rod before impact is shown beside it. The stabilizer flare at the rear of each rod is evident. Clearly most of the mass of the original rod has been lost. A measurement of the length of the residual rod gives us a rough estimate of the residual mass if we multiply this length by the original cross-sectional area and the density. However, this estimate

$D=12.0 \text{ mm}, 0.977 \text{ mm}/\mu\text{s}$



Fig. 4.1a. Compact steel rod deformed to a mushroom cap (axial section). $S_0 = .977 \text{ mm}/\mu\text{s}$



$0.735 \text{ mm}/\mu\text{s}$

$D = 5.4 \text{ mm}$



Fig. 4.1b. $L_0/D_0 = .10$ steel rod deformed to a mushroom cap with stem. $S_0 = .735 \text{ mm}/\mu\text{s}$

must be corrected by adding the mass which is still present in the ragged mushroom cap which tops off a somewhat fattened stem. Weighing the residual projectile would give us the answer, but this measurement was not reported (4.1). The diameter of the cap is about three times the original rod diameter.

Fig. 4.2a shows a time sequence of four X-ray pictures of a tungsten alloy rod penetrating a steel target at 1.4 mm/ μ s, while Fig. 4.2b shows a similar sequence for a copper rod penetrating an aluminum target at about the same speed (4.2). Similar pictures for steel on steel are not possible because of a lack of contrast, but a similar mushrooming of the nose occurs as is evident from Fig. 4.1b. The pictures in Figs. 4.1 and 4.2 have an important feature in common. In all of these metal/metal impacts, the crater is sufficiently wider than the projectile body that the thin tube of eroded projectile material seems to line the cavity walls without making significant contact with the incoming projectile during penetration. This is why we can neglect external friction as well as viscosity (internal friction) for typical metal/metal penetrations and deal only with forces on the projectile nose. We cannot do this if yaw is significant or for metal projectiles impacting very hard, brittle targets like glass or various ceramics, as we have noted.

Fig. 4.3 (4.3) shows a sequence of drawings depicting the formation of a copper tube from a fully annealed soft copper rod penetrating a metal target. Only the upper half of each cutaway is shown because of axial symmetry. The last sketch at the bottom of the series shows that most of the rod has eroded near the end of the penetration, since most of the rod elements have lost any forward component of velocity. However, there is still a central stem attached to the mushroomed nose. The impact speed in this example was 1.15 mm/ μ s. At higher impact speeds this residual stem will be shorter, but never seems to disappear completely. During most of a penetration the mass of this stem pushes on the nose and helps to make the eroded material turn back. However, this stem has less mass near the end of a penetration and exerts an ever smaller force. The net result is that such projectiles never seem to turn completely inside out, but always retain a cap of projectile material at the forward end. As a penetration by a long rod nears its end, the rod becomes a compact projectile and never quite completely erodes since the central stem becomes so short it no longer can push cap material aside. This

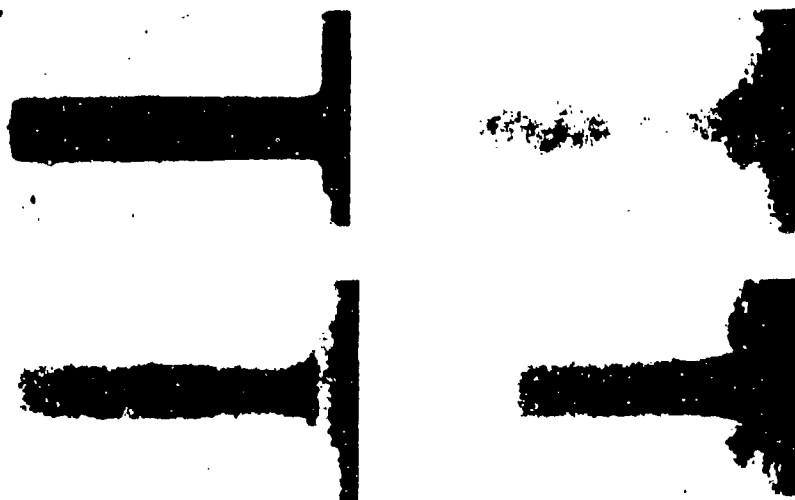


Fig. 4.2a. Tungsten rod versus steel at $1.4\text{mm}/\mu\text{s}$.

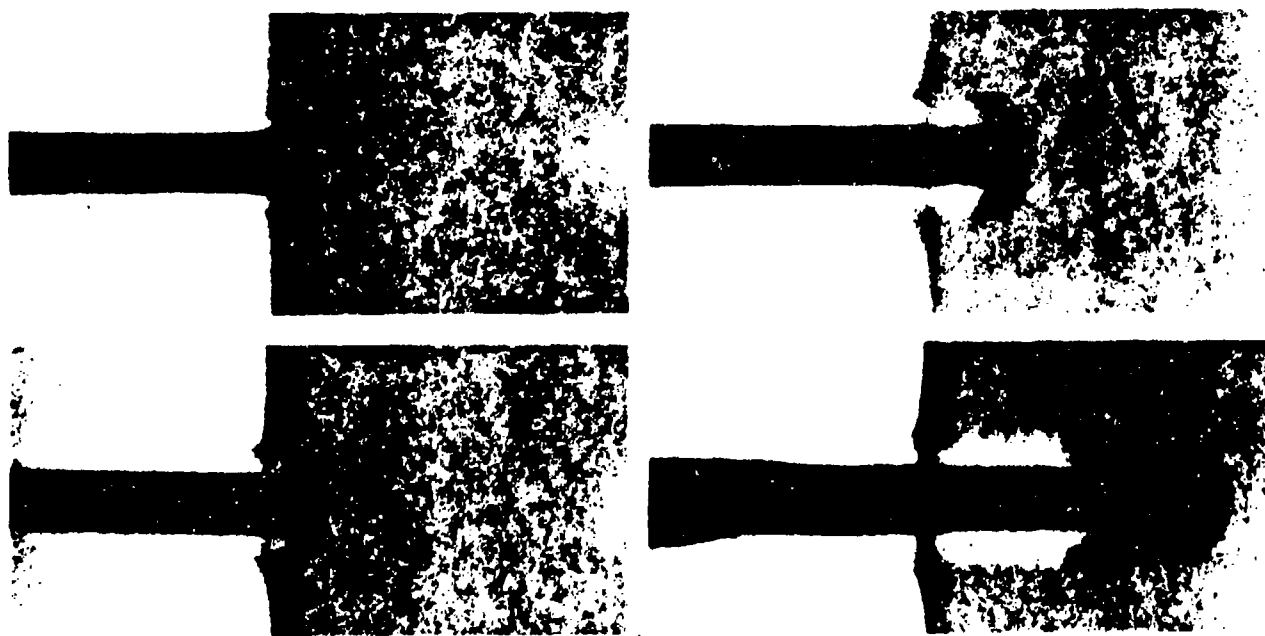


Fig. 4.2b. Copper rod versus aluminum at $1.4\text{mm}/\mu\text{s}$.

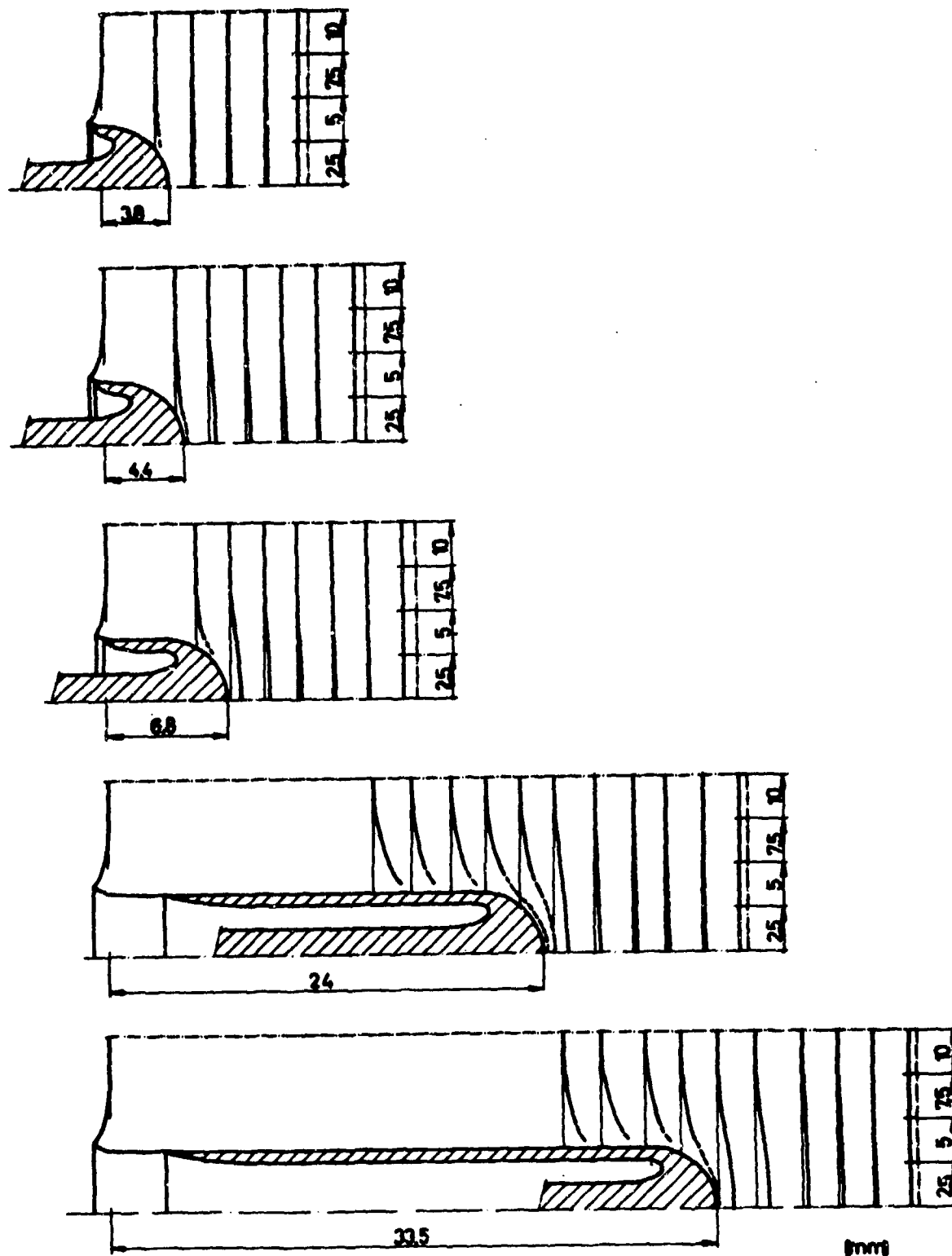


Fig. 4.3. Deformation of annealed copper target at various penetrating depths of the penetrating hydrodynamic head at the impact velocity of 1150 m/s (projectile material: copper).

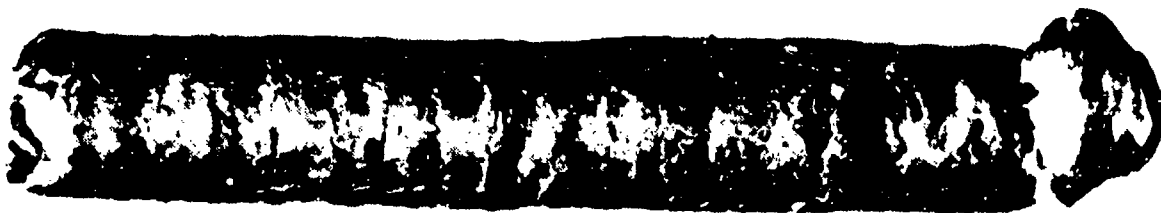


Fig. 4.4a. Copper tube (inverted copper rod) recovered from a target.



Fig. 4.4b. Axial section of same copper tube.

agrees with our theory which predicts some residual mass in physically reasonable cases even if this mass is too small to observe easily. Fig. 4.4a shows a copper rod which has been inverted to a tube after penetrating a target. Notice the cap at one end. Fig. 4.4b shows this same tube cut in half lengthwise (an axial section). Again the cap at the end is clear. These figures are also from Weihrauch ^(4.4).

B. Calculational Aids

In Chapter Three for compact ($L_0/D_0 = 1$) projectiles, we were able to account for the available experimental data with one equation, Eq (2.11). Since we had no time-dependent information, we did not need Eqs (2.2) or (2.3). Eq (2.11) is so simple that no special discussion was needed concerning its use. All parameters were known experimentally except for the flattening factor, (A/A_0) . Even here estimates could be made from experimental information, although final numerical values came from adjustment to experiment. Remarkably, a single value seemed to suffice for all striking speeds greater than those for which either shattering or plastic deformation occurred. For higher striking speeds, we may conjecture that flattening occurs early in a penetration, so that a single value of (A/A_0) holds for most of the penetration at such speeds.

Eq (2.11) says that the penetration depth will increase without limit as the striking speed increases without limit. Of course, this is not true when striking speeds are so high that liquifaction and/or vaporization of materials becomes important. Additional terms are needed in these cases. However, the available data indicates that Eq (2.11) is good enough up to $\dot{S}_0 = 10 \text{ mm}/\mu\text{s}$, and quite adequate at ordnance speeds up to $2 \text{ mm}/\mu\text{s}$.

In Chapter Four we wish to describe cases in which erosion occurs. Consequently, our principal equation will be Eq (2.22). In the few cases where we have time-dependent information we will also use Eqs (2.28) to (2.30). Now we wish to discuss the use of these equations in some detail before illustrating them with examples.

We can write Eq (2.22) as

$$P_E = (M_o/\mu_o) \{1 - [1 + (\dot{S}_o/\beta)^2]^{-\epsilon}\} = \left(\frac{M_o}{\mu_o}\right) Q \quad (4.1)$$

where

$$\beta = k \sqrt{a/c} \quad (4.2)$$

and

$$\epsilon = \mu_o k / (2\bar{c}) \quad (4.3)$$

In Eq (4.1), the definition of the factor, Q , is obvious. Here (4.2) is somewhat larger than the inflection point in Eq (2.24). We recall from Chapter II that Eq (2.22) or (4.1) reduces to Eq (2.11) if $\mu_o \rightarrow 0$. Without erosion Eq (2.11) says that P_E can increase without limit as S_o increases, within the limitations of the model. However, for $\mu_o > 0$, Eq (4.1) says that P_E approaches a finite limit, M_o/μ_o , as \dot{S}_o increases.

We will be able to determine μ_o from experiment in only three examples below. To estimate μ_o in other cases from these three cases, we will make an assumption that lesser erosion rates follow the same trend as the maximum erosion rate in Eq (2.19). That is, we will assume

$$\mu_o = f A_o \sqrt{\rho_p \rho_t (A/A_o)} \quad (4.4)$$

where $0 < f < 1$. By adopting Eq (4.4), we are assuming that f and (A/A_o) are approximately independent of A_o , ρ_p and ρ_t as well as projectile and target hardness. In most cases of interest this turns out to be a fairly good assumption. Exceptions will be mentioned as they occur. Our theory requires μ_o to be independent of speed for given \dot{S}_o . However, it is possible that μ_o might depend on \dot{S}_o . Therefore, $f \sqrt{A/A_o}$ in Eq (4.4) must be independent of speed for given \dot{S}_o , and, if μ_o depends on \dot{S}_o so must this product. However, f and (A/A_o) might individually depend on \dot{S}_o , even if μ_o is independent of \dot{S}_o . Eq (4.4) also says nothing about aspect ratio. As it turns out, (A/A_o) seems to depend on aspect ratio at low speeds, and becomes independent of aspect ratio at high speeds (see Fig. 4.15). A minor dependence of (A/A_o) on ρ_p and ρ_t

also seems evident at high speeds, but is relatively weak for the density range of common interest.

For a rod,

$$M_o = \rho_p A_o L_o = \rho_p [(\pi/4) D_o^2] L_o \quad (4.5)$$

If we divide Eq (4.5) by Eq (4.4), we find

$$(P_E)_{LIMIT} = (M_o / \mu_o) = (L_o \sqrt{\rho_p / \rho_t}) / (f \sqrt{A/A_o}), \quad (4.6)$$

which we can compare to Eq (2.27) as $\dot{S}_o \rightarrow \infty$. As expected, we find $f = 1$ for Eq (2.27), since we used $\mu_o(\max)$ from Eq (2.19) in this equation. For rods of interest, $f < 1$ and $(A/A_o) > 1$, so $f \sqrt{A/A_o} \gtrless 1$ are all possibilities. In other words, Eq (4.6) says there is a high speed penetration limit which can be greater than, equal to or even less than what is usually called the hydrodynamic limit, $(L_o \sqrt{\rho_p / \rho_t})$. We will discuss this again in Chapter V. In our examples below, we will find that $(P_E)_{LIMIT}$ is usually higher than the hydrodynamic limit, sometimes much higher.

If we have penetration data over a wide enough range of striking speeds, we can estimate $(P_E)_{LIMIT}$ experimentally. In such cases, Eq (4.6) enables us to estimate an upper bound for μ_o , since we know M_o . That is,

$$\mu_o \leq M_o / (P_E)_{LIMIT} \quad (4.7)$$

It is always dangerous to estimate such limits from incomplete experimental information, so we will generally use Eq (4.7) as a check on the following procedure.

Suppose we know μ_{o2} for rod/target combination 2, and wish to estimate μ_{o1} for rod/target combination 1. From Eq (4.4),

$$\mu_{o1} = \mu_{o2} [f_1 A_{o1} \sqrt{\rho_{p1} \rho_{t1} (A/A_o)_1}] / [f_2 A_{o2} \sqrt{\rho_{p2} \rho_{t2} (A/A_o)_2}] \quad (4.8)$$

If $f \sqrt{A/A_o}$ is the same, as it is for rods of the same aspect ratios,

$$\mu_{o1} = \mu_{o2} [A_{o1} \sqrt{\rho_{p1} \rho_{t1}}] / [A_{o2} \sqrt{\rho_{p2} \rho_{t2}}] \quad (4.9)$$

If, in addition, identical targets ($\rho_{t1} = \rho_{t2}$) are struck by rods of the same density ($\rho_{p1} = \rho_{p2}$), μ_{o1}/μ_{o2} is equal to the ratio of the respective masses per unit length, since $A_{o1}/A_{o2} = (M_o/L_o)_1 / (M_o/L_o)_2$ by Eq (4.5).

Now let us recall that $a = 3Y_t A_o (A/A_o)$, $c = .5\rho_t A_o (A/A_o)$, and $I_o = (2\rho_p A_o)^{-1}$. Then by Eq (4.4)

$$I_o \mu_o = (.5 \sqrt{\rho_t / \rho_p}) (f \sqrt{A/A_o}) \quad (4.10)$$

and

$$I_o \mu_o^2 = f^2 [.5 \rho_t A_o (A/A_o)] = f^2 c \quad (4.11)$$

From Eq (2.18) we recall that

$$\bar{c} = c - I_o \mu_o^2 \quad (4.12)$$

Now, if we use Eq (4.11) and the definition of c ,

$$\bar{c} = c (1-f^2) = [.5 \rho_t A_o (A/A_o)] (1-f^2) \quad (4.13)$$

Then Eqs (4.2) and (4.3) can be written as

$$\beta = \alpha (1 + I_o \mu_o) / \sqrt{1-f^2} \approx \alpha \quad (4.14)$$

and

$$\begin{aligned} \epsilon &= \{(\mu_o/A_o) / [\rho_t (A/A_o)]\} \{(1 + I_o \mu_o) / (1-f^2)\} \\ &\approx (\mu_o/A_o) / [\rho_t (A/A_o)] \end{aligned} \quad (4.15)$$

where $\alpha = \sqrt{6Y_t / \rho_t}$ as before. The approximate forms hold if $I_o \mu_o \ll 1$ and $f^2 \ll 1$. Then Q in Eq (4.1) becomes

$$Q = 1 - [1 + (\dot{S}_0/3)^2]^{-\epsilon}$$

$$\approx 1 - [1 + (\dot{S}_0/\alpha)^2]^{-(\mu_0/A_0)/[\rho_t(A/A_0)]} \quad (4.16)$$

Finally, from Eqs (4.1),

$$P_E = (M_0/\mu_0) Q \quad (4.17)$$

Once we have an estimate of μ_0 , then only (A/A_0) is unknown and appears only in Q . Since (A/A_0) seems to depend on \dot{S}_0 , at least at low speeds, then Q depends both explicitly and implicitly on \dot{S}_0 , as we see from Eq (4.16). If we can use the approximate form of Q , (A/A_0) appears only in the exponent and at high speeds should be independent of \dot{S}_0 . With this as a starting point, we can estimate (A/A_0) for lower striking speeds, and then refine our estimate by using the exact form of Eq (4.16).

This analysis allows us to describe at least five simple ways of studying the effect that rod geometry (L_0 and D_0) and density (ρ_p) have on penetration into a given semi-infinite target (given ρ_t , Y_t and α). In the first two ways we keep the aspect ratio the same, while varying either the size or density of our rods. In the other three ways, we vary the aspect ratio, and either keep the mass constant or allow the mass to vary by changing either L_0 or D_0 but not both.

In the first way, we multiply L_0 and D_0 by a common factor, while keeping ρ_p the same. This produces a family of rods with a common aspect ratio and $f\sqrt{A/A_0}$, so Eq (4.9) gives their different erosion rates which depend on their area, A_0 , or mass per unit length. Then A_0 cancels in the product $I_C\mu_0$ which is the same for all such rods by Eq (4.10). Of course, (μ_0/A_0) is also the same by Eq (4.4). It also appears that f and $\sqrt{A/A_0}$ are individually the same for all such rods, so that ζ , ϵ and Q are all exactly the same for this family by Eqs (4.14) to (4.16). Since $M_0 \sim L_0 A_0$ and $\mu_0 \sim A_0$, then $(M_0/\mu_0) \sim L_0$ and $P_E \sim L_0$ in Eq (4.17). Thus, a plot of P_E/L_0 versus S_0 should give a single curve for all rods in this family. Since we also have $L_0 \sim D_0$, a plot of P_E/D_0 should do the same. Here we have an example where the use of a dimensionless variable in plotting experimental data can reveal an important relation and

prompt us to look for an explanation if we don't have one. Or, as we are now doing, it can illustrate the descriptive power of a proposed explanation. Indiscriminate use of dimensionless variables can be more confusing than helpful, as we shall point out. This is especially true if only dimensionless variables are reported without any way to recover the original dimensional observations.

In the second way, we keep the aspect ratio the same by leaving L_o and D_o unchanged, while varying the rod density, ρ_p . This can be done gradually by alloying. However, because of experimental uncertainties, we need to compare two metals of quite different densities, like steel and tungsten. We have assumed that $f \sqrt{A/A_o}$ is only slightly affected by such a change in density, so $\mu_o \sim \sqrt{\rho_p}$ in Eq (4.4). An increase in ρ_p will decrease ζ and increase ϵ in Eq (4.14) and (4.15). Both of these changes will increase Q in Eq (4.16). Since $M_o \sim \rho_p$ and $\mu_o \sim \sqrt{\rho_p}$, $P_E \sim \sqrt{\rho_p} Q$ in Eq (4.17) should increase somewhat faster than $\sqrt{\rho_p}$ as ρ_p increases.

In the third way, we keep M_o constant in Eq (4.5) while keeping ρ_p constant and varying the aspect ratio (L_o/D_o). This implies that we keep $D_o^2 L_o = D_o^3 (L_o/D_o)$ constant, so we must decrease D_o , if we increase (L_o/D_o), and increase L_o , if we decrease D_o . If we decrease D_o or A_o , we decrease μ_o by Eq (4.4), but keep (μ_o/A_o) the same, provided $f \sqrt{A/A_o}$ is unchanged. We also keep $I_o \mu_o$ the same for all rods in this family by Eq (4.10). Thus ζ , ϵ and Q will remain exactly the same. Thus by Eq (4.17), $P_E \sim 1/\mu_o \sim 1/D_o^2$ will increase as μ_o or D_o decreases. Even for $L_o/D_o \rightarrow 1$, $\mu_o \rightarrow 0$, the case for which Eq (2.11) applies, $P_E \sim 1/D_o^2$, since $c \sim A_c \sim D_o^2$. This simple result should hold for high striking speeds when (A/A_o) becomes independent of \dot{S}_o , but will be modified at low speeds when (A/A_o) depends on \dot{S}_o .

In the fourth way, we keep ρ_p and D_o constant, while varying L_o . Although M_o changes, M_o/L_o does not, so μ_o should be the same for all rods in this family as should $I_o \mu_o$ and μ_o/A_o . Then ζ , ϵ and Q will be the same, so $P_E \sim L_o$ by Eq (4.17). Once more a plot of P_E/L_o versus \dot{S}_o should give a single curve for the family. This result will also be modified, if (A/A_o) depends on aspect ratio as for low \dot{S}_o . If $L_o/D_o \rightarrow 1$, Eq (2.11) gives the same result.

In the fifth way, we keep ρ_p and L_o constant, while varying D_o . Then $\mu_o \sim D_o^2$ will change, but μ_o/A_o and $I_o \mu_o$ will remain the same. Thus ζ , ϵ and

Q are exactly the same. Since $M_0 \sim D_0^2$ also, (M_0/μ_0) will be unchanged as will P_E . Consequently, changing the rod diameter will not affect high speed penetration, since we change the erosion rate as fast as we change the mass. This result too will be modified if (A/A_0) depends on aspect ratio. Again for $L_0/D_0 \rightarrow 1$, Eq (2.11) gives the same result.

Much of what we have said is not obvious, and will become clear only through examples.

Obviously, there are many other ways to vary rod geometry, density and hardness. Significant changes in rod hardness can affect nose shatter and alter penetration, at least over a limited range of striking speeds. In most cases of interest, projectile hardness is relatively unimportant. Many of the other ways we can vary geometry and density would not qualify as "simple," and do not seem to have been used in systematic series of experiments as these five ways have been used.

Finally, we wish to describe the few cases in the literature where some time-dependent data exists. This is important, not only because these cases provide a severe proving ground for our theory, but also because we want to use the few values of μ_0 which can be determined from experiment as a starting point for estimating μ_0 for the majority of cases where no such information yet exists.

Let us combine Eqs (2.28) and (2.29) to obtain

$$D = [(X_0^\epsilon \zeta/k)/(\epsilon M_0/\mu_0)] t = vt = \int_{X_0}^X x^{\epsilon-1} (x-1)^{-1/2} dx \quad (4.18)$$

and

$$X = [1 + (\dot{S}_0/\zeta)^2] [1 - P/(M_0/\mu_0)]^{1/\epsilon} = X_0 (M/M_0)^{1/\epsilon} \quad (4.19)$$

Here we have taken $t_0 = 0$, while ζ and ϵ are given by Eqs (4.2) and (4.3). The definition of the frequency ν is obvious from Eq (4.18). The final form of Eq (4.19) comes from Eq (2.15). The integral in Eq (4.18) must be evaluated numerically, unless ϵ happens to be zero, integer or half-integer, as we will now illustrate with a few examples.

The first example below can be described by using the parameters $\epsilon = 1$, $v = .2 \text{ s}^{-1}$ and $X_0 = 17$, as we shall see. Since $\epsilon = 1$, we can evaluate the integral in Eq (4.18) without numerical approximations:

$$D = .2t = \int_X^{17} dx/\sqrt{x-1} = 2(4 - \sqrt{X-1}) \quad (4.20)$$

and

$$X = 17 (1 - P/64) \quad (4.21)$$

since $(M_0/\mu_0) = 64 \text{ mm}$. Eqs (4.20) and (4.21) relate P and t parametrically through X . In a simple case like this, we can eliminate X to find

$$P = 64\{1 - [1 + (4-.1t)^2]/17\} \quad (4.22)$$

From this we can find $\dot{P}(t)$ also, if we desire. The smallest value of X which gives real t in Eq (4.20) is $X = 1$. When $X = 1$ in Eq (4.20) we find the embedment time, $t_E = 40\mu\text{s}$. When $X = 1$ in Eq (4.21) we find $P_E = 60 \text{ mm}$, as we find from Eq (4.22), when $t = 40\mu\text{s}$.

Usually, we must evaluate integrals like D numerically. There are many ways to do this. Here we will select one for purposes of illustration, namely, the four-point Gauss method. This is quite simple, yet accurate enough for our purposes. In what follows, we will use the notation of Margenau and Murphy ^(4.5). First, we transform the range of integration to the unit interval by introducing a new variable, v , in the linear transformation

$$x = X + (17-X) v \quad (4.23)$$

in our case where X is the lower limit and 17 is the upper limit. Then the integral becomes

$$D = (17-X) \int_0^1 F(v) dv \quad (4.24)$$

with

$$F(v) = (x-1)^{-1/2} = [X + (17-X)v - 1]^{-1/2} = F(x) \quad (4.25)$$

by Eq (4.23). In the four point Gauss method, D is approximated by the sum of four products as follows:

$$D \approx (17-X) \{ .174 [F(v_0) + F(v_3)] + .326 [F(v_1) + F(v_2)] \} \quad (4.26)$$

where $v_0 = .069$, $v_1 = .330$, $v_2 = .670$ and $v_3 = .931$ are the four points on the unit interval which optimize the method. These points are given with greater precision in texts, as are the coefficients, .174 and .326. Here we have retained only three significant figures for the v_i as good enough for our purpose.

Now, suppose $X = 5$ in Eq (4.23), so $x = 5 + 12v$. The x -values which correspond to the four pre-selected v -values, together with the associated values of the integrand, $F(v) = F(x)$ in Eq (4.25) are $x_0 = 5.84$, $F_0 = .455$, $x_1 = 8.96$, $F_1 = .354$, $x_2 = 13.04$, $F_2 = .288$ and $x_3 = 16.16$, $F_3 = .257$. Then Eq (4.26) becomes

$$D \approx 12 [.174 (.455 + .257) + .326 (.354 + .288)] = 3.999 \quad (4.27)$$

This is very close to the value $D = 4$ which we find by letting $X = 5$ in Eq (4.20).

Other exact integral forms are available for integer and half-integer values of ϵ which can serve to bound whatever method we choose for a numerical evaluation. For example, if $\epsilon = .5$,

$$D = \int_X^{X_0} dx / \sqrt{x(x-1)} = \ln \{ [\sqrt{X_0} + \sqrt{X_0-1}] / [\sqrt{X} + \sqrt{X-1}] \}^2 \quad (4.28)$$

which, together with Eq (4.20), can bound D, if $.5 < \epsilon < 1$. Similarly, if $\epsilon = 1.5$,

$$D = \int_X^{X_0} \sqrt{x} dx / \sqrt{x-1} = \sqrt{X_0(X_0-1)} - \sqrt{X(X-1)} + \ln \{ [\sqrt{X_0} + \sqrt{X_0-1}] / [\sqrt{X} + \sqrt{X-1}] \} \quad (4.29)$$

while, if $\epsilon = 2$,

$$D = \left(\frac{2}{3}\right) [(2+X_0)\sqrt{X_0-1} - (2+X)\sqrt{X-1}] , \quad (4.30)$$

and so on. In every case we see that $X = 1$ is the smallest, physically meaningful value of X , giving real t .

When a numerical integration is required, it is helpful to plot $F(v)$ versus v to discover whether or not the integrand has a steep slope in the unit interval. If it does, a significant portion of the area under the curve may be neglected by a four-point approximation. It may be necessary to use two or more sub-intervals selected to accommodate the curve and/or use more points in each sub-interval.

C. Semi-infinite Targets

1. Examples with Time-dependent Data

a. Steel/Magnesium

The most extensive collection of time-dependent information on eroding penetrators has been reported by Perez ^(4.6). This is a summary and continuation of his earlier work ^(4.7, 4.8). In his more recent work he used flash X-rays to follow the loss in length suffered by a rod while penetrating low density metal targets of magnesium and aluminum. This kind of information is very valuable for learning about penetration and provides an excellent testing ground for a theory.

First, consider Perez' data ^(4.9) for a steel rod ($\rho_p = 7.8 \text{ g/cm}^3$, $L_0/D_0 = 22 \text{ mm}/2 \text{ mm} = 11$ reported and $M_0 = 0.54 \text{ g}$ calculated) striking a magnesium target ($\rho_t = 1.8 \text{ g/cm}^3$ reported, $Y_t = 10 \times 10^8 \text{ dyne/cm}^2$ estimated) at $\dot{S}_0 = 3.27 \text{ mm}/\mu\text{s}$. Fig. 4.5 shows the positions of the rod nose, P , and rear, R , and so its remaining length, $L = P - R$, as a function of time, t . The following values were estimated from his figure. Initially, $P = 0$, $R = -22 \text{ mm}$, $L = 22 \text{ mm}$. Near $t = 6 \mu\text{s}$, $P = 16 \text{ mm}$, $R = 0$, $L = 16 \text{ mm}$. Near

$t = 11\mu s$, $P = 28$ mm, $R = 16$ mm and $L = 12$ mm. Near 18, 23 and $25\mu s$, P is 41, 48 and 50 mm, and L is about 7, 4.5 and 3.5 mm. At the end of the penetration P_E is about 60 mm while the remaining length is difficult to estimate but is probably about 2 mm since the rod has been reduced to a crushed cap.

Eq (2.15) can be written as

$$\mu_o = (\rho_p A_o)(L_o - L)/P \quad (4.31)$$

Here $A_o = .0314$ cm² so $\rho_p A_o = .245$ g/cm = .0245 g/mm and $L_o = 22$ mm. If we use the L and P values estimated above, we find $\mu_o = .009$ g/mm for the erosion rate. At the end of the penetration, the X-ray length is no longer a good estimator of the residual mass because of severe rod distortion. The fact that the data points give a single value of μ_o supports our assumption that $\dot{M} = -\mu_o \dot{P}$ in Eq (2.14) with μ_o independent of speed for given \dot{S}_o . It does not tell us, however, whether μ_o depends on \dot{S}_o .

Perez (4.10) also reported penetration depths for the same steel rod impacting this magnesium target at various striking speeds. In Fig. 4.6 we see a dip in penetration similar to what we saw in Figs. 3.6 to 3.8 above (steel spheres versus steel). In the case of steel spheres we had independent experimental evidence from recovered projectiles that such a dip was associated with shatter. Here we have no such direct evidence, although we will see such evidence below for other rods. Because of this it seems reasonable to suppose that the dip in Fig. 4.6 is associated with nose shatter. For steel spheres versus magnesium, we saw that shatter began near 2.3 mm/ μs (Fig. 3.9). Here it begins closer to 3 mm/ μs , which is not unexpected in view of the length of the rod and the time it would take for a wave from the nose to reflect from the rear and travel back to the nose. This implies that a dip indicating the onset of nose shatter should occur at a lower speed for a shorter steel rod against this magnesium target. In fact, this is what Perez observed as shown by the middle curve in Fig. 4.6 for $L_o/D_o = 3$ where the dip begins near $\dot{S}_o = 2.5$ mm/ μs .

Fig. 4.7a shows three radiographs at different times during the penetration of the $L_o/D_o = 11$ rod into magnesium for $\dot{S}_o = 2.85$ mm/ μs . Even the stabilizer flare is clearly visible in the earliest picture as is the mushrooming of the nose. There also appears to be no contact between incoming

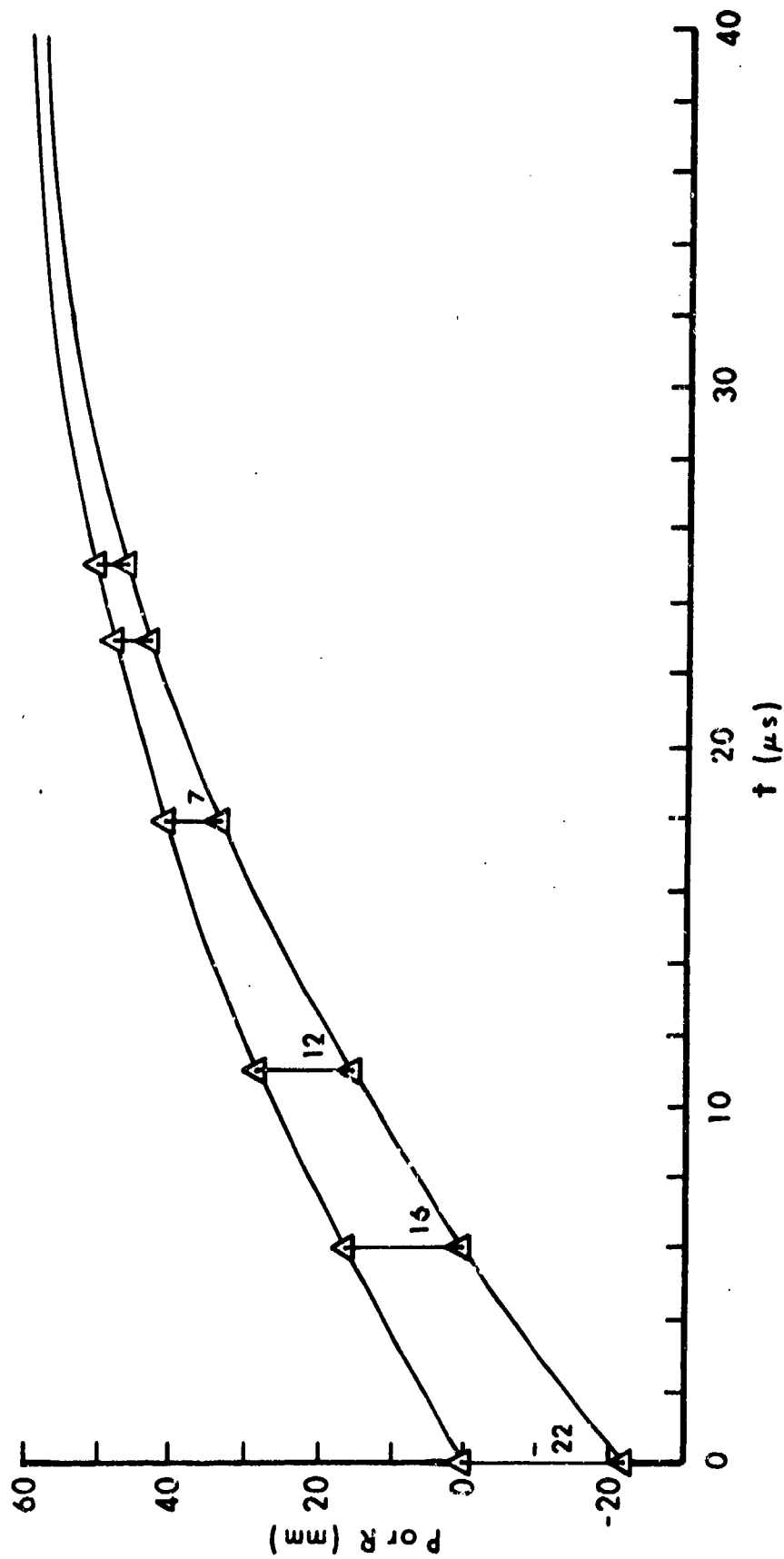


Fig. 4.5. Rod nose (P) and rear (R) positions versus time with remaining length L shown by vertical lines. Steel rod ($L_0/D_0 = 11$) versus magnesium for $\dot{S}_0 = 3.27 \text{ mm}/\mu\text{s}$.

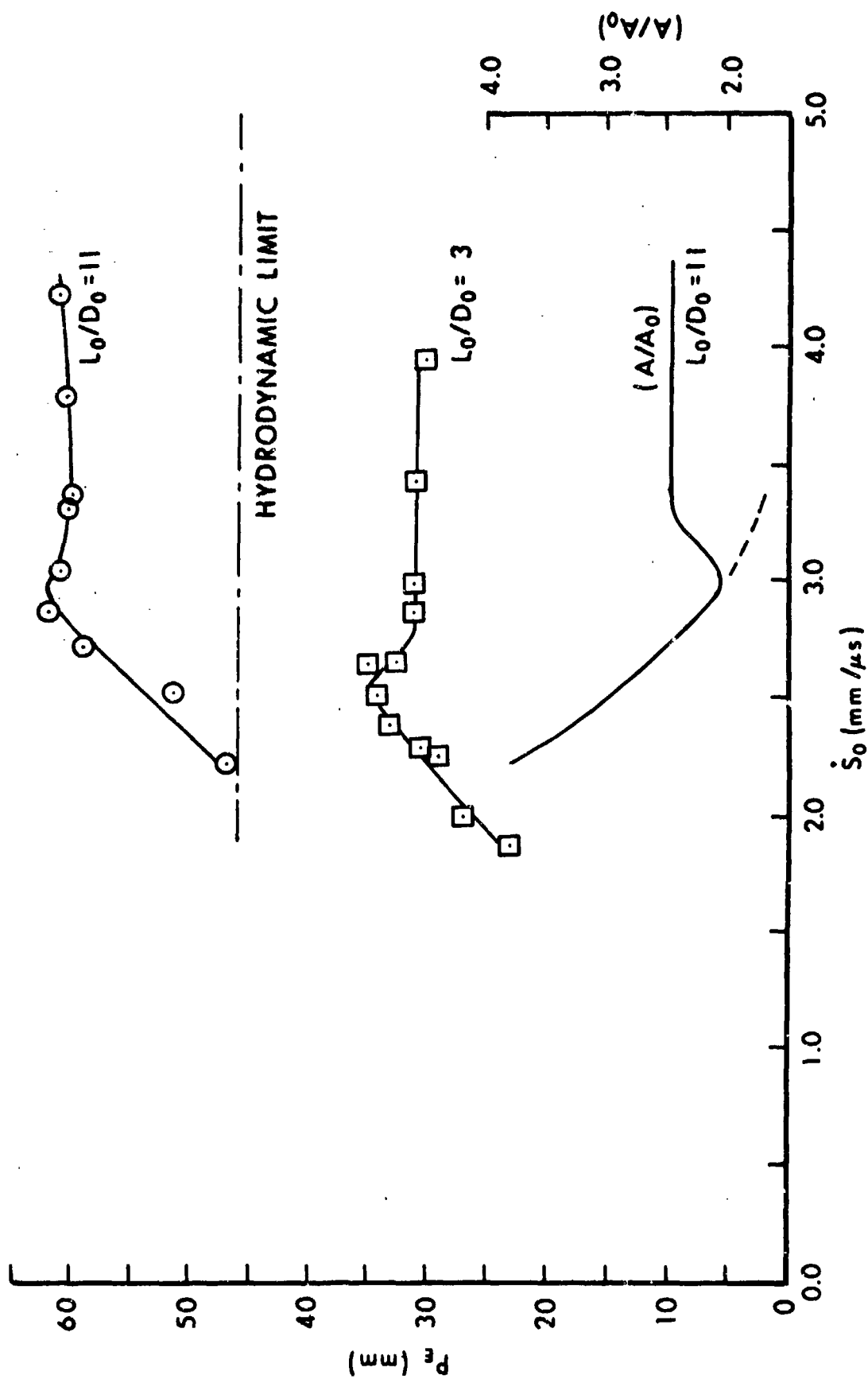


Fig. 4.6. Steel rods versus magnesium.

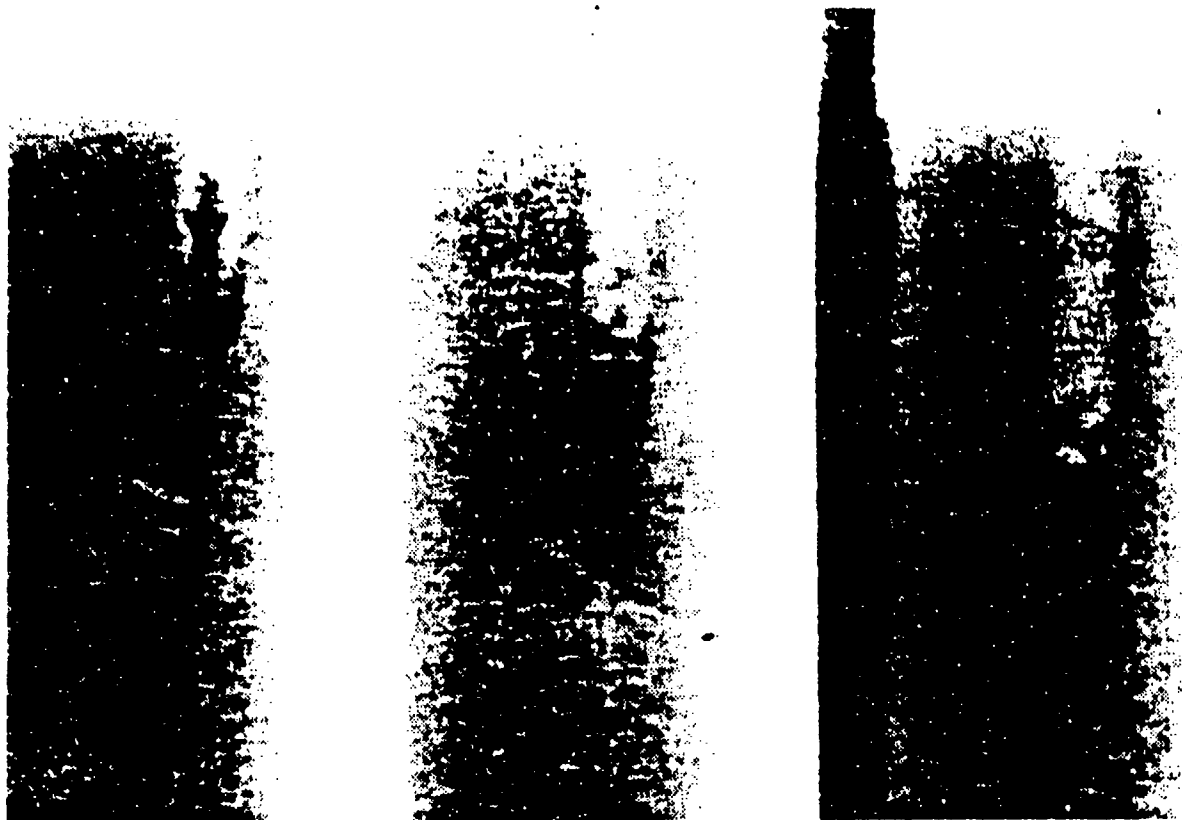


Fig. 4.7a. Steel rod ($L_o/D_o = 11$) versus magnesium target at 2.85mm/ μ s.

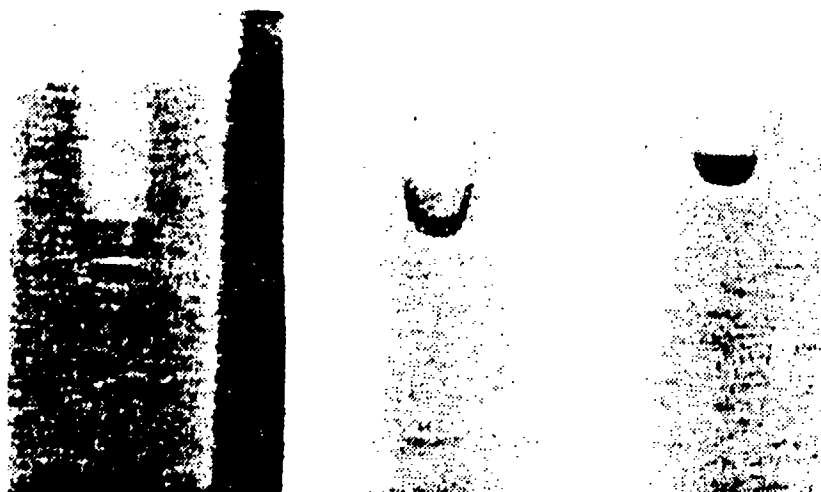


Fig. 4.7b. Steel rod ($L_o/D_o = 3$) versus magnesium target at 2.63mm/ μ s.

projectile body and eroded material. Fig. 4.7b shows three radiographs at different times during the penetration of the $L_0/D_0 = 3$ rods into magnesium for $\dot{S}_0 = 2.63$ mm/ μ s, about the same striking speed as in Fig. 4.7a. Seen at the earliest time, the rod has mushroomed and resembles Fig. 4.1a. No estimates of residual length versus time are possible.

Fig. 4.8 shows penetration by this steel rod into a stack of magnesium plates separated by thin (0.1 mm thick) brass sheets. Fig. 4.8a shows three radiographs taken at different times during the penetration while Fig. 4.8b shows a cross-section afterward. Perez did not report either the striking speed or the thickness of the magnesium plates (or final penetration depth). He only wished to point out the deformation was essentially the same during and after penetration, except perhaps near the top and bottom of the crater. We would also like to point out that the crater in Fig. 4.8b has a balloon shape. That is, it is wider over most of its length than at the impact surface where crater diameters or areas are usually measured. We will comment on this later.

Now let us use Eq (4.1) to calculate the uppermost curve in Fig. 4.6. The mass of the rod was not reported, and the value .54 g was calculated from the reported density and geometry. Perez mentioned that he added stabilizing flares at the rear of his rods, which should increase the calculated mass a bit. Since neither the mass nor geometry of these flares was reported, we will estimate an additional mass of .036 g for the flare, giving $M_0 = .576$ g. We have chosen this particular number to make $M_0/\mu_0 = 64$ mm with $\mu_0 = .009$ g/mm. This seems reasonable in view of the data in Fig. 4.6. We also find $a = .001 (A/A_0)$ g mm/ μ s², $c = .0028 (A/A_0)$ g/mm, $I_0 = 20.4$ mm/g, $I_0\mu_0 = .18$, $I_0\mu_0^2 = .0017$ g/mm, and $k = 1.18$. Of course, $\bar{c} = (c - .0017)$ g/mm, so we can find $\zeta = 1.18 \sqrt{a/\bar{c}}$ mm/ μ s and $\epsilon = .5\mu_0 k/\bar{c} = .0053/\bar{c}$, once we decide on (A/A_0) for a particular striking speed. If we use $(A/A_0) = 2.5$, we find $\zeta = .8$ mm/ μ s and $\epsilon = 1$. Then, for example, when $\dot{S}_0 = 4$ mm/ μ s, $P_E = 64 \{1 - [1 + (4/.8)^2]^{-1}\} = 61.5$ mm. Similarly, if we use the values of (A/A_0) shown at the bottom of Fig. 4.6, we can calculate the uppermost curve, which agrees well with experiment. The horizontal dashed curve is the hydrodynamic limit, $L_0 \sqrt{\rho_p/\rho_t} = 22 \text{ mm} \sqrt{7.8/1.8} = 45.8$ mm. All of Perez' data points lie above this limit and seem to approach 64 mm, 40% higher.

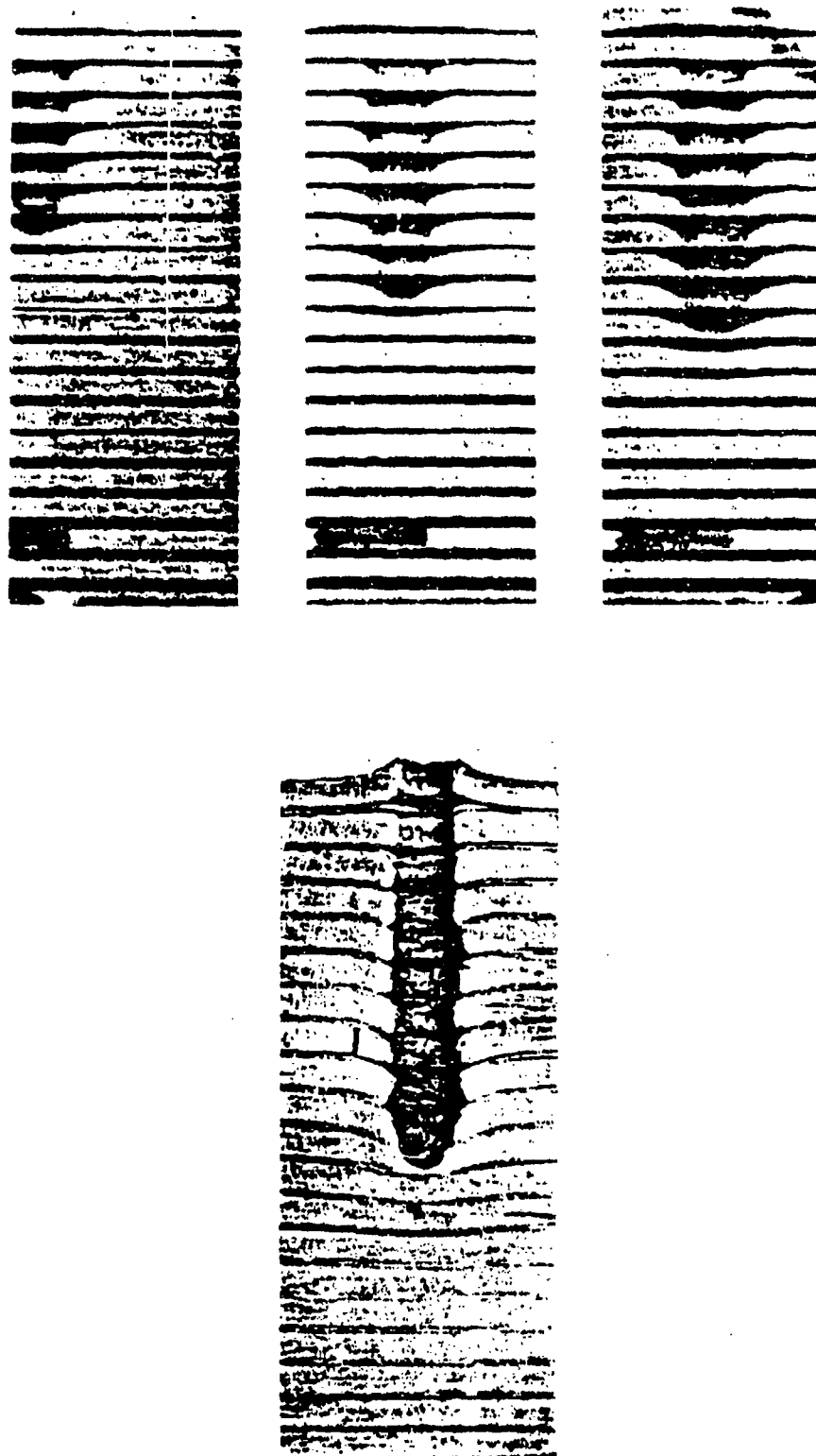


Fig. 4.8. Craters Made by a Steel Rod Penetrating a Layered Magnesium Target.

In Fig. 4.6 we have found that (A/A_0) declines from about 4 near $\dot{S}_0 = 2$ mm/ μ s to about 2 near $\dot{S}_0 = 3$ mm/ μ s. This is similar to the decline in (A/A_0) from 1.8 to 1.5 experienced by the softened spheres in Fig. 3.6 as \dot{S}_0 increased from 1 to 1.5 mm/ μ s. As the impact speed increases it is likely that the rod mushrooms earlier in the penetration and on average presents a more streamlined nose, that is a lower value of (A/A_0) . Except for the onset of nose shatter near $\dot{S}_0 = 3$ mm/ μ s, this trend might have continued as indicated by the dashed curve. However, the shattered nose spreads out more and (A/A_0) increases, levelling off at 2.5 above $\dot{S}_0 = 3.3$ mm/ μ s. For impact speeds higher than this, none of the parameters change. The gradual increase in penetration is due entirely to the increase in \dot{S}_0 .

Finally, let us use Eqs (4.18) and (4.19) to calculate $P(t)$ in Fig. 4.5. Since $(A/A_0) = 2.5$ at $\dot{S}_0 = 3.27$ mm/ μ s, $\epsilon = 1$, $\nu = .2\mu\text{s}^{-1}$ and $X_0 = 17$. Since $\dot{P}_0 = \dot{S}_0/k = 2.8$ mm/ μ s, $\dot{P}_0^2 = .04$ gmm/ μs^2 which is much larger than the target strength term, $a = .0025$ gmm/ μs^2 initially. However, by the time \dot{P} drops below .7 mm/ μ s, the strength term begins to dominate the inertial term. As $\dot{P} \rightarrow 0$, only target strength remains. Since $\epsilon = 1$, we can use Eq (4.22) to calculate the upper curve in Fig. 4.5. Eq (2.15) gives the remaining mass, $M = M_0 - \mu_0 P = (.576 - .009P)$ g. For $P_E = 60$ mm, we find $M_E = .036$ g, so only the flare mass has not been eroded in this estimate. A crude estimate of the depth of the crushed residue might be $L_E = M_E/(\rho_p A_0) = .15$ cm = 1.5 mm. A good estimate of the remaining length at early time is $L = M/(\rho_p A_0)$, while the position of the rear is $R = P - L$, the lower curve in Fig. 4.5, which is also in reasonable agreement with experiment.

b. Aluminum/Magnesium

Fig. 4.9 shows Perez' (4.11) time-dependent data for an aluminum rod impacting the same magnesium target, but at $\dot{S}_0 = 3.35$ mm/ μ s. The X-ray contrast was not as good as for steel/magnesium, so the length measurements are more uncertain. Perez also made a few time-dependent measurements for the same rod/target combination, with $\dot{S}_0 = 2.2$ mm/ μ s (4.12). However, there were too few measurements to make a separate determination of the erosion rate. The one measurement reported which included both tip and rear positions confirms our assumption that μ_0 is independent of striking speed for a given rod/target combination. In the present case, $L_0/D_0 = 33$ mm/3 mm = 11 and

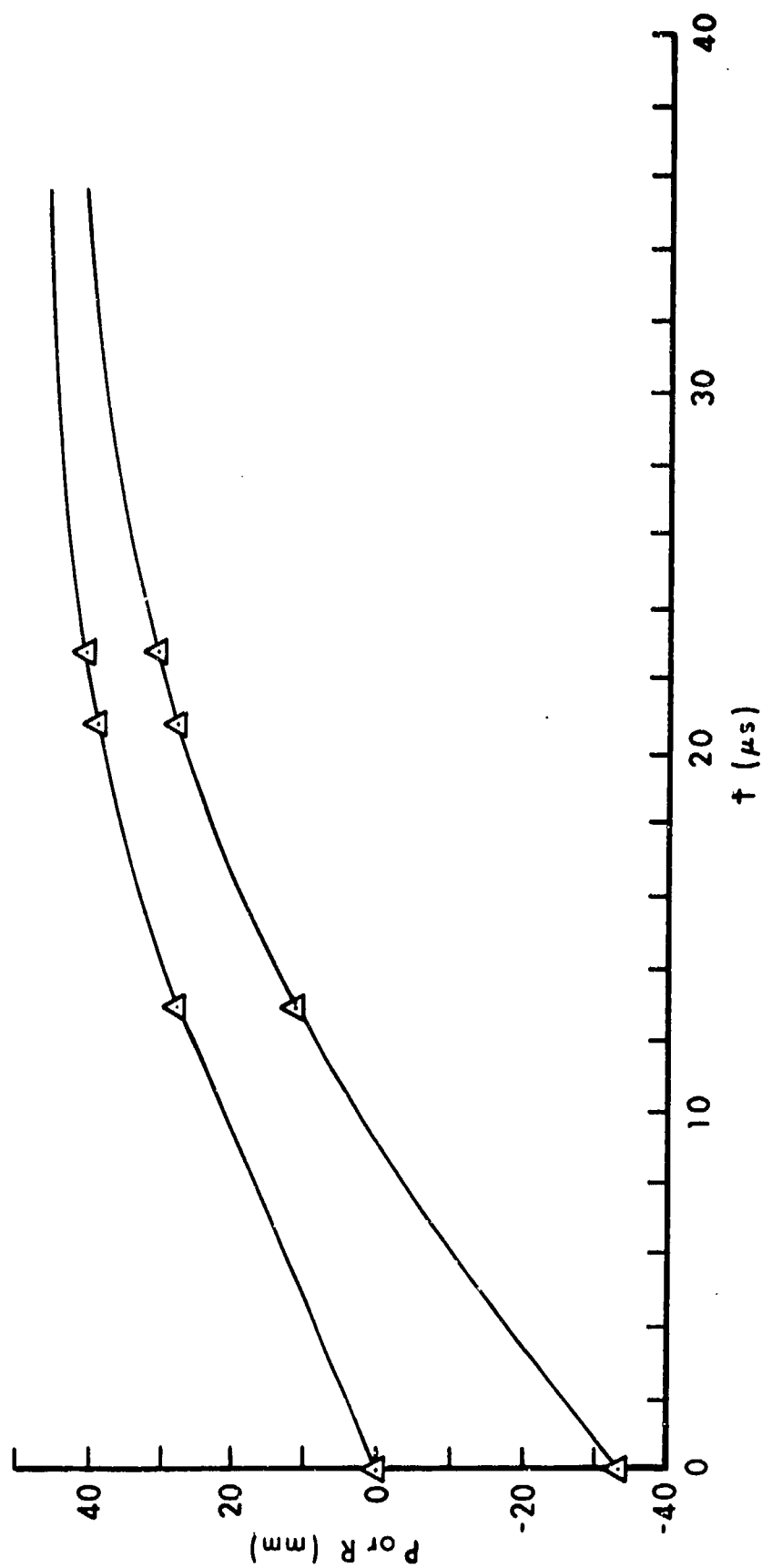


Fig. 4.9. Rod tip and rear positions versus time (Al/Mg)
($S_0 = 3.35 \text{ mm}/\mu s$).

$\rho_p = 2.8 \text{ g/cm}^3$ for Perez' aluminum rod, compared to $L_o/D_o = 22 \text{ mm}/2 \text{ mm} = 11$, $\rho_p = 7.8 \text{ g/cm}^3$ for his steel rod. He kept the aspect ratio the same, while multiplying both L_o and D_o by 1.5. However, this is not our first way above, since he also changed the density, ρ_p .

When we apply Eq (4.31) to Fig. 4.9, we find $\mu_o = .013 \text{ g/mm}$ for all times, again supporting our assumption that the erosion rate is independent of speed during a penetration. From the reported density and geometry of the rod, we calculate a mass of .653 g. If we add .075 g for the larger flare on this larger rod, we find $M_o = .728 \text{ g}$, so $M_o/\mu_o = 56 \text{ mm}$. This is a reasonable value for the high speed limit in view of Fig. 4.10 which shows P_E versus \dot{S}_o for this rod/target combination (4.13).

We can also estimate μ_o from Eq (4.9). Let aluminum/magnesium be combination 1, and steel/magnesium be combination 2, with $\mu_{o2} = .009 \text{ g/mm}$ as above. Since the targets are the same, $\rho_{t1} = \rho_{t2}$. The square root of the ratio of the projectile densities is $\sqrt{2.8/7.8} = .6$. Since the ratio of the initial diameters is $D_{o1}/D_{o2} = 3 \text{ mm}/2 \text{ mm} = 1.5$, the ratio of the initial areas is $A_{o1}/A_{o2} = (1.5)^2 = 2.25$. Then

$$\mu_{o1} = (.009 \text{ g/mm})(2.25)(.6) = .012 \text{ g/mm} \quad (4.32)$$

which is in reasonable agreement with our estimate from Fig. 4.8, considering the uncertainties and assumptions involved. This indicates that Eq (4.8) or (4.9) may be useful.

Next, let us use Eq (4.1) to calculate the upper curve in Fig. 4.9. Since $A_o = .0707 \text{ cm}^2$, $a = .00212 (A/A_o) \text{ g mm}/\mu\text{s}^2$, $c = .00636 (A/A_o) \text{ g/mm}$, $I_o = 25.26 \text{ mm/g}$, $I_o\mu_o = .328$, $I_o\mu_o^2 = .00427 \text{ g/mm}$, $k = 1.328$, $\zeta = 1.328 \sqrt{a/c} \text{ mm}/\mu\text{s}$, $\epsilon = .00863/\zeta$ and $M_o/\mu_o = 56 \text{ mm}$. If we use the values of (A/A_o) shown in Fig. 4.9 we can calculate the upper curve which agrees with experiment. Here the limit of 56 mm is about 36% higher than the hydrodynamic limit, $33 \sqrt{2.8/1.8} = 41 \text{ mm}$. We note that (A/A_o) for aluminum/magnesium levels off at 2.8 above $\dot{S}_o = 4 \text{ mm}/\mu\text{s}$. There is no evidence of nose shatter for this softer aluminum rod with an impedance closer to that of magnesium than steel. The limit value $(A/A_o) = 2.8$ is slightly larger than for steel/magnesium. If we multiplied .012 g/mm by $\sqrt{2.8/2.5}$ we would obtain .013 g/mm as from Fig. 4.8.

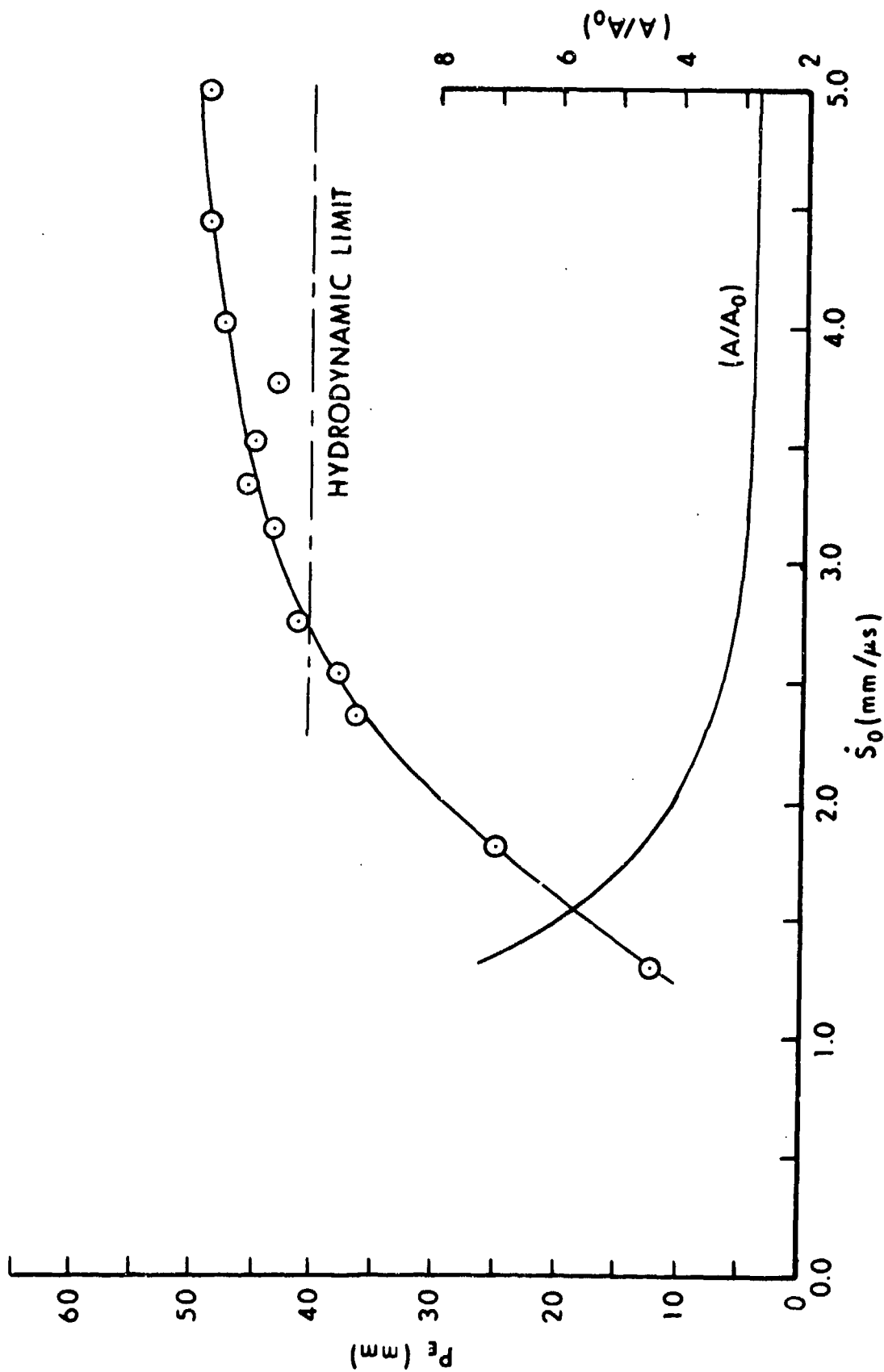


Fig. 4.10. Aluminum rod ($L_0/D_0 = 11$, $M_0 = 0.65g$) versus Magnesium.

Finally, let us apply Eqs (4.18) and (4.19) to Fig. 4.8 with $(A/A_0) = 2.8$ near $\dot{S}_0 = 3.35 \text{ mm}/\mu\text{s}$. Since $\epsilon = .637$ we must evaluate the D integral numerically. Since $X_0 = 15.5$ and $\nu = .11\mu\text{s}^{-1}$,

$$D = .11t = \int_X^{15.5} x^{-.363} (x-1)^{-.5} dx \quad (4.33)$$

with

$$X = 15.5 (1 - P/56)^{1.57} \quad (4.34)$$

so for any P we can find X, D and t, as well as $M = M_0 (1 - P/56) = \rho_p A_0 L$ and $R = P - L$. For example, when $P = 40 \text{ mm}$, $X = 2.168$, so

$$D = 13.33 [.174 (.327 + .103) + .326 (.214 + .131)] = 2.5 \quad (4.35)$$

in the four-point Gauss approximation. Then $t = D/\nu = 22.7\mu\text{s}$, which agrees closely with Fig. 4.8. At this time $M = .208 \text{ g}$, $L = 10.5 \text{ mm}$ and $R = 29.5 \text{ mm}$. Similarly, for $P = 20 \text{ mm}$, $X = 7.746$, and

$$D = 7.754 [.174 (.172 + .100) + .326 (.141 + .114)] = 1.012 \quad (4.36)$$

so $t = 9.2\mu\text{s}$, $M = .468 \text{ g}$, $L = 23.6 \text{ mm}$, $R = -3.6 \text{ mm}$, and so on. When $X_E = 1$, $P_E = 46.2 \text{ mm}$ from Eq (4.34)

$$D = 14.5 [.174 (.770 + .103) + .326 (.242 + .136)] = 3.99 \quad (4.37)$$

so $t_E = 36\mu\text{s}$, $M_E = .127 \text{ g}$, $L_E \approx 6.4 \text{ mm}$ and $R_E \approx 39.8 \text{ mm}$.

c. Steel/Aluminum

Fig. 4.11 is also from Perez' paper ^(4.14) and is for a steel rod with $L_0/D_0 = 22 \text{ mm}/2 \text{ mm} = 11$, impacting an aluminum target at $\dot{S}_0 = 2.3 \text{ mm}/\mu\text{s}$ to reach a final depth of 34 mm. This is less than the final depth in Fig. 4.5 for the same steel rod striking a weaker, less dense magnesium target at a

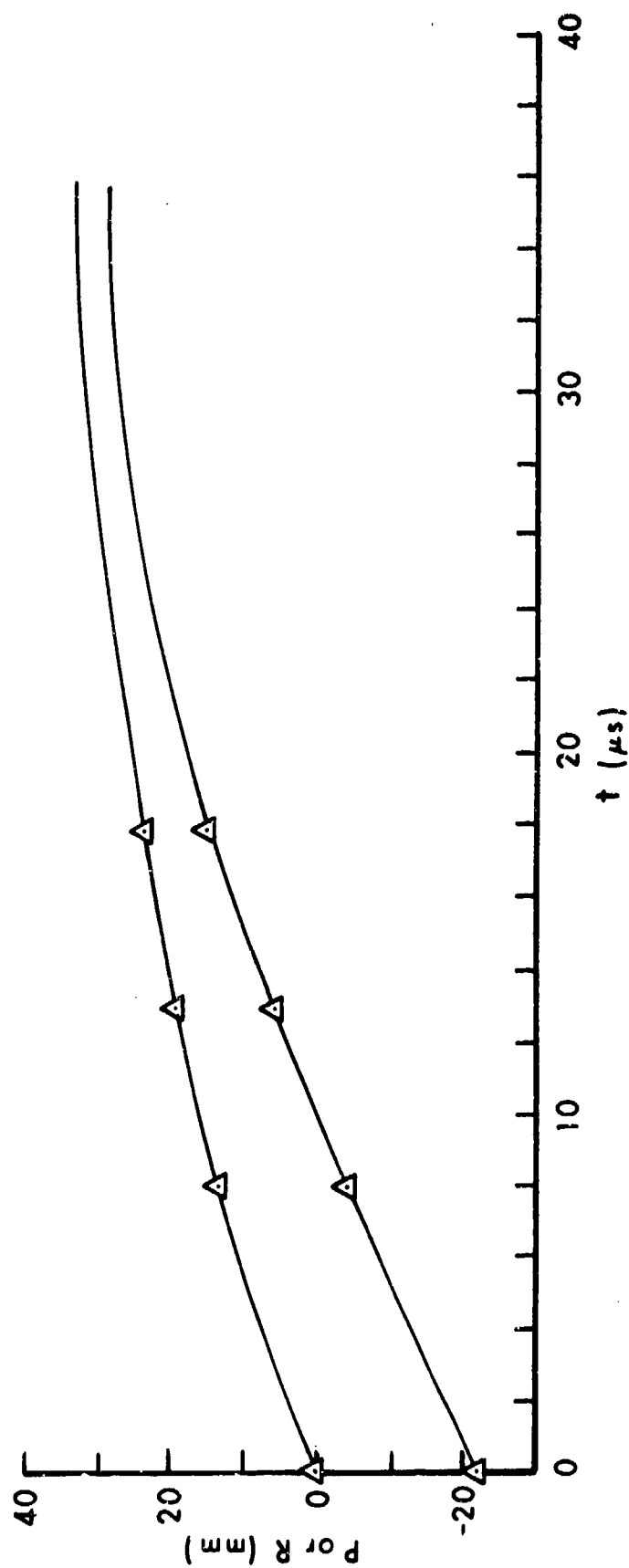


Fig. 4.11. Rod tip and rear positions vs. time. Steel ($L_0/D_0 = 11$) vs. Al at $S_0 = 2.3 \text{ mm}/\mu s$.

higher speed, $\dot{S}_0 = 3.27 \text{ mm}/\mu\text{s}$. It is also less than the depth for that rod/target combination at the same speed as here, $\dot{S}_0 = 2.3 \text{ mm}/\mu\text{s}$, as we see from Fig. 4.6.

Fig. 4.12 from Perez ^(4.15) shows some evidence of nose shatter beginning near $\dot{S}_0 = 2.2 \text{ mm}/\mu\text{s}$, although the dip in penetration is slight compared to that in Fig. 4.6 which begins near $\dot{S}_0 = 3 \text{ mm}/\mu\text{s}$. We expect a difference in threshold speed from Fig. 3.9. The difference in the magnitude of the effect might be attributed to a closer impedance match between steel and aluminum.

If we apply Eq (4.31) to Fig. 4.11, we find $\mu_0 = .012 \text{ g/mm}$. We can also use Eq (4.9) with steel/magnesium as combination two, $\rho_{p1} = \rho_{p2}$ and $\sqrt{\rho_{t1}/\rho_{t2}} = 1.245$, so $\mu_0 = (.009 \text{ g/mm})(1.245) = .011 \text{ g/mm}$, reasonably close to our estimate from Fig. 4.11.

Now let us apply Eq (4.1) to Fig. 4.12. As before, we take $M_0 = .576 \text{ g}$, which for $\mu_0 = .012 \text{ g/mm}$, gives $M_0/\mu_0 = 48 \text{ mm}$ which seems reasonable in view of Fig. 4.12. Perez did not report measured hardness values for his targets either, although he gave some estimates. Here we will take $Y_t = 20 \times 10^8 \text{ dyne/cm}^2$, so for $A_0 = .0314 \text{ cm}^2$, $a = .00188 (A/A_0) \text{ g mm}/\mu\text{s}^2$, $c = .00438 (A/A_0) \text{ g/mm}$, and of course $I_0 = 20.4 \text{ mm/g}$ as before. Then $\bar{c} = c - .00294 \text{ g/mm}$, $\tau = 1.245 \sqrt{a/\bar{c}} \text{ mm}/\mu\text{s}$ and $\epsilon = .00747/\bar{c}$. If we use the (A/A_0) values in Fig. 4.12, we can calculate the upper curve in agreement with experiment. Our high speed limit of 48 mm is about 30% higher than the hydrodynamic limit of 37 mm.

In Fig. 4.12 (A/A_0) again reaches a constant value above a certain striking speed, a behavior we now expect. The limit value $(A/A_0) = 3.5$ is larger than we found for steel/magnesium where the limit value was 2.5 in Fig. 4.6. These values are both estimates which depend on the target strengths we have assumed, $Y_t = 10 \times 10^8 \text{ dyne/cm}^2$ for magnesium and $Y_t = 20 \times 10^8 \text{ dyne/cm}^2$ for aluminum, in the absence of measured values. Better values of (A/A_0) will have to await measured values of target strengths. The important thing to note is the shape of the (A/A_0) versus \dot{S}_0 curves, not their exact values. A theory of (A/A_0) versus \dot{S}_0 based on first principles will also have to await better information.

Before discussing Fig. 4.11, let us note that Perez used two other types of steel rod against the same aluminum target ^(4.16). These rods had $L_0/D_0 = 33 \text{ mm}/3 \text{ mm}$ and $44 \text{ mm}/4 \text{ mm}$ respectively. These rods together with

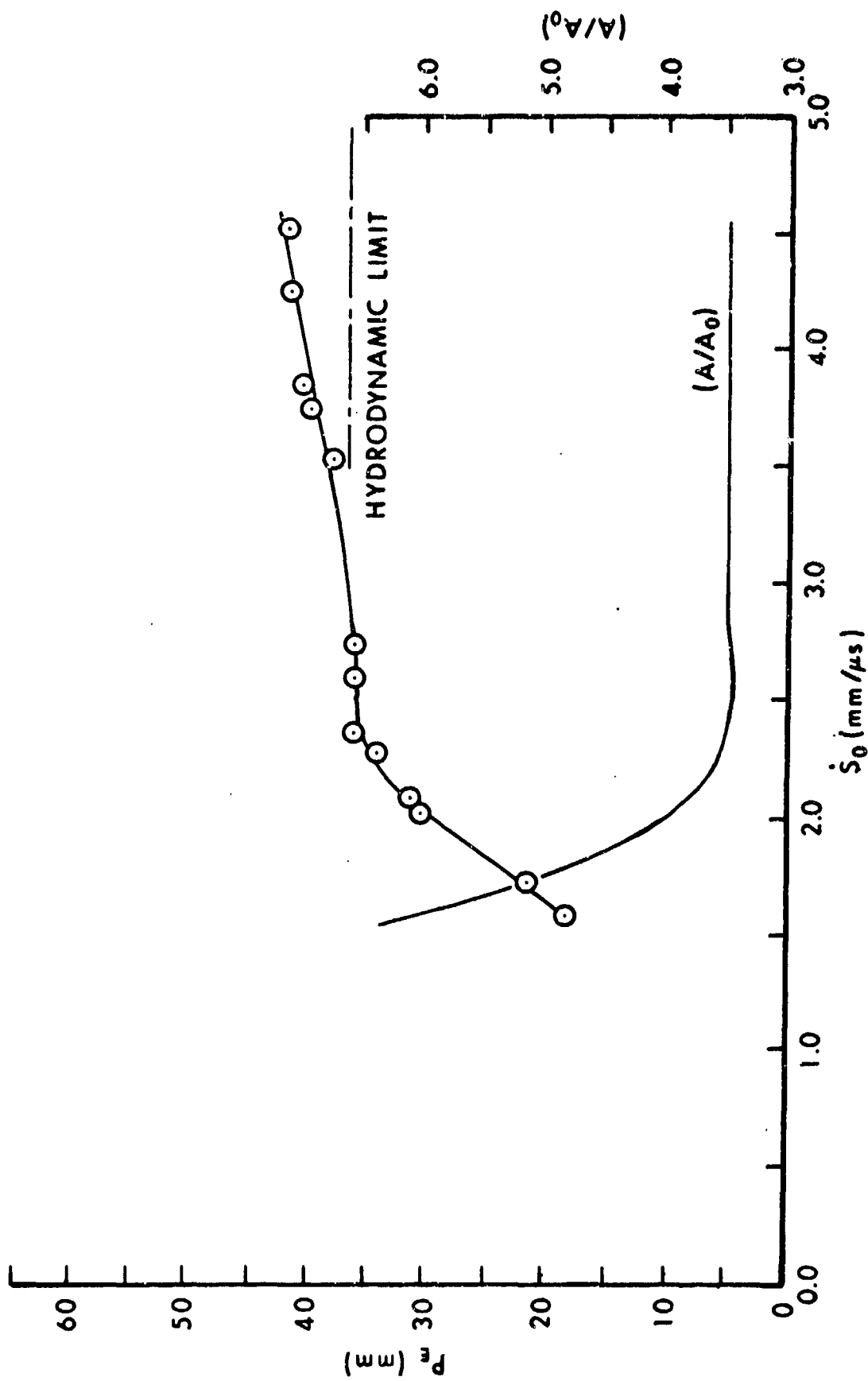


Fig. 4.12. Steel rod ($L_0/D_0 = 11$) vs. aluminum.

those used in Fig. 4.12 with $L_0/D_0 = 22 \text{ mm}/2 \text{ mm}$ form a family with the same density and aspect ratio but different mass. This is an example of our first way above. When Perez plotted P_E/L_0 versus \dot{S}_0 , he found that a single curve applied to all three rods. This is exactly what our theory predicts, and provides further evidence in its support. Perez also used various steels for these rods versus aluminum targets, but found no detectable difference (4.17). Later we will see a case where projectile strength made a detectable difference, at least for low striking speeds.

Finally, let us apply Eqs (4.18) and (4.19) to Fig. 4.11. Since $\epsilon = .6$ for $(A/A_0) = 3.5$ when $\dot{S}_0 = 2.3 \text{ mm}/\mu\text{s}$, we must evaluate the D integral numerically. We find $X_0 = 7.4$ and $\nu = .084\mu\text{s}^{-1}$, so

$$D = .084t = \int_X^{7.4} x^{-.4} (x-1)^{-.5} dx \quad (4.38)$$

with

$$X = 7.4 (1-P/48)^{1.67} \quad (4.39)$$

Since we have already given several examples of using the four-point Gauss method, we will restrict ourselves to one example here. For $P = 20 \text{ mm}$, Eq (4.39) gives $X = 3.0$, so

$$D = .44 [.174 (.408 + .185) + .326 (.296 + .220)] = 1.195 \quad (4.40)$$

and $t = D/\nu = 14\mu\text{s}$ which agrees with Fig. 4.11. At this time, $M = .576 \text{ g} (1-20/48) = .336 \text{ g} = (.0245 \text{ g/mm}) L$ so $L = 13.7 \text{ mm}$ and $R = P - L = 8.3 \text{ mm}$. Similarly, for $X_E = 1$, $P_E = 33.6 \text{ mm}$, $t_E = 36.6\mu\text{s}$ and $M_E = .173 \text{ g}$ from which we can estimate L_E and R_E , and so on.

2. Other Examples

a. Aluminum/Lead

Fig. 4.13 shows Perez' data (4.18) for the same aluminum rod impacting lead targets. Once more there is evidence of nose shatter at an expected

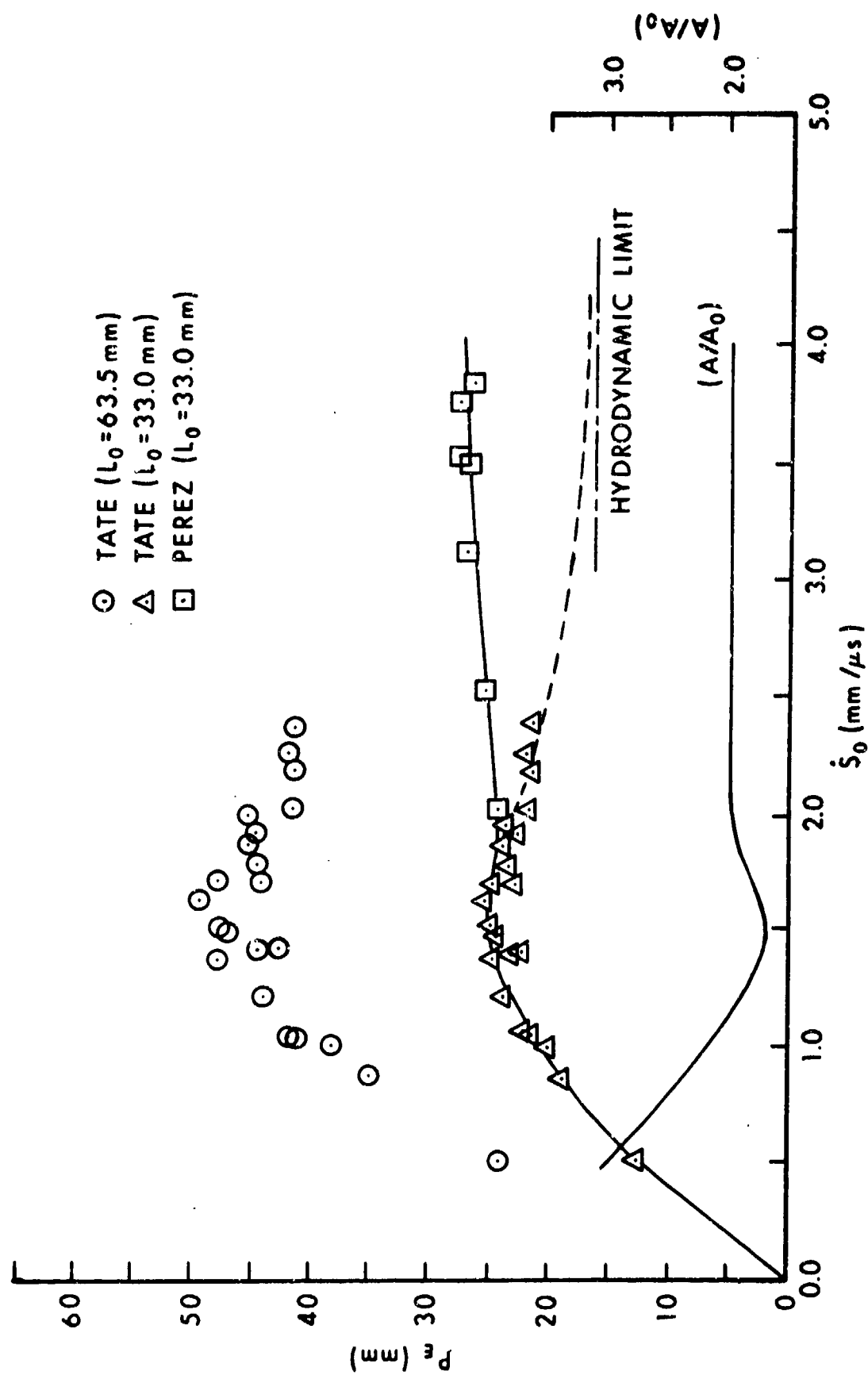


Fig. 4.13. Aluminum rods versus lead.

lower speed (near 1.5 mm/ μ s). Perez extended previous data reported by Tate (4.19). The seven open squares in Fig. 4.13 are Perez' data points, while the circles were reported by Tate. Tate used a larger aluminum rod ($L_0/D_0 = 63.5 \text{ mm}/6.35 \text{ mm} = 10$, $M_0 = 5.43 \text{ g}$) against 101.6 mm diameter lead targets. Since these targets showed severe lateral distortion in preliminary experiments, they were encased in steel to provide enough lateral confinement to simulate a semi-infinite target. Differences between truly semi-infinite lead targets and Tate's targets might be expected at higher striking speeds. Such steel confinement could cause greater target resistance and decrease the penetration depth compared to a truly semi-infinite lead target. Perez used lead targets which were 280 mm in diameter impacted by less massive ($L_0/D_0 = 33 \text{ mm}/3 \text{ mm} = 11$, $M_0 = .728 \text{ g}$) aluminum rods. He judged his targets to be truly semi-infinite because they exhibited no observable distortion at the sides or rear after a penetration event.

Both Tate and Perez reported their results as P_E/L_0 versus \dot{S}_0 . In Fig. 4.13 we show Tate's data in two ways. The upper set of data points (open circles) consists of his P_E/L_0 values multiplied by 63.5 mm, while the lower set (open triangles) consists of his P_E/L_0 values multiplied by 33 mm, Perez' rod length. The open square data points are Perez' P_E/L_0 values multiplied by 33 mm. The more or less smooth joining of the two data sets near 2 mm/ μ s is expected as we saw above in connection with steel/aluminum. The rods have about the same aspect ratio, so P_E/L_0 should be independent of D_0 . The lower values found by Tate for $2 < \dot{S}_0 < 2.35 \text{ mm}/\mu\text{s}$ might be attributed to his use of steel confinement. It is too bad that Perez did not report data at lower speeds using his projectile/target combination. If he had, we might have better evidence than is available.

The possibility of nose shatter is a relatively unimportant feature of Fig. 4.13. The important thing to note is that Perez found an increase in penetration with increasing speed from 2 to 4 mm/ μ s. As Perez points out, this contradicts the prediction of Tate's model that there should be an approach to the hydrodynamic limit in this range as indicated by the dashed curve in Fig. 4.13 and the horizontal line at $P_E = L_0 \sqrt{\rho_p/\rho_t} = 16.4 \text{ mm}$, using $L_0 = 33 \text{ mm}$. Instead, Perez' data seem to be tending toward a limit almost twice this hydrodynamic limit. Perez noted that his steel versus aluminum data (Fig. 4.12 above) also contradict the prediction of Tate's model. Perez

went on to generalize that the predictions of hydrodynamic models are usually too high for impact speeds below 3 mm/ μ s and too low for speeds greater than 3 mm/ μ s. In fact, the discrepancies are much too large to be explained by conjectured "afterflow" giving "secondary penetration." We will return to this point again below.

Unfortunately, Perez was not able to obtain time-dependent information about penetration into his lead targets, using the X-ray equipment available to him. Consequently, we have no direct evidence for either erosion rate, μ_o , or nose mushrooming, (A/A_o) , as we did in the three previous examples. This is the usual situation in penetration mechanics. More powerful flash X-ray systems exist (4.20) as well as very intense continuous X-ray sources (4.21), but applications to penetration mechanics have been either very restricted or non-existent.

If we wish to apply our theory to the data in Fig. 4.13, we are forced to estimate both μ_o and (A/A_o) . From our previous experience in the last three examples, we expect μ_o to be independent of \dot{S}_o while (A/A_o) should initially decline with increasing \dot{S}_o , and eventually level off at high speed. We recall from Fig. 4.10 for aluminum versus magnesium that the high speed limit of (A/A_o) was estimated to be 2.8 and μ_o was .013 g/mm. Now we need the limit of (A/A_o) and μ_o for lead which is six times more dense than magnesium and an order of magnitude softer. It might be too much to expect that Eq (4.8) or (4.9) will be accurate in such an extrapolation, even though it did fairly well in making transitions between steel, aluminum and magnesium. For example, if $\mu_{o2} = .013$ g/mm and $\sqrt{\rho_{t1}/\rho_{t2}} = \sqrt{11.3/1.8} = 2.5$ with $A_{o1} = A_{o2}$ and $\rho_{p1} = \rho_{p2}$ in Eq (4.9), we would find $\mu_o = .032$ g/mm for the lead target. This is clearly too high, since $M_o/\mu_o = 23$ mm when $M_o = .728$ g, which is too low in view of Fig. 4.13. With Fig. 4.13 as a guide, $M_o/\mu_o = 30$ mm is a more reasonable estimate. This implies $\mu_o = .024$ g/mm for the lead target. In turn, this implies that $[f_1 \sqrt{(A/A_o)_1}]/[f_2 \sqrt{(A/A_o)_2}] = 3/4$ in Eq (4.8) without knowing either f_1/f_2 or $(A/A_o)_1/(A/A_o)_2$. If target density controls (A/A_o) at high speed, then $(A/A_o)_1$ for lead should be smaller since lead permits less lateral spreading than magnesium. If f_1 for lead were also less than f_2 , then perhaps the limit might be $(A/A_o) = 2$ for lead. In all of our other examples, Eq (4.8) will be more useful. However, an estimate from Fig. 4.13 is more useful in the present case. Eq (4.8) would give us

$$\mu_o = (.013) (2.5) (.75) = .024 \text{ g/mm} \quad (4.41)$$

only with the help of Fig. 4.13.

If we assume $Y_t = .5 \times 10^8 \text{ dyne/cm}^2$ for lead as we did before in Fig. 3.11 and use $A_0 = .0707 \text{ cm}^2$ for this aluminum rod with $M_0/\mu_0 = 30 \text{ mm}$, we find $\xi = 1.6\sqrt{a/\bar{c}} \text{ mm/us}$ and $\epsilon = .0192/\bar{c}$, with $a = .000106 (A/A_0) \text{ g mm/us}^2$, $\mu = .04 (A/A_0) \text{ g/mm}$ and $I_0 = 25.26 \text{ mm/g}$ as before. Then using the values of (A/A_0) shown in Fig. 4.13 we can calculate the upper solid curve in agreement with experiment. The closeness of this agreement is not a strong support for our theory in this case, considering the fact that incomplete data sets from two different laboratories are being superimposed. However, the trends predicted by the theory and the similarity of these trends with other cases where better information is available, is of some significance.

b. Steel/Steel

Figs. 4.14 and 4.15 show data from Hohler and Stilp ^(4.1) for $L_0/D_0 = 10$ and $L_0/D_0 = 1$ steel rods impacting mild steel targets ($\text{BHN} = 135 \text{ kg/mm}^2$) and armor steel targets ($\text{BHN} = 260\text{--}330 \text{ kg/mm}^2$). The rods were made of a third kind of steel of intermediate hardness ($\text{BHN} = 230 \text{ kg/mm}^2$). The upper two full curves in each figure are for $L_0/D_0 = 10$ rods, one with $L_0/D_0 = 54 \text{ mm}/5.4 \text{ mm}$ ($M_0 = 9.85 \text{ g}$), the other with $L_0/D_0 = 25 \text{ mm}/2.5 \text{ mm}$ ($M_0 = 0.96 \text{ g}$). The lower two curves in each figure are for $L_0/D_0 = 1$ rods, one with $L_0/D_0 = 12 \text{ mm}/12 \text{ mm}$ ($M_0 = 10.5 \text{ g}$), the other with $L_0/D_0 = 5.5 \text{ mm}/5.5 \text{ mm}$ ($M_0 = 1.03 \text{ g}$). The masses reported include the mass of a stabilizing flare at the rear of each rod. Only smooth curves without data points were reported in this paper for steel rods, and consisted of plots of P_E/L_0 versus \dot{S}_0 . The mass pairs in each case are close enough to 10 g and 1 g that, for some purposes, we have here examples of our first way (vary the mass but keep the aspect ratio constant) and our third way (keep the mass constant but vary the aspect ratio). As we recall, for the first way a plot of P_E/L_0 versus \dot{S}_0 reduces similar curves to a single curve. In Figs. 4.14 and 4.15 we have multiplied their P_E/L_0 curves by the appropriate values of L_0 . This brings out more clearly the advantages of high aspect ratio rods over compact rods in achieving greater penetration. If we had plotted P_E/L_0 instead of P_E , the curves for $L_0/D_0 = 1$ would be higher than those for $L_0/D_0 = 10$. In Fig. 4.15 we have plotted a fifth curve for $L_0/D_0 = 156.8 \text{ mm}/4.9 \text{ mm} = 32$, $M_0 = 23 \text{ g}$ from a more recent paper by Hohler and Stilp ^(4.22). The target was a

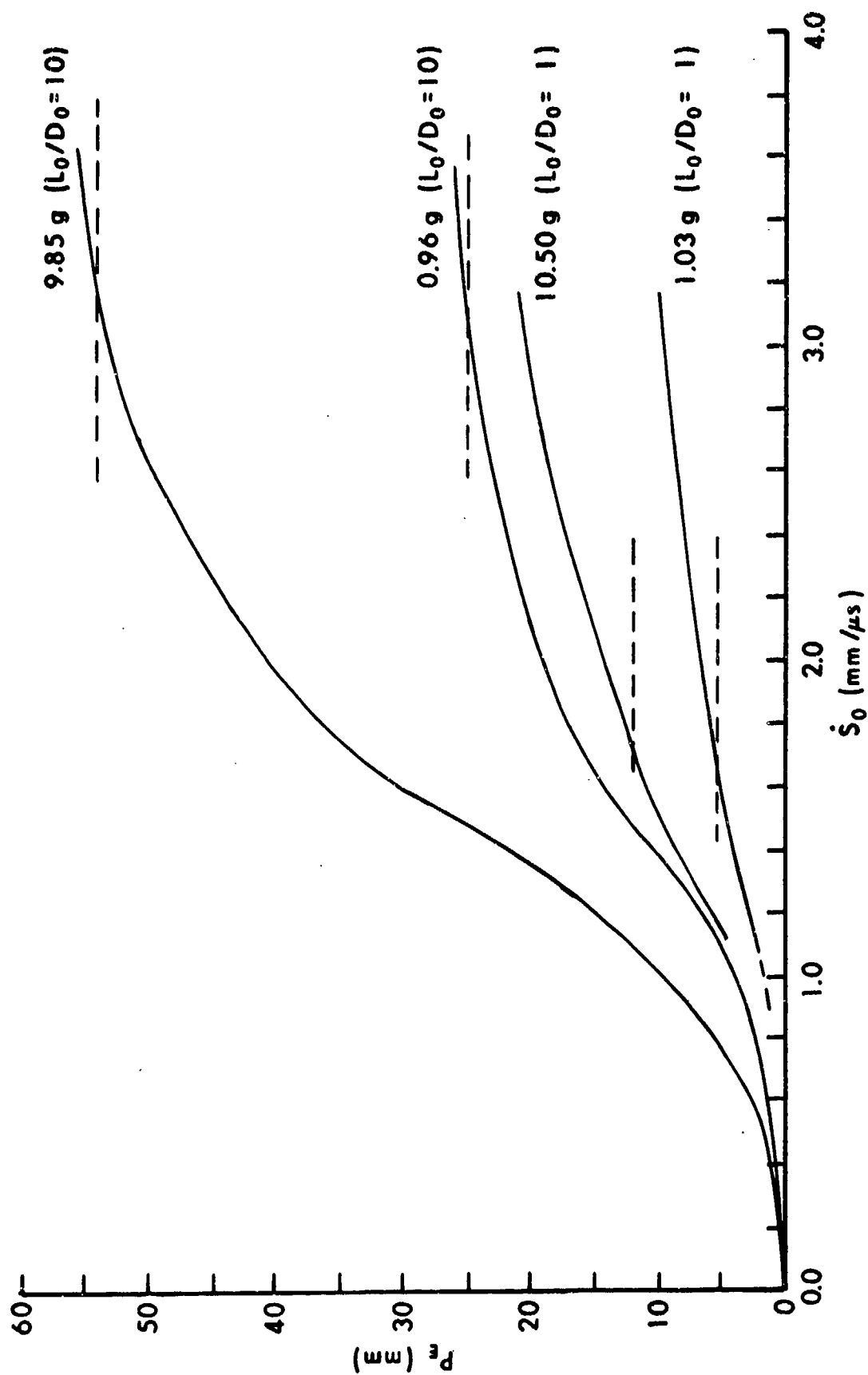


Fig. 4.14. Steel rods versus mild steel targets.

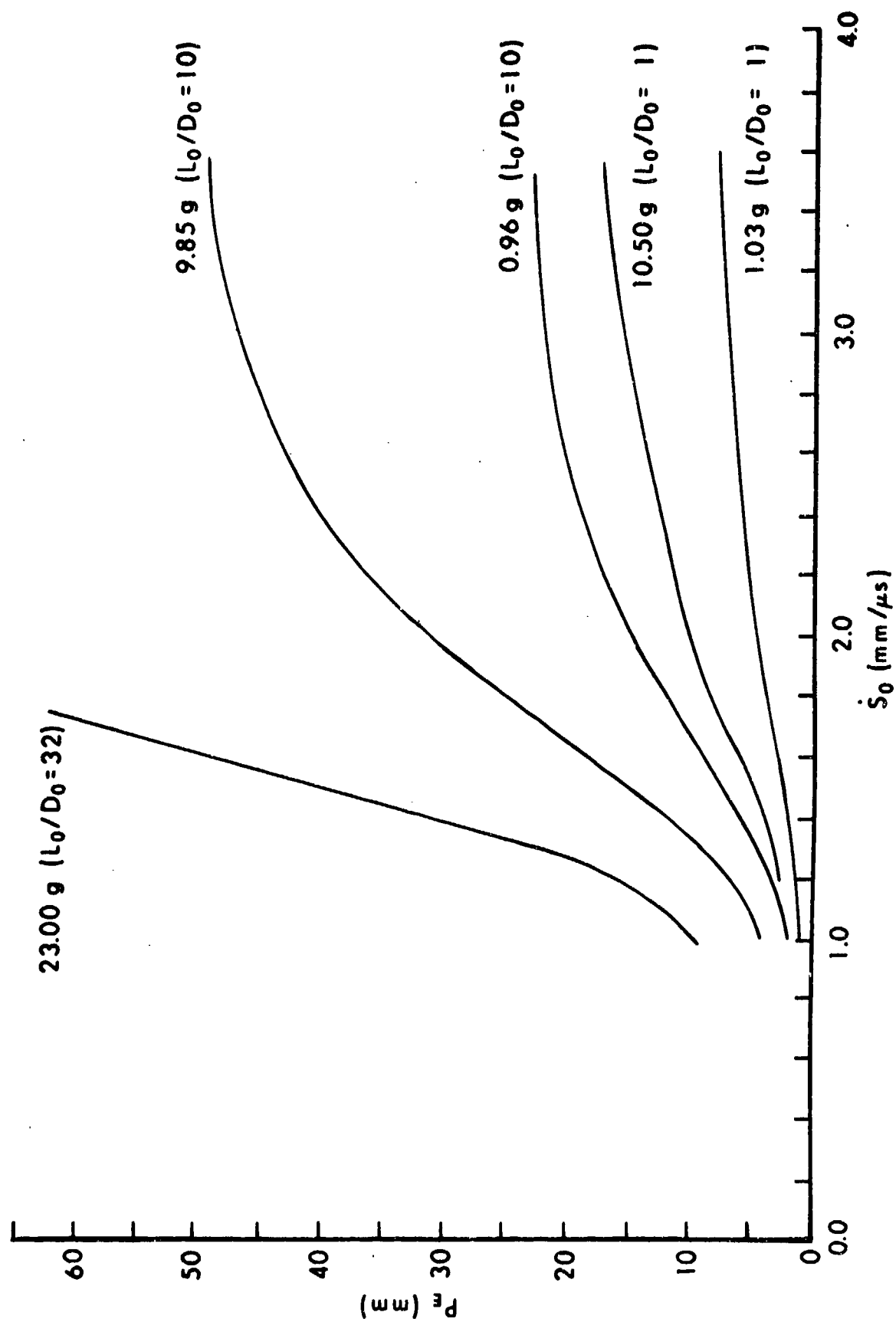


Fig. 4.15. Steel rods versus armor steel targets.

slightly different armor steel and the projectile steel for this very long rod was also slightly different from that of the other rods, but not enough to make any difference to our purpose here. They reported 2 data points for $\dot{S}_0 > 1.5 \text{ mm}/\mu\text{s}$ for the $L_0/D_0 = 32$ rod but these are not included to avoid compressing the scale of the figure. The dashed lines in Fig. 4.14 are the hydrodynamic limits (the same for either figure of course).

We recall the deformation of Hohler and Stilp's $L_0/D_0 = 1$ and $L_0/D_0 = 10$ rods shown in Figs. 4.1a and 4.1b. Since $D/D_0 \sim 3$ for the deformed cap of the recovered long rod at $\dot{S}_0 = .735 \text{ mm}/\mu\text{s}$, we expect $A/A_0 \sim 9$ for this rod at this speed.

Let us assume that $\mu_0 = 0$ for the compact ($L_0/D_0 = 1$) rods in both figures, since there is no evidence of erosion. Then Eq (2.11) applies. If $Y_t = 40 \times 10^8 \text{ dyne/cm}^2$ for the mild steel target and $Y_t = 90 \times 10^8 \text{ dyne/cm}^2$ for the armor steel target, we find $\alpha = \sqrt{a_0/c_0} = .55 \text{ mm}/\mu\text{s}$ and $.83 \text{ mm}/\mu\text{s}$ respectively. If we use the (A/A_0) values shown in Fig. 4.16 for $L_0/D_0 = 1$, we can calculate the lower curves in Figs. 4.14 and 4.15 in agreement with experiment.

Now let us apply Eq (4.1) to the long rod curves in these figures. For Perez' steel rods with $L_0/D_0 = 22 \text{ mm}/2 \text{ mm} = 11$ ($M_0 = .576 \text{ g}$) versus aluminum, μ_0 was $.012 \text{ g/mm}$. In Eq (4.9) with Perez' rod/target as combination two, $\sqrt{\rho_{t1}/\rho_{t2}} = \sqrt{7.85/2.8} = 1.67$. For Hohler and Stilp's 0.96 g rod with $L_0/D_0 = 25 \text{ mm}/2.5 \text{ mm} = 10$, $A_{01}/A_{02} = (D_{01}/D_{02})^2 = (2.5/2)^2 = 1.56$, so μ_0 is $.031 \text{ g/mm}$. Since the aspect ratio is not quite the same, we will adopt $\mu_0 = .033 \text{ g/mm}$ as our estimate for the 0.96 rod. Since this rod has $M_0/L_0 = .1467 \text{ g/mm}$, we find $\mu_0 = .156 \text{ g/mm} (.1467/.1824) = .125 \text{ g/mm}$ for this very long rod. For the $L_0/D_0 = 10$ rods we will also assume that the erosion rates are the same for either target. This may not be quite true but seems good enough for our purpose, especially in the absence of measured values. this puts the entire burden of accounting for the observed differences on the hardness values we have estimated for each type of target. Of course μ_0 is also assumed to be independent of striking speed as well as any lesser speed during penetration. This enables us to assign any speed dependence beyond the explicit \dot{S}_0^2 factor in Eq (4.1) to the flattening factor, (A/A_0) . If we use the flattening factors labelled $L_0/D_0 = 10$ and $L_0/D_0 = 32$ in Fig. 4.16, we can calculate the upper curves in Figs. 4.14 and 4.15. The fact that (A/A_0) depends only on aspect ratio and not on projectile mass (for the mass

range examined) for any striking speed is an encouraging simplification. For $L_0/D_0 = 10$ we note that $(A/A_0) \sim 9$ as expected.

Hohler and Stilp also reported the area, A_c , of their target craters measured at the original impact surface, at least for aspect ratios of 1 and 10^(4.1). The ratios, (A_c/A_0) , are shown in Fig. 4.17, together with the flattening factors, (A/A_0) , from Fig. 4.15. The increase of (A_c/A_0) with \dot{S}_0 corresponds to an increase in taper of the crater cross sections. These were roughly right circular cylinder for \dot{S}_0 near 2 or 3 mm/ μ s, but acquired mouths wider than the lower portions of the craters at higher speeds. For $\dot{S}_0 > 1.5$ mm/ μ s, the flattening factors we have assumed are less than the values of (A_c/A_0) . This provides a consistent picture at high speeds. Unfortunately, Hohler and Stilp did not include any crater cross-section photographs for $\dot{S}_0 < 2$ mm/ μ s so we do not know the shape. However, for $\dot{S}_0 < 1.5$ mm/ μ s, we have assumed flattening factors which exceed the reported values of (A_c/A_0) . As we have noted, $(A/A_0) \sim 9$ is consistent with Fig. 4.1b. A reasonable conjecture is that at low impact speeds, the craters tend to have a balloon shape like that in Fig. 4.8b for a long steel rod versus magnesium. We might speculate that at low impact speeds, nose mushrooming takes place during a relatively long time which is a significant portion of the entire penetration time. After impact the nose blooms and then later in the penetration the mushroom cap rim reverses and begins to slim down and present a more compact profile. This gives a balloon shape, with the diameter (or area) of the crater mouth smaller than for most of the crater. At high impact speeds the entire cap formation takes place early in the penetration and makes the crater mouth wider than the rest of the crater. The time average area presented by a high speed rod is unchanged for most of a penetration and becomes independent of \dot{S}_0 as well.

An alternate explanation for the discrepancy noted in Fig. 4.17 for $\dot{S}_0 < 1.5$ mm/ μ s is that $\mu_0 \sim \sqrt{A/A_0}$ as suggested by Eq (4.4). Thus, for low impact speeds when A/A_0 is significantly larger than 1 or 2, we cannot neglect a dependence of the erosion rate on impact speed. If μ_0 is higher at low speed, perhaps three or four times higher near $\dot{S}_0 = 0.5$ mm/ μ s for $\dot{S}_0 > 3.0$ mm/ μ s, then (A/A_0) need not be so high at low speeds. If low speed craters are observed to be approximately right circular cylinders instead of balloons, then we should adopt this explanation, so $(A/A_0) \leq (A_c/A_0)$ at low speeds instead of as shown in Fig. 4.17. This would make our calculation a

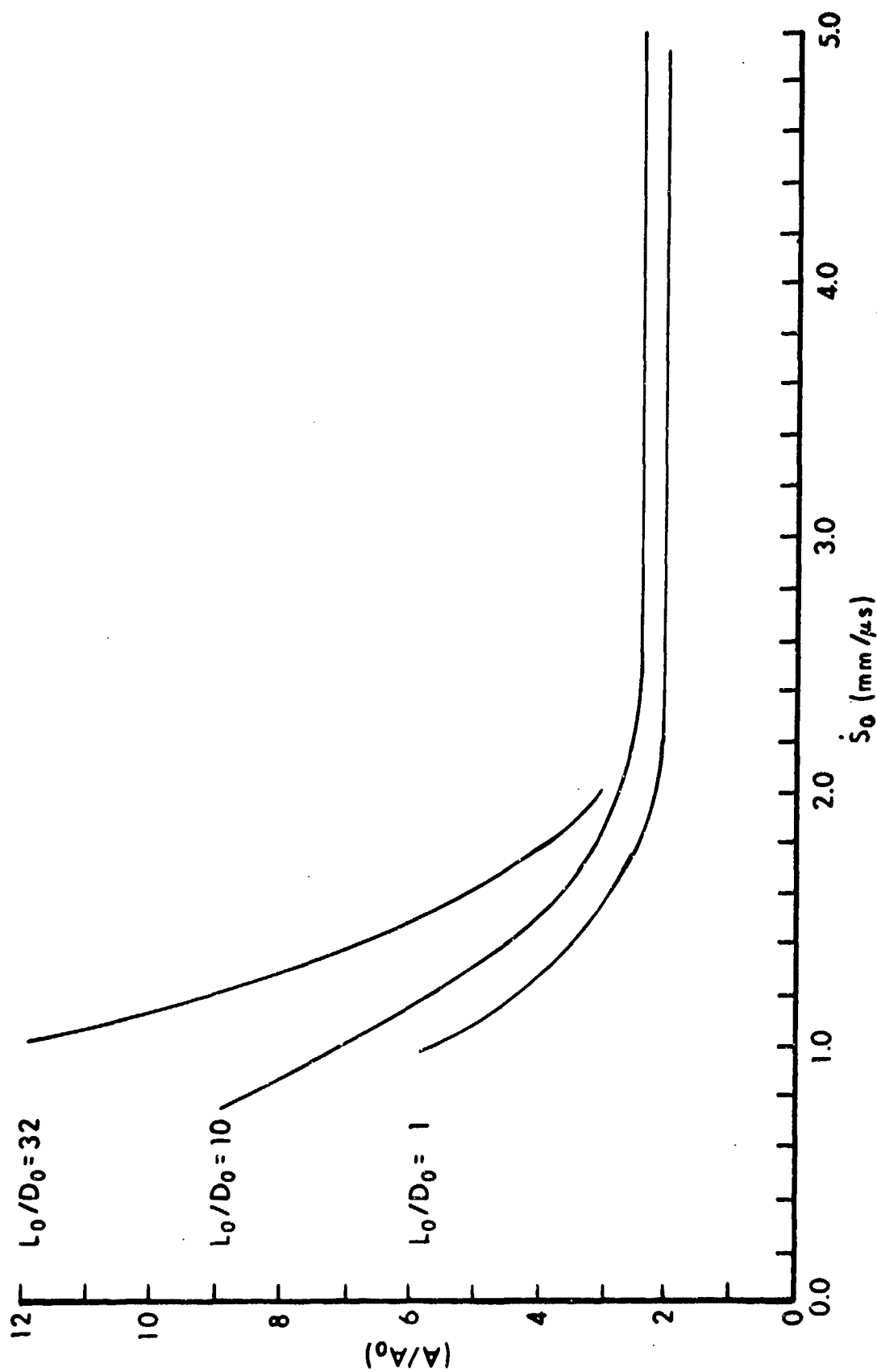


Fig. 4.16. (A/A_0) for long rods and compact rods (steel/steel).

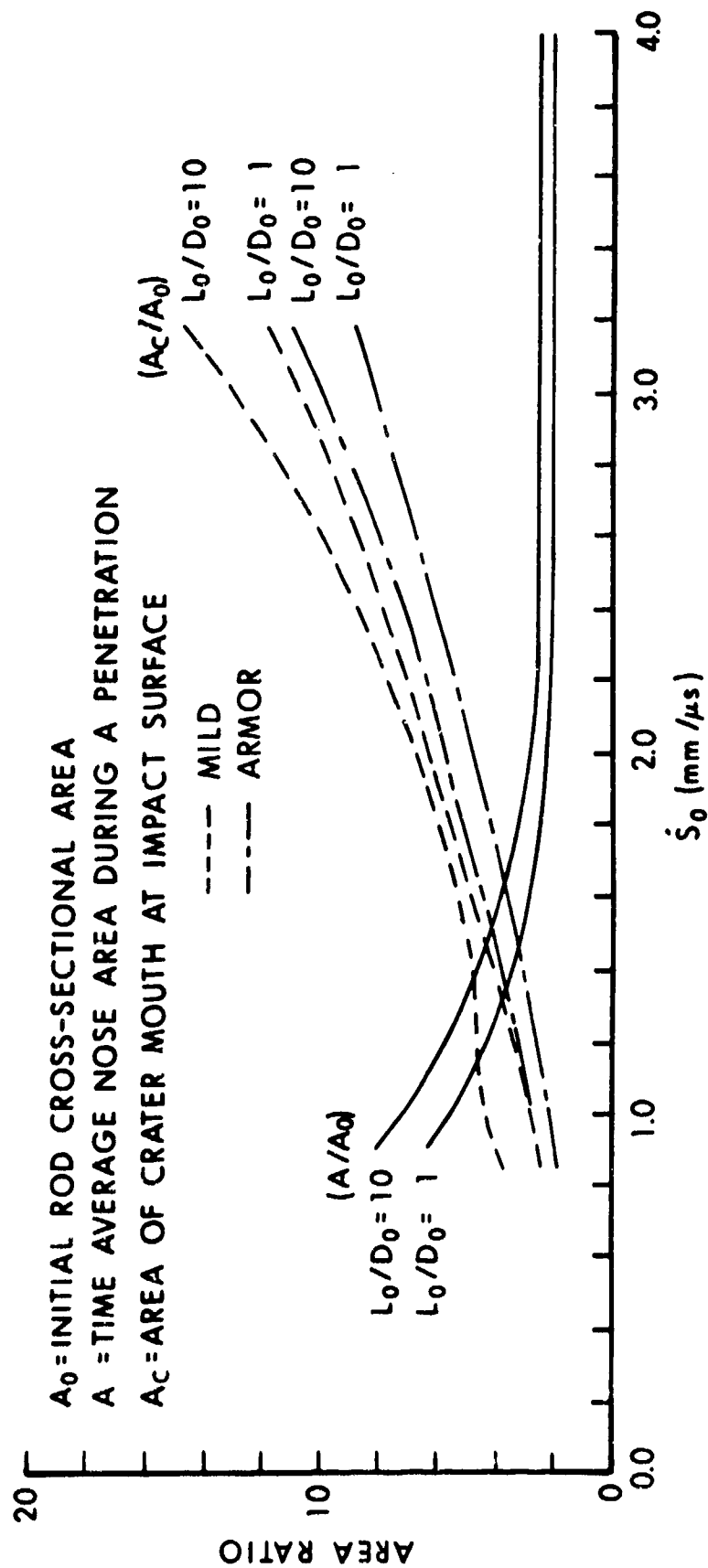


Fig. 4.17. Area ratios (A/A_0) and (A_c/A_0) for steel rods versus steel.

little more complicated since both μ_o and (A/A_o) would depend on \dot{S}_o instead of just (A/A_o) . For some projectile/target combinations, μ_o dependent on \dot{S}_o may be correct, while for other combinations it may be independent of \dot{S}_o as we assumed above. We don't have enough information to answer this question, although, in the present case, the agreement between $(A/A_o) \approx 9$ and Fig. 4.1b seems to favor μ_o independent of \dot{S}_o . We will assume this to be true in the calculations which follow, with the understanding that experimental evidence may eventually require a change.

Now let us turn to a case which illustrates our third way. In Fig. 4.18, Christman and co-workers (4.23) held the mass of their mild steel rods constant ($M_o = 0.6$ g) while varying the aspect ratio as indicated in the lower right. They launched these rods at the same speed, $\dot{S}_o = 3.4$ mm/ μ s against targets made of the same mild steel (BHN = 110 kg/mm² reported) as the rods. For one aspect ratio, $L_o/D_o = 9.525$ mm/3.175 mm = 3, they also reported penetration as a function of striking speed, as shown in Fig. 4.19.

In Fig. 4.18 we have also plotted P_E/L_o versus (L_o/D_o) . A casual reader, unfamiliar with such a plot, might think that penetration decreases as aspect ratio increases, exactly the opposite of the truth. It seems better to plot P_E versus \dot{S}_o , since plotting P_E/L_o serves no useful purpose here, unlike the examples of our first way, discussed above.

From Fig. 4.16 we expect (A/A_o) to vary with aspect ratio and striking speed in the manner indicated. This means that for $\dot{S}_o = 3.4$ mm/ μ s, we expect (A/A_o) to be almost independent of aspect ratio. Since material properties, striking speed and rod mass are all constant in Fig. 4.18, and since (A/A_o) is practically independent of aspect ratio, we conclude that μ_o must vary with aspect ratio. This is hardly a surprise since we have already assumed that $f = 0$ in Eq (4.8) for $L_o/D_o = 1$, while f is a significant fraction of the maximum erosion rate for $L_o/D_o \geq 10$. We can still use Eq (4.9) to go from one rod to another of equal aspect ratio. Thus we estimate $\mu_o = .033$ g/mm $(.0284/.0384) = .024$ g/mm for the .6 g, $L_o/D_o = 10$ rod here with $M_o/L_o = .6$ g/21.1 mm = .0284 g/mm from the value we found for Hohler and Stilp's .96 g, $L_o/D_o = 10$ rod with $M_o/L_o = .96$ g/25 mm = .0384 g/mm. However, we do not know how f varies for intermediate values of the aspect ratio like 2, 3 and 4. Fortunately, the data in Fig. 4.19 for $L_o/D_o = 3$ extend to high enough striking speeds that we can estimate the high speed limit to be $M_o/\mu_o = .6$ g/ $\mu_o = 18$ mm. This gives $\mu_o = .033$ g/mm and implies

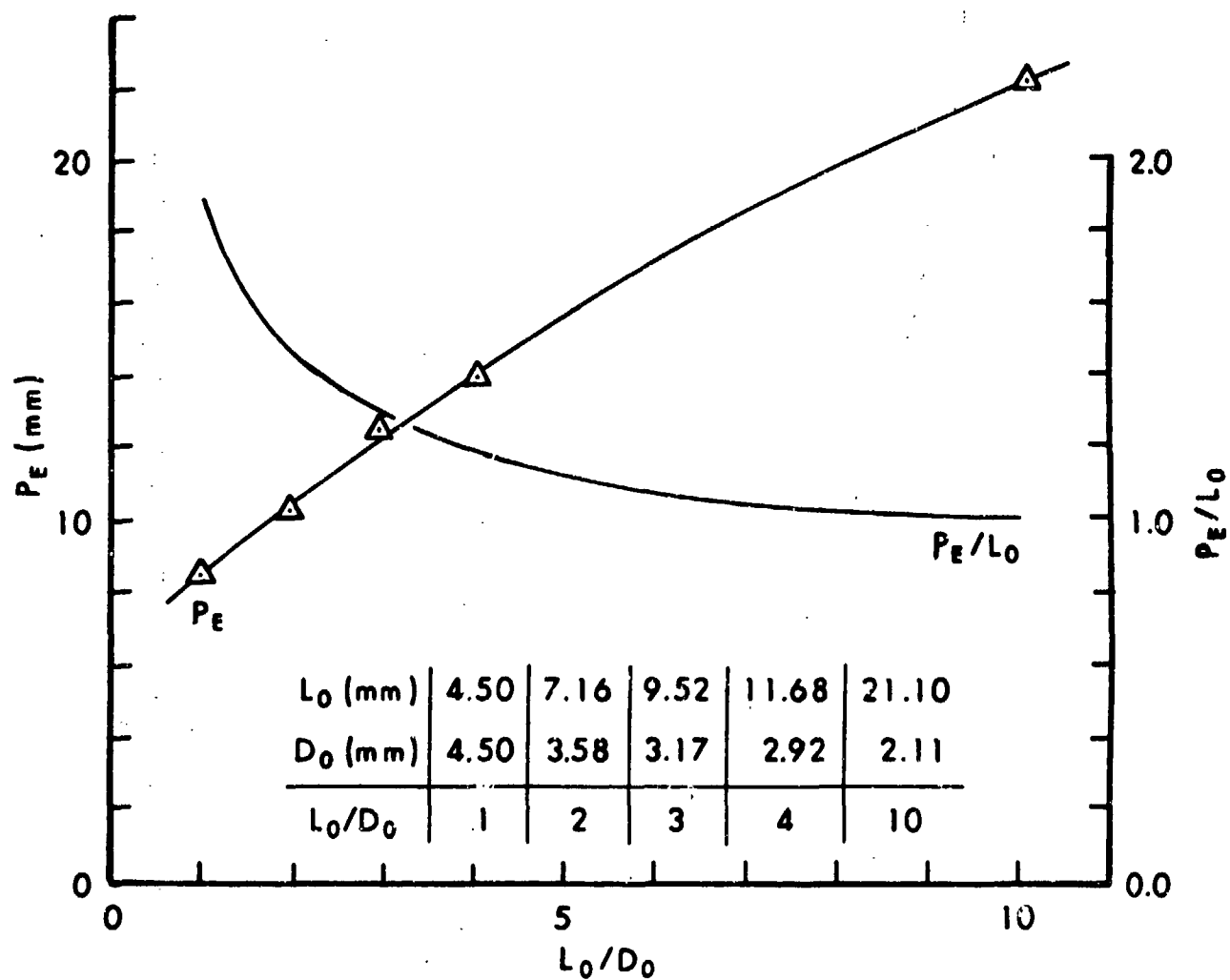


Fig. 4.18. Steel rods ($M_0 = 0.6g$, $\hat{S}_0 = 3.4\text{mm}/\mu\text{s}$) versus same steel.

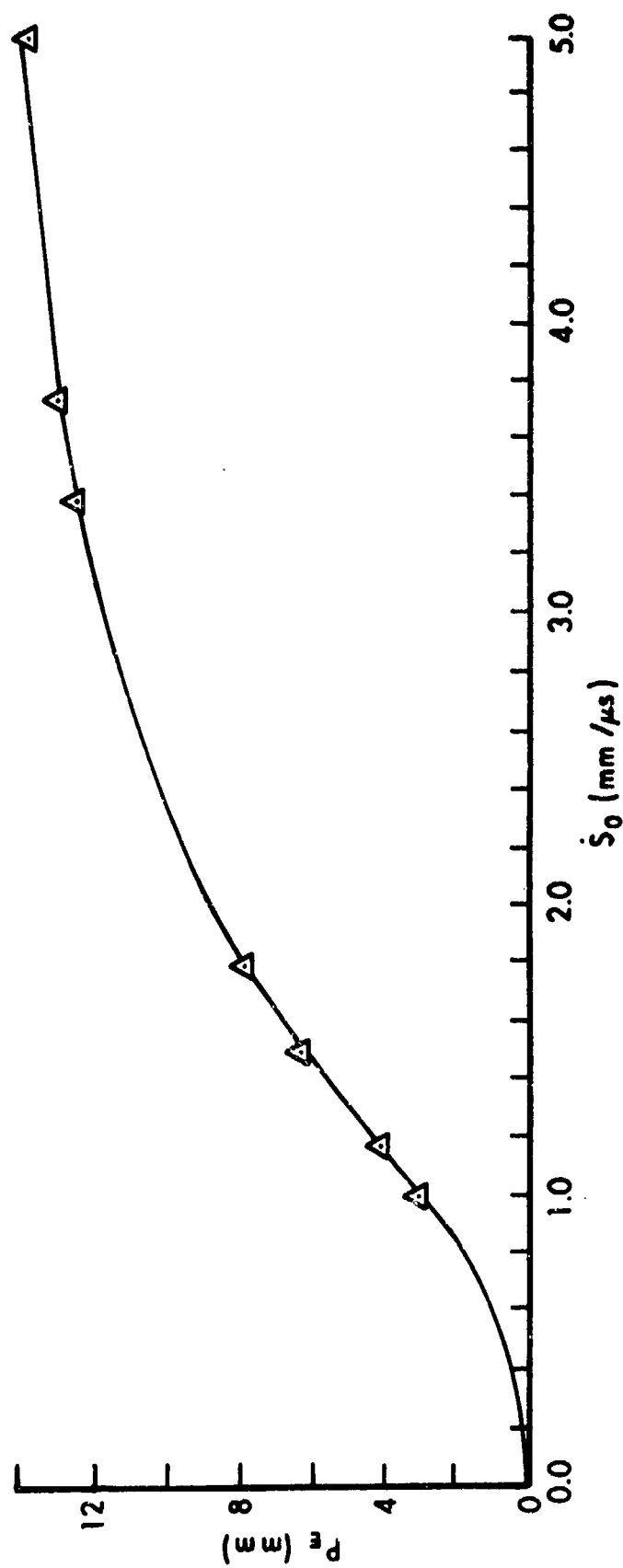


Fig. 4.19. Mild steel rods ($M_0 = 0.6g$, $L_0/L_0 = 9.525mm/3.175mm =$
3) versus mild steel.

that f for $L_0/D_0 = 3$ is about 6/10 of f for $L_0/D_0 = 10$ in this case. For $L_0/D_0 = 32$ we earlier assumed that f was about the same as for $L_0/D_0 = 10$.

Now let us apply Eq (4.1) to Fig. 4.18. For $L_0/D_0 = 10$, $\mu_0 = .024$ g/mm, so $M_0/\mu_0 = 25$ mm. With $Y_t = 33 \times 10^8$ dyne/cm² (for BHN = 110 kg/mm²) and $(A/A_0) = 2.4$ from Fig. 4.16 for $\dot{S}_0 = 3.4$ mm/ μ s, we find $P_E = 22$ mm in agreement with experiment. Similarly, for $L_0/D_0 = 3$, $\mu_0 = .033$ g/mm, and $(A/A_0) = 2.2$ from Fig. 4.18 we find $P_E = 12.5$ mm. If we assume the same μ_0 and (A/A_0) values for $L_0/D_0 = 2, 3$ and 4 and merely use the variation in A_0 to find variations in I_0, k, a_0, c_0, ζ and ϵ , we find $P_E = 10.5$ mm for $L_0/D_0 = 2$ and $P_E = 14$ mm for $L_0/D_0 = 4$. Since $\mu_0 = .024$ g/mm for $L_0/D_0 = 10$ and $\mu_0 = 0$ for $L_0/D_0 = 1$, this implies a maximum μ_0 in the vicinity of $L_0/D_0 = 3$.

Next we apply Eq (2.11) for $L_0/D_0 = 1$, $\mu_0 = 0$ and $(A/A_0) = 2$ from Fig. 4.18. We find $P_E = 9$ mm which is a bit high compared to experiment. Perhaps there is some erosion for a compact rod, or perhaps the flattening factors for mild steel versus mild steel are not quite the same as in Fig. 4.16 as we have been assuming.

Finally, we apply Eq (4.1) to Fig. 4.19 with $\mu_0 = .033$ g/mm and (A/A_0) estimated from Fig. 4.16 to be slightly more than 2 for $\dot{S}_0 \approx 2.0$ mm/ μ s, about 2.5 near $\dot{S}_0 = 2$ mm/ μ s and about 6 near $\dot{S}_0 = 1$ mm/ μ s. In this way we calculate the curve in Fig. 4.19 which agrees with experiment.

Let us complete this section by considering two examples which illustrate our fourth and fifth ways.

Tate and co-workers (4.24) impacted steel rods with various aspect ratios against armor steel targets. The impact speed range they investigated was small and low, generally from 1 to 1.5 mm/ μ s, so little can be said about the effect of speed from their data. However, in some cases they kept the impact speed constant and changed the rod aspect ratio either by changing the length with constant diameter (our fourth way) or changing the diameter while holding the length constant (our fifth way). Here we will only consider an example of each procedure.

In one set of experiments, they kept $D_0 = 7.5$ mm and doubled L_0 from 22.5 mm to 45 mm, which doubled the aspect ratio from 3 to 6 as well as doubling the mass from 7.75 g to 15.5 g. For a constant striking speed of $\dot{S}_0 = 1.525$ mm/ μ s, they found $P_E = 13$ mm for the shorter rod and $P_E = 20$ mm for the longer rod.

In our discussion of the fourth way above, we assumed that the erosion rate in g/mm should not change if A_0 is kept constant and the aspect ratio is changed by varying L_0 . If (A/A_0) does not change either (as for higher speeds), then doubling L_0 should double P_E . However, at a low speed like 1.525 mm/ μ s, Fig. 4.16 leads us to expect an increase in (A/A_0) as the aspect ratio increases. Consequently, the longer rod will flatten more and its penetration will be less than double that of the shorter rod. We estimate $\mu_0 = .15$ g/mm for either rod with A_0 , I_0 , a_0 , c_0 and k the same for either rod also. This value of μ_0 is slightly less than we might estimate from Eq (4.9) since the rods used were considerably harder than the targets (2.19). For the same reason we expect somewhat less flattening than is indicated from Fig. 4.16. If we use $Y_t = 90 \times 10^8$ dyne/cm² as usual with $A/A_0 = 2.2$ for $L_0/D_0 = 3$ and $A/A_0 = 3$ for $L_0/D_0 = 6$, we find $P_E = 13$ mm and 20 mm respectively.

In another set of experiments, these authors kept $L_0 = 56.7$ mm, while reducing D_0 from 9.45 mm to 4.72 mm. This increased the aspect ratio from 6 to 12, while reducing the mass from 31.1 g to 7.75 g. When they used the same striking speed, $\dot{S}_0 = 1.45$ mm/ μ s, for each rod, they found $P_E = 23.5$ mm for the shorter, heavier rod and $P_E = 15.5$ mm for the longer, lighter rod. This is a clear example where a decrease in mass is more important than an increase in aspect ratio in determining penetration depth. Of course the mass was decreased by a factor of four, while the aspect ratio was only doubled. For the $L_0/D_0 = 6$ rod we keep $(A/A_0) = 3$ as before, and estimate $\mu_0 = .24$ g/mm we find $P_E = 23.5$ mm. For the $L_0/D_0 = 12$ rod, the mass per unit length is lower by a factor of four, so $\mu_0 = .06$ g/mm. However, M_0 is also reduced by the same factor, so $(M_0/\mu_0) = 129$ mm again. Now $P_E = 15.5$ mm.

It would be a better test of our theory, of course, if we had independent, experimental determinations of μ_0 and (A/A_0) . Since these are not available, we have been forced to make estimates. However, our estimates are not arbitrary, and fit well with a variety of experimental information gathered by various workers. This illustrates one of the most important characteristics of a good theory, namely, its ability to connect pieces of a puzzle into a coherent pattern.

c. Steel/Aluminum

Fig. 4.20 is from Christman and co-workers (4.23) and shows cross-sections of three craters made by their 0.6 g, $L_0/D_0 = 3$ mild steel rods striking soft aluminum targets (1100-0, BHN = 25 kg/mm²) at three different speeds. The lowest striking speed, $\dot{S}_0 = 1.9$ mm/s, is a little below the shatter threshold evident in Fig. 4.21. As these authors remark, this is the beginning of "the region where the projectile goes from gross plastic deformation to complete fragmentation" (4.25). In Fig. 4.20a, the narrow crater has a smooth, rounded bottom where the deformed mushroom cap came to rest. The next highest striking speed, $\dot{S}_0 = 2.9$ mm/ μ s, is near the minimum penetration in the shatter region. The crater in Fig. 4.20b is wider and ragged near the bottom where pieces of the rod are strewn about. The highest striking speed shown is $\dot{S}_0 = 4.4$ mm/ μ s. This is near the end of the shatter gap, where the penetration starts to exceed its previous maximum value. In Fig. 4.20c, the crater is still wider, quite ragged, and bulbous in shape. The authors comment that, at lower speeds, "most of the projectile remains intact at the bottom of the crater, although grossly deformed." By $\dot{S}_0 = 5.3$ mm/ μ s, "the steel projectile has been completely broken up, as evidenced by the 'scouring' of the crater wall by the projectile fragments; and the crater has taken a 'bottle' shape with the maximum diameter approximately halfway down the crater rather than at the surface" (4.26). Presumably, at much higher striking speeds, the crater will approach a hemi-spherical shape.

The three pictures in Fig. 4.20 correspond to the three data points with flags in Fig. 4.21. This figure also shows a lower curve for the same steel rods impacting harder aluminum targets (2024-T3, BHN = 125 kg/mm²). The effect of target hardness on penetration is obvious over the entire striking speed range investigated, and is still 25 to 30% near $\dot{S}_0 = 5$ mm/ μ s. The softer target shows a clearer shatter threshold at a lower speed. The harder target curve resembles Fig. 4.12 (also steel/2024 aluminum), although the rods in Fig. 4.12 had a larger aspect ratio. Since the projectiles in Fig. 4.21 were the same for both target materials, it is clear that target hardness as well as target density can influence the shatter threshold. If we compare Figs. 4.21 and 4.19, we see the effect of target density on penetration. The effect of target density on nose shatter is not evident, however, since there

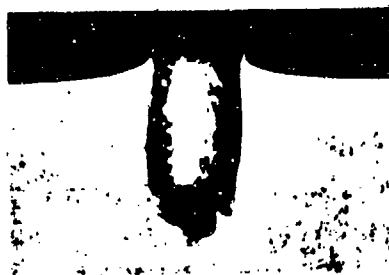
C1015 STEEL RODS

$L_0/D_0=3.0$, 0.6 g

1100-0 ALUMINUM TARGETS



1.90 mm / μ s
(a)



2.90
(b)



4.40
(c)

Fig. 4.20. Crater Sections, Velocity Effects

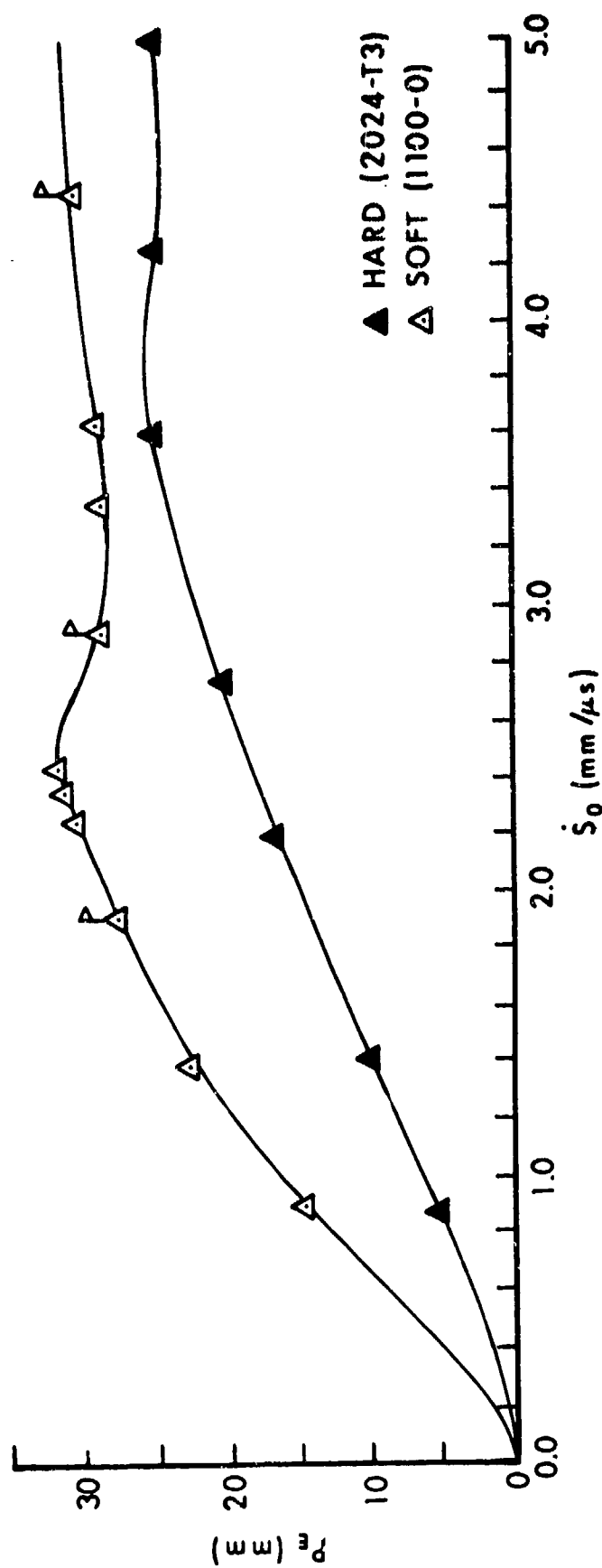


Fig. 4.21. Mild steel rods ($L_0/D_0 = 3$, $M_0 = 0.6g$) vs. soft and hard aluminum.

is no information in Fig. 4.19 for $\dot{S}_0 < 1 \text{ mm}/\mu\text{s}$ where we might expect shatter, if the rod were hard enough.

Fig. 4.22 is also from Christman and co-workers (4.23) and is comparable to Fig. 4.18 (steel/steel) with the addition of two data points for $L_0/D_0 = 15$ and 20. The table in Fig. 4.18 is easily extended to give $L_0/D_0 = 27.75 \text{ mm}/1.85 \text{ mm} = 15$ and $L_0/D_0 = 34 \text{ mm}/1.7 \text{ mm} = 20$, both with $M_0 = .6 \text{ g}$. The same striking speed, $\dot{S}_0 = 3.4 \text{ mm}/\mu\text{s}$, was used in both Fig. 4.18 and Fig. 4.22. Only the targets were different. Penetrations into soft aluminum are about twice as deep as into mild steel for any aspect ratio at this speed.

We recall that Perez (4.14) also impacted steel rods ($L_0/D_0 = 11$) against aluminum targets which were a bit harder ($\text{BHN} \sim 40 \text{ kg/mm}^2$) than the soft aluminum targets here ($\text{BHN} = 25 \text{ kg/mm}^2$). From Perez' data in Fig. 4.11 we found an erosion rate of $.012 \text{ g/mm}$. For the $L_0/D_0 = 10$ rod in Fig. 4.22, we might expect about the same rate, perhaps a bit smaller. This gives us a starting point from which to estimate erosion rates for the other aspect ratios in Fig. 4.22. From Fig. 4.18 for the same steel rods versus steel, we recall our estimates of $.024 \text{ g/mm}$ for $L_0/D_0 = 10$ and $.033 \text{ f/mm}$ for $L_0/D_0 = 3$. That is, the shorter rod had an erosion rate about one-third larger than the longer rod. In this way, we can estimate $\mu_0 = .015 \text{ g/mm}$ for the $L_0/D_0 = 3$ rod versus aluminum. As the rod diameter decreases for $L_0/D_0 > 10$, we expect the erosion rate to decrease somewhat, provided the flattening factor is independent of aspect ratio at this high striking speed. Thus, we estimate $\mu_0 = .010 \text{ g/mm}$ for $L_0/D_0 = 15$ and $\mu_0 = .0094 \text{ g/mm}$ for $L_0/D_0 = 20$. This decrease is also required if the very high speed limit (M_0/μ_0) is to exceed the penetration values reported in Fig. 4.22. For $L_0/D_0 = 1$, we assume $\mu_0 = 0$ as before, and use Eq (2.11) instead of Eq (4.1) to calculate the penetration. We also assume $(A/A_0) = 2.4$ for any aspect ratio in Fig. 4.22. This lets us calculate the curve which seems to agree well with the observations.

In order to calculate the two curves in Fig. 4.21, we assume $\mu_0 = .015 \text{ g/mm}$ to be the same for both targets. This is similar to the assumption we made for mild and armor steel targets in Figs. 4.14 and 4.15 where the hardness values differed by a factor of about 2.25. In Fig. 4.21 the hardness values differ by a factor of 5, so this assumption may be less correct. Still, it allows us to make the target hardness responsible for the observed differences in penetration. If we proceed in this way, we have

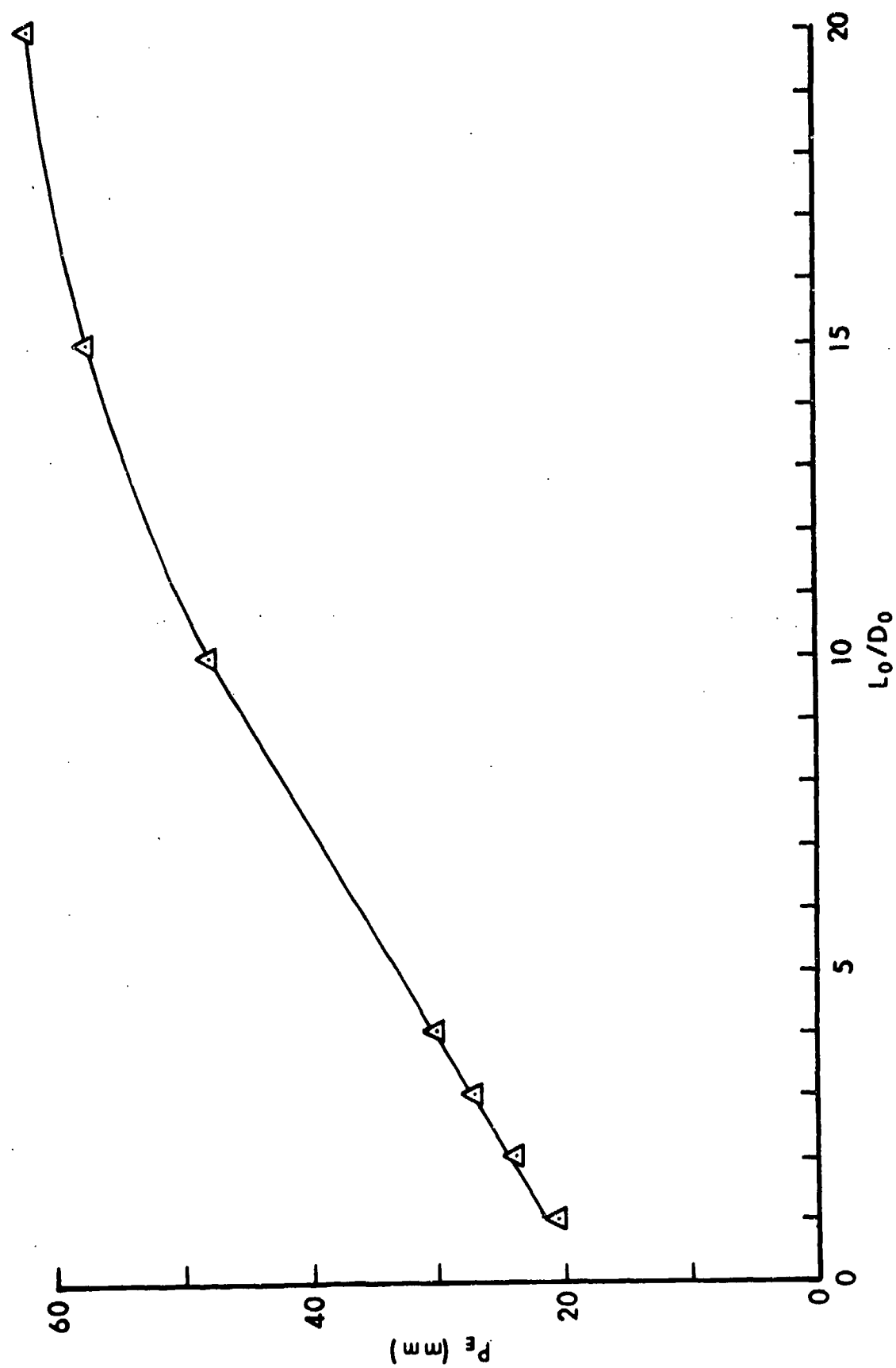


Fig. 4.22. Steel rods ($M_0 = 0.6g$, $\dot{S}_0 = 3.4mm/\mu s$) versus soft aluminum.

$A_0 = .079 \text{ cm}^2$ and $I_0 = 8 \text{ mm/g}$ for the $L_0/D_0 = 3$ rod, as before. For either aluminum target we have $c_0 = .0107 \text{ g/mm}$. For the hard aluminum target, we find $a_0 = .009 \text{ g mm}/\mu\text{s}^2$, and for the soft aluminum target, $a_0 = .0019 \text{ g mm}/\mu\text{s}^2$. Then we can use the (A/A_0) values shown in Fig. 4.23 to calculate the two curves in Fig. 4.21.

Both (A/A_0) curves in Fig. 4.23 have the same form, decreasing as \dot{S}_0 increases from a low value, then increasing above the shatter threshold, and levelling off at high speed. This occurs for $\dot{S}_0 \geq 4.5 \text{ mm}/\mu\text{s}$ for the hard target and for $\dot{S}_0 \geq 3.2 \text{ mm}/\mu\text{s}$ for the soft target. The latter value is just below $\dot{S}_0 = 3.4 \text{ mm}/\mu\text{s}$ in Fig. 4.22, and the value $(A/A_0) = 2.7$ is what we used for all aspect ratios there. Both curves in Fig. 4.23 approach the same high speed limit, since density rather than hardness seems to control lateral confinement at such speeds. Of course, hardness as well as density controls penetration depth as we have seen. The value $(A/A_0) = 2.7$ is not much different for steel/aluminum than for steel/steel in Fig. 4.16, where (A/A_0) versus \dot{S}_0 has the same general form, as expected.

The vertical scale in Fig. 4.23 has been made the same as in Fig. 4.16 to facilitate comparisons. An obvious difference is the absence of a minimum in Fig. 4.16. Another difference occurs for striking speeds less than $1.5 \text{ mm}/\mu\text{s}$. For example, near $\dot{S}_0 = 1 \text{ mm}/\mu\text{s}$, we can estimate $(A/A_0) = 6$ for $L_0/D_0 = 3$ steel rods versus steel from Fig. 4.16. From Fig. 4.23, we see that near $\dot{S}_0 = 1 \text{ mm}/\mu\text{s}$, $(A/A_0) \approx 3$ for the same steel rods versus aluminum. Apparently, the less dense aluminum targets are less effective at initiating flattening of these rods at low speeds. Of course, the opposite is true at high speeds where the less dense aluminum provides less lateral confinement than steel. Of course both aluminum targets are softer than the softest steel target, although the hard aluminum is almost as hard as the mild steel ($\text{BHN} = 125 \text{ kg/mm}^2$ versus $\text{BHN} = 135 \text{ kg/mm}^2$).

We recall from Fig. 3.13 that an aluminum target did not flatten a hardened steel sphere at all for $\dot{S}_0 \leq 1.5 \text{ mm}/\mu\text{s}$. It flattened a softened steel sphere somewhat, giving $(A/A_0) = 1.67$ near $\dot{S}_0 = 1.5 \text{ mm}/\mu\text{s}$. A mild steel sphere has a value of (A/A_0) between 1 and 1.67. As we see from Fig. 4.23, a short mild steel rod has $(A/A_0) \geq 2$ near $\dot{S}_0 = 1.5 \text{ mm}/\mu\text{s}$ for either aluminum target. This agrees with our expectation that a blunt rod deforms more than a sphere under similar conditions.

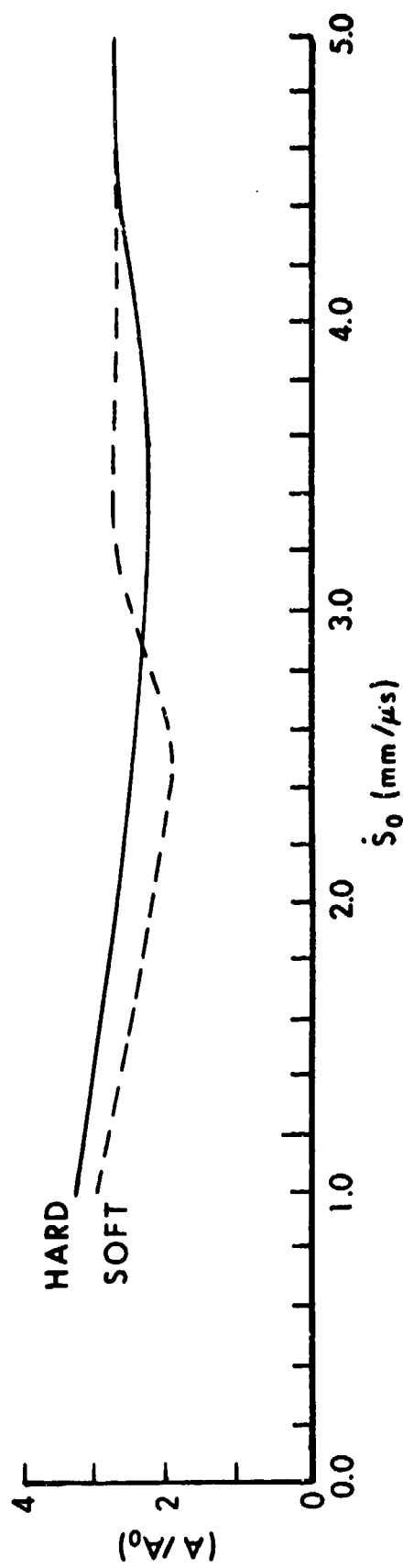


Fig. 4.23. (A/A_0) for 0.6g mild steel rods ($L_0/D_0 = 3$) vs. aluminum targets (soft and hard).

We recall from Fig. 3.6 that a mild steel target was more effective at flattening the same softened steel sphere than an aluminum target, giving $(A/A_0) = 1.8$ at a lower speed, $\dot{S}_0 = .7$ mm/ μ s. This trend agrees with what we see in Figs. 4.16 and 4.23, although the differences are more pronounced for rods than for spheres.

The two curves in Fig. 4.21 also remind us of the two curves in Fig. 3.16 where hard and soft aluminum targets were also used to stop the same projectile (aluminum spheres in that case). In Fig. 3.16 there was a 40 to 50% difference in penetration depth up to $\dot{S}_0 = 9$ mm/ μ s. In Fig. 4.21, the difference is 30 to 40% up to $\dot{S}_0 = 5$ mm/ μ s. In Fig. 3.16 a single flattening factor, $(A/A_0) = 1.3$, sufficed for aluminum spheres/aluminum over the entire range studied from $\dot{S}_0 = 3$ mm/ μ s to $\dot{S}_0 = 9$ mm/ μ s. Most likely, this is the high speed limit value of (A/A_0) for this projectile/target combination. It is less than the comparable high speed limit value for steel rod in Fig. 4.23 as expected, both because rods tend to deform more than spheres and steel will spread laterally more in an aluminum target than aluminum will.

Finally, let us recall that for Fig. 3.13, we conjectured that the F_E curves for hardened and softened steel spheres might converge at higher striking speeds and have a single (A/A_0) value between 1 and 1.67, as they did in Fig. 3.6, with $(A/A_0) = 1.5$ as the high speed limit value for steel spheres on steel. This is close to the value $(A/A_0) = 1.3$ for aluminum spheres on aluminum. In the next section (Fig. 4.24) we will see a case where soft and hard short aluminum rods have somewhat different penetrations against the same aluminum target at low speeds, but have the same penetration (and same high speed flattening factor) for $\dot{S}_0 \geq 4.5$ mm/ μ s.

d. Aluminum versus Steel and Aluminum

The lower curve in Fig. 4.24 is for $M_0 = .2$ g, $L_0/D_0 = 3$ aluminum rods versus mild steel targets. It is also from Christman and co-workers (4.23) who used both soft and hard aluminum rods, but found no difference in penetrating steel targets. The upper curve in Fig. 4.24 is the same as Fig. 4.19 for 0.6 g, $L_0/D_0 = 3$ mild steel rods versus mild steel targets and is included here for comparison purposes. The target materials as well as the projectile geometries are identical for both curves in Fig. 4.24. They differ only in projectile density which leads to a factor of three difference in

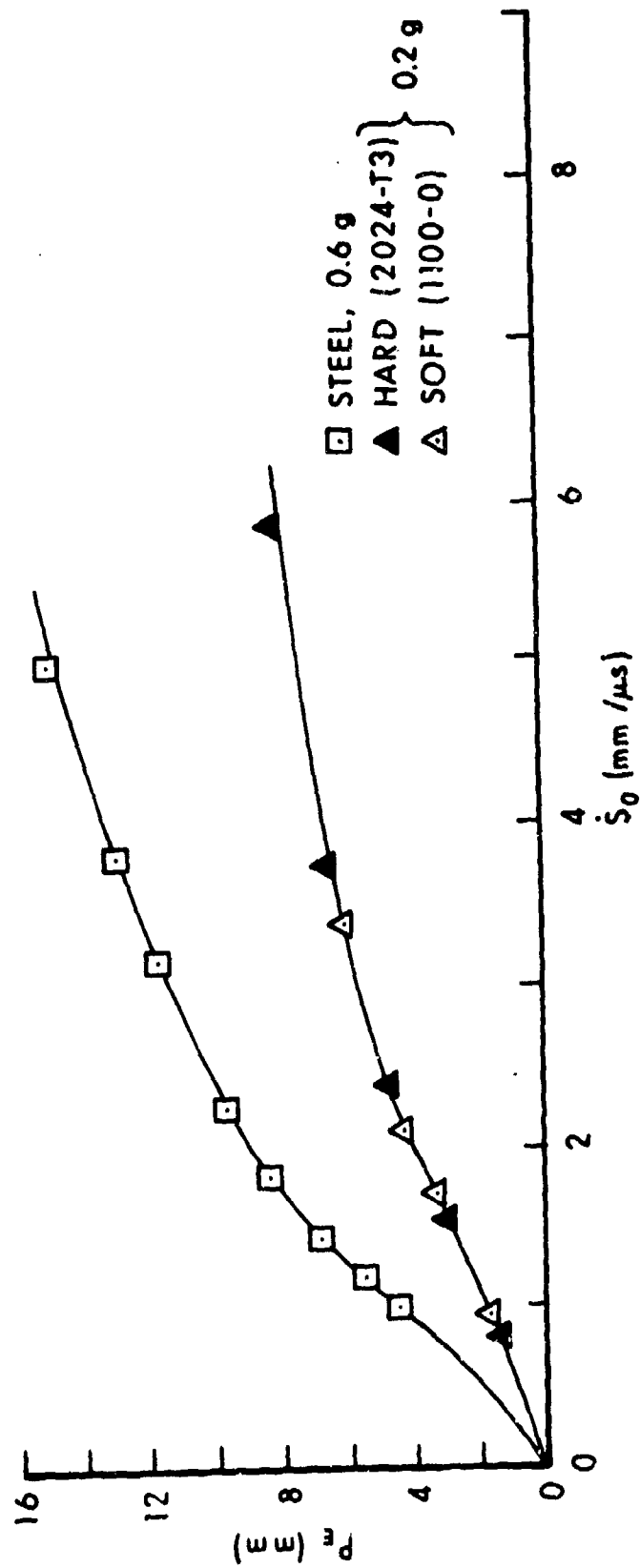


Fig. 4.24. Steel and Al rods ($L_0/D_0 = 9.52/3.17 = 3$) vs. mild steel targets.

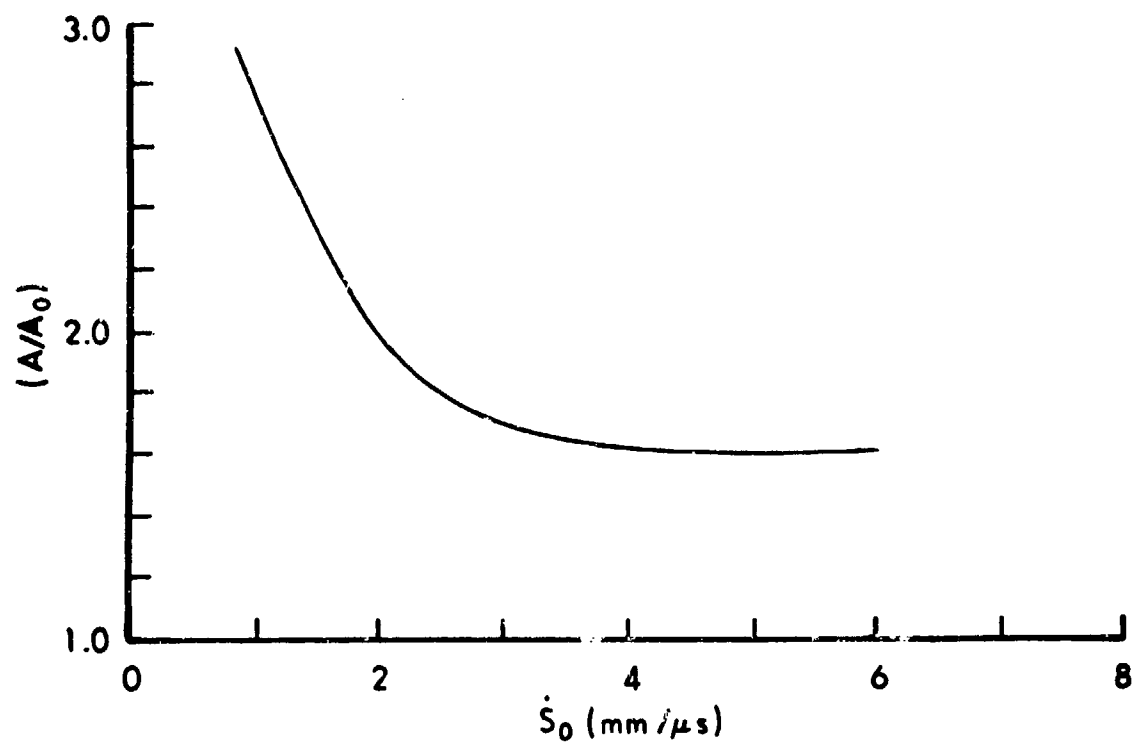


Fig. 4.25. Flattening factor for aluminum rods ($M_0 = .2g$, $L_0/D_0 = 3$) of different strengths versus mild steel.

projectile mass. However, the penetration depths differ by a factor of two because of differences in erosion rate and flattening. This is an example of our second way.

In the usual way, we estimate $\mu_o = .019$ g/mm, assuming a smaller high-speed flattening limit than for steel/steel because of the smaller projectile density. If we use the (A/A_o) values shown in Fig. 4.25, then Eq (4.1) lets us calculate the lower curve in Fig. 4.24. Once more the agreement with experiment is satisfactory.

Christman and co-workers ^(4.23) also impacted a variety of aluminum rods against aluminum targets. Fig. 4.26 shows three soft (1100-0) aluminum rods which were recovered after striking soft (1100-0) aluminum targets at three different speeds. All of the rods had $M_o = .2$ g, $L_o/D_o = 3$. The increase in deformation with striking speed is clear. For $\dot{S}_o = .31$ mm/ μ s the diameter of the nose has increased by about 50% so the flattening factor is about two. For $\dot{S}_o = .45$ mm/ μ s, the final diameter has doubled, so (A/A_o) is probably 4. For $\dot{S}_o = .98$ mm/ μ s, we see the formation of a mushroom cap and a decrease in (A/A_o) as the projectile becomes more streamlined at higher striking speeds.

Fig. 4.27 shows three aluminum rods with different hardness values recovered after striking soft (1100-0) aluminum targets at the same speed, $\dot{S}_o = .9$ mm/ μ s. All three had $M_o = .2$ g, $L_o/D_o = 3$ as in the previous figure. Since the striking speed here is almost the same as that in Fig. 4.26c, it is not surprising that the mushroom shape is about the same. The medium-hard rod in Fig. 4.29b has deformed much less, while the hardest rod in (c) has only begun to deform with a combination of plastic flow and chipping. Tiny flares for flight stability are visible in some of the pictures.

Fig. 4.28 gives data for soft (1100-0) and medium-hard (2024-T3) aluminum rods versus soft (1100-0) and medium hard (2024-T3) aluminum targets. Once more the undiminished importance of target hardness is evident to $\dot{S}_o > 6$ mm/ μ s. Christman and co-workers ^(4.23) also reported experiments with inhibited jets against these targets. Inhibited jets are jet tips with the rest of the jet removed. Usually they are produced from small angle cones and have high tip speeds approaching twice the explosive detonation rate ^(4.27, 4.28). These authors found that the importance of target strength was undiminished up to 15.7 mm/ μ s, far above normal jet tip speeds. From such experiments it is clear that one simply cannot neglect target strength at any such speed, at least for compact projectiles.

1100-0 ALUMINUM RODS

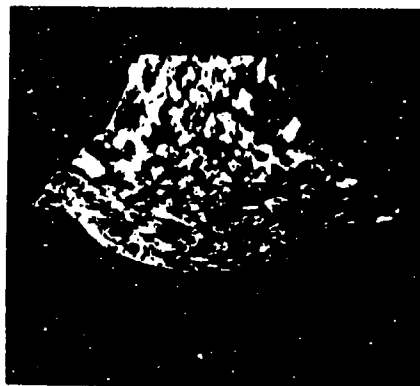
$L_0/D_0=3.0$, 0.2 g

1100-0 ALUMINUM TARGETS



0.31 mm/ μ s

(a)



0.45

(b)



0.98

(c)

Fig. 4.26. Recovered Projectiles, Velocity Effects

Another important feature in Fig. 4.28 is the low speed difference in penetration for soft and hard projectiles against the soft target. This is comparable to Fig. 3.6 for soft and hard steel spheres versus a mild steel target. But in Fig. 4.28 there is no observable difference against the harder target. The shape of the curve for the harder aluminum (2024-T3) rod versus the soft aluminum (1100-0) target is similar to that of the upper curve in Fig. 4.21 for a geometrically identical steel rod versus the same aluminum target. If softened steel rods had also been used in Fig. 4.21, presumably there would be another set of data points somewhat below the upper curve at low speeds, which would merge with the upper curve for $\dot{S}_0 > 3.5$ mm/ μ s. The uppermost curve in Fig. 4.28 offers some evidence of nose shatter, but only for the harder rod, and only against the softer target. Against a target of equal (or greater) hardness, any difference there may be between plastic deformation and shatter is not observable. Perhaps the hard target provides enough lateral confinement to prevent the onset of spreading, if shatter occurs, something a much softer target cannot do.

Figs. 4.27a and 4.27b show soft and hard rods recovered from the soft target after striking it at a speed where the difference in penetration in Fig. 4.28 starts to be observable. Clearly, the harder rod has flattened less. There also seems to be a chip missing similar to what is seen for the still harder rod in Fig. 4.27c. This suggests a beginning of shatter.

It is interesting to compare Fig. 4.28 with Fig. 3.16 for aluminum spheres ($D_0 = 4.76$ mm, $M_0 = .158$ g) versus soft and hard aluminum targets. The rods in Fig. 4.28 are 25% heavier than the spheres. However, their penetration is more than 25% greater against comparable targets in spite of erosion and greater flattening, because of their greater aspect ratio as well as their greater mass.

The curve in Fig. 4.28 for the soft aluminum rod versus the soft aluminum target is comparable to that in Fig. 4.19 for a geometrically similar mild steel rod versus a mild steel target. Christman and co-workers also reported data for aluminum/aluminum similar to that in Fig. 4.18 for steel/steel, which we will not discuss here, since the principles involved have already been illustrated.

By the usual procedures, we estimate $\mu_0 = .008$ g/. which we will assume to be the same for either rod versus either target. This approximation may not be as close to the truth as it was in other cases where the target

ALUMINUM RODS

$L_0/D_0=3.0$, 0.2 g, 0.90 mm/ μ s

1100-0 ALUMINUM TARGETS



1100-0
(a)



2024-T3
(b)



7075-T6
(c)

Fig. 4.27. Recovered Projectiles, Material Effects

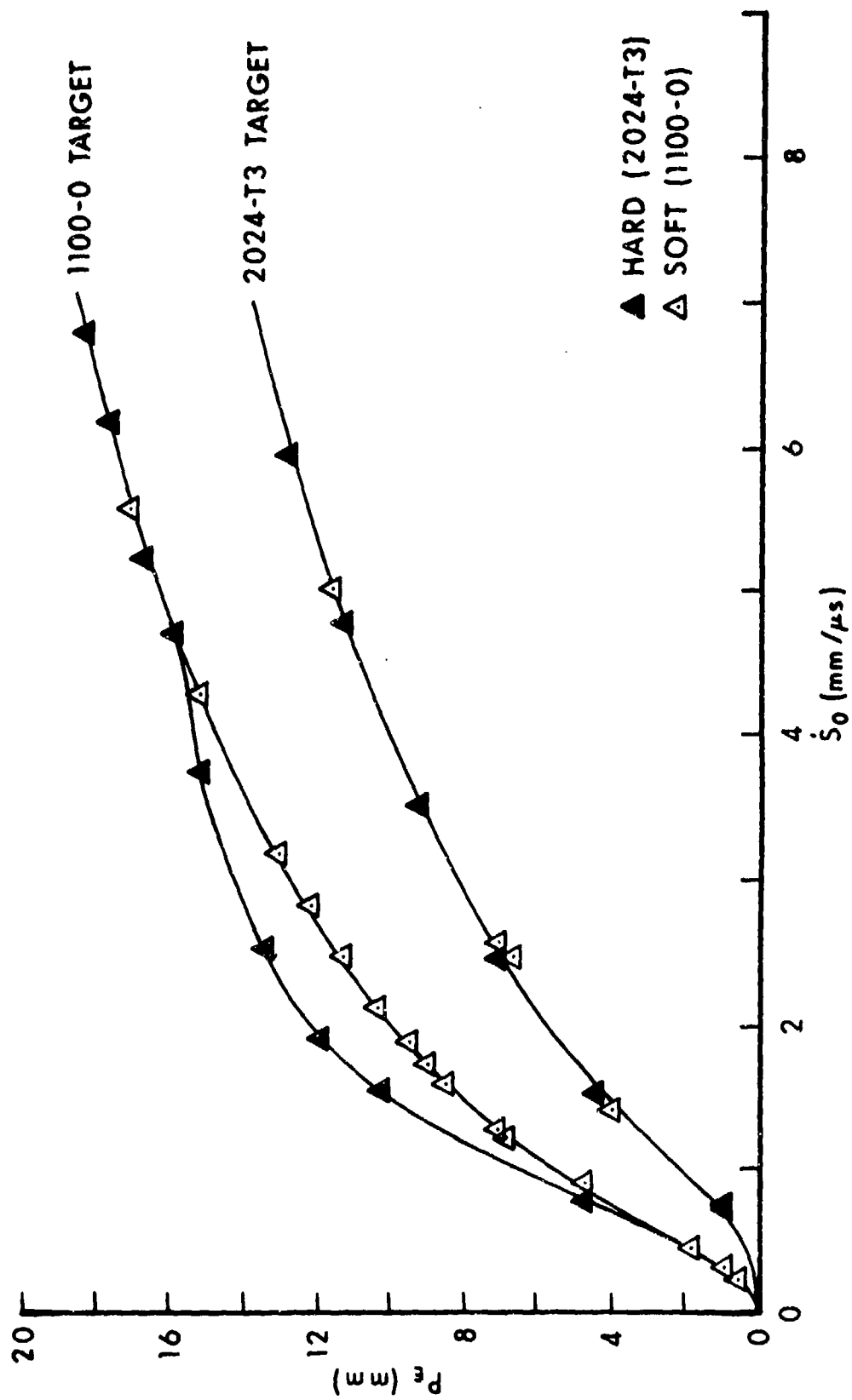


Fig. 4.28. Aluminum rods ($M_0 = .28$, $L_0/D_0 = 9.525\text{mm}/3.175\text{mm} = 3$) versus aluminum targets.

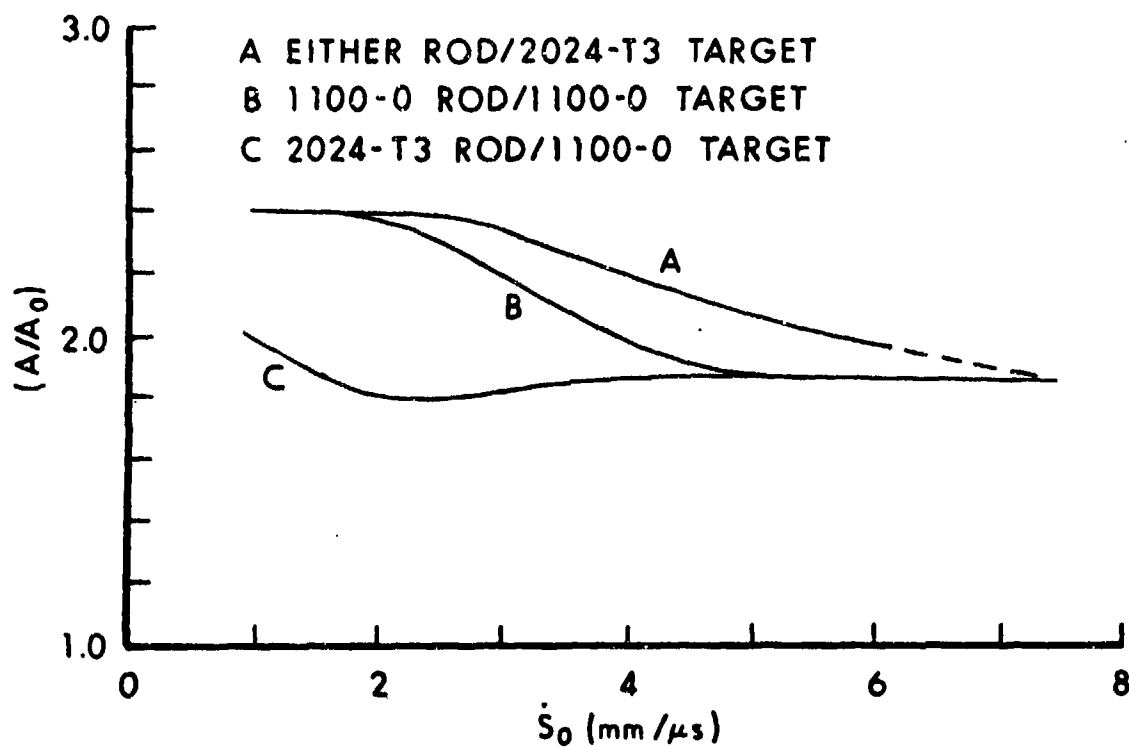


Fig. 4.29. Flattening factors for aluminum rods ($M_R = .2\text{g}$, $L_0/D_0 = 3$) of different strengths versus targets of different strengths.

strengths differed by less than a factor of five. Again, this assumption puts the burden on (A/A_0) . If we use the (A/A_0) values shown in Fig. 4.29, together with target strengths of $10 \times 10^8 \text{ dyne/cm}^2$ and $50 \times 10^8 \text{ dyne/cm}^2$ for the soft and hard targets respectively, we can calculate the curves in Fig. 4.28 from Eq (4.1). In Fig. 4.29 we see the expected shapes for the soft target with a merger of the two curves at high speed. For the hard target, however, we see a slightly larger flattening factor out to 6 mm/ μs . The difference is only about 10%, and may be due to our assumption that μ_0 is the same for all rod/target combinations.

e. Tungsten versus Aluminum, Steel and Tungsten

Hohler and Stilp (4.1) used two sizes of tungsten alloy rods ($\rho_p = 17 \text{ g/cm}^3$, $M_0 = 3.2 \text{ g}$, $L_0/D_0 = 29.1 \text{ mm}/2.8 \text{ mm} = 10.4$ and $M_0 = 30.9 \text{ g}$, $L_0/D_0 = 62.4 \text{ mm}/6 \text{ mm} = 10.4$) versus mild and armor steel targets. Later (4.28) they used similar rods against two slightly different aluminum targets, both with $\rho_t = 2.85 \text{ g/cm}^3$ and BHN close to 80 kg/mm^2 . In addition, they used targets made from the same tungsten alloy as the rods (BHN = 270 kg/mm^2). Still later (4.22) they used a slightly stronger version of this tungsten alloy to make rods of various aspect ratios and fired them against armor steel targets (BHN = 330 kg/mm^2). As expected, small changes in projectile hardness made no observable difference.

Fig. 4.30 shows data for their smaller tungsten rod versus aluminum, mild steel and tungsten. The horizontal dashed line is the aluminum hydrodynamic limit which is about 50% low at high speeds. The hydrodynamic limits for steel and tungsten are not shown, but are only 10-15% low.

Let us estimate erosion rates by starting with our estimate for Hohler and Stilp's 0.96 g steel rod, $L_0/D_0 = 25 \text{ mm}/2.5 \text{ mm} = 10$ versus steel, which was .033 g/mm. Eq (4.8) involves not only the ratio of the areas, $(2.8/2.5)^2 = 1.25$, but also the square root of the ratio of the rod densities, $\sqrt{17/7.85} = 1.47$, so for this tungsten rod versus the steel target we have $\mu_0 = (.033 \text{ g/mm})(1.25)(1.47) = .06 \text{ g/mm}$. This gives a high-speed penetration limit of $M_0/\mu_0 = 3.2 \text{ g}/.06 \text{ g/mm} = 53 \text{ mm}$, which agrees with the trend in Fig. 4.30. For the tungsten target we must multiply .06 g/mm by the ratio $\sqrt{\rho_{t1}/\rho_{t2}} = \sqrt{17/7.85} = 1.47$ to obtain .088 g/mm. This gives a high-speed penetration limit near 36 mm which seems a bit low in view of Fig. 4.30. If

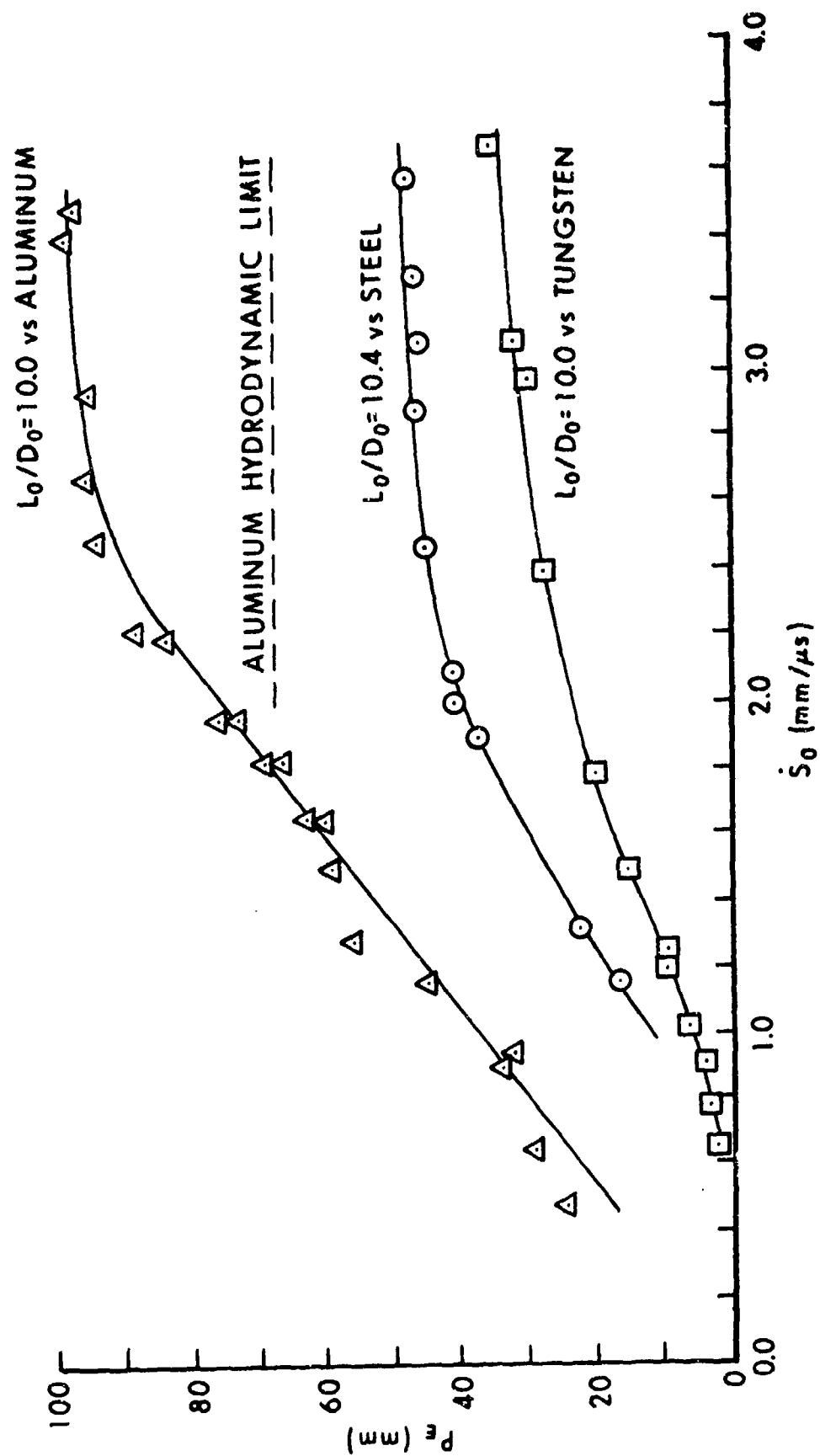


Fig. 4.30. Tungsten alloy rods ($D_0 = 2.8$ mm, $L_0/D_0 = 10$ or 10.4) versus aluminum, mild steel and tungsten alloy targets.

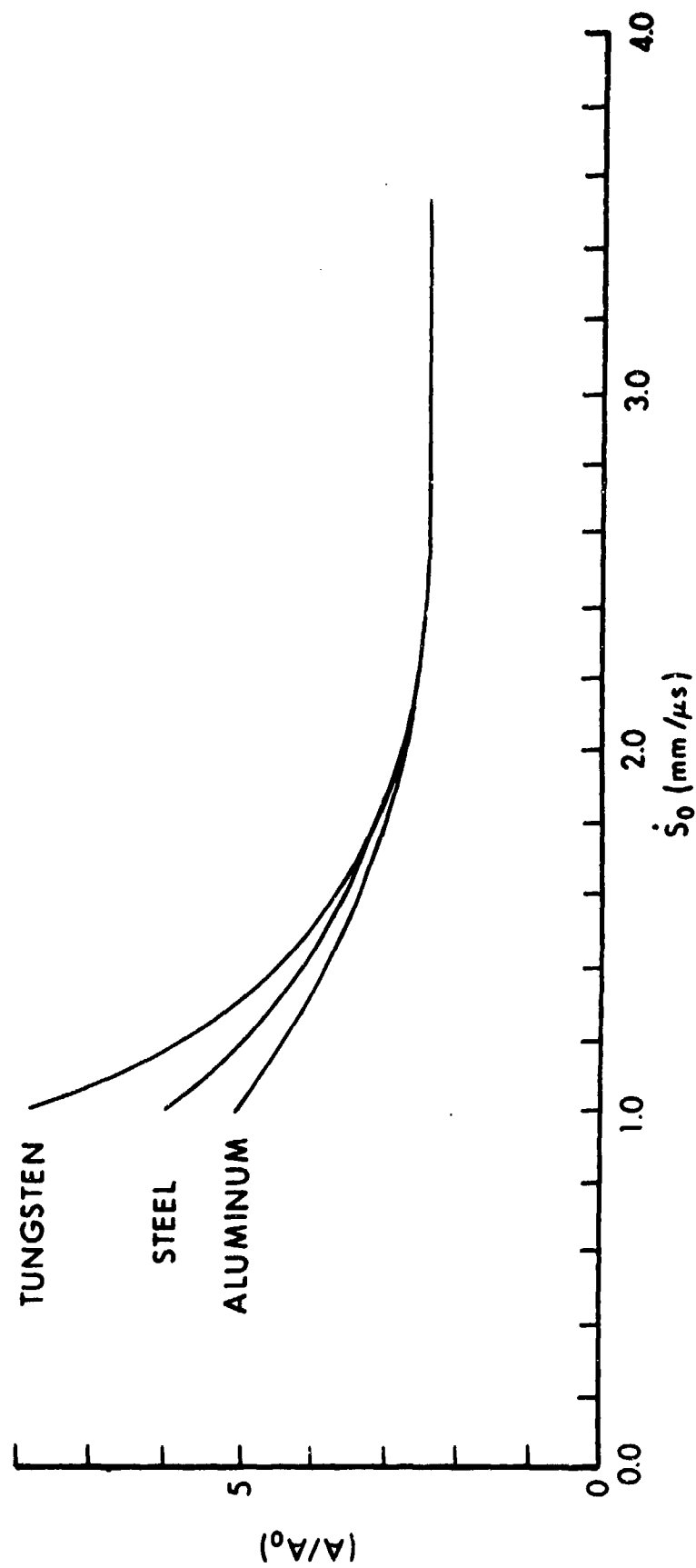


Fig. 4.31. Flattening factors for tungsten rods versus three target materials.

we adopt $\mu_o = .08$ g/mm, we obtain a more reasonable limit values. Then, for the aluminum target, we can multiply .08 g/mm by the appropriate square root of the target densities to obtain $\mu_o = .03$ g/mm and a limit in agreement with Fig. 4.30. Such rough estimates are about the best we can do with the information available. Now when we use Eq (4.1) with the flattening factors shown in Fig. 4.31 we calculate the curves in Fig. 4.30 in reasonable agreement with experiment. At low speeds we expect the highest (A/A_o) value for the tungsten target and the lowest for the aluminum target. The lack of any difference at high speeds may be due to the approximate nature of our calculations.

Fig. 4.32 shows some of Hohler and Stilp's ^(4.22) data for tungsten rods of various aspect ratios versus armor steel. In particular, the examples shown are for $L_o/D_o = 163.2$ mm/5.1 mm = 32, $L_o/D_o = 41.7$ mm/4.17 mm = 10, and $L_o/D_o = 9$ mm/9 mm = 1. For this last case we again assume that there is no erosion and use Eq (2.11) with the flattening factor shown in Fig. 4.33, which is almost independent of striking speed. The $L_o/D_o = 10$ example chosen here was selected because it has about the same mass as the $L_o/D_o = 1$ example. With an erosion rate $\mu_o = .13$ g/mm and the (A/A_o) values in Fig. 4.33, Eq (4.1) gives us the curve shown. Finally, the $L_o/D_o = 32$ example was almost six times as massive as the other two rods, so the deeper penetration evident in Fig. 4.32 is not simply due to larger aspect ratio. A better comparison is with the $L_o/D_o = 32$ steel rod in Fig. 4.15, which was about the same size and somewhat less than half the mass. An erosion rate $\mu_o = .2$ g/mm was determined in the usual way, and this together with the (A/A_o) values in Fig. 4.33 used in Eq (4.1) give us the curve in Fig. 4.32. In all cases there is reasonable agreement with experiment. The trends in Fig. 4.33 are similar to those in Fig. 4.16 for steel rods, except for $L_o/D_o = 1$. We recall Fig. 4.1a where the compact steel rod was considerably flattened at low speed. Unfortunately, Hohler and Stilp did not give a comparable photograph for a compact tungsten rod at low speed. They did, however, show photographs of $L_o/D_o = 10$ tungsten rods deformed at low speeds ^(4.1) which are presented here in Fig. 4.34. If we compare with Fig. 4.1b, it is obvious that the mushroom cap rim has broken off the tungsten rods at some point in time, while it is still present on the recovered steel rod. From Fig. 4.2a, the rim appears to be present on a tungsten rod at the beginning of a penetration into steel. We may conjecture that it is present during most of the penetration and breaks off near the end.

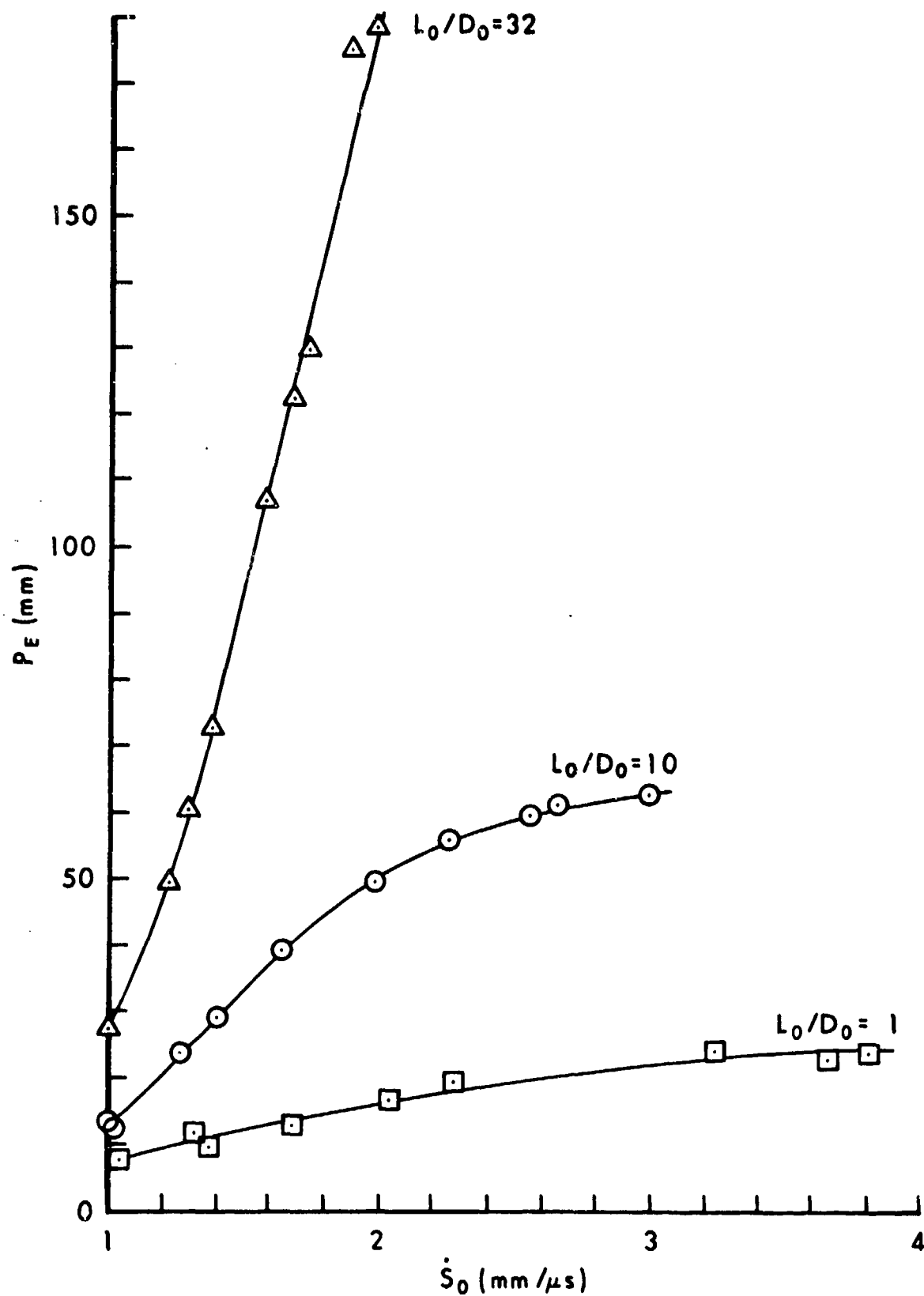


Fig. 4.32. Tungsten alloy rods versus armor steel.

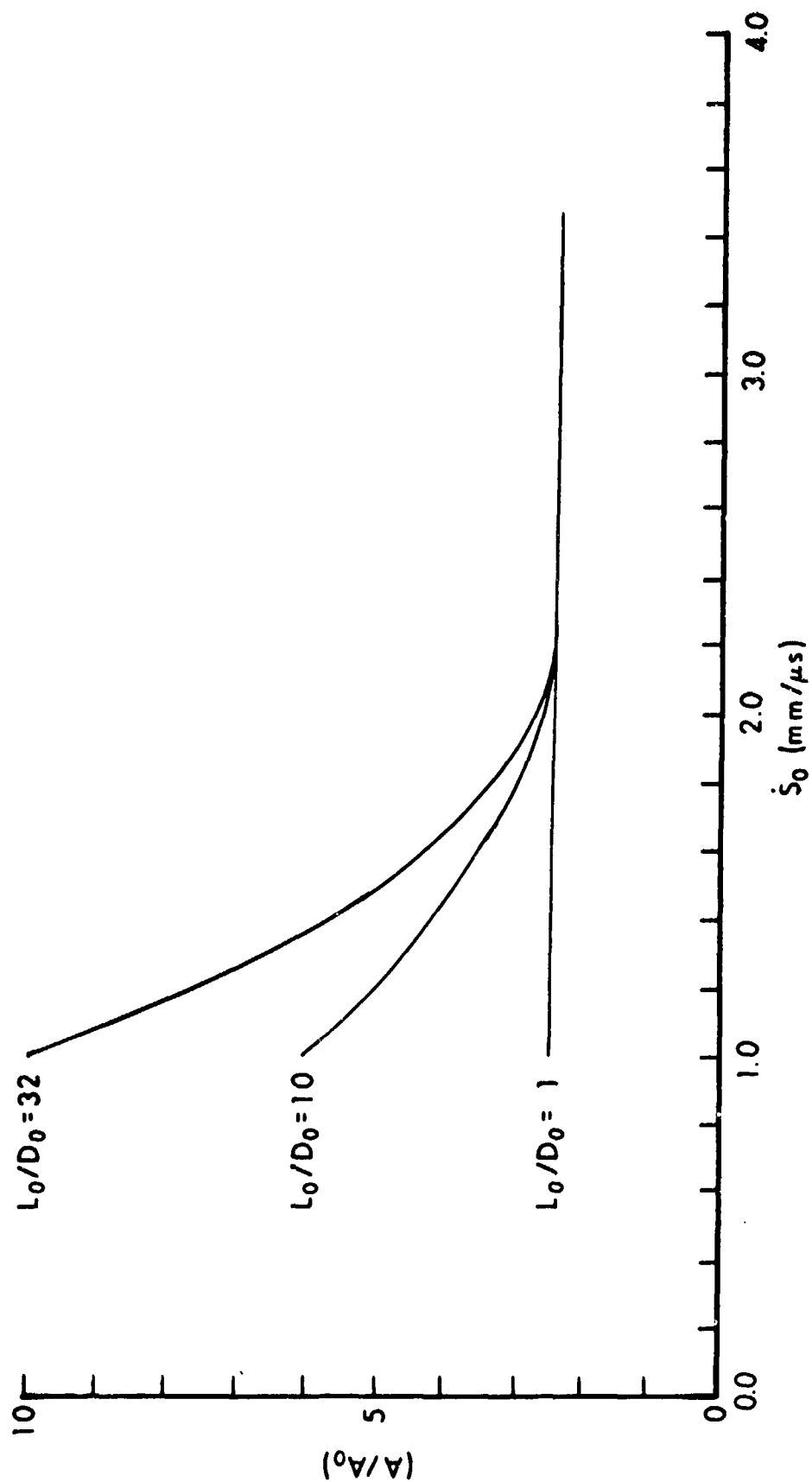


Fig. 4.33. Flattening factors for tungsten rods of various aspect ratios versus armor steel targets.

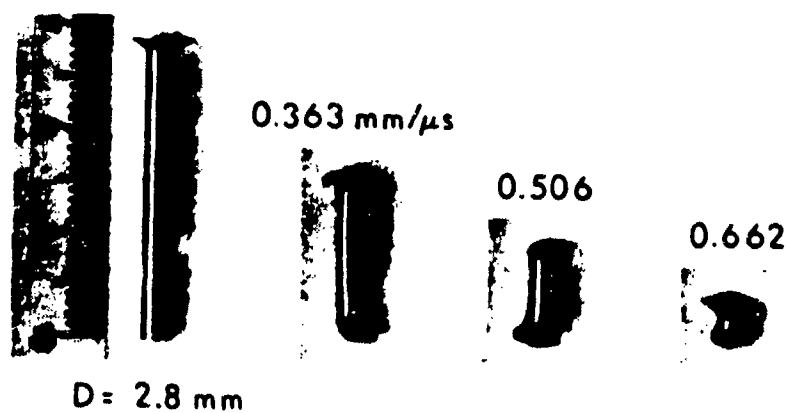
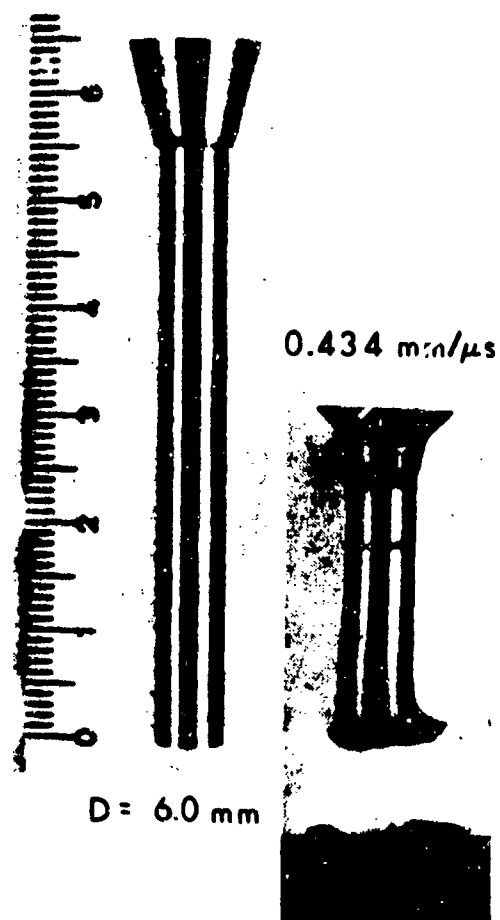


Fig. 4.34. $L_0/D_0 = 10$ tungsten rods with mushroom cap broken off.

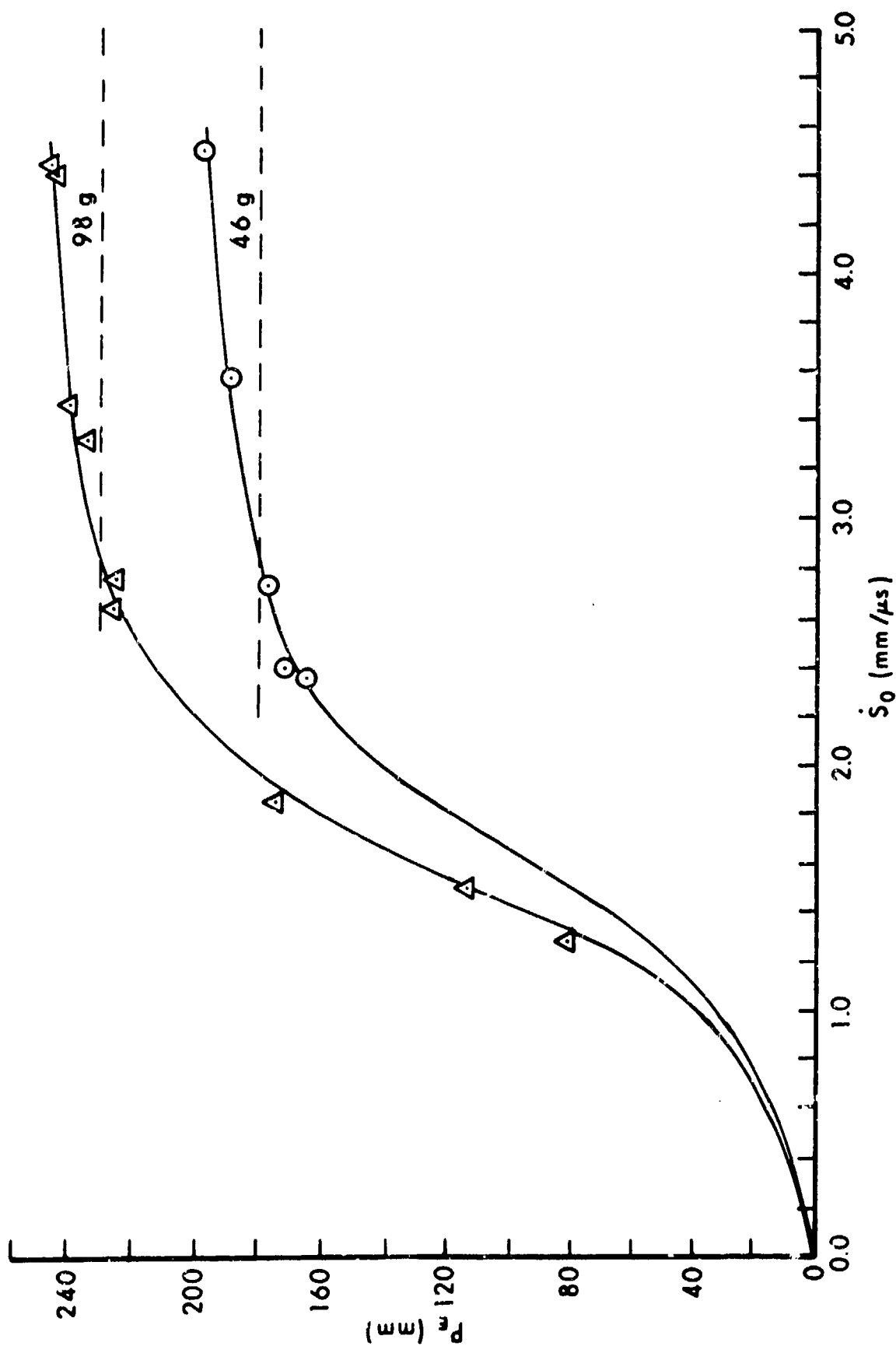


Fig. 4.35. Two tungsten alloy rods ($L_0/D_0 = 23$) vs. armor steel.

We might also conjecture that a compact tungsten rod which produces only a shallow crater, breaks much sooner and so does not have a much larger (A/A_0) value at low speed than at high speed.

Silsby (4.30) also reported data for tungsten alloy rods ($\rho_p = 17.3 \text{ g/cm}^3$) versus steel targets ($\text{BHN} = 230 \text{ to } 270 \text{ kg/mm}^2$). He used two rod sizes $M_0 = 98 \text{ g}$, $L_0/D_0 = 155.8 \text{ mm}/6.77 \text{ mm} = 23$ and $M_0 = 46 \text{ g}$, $L_0/D_0 = 121.8 \text{ mm}/5.3 \text{ mm} = 23$. His data points are shown in Fig. 4.35 together with horizontal dashed lines representing the hydrodynamic limits.

By the usual method we estimate $\mu_0 = .217 \text{ g/mm}$ for the 46 g rod and $\mu_0 = .37 \text{ g/mm}$ for the 98 g rod. Then Eq (4.1) together with (A/A_0) values for $L_0/D_0 = 23$ from Fig. 4.33 gives the two curves in Fig. 4.35 in agreement with experiment. For example, for $\dot{S}_0 = 1$, we can use $(A/A_0) = 8$, and so on.

Tate and co-workers (4.24) also impacted tungsten rods of various aspect ratios against steel targets over a rather small speed range. We could use this data as we did their steel rod data, but nothing new would be learned.

f. Copper versus Copper, Aluminum and Steel

Finally, let us examine some data reported by Weihrauch (4.3) for copper rods ($\rho_p = 8.96 \text{ g/cm}^3$, $M_0 = 3.8 \text{ g}$, $L_0/D_0 = 60 \text{ mm}/3 \text{ mm} = 20$) impacting copper, aluminum and steel targets.

Fig. 4.36 (4.304) is a sequence of photographs of copper rods which were recovered after striking copper targets at various speeds. The targets were annealed and somewhat softer ($Y_t \sim 10 \times 10^8 \text{ dyne/cm}^2$) than the rods ($Y_t \sim 20 \times 10^8 \text{ dyne/cm}^2$). For the lowest striking speed used, $\dot{S}_0 = .050 \text{ mm}/\mu\text{s}$, compression of the rod nose is barely perceptible and there is only a shallow dimple, .06 mm deep, in the target face shown at the right. As the striking speed increases, the recovered rod appears shorter and fatter and the crater depth gradually increases. A round head backed by a flare appears on the rod nose, until, by $\dot{S}_0 = .689 \text{ mm}/\mu\text{s}$, the rod has been turned into a mushroom cap. At this speed, the crater in the target is still only 6 mm deep, so the projectile was easily recovered. For the highest striking speed shown, $\dot{S}_0 = .893 \text{ mm}/\mu\text{s}$, the crater is 17 mm deep and the target must be sectioned in order to examine the remains of the rod, as shown in the final picture. Part of the rod has become a hollow tube which lines the crater wall, while the rest fills the bottom of the hole. Recall Fig. 4.4 above for the condition of the rod after impact at still higher speeds.

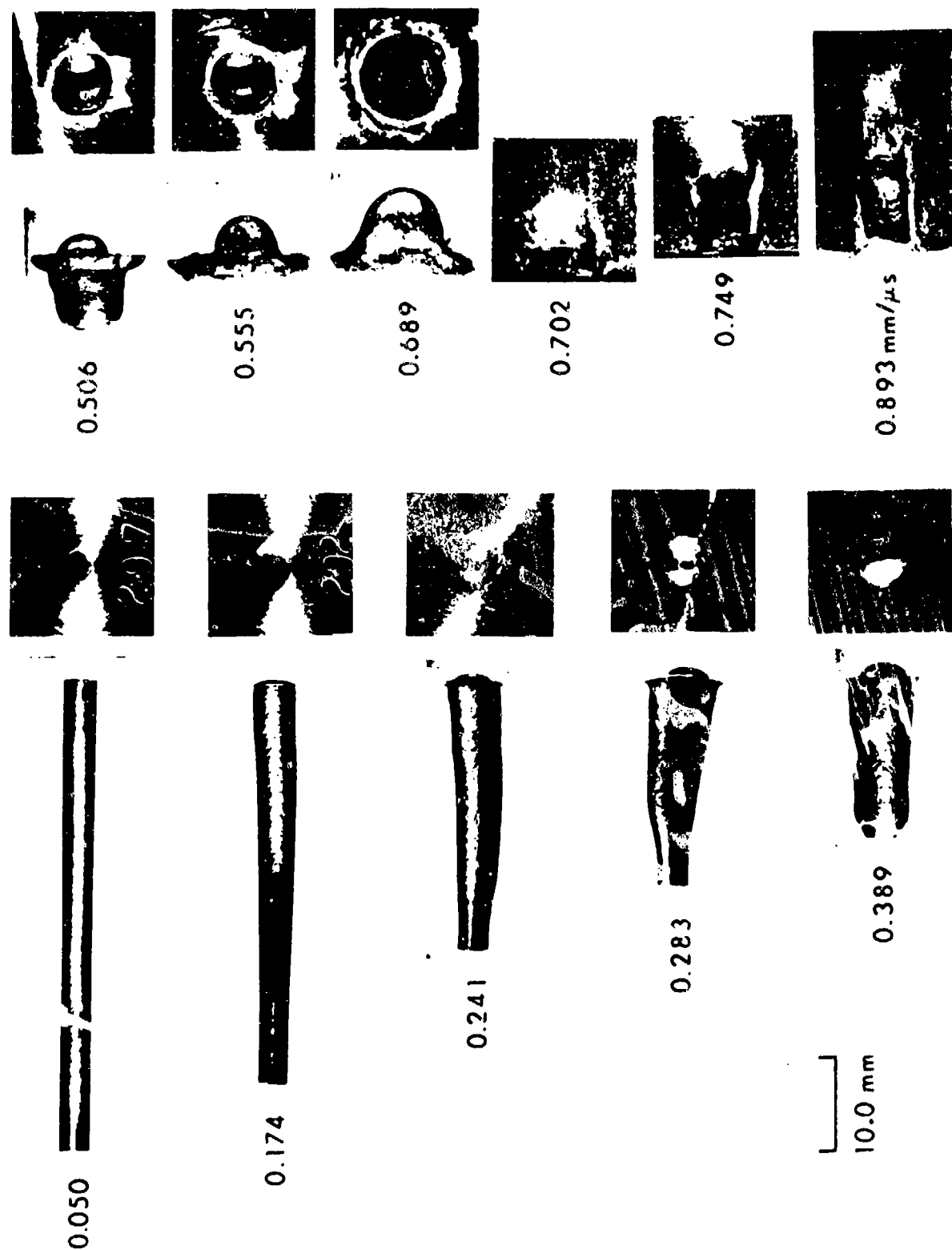


Fig. 4.35. Deformed Copper Rods Recovered after Impacting Copper Targets.

Fig. 4.37 (4.31) shows a similar sequence of photographs of the same rod recovered after striking a very hard steel target (steel RHF11, $Y_t \sim 200 \times 10^8 \text{ dyne/cm}^2$) an order of magnitude harder than the rod. For $\dot{S}_0 = .05 \text{ mm}/\mu\text{s}$, the target dimple depth was too shallow to be measured. For $\dot{S}_0 = .461 \text{ mm}/\mu\text{s}$, the depth was only .065 mm, about the same as for the copper target when $\dot{S}_0 = .050 \text{ mm}/\mu\text{s}$. For \dot{S}_0 about .4 mm/ μs , the rod nose petals and the projectile can be said to splatter on the target face.

Fig. 4.38 (4.32) shows penetration depth versus striking speed for these copper rods against three types of target, annealed copper (which has already been described), hard aluminum ($Y_t \sim 45 \times 10^8 \text{ dyne/cm}^2$) and a steel which is still harder, but much softer ($Y_t \sim 180 \text{ dyne/cm}^2$) than the RHF11 steel used in Fig. 4.35. At the lowest speed used against this (St 50) steel target, namely, $\dot{S}_0 = .22 \text{ mm}/\mu\text{s}$, the crater depth was .038 mm compared to .014 mm in the very hard steel target (4.33).

Copper rods are not generally used in practical applications. However, they provide an example of a very weak, ductile penetrator material of medium density which can be compared with penetrator materials we have already examined, such as aluminum, steel and tungsten (of low, medium and high density, but much stronger than the copper used here, which is more comparable to lead, commonly used for bullets). Copper is also widely used to form shaped charge jets, so long rods made of copper can provide some basis for comparison there as well. Fig. 4.38 gives us a good example at low speeds of the importance of target strength versus target density. If target density were the only important factor, then the penetration curve for the copper target ought to lie below the curves for steel and aluminum, instead of above. The copper target material is so weak, however, that its greater density does not compensate for its lack of strength. We have already seen another example not quite as extreme as this. The hard (2014) aluminum target in Fig. 3.12 above does about as well against a tungsten sphere as the much softer lead target up to at least $\dot{S}_0 = 3 \text{ mm}/\mu\text{s}$, in spite of the relatively low density of aluminum.

Once more, we are dealing with a rod material for which we have no measurements we can use to estimate an erosion rate. If we follow the same procedure we used for tungsten rods, we estimate μ_0 to be .059, .032 and .055 g/mm for the copper, aluminum and steel targets respectively. Since $M_0 = 3.8 \text{ g}$, the high speed-limit penetration, M_0/μ_0 , is 64.4, 119 and 69 mm

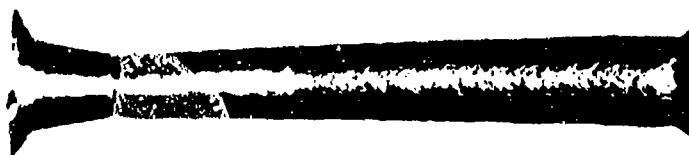
0.047



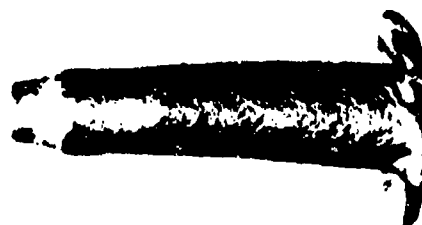
0.125



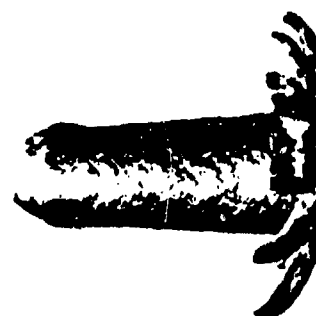
0.145



0.235



0.380



0.461 mm/μs



Fig. 4.37. Deformed Copper Rods Recovered after Impacting a Very Hard Steel Target.

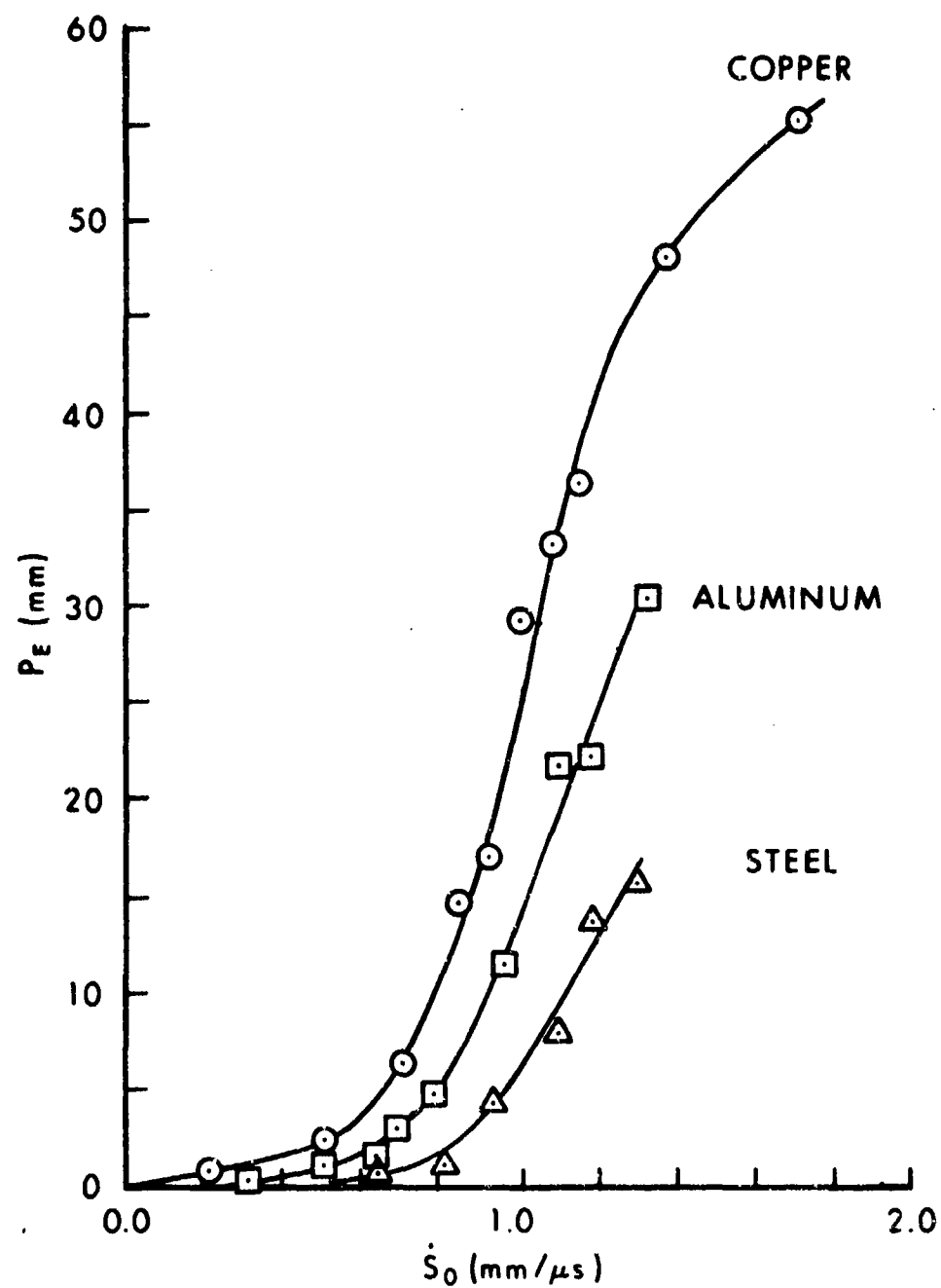


Fig. 4.38. Copper rods ($M_0 = 3.8\text{g}$, $L_0/D_0 = 20$) versus copper, aluminum and steel targets.

respectively. These values are only about 8% higher than the hydrodynamic limits. The first value seems reasonable in view of the bending of the copper curve in Fig. 4.38. However, the highest speeds used for the aluminum and steel targets were too low to indicate bending of the curves. The three values of M_0/μ_0 increase as the density decreases, following the $1/\sqrt{\rho_t}$ rule in Eq (4.8). Thus, we expect the curves in Fig. 4.38 to cross at higher speeds. However, we have no experimental information on this point.

If we use the parameters already given, together with the flattening curves in Fig. 4.39 in Eq (4.1), we calculate the penetration curves in Fig. 4.38. Again, the influence of target strength is evident in Fig. 4.39 since the copper target flattens the rod less than the other targets in spite of its greater density. The relative flattening by copper and steel agrees with the trend in Figs. 4.36 and 4.37 as well. However, the steel used in Figs. 4.38 and 4.39 is much softer than that in Fig. 4.37 and does not petal and splatter the rod as the very hard steel target does. Still, the (A/A_0) value for steel near $\dot{S}_0 = 0.9$ mm/ μ s is about 16, so the mushroom cap diameter is about 4 times the original rod diameter, compared to only 3 times for the copper target at this speed. The latter value agrees with the last photograph in Fig. 4.36.

D. Finite Target Examples

1. Steel/Steel

Compared to studies of penetration into semi-infinite targets, there are relatively few examples of target perforation in the open literature, which contain enough data above the ballistic limit that the shape of residual speed or residual mass curves can be determined as a function of striking speed. Consequently, this section will be much shorter than the previous section.

Fig. 4.40 shows a series of superimposed X-ray photographs of a 7.73 g steel rod (BHN = 555 kg/mm², $L_0/D_0 = 50$ mm/5 mm = 10) perforating an armor steel plate (BHN = 400 kg/mm², $T_0 = 6.35$ mm), reported by Herr and Grabarek (4.34). The striking speed was 1.657 mm/ μ s, the highest speed in Fig. 4.41. From the latter figure we see that both the residual speed and the residual mass increase as striking speed increases above the ballistic limit. From Fig. 4.40 it is clear that there is a lot of debris around the penetrator as

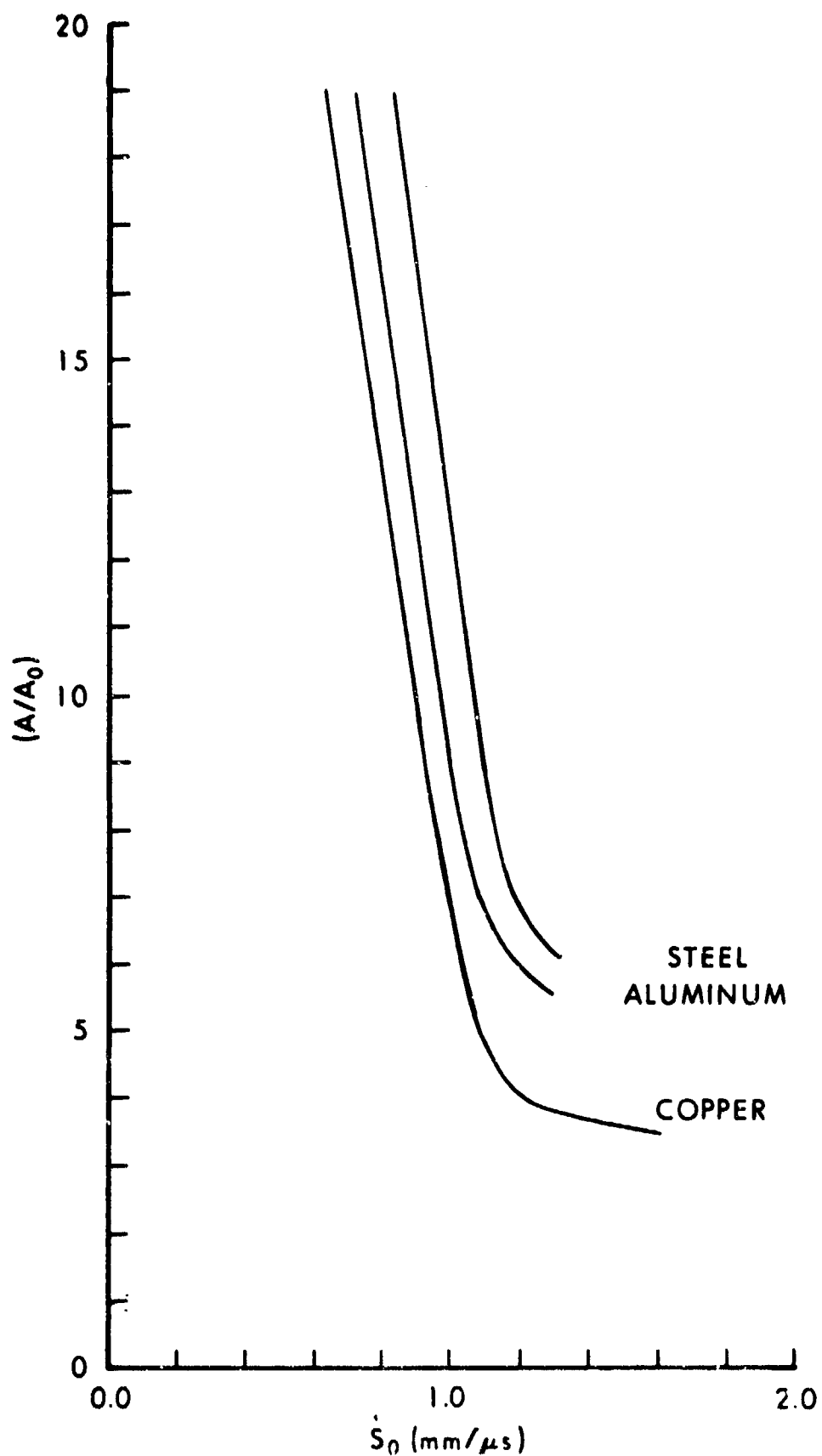


Fig. 4.39. Flattening factors for $L_0/D_0 = 20$, copper rods versus copper, aluminum and steel.

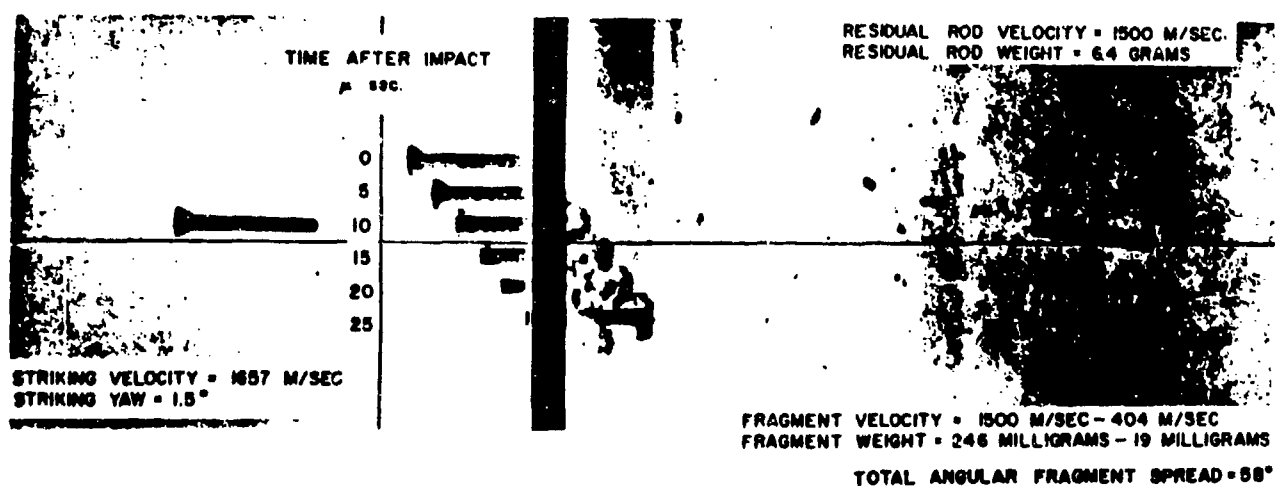
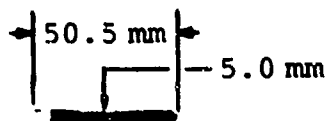


Fig. 4.40. 7.78 gram Bearcat Rod, BHN 555, $L/d \approx 10$, perforating 6.35mm RH Steel Armor, BHN 400, at normal obliquity.



STRIKING VELOCITY (m/s)	678	719	803	969	1657
RESIDUAL VELOCITY (m/s)	308	369	556	826	1518
IMPACT YAW (°)	1.5	2.6	1.5	2.1	1.4
<u>RESIDUAL WEIGHT</u> <u>ORIGINAL WEIGHT</u>	0.56	0.61	0.73	0.78	0.82
<u>RESIDUAL LENGTH</u> <u>ORIGINAL LENGTH</u>	0.59	0.61	0.74	0.78	0.81

Fig. 4.41. 7.78 gram Bearcat steel rod, GHN 555, L/d = 10, perforating 6.35mm RH Steel Armor, BHN 400, at 0° obliquity.

it exits from the back of the target. This is not surprising, if we recall our discussion of breakout effects in Chapter III, especially the crater formed at the back of the target, illustrated in Fig. 3.17. Herr and Grabarek report that just above the ballistic limit an intact plug is visible. In the case we are considering, this plug has a diameter about 1.75 times the original rod diameter, a thickness equal to 0.65 times the plate thickness, and a mass near 25% of the original rod mass for the 6.35 mm target, or twice this mass for a 12.7 mm thick plate. As the impact speed increases above the ballistic limit, this plug begins to break up. Well above the ballistic limit, it shatters into small pieces, as illustrated in the far right picture in Fig. 4.40. The shape of the debris cloud around the penetrator nose in the pictures at the center of Fig. 4.40 suggests that the mushroom cap formed at impact is suddenly released from lateral target confinement when the plug forms and the target fails. For a high speed impact such as the one illustrated, it is not possible to distinguish shattered target plug material from eroding rod nose material. However, a careful inspection of the length of the rod in the last few pictures at the center of Fig. 4.40 suggests that the rod continues to lose mass after it has pierced the plate. This is not unexpected, since the shocked nose material is still pushing against the remnants of the shattered plug, at least for a short time. Just above the ballistic limit, the shocked nose is pushing against a massive, intact plug for a longer time, since the exit speed is lower. Consequently, we expect more mass loss after perforation at lower impact speeds than at higher impact speeds, as observed.

The residual speed and residual mass data shown in Fig. 4.41 for the 6.35 mm thick plate have been plotted in Figs. 4.42 and 4.43. Similar data for a target plate twice as thick were also reported and are included in these figures. The reported velocity ballistic limits are also included in Fig. 4.42. Obviously, more data points at other speeds would help delineate the shapes of these curves. However, we must make do with the data available, which is the best there is. At least trends are evident which are beyond the uncertainties of the experiments.

Now let us examine an explanation which is consistent with these observations. We expect to be able to use Eq (2.20) to calculate the residual speed, \dot{S}_R . This speed was measured using two X-ray flashes at distances far enough behind the target plate that all parts of the rod are travelling at the

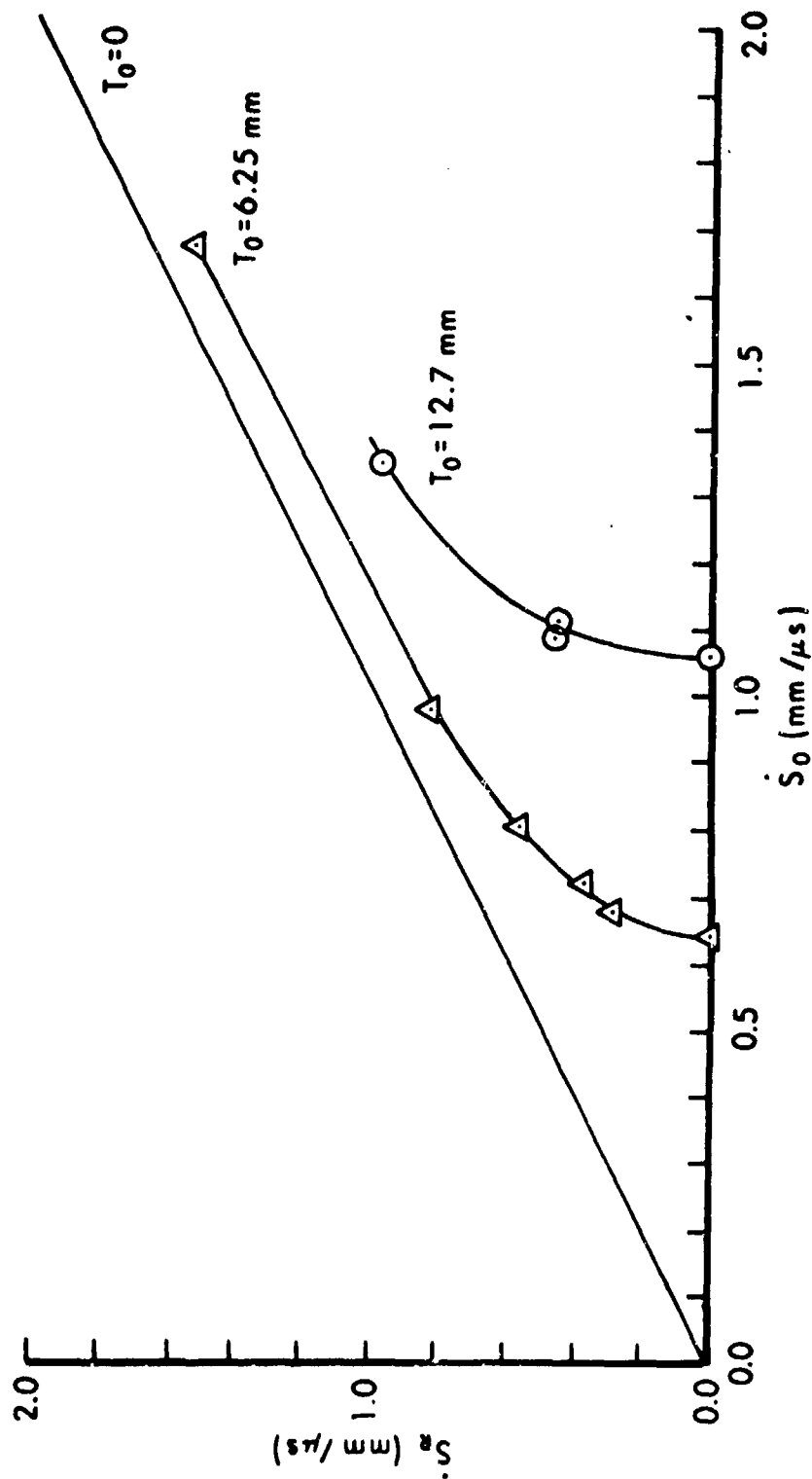


Fig. 4.42. Residual speed of steel rods ($M_0 = 7.78$ g, $L_0/D_0 = 10$) perforating armor steel target plates ($T_0 = 6.35$ and 12.7mm).

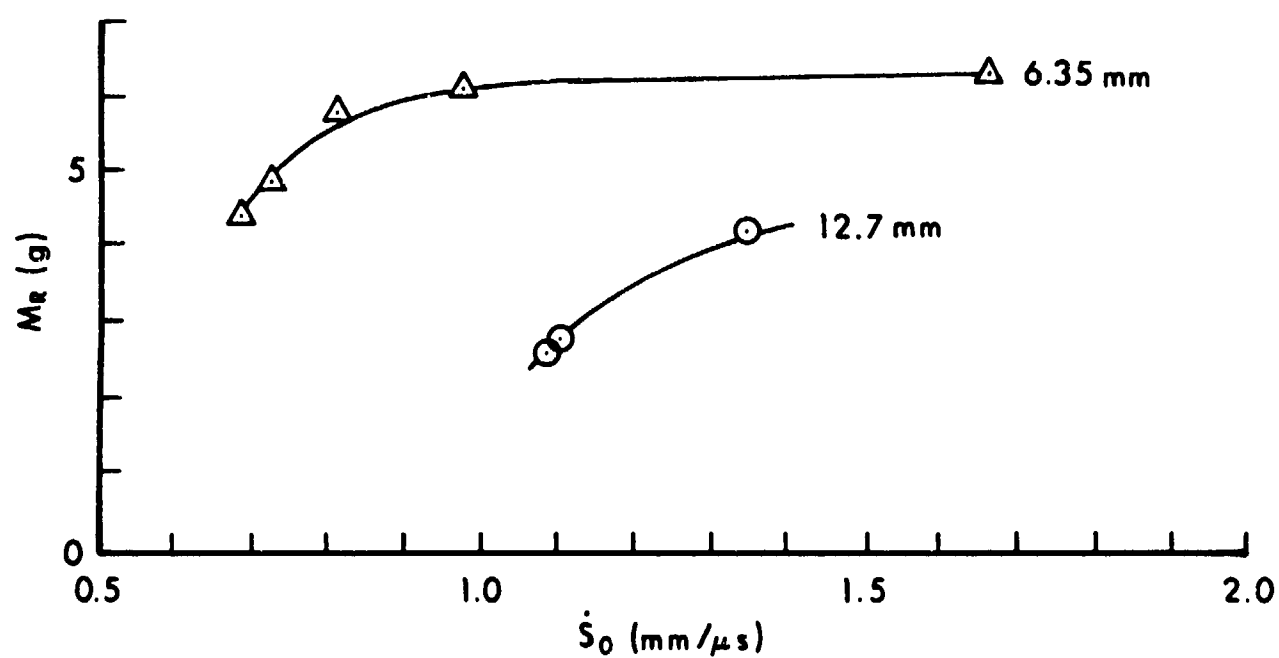


Fig. 4.43. Residual mass of steel rods ($M_0 = 7.78\text{g}$, $L_0/D_0 = 10$) perforating armor steel target plates ($T_0 = 6.35$ and 12.7mm).

same speed, the residual speed of the center of mass, $\dot{S}_R = k\dot{P}_R$, where \dot{P}_R is the penetration speed at the moment of target failure. Consequently, we can re-write Eq (2.20) as

$$\dot{S}_R = \sqrt{[\zeta^2 + \dot{S}_O^2] (M_R/M_O)^{1/\epsilon} - \zeta^2} \quad (4.42)$$

where $\zeta = k\sqrt{a/\bar{c}}$ and $\epsilon = .5\mu_O k/\bar{c}$ as before, and

$$M_R/M_O = 1 - (\mu_O/M_O) T \quad (4.43)$$

from Eq (2.15) with $P = T$ at breakout. We can estimate μ_O from mass per unit length considerations as usual, using 0.156 g/mm estimated above for Hohler and Stilp's 9.85 g, $L_O/D_O = 10$ rod with $M_O/L_O = .1824$ g/mm. Here Herr and Grabarek's rod has $M_O/L_O = .154$ g/mm, so $\mu_O = .132$ g/mm. Similarly, we find $I_O = 3.185$ mm for this 7.78 g rod. Since the target hardness is BHN = 400 kg/mm² or $Y_t = 120 \times 10^8$ dyne/cm², we find $a_O = .072$ g mm/ μs^2 and $c_O = .0785$ g/mm for the rod. Our estimate of μ_O gives us $k = 1 + I_O\mu_O = 1.42$, while an estimate of (A/A_O) for given \dot{S}_O will give us $a = a_O (A/A_O)$ and $\bar{c} = c_O (A/A_O) - I_O\mu_O^2$. The only parameter we need is T in Eq (4.43).

First, let us consider the 12.7 mm plate. Just above the ballistic limit a plug was seen with thickness $0.65 T_O \approx 8.2$ mm. This implies that the target failed when $T = 0.35 T_O \approx 4.5$ mm = P . Since $(\mu_O/M_O) \approx .017$ mm⁻¹ in Eq (4.43), then $M_R/M_O \approx .92$ at this moment. In order to estimate (A/A_O) versus \dot{S}_O , we turn to the curve labelled $L_O/D_O = 10$ in Fig. 4.16 above. This appears as the upper curve in Fig. 4.44 labelled 12.7 mm. Here we are assuming that the 12.7 mm thick plate is thick enough to produce a time average area, A , about the same as a semi-infinite target, at least in the speed range of interest here, which is above 1 mm/ μs . Thus, for example, (A/A_O) is about 7 for the ballistic limit reported, $\dot{S}_O = 1.06$ mm/ μs . This gives $a = .504$ g mm/ μs^2 , $c = .549$ g/mm, $\bar{c} = .493$ g/mm, $\zeta = 1.43$ mm/ μs and $\epsilon = .19$. Eq (4.42) becomes

$$\dot{S}_R = \sqrt{[(1.43)^2 + (1.06)^2] (.92)^{1/.19} - (1.43)^2} = 0. \quad (4.44)$$

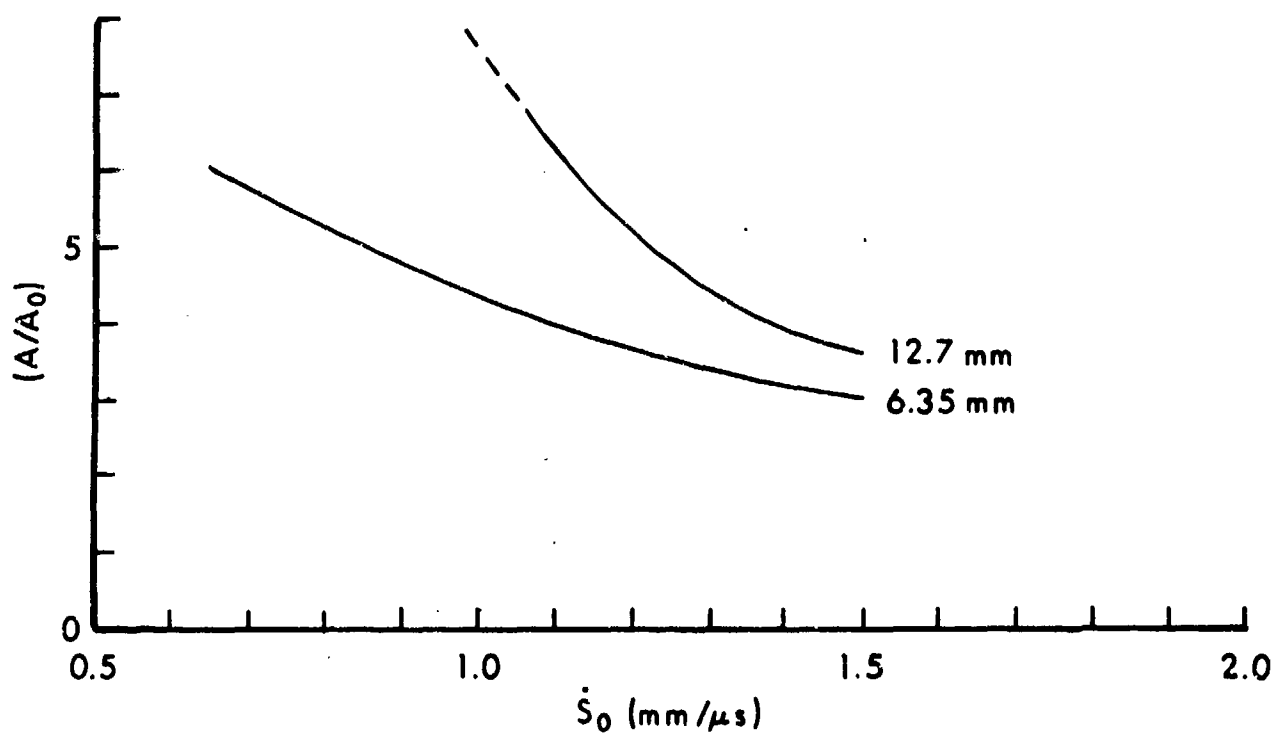


Fig. 4.44. Flattening factors for $L_0/D_0 = 10$ steel rod versus armor steel plates of two different thicknesses.

Similarly for $\dot{S}_0 = 1.1 \text{ mm}/\mu\text{s}$, we have (A/A_0) near 6 so $\zeta = 1.45 \text{ mm}/\mu\text{s}$ and $\epsilon = .22$, so

$$\dot{S}_R = \sqrt{[(1.45)^2 + (1.1)^2] (.92)^{1/.22} - (1.45)^2} = .45 \text{ mm}/\mu\text{s} \quad (4.45)$$

Likewise, for $\dot{S}_0 = 1.34 \text{ mm}/\mu\text{s}$, we have $(A/A_0) \approx 4$, so $\zeta = 1.5 \text{ mm}/\mu\text{s}$, $\epsilon = .36$, and

$$\dot{S}_R = \sqrt{[(1.50)^2 + (1.34)^2] (.92)^{1/.36} - (1.50)^2} = .98 \text{ mm}/\mu\text{s}. \quad (4.46)$$

These values are all in reasonable agreement with experiment as can be seen from Fig. 4.42. For still higher speeds, we expect (A/A_0) to approach 2.4 as in Fig. 4.16 so that $\zeta \rightarrow 1.6 \text{ mm}/\mu\text{s}$ and $\epsilon \rightarrow 0.7$. Since ζ^2 and $(M_R/M_0)^{1/\epsilon}$ reach fixed, finite values above $\dot{S}_0 = 2.5 \text{ mm}/\mu\text{s}$, then $\dot{S}_R \rightarrow \dot{S}_0$ in Eq (4.42) as \dot{S}_0 increases without limit. This means an approach to the straight line in Fig. 4.42 marked $T_0 = 0$ for which $\dot{S}_R = \dot{S}_0$, as in the case of no target at all. In other words, at sufficiently high impact speeds, the rod loses little speed. However, it should continue to lose 8% of its mass before target failure, being reduced to 7.2 g at that moment. In addition, it will probably lose up to a gram more after target failure as the shocked nose continues to interact with the shattered plug.

Next, let us consider the 6.35 mm plate. The plug thickness was about $0.65 T_0 \approx 4.15 \text{ mm}$ just above the ballistic limit, implying target failure for $P = T = 0.35 T_0 = 2.2 \text{ mm}$. With $(\mu_0/M_0) \approx .017 \text{ mm}^{-1}$ as before in Eq (4.43), we find $M_R/M_0 = .96$ when the target fails, implying a residual mass near 7.5 g at this time. Since this target fails earlier than the thicker target, we might expect that the time average area, A , at any impact speed in the range of interest should be smaller. In other words, there is not enough time to flatten the nose as much as a thicker target does. If we use the lower curve in Fig. 4.44 for this thinner target, then we can calculate the upper curve in Fig. 4.42 in agreement with experiment. For example, at the reported ballistic limit, $\dot{S}_0 = .65 \text{ mm}/\mu\text{s}$, we find (A/A_0) near 6, so

$$\dot{S}_R = \sqrt{[(1.45)^2 + (.65)^2] (.96)^{1/.22} - (1.45)^2} = 0 \quad (4.47)$$

Similarly, for $\dot{S}_0 = 1.5 \text{ mm}/\mu\text{s}$, we find $(A/A_0) = 3$, so

$$\dot{S}_R = \sqrt{[(1.56)^2 + (1.5)^2] (.96)^{1/.53} - (1.56)^2} = 1.38 \text{ mm}/\mu\text{s} \quad (4.48)$$

with intermediate values for intermediate speeds. Again, there is reasonable agreement with experiment.

As we reduce the target thickness to zero ($T_0 \rightarrow 0$) then $T \rightarrow 0$ in Eq (4.43) and $M_R/M_0 \rightarrow 1$ in Eq (4.42) so $\dot{S}_R = \dot{S}_0$, the straight line in Fig. 4.42.

Thus we are able to calculate residual speed versus striking speed curves with this model. However, Eq (4.43) only gives us the residual mass when target failure occurs, which is an upper limit on the residual mass, but is much larger than the residual mass observed at later times. Now let us try to estimate the residual mass at later times as a function of striking speed for these two target plates.

First, consider the 12.7 mm plate which for $\dot{S}_0 = 1.1 \text{ mm}/\mu\text{s}$ has a residual mass of $M_R \approx 2.8 \text{ g}$, implying a loss of about 5 grams. A rough estimate of the time to failure is $T/\dot{S}_0 = 4.5 \text{ mm}/1.1 \text{ mm}/\mu\text{s} = 4.1 \mu\text{s}$. A rough estimate of the total interaction time between the rod and the plate is $T_0/\dot{S}_0 = 12.7 \text{ mm}/1.1 \text{ mm}/\mu\text{s} = 11.5 \mu\text{s}$. The difference, $11.5 - 4.1 = 7.4 \mu\text{s}$, is an estimate of the interaction time between the rod and the plug. Suppose the deformation wave in the rod travelled from its nose to its rear at about $4 \text{ mm}/\mu\text{s}$. Then in $7.4 \mu\text{s}$ it has moved about 30 mm or 60% of the rod length. If all of this mass is lost by interacting with the plug, then only 40% or about 3 g remains, in rough agreement with Fig. 4.43. For $\dot{S}_0 = 1.34 \text{ mm}/\mu\text{s}$, $T/\dot{S}_0 = 4.5 \text{ mm}/1.34 \text{ mm}/\mu\text{s} = 3.35 \mu\text{s}$, while $T_0/\dot{S}_0 = 12.7 \text{ mm}/1.34 \text{ mm}/\mu\text{s} \sim 9.45 \mu\text{s}$, so the difference is $6.1 \mu\text{s}$, an estimate of the interaction time between rod and plug. At $4 \text{ mm}/\mu\text{s}$ in $6.1 \mu\text{s}$, about 25 mm or half the rod length will be affected during this time. If half the rod is lost then, half remains, or $M_R = 3.9 \text{ g}$ in rough agreement with Fig. 4.43. The broken state of the plug might reduce the erosion and increase the residual mass. The experimental data is very sparse and the statistics are inadequate. Because fracture is involved we expect fairly large experimental variations. At least this crude model can predict the trend of the experimental data.

Now consider the 6.35 mm plate. For $\dot{S}_0 = 0.7 \text{ mm}/\mu\text{s}$, an estimate of the total interaction time is $6.35 \text{ mm}/0.7 \text{ mm}/\mu\text{s} = 9.1 \mu\text{s}$, while an estimate of

the penetration time up to failure is $T/\dot{S}_0 = 2.2 \text{ mm}/0.7 \text{ mm}/\mu\text{s} = 3.1\mu\text{s}$, giving about $6\mu\text{s}$ for interaction between the shocked rod and the intact plug. Now suppose the deformation wave speed is a bit less at this lower striking speed. If it moves at about $3.5 \text{ mm}/\mu\text{s}$ for $6\mu\text{s}$, then 21 mm or 42% of the rod will be affected. If all of this mass is lost, then about 58% will remain, giving $M_R = 4.5 \text{ g}$ in rough agreement with experiment. Similarly, for $\dot{S}_0 = 1.0 \text{ mm}/\mu\text{s}$ we have $(6.35 - 2.2) \approx 4.15\mu\text{s}$ for the rod/plug interaction time. If the speed is still $3.5 \text{ mm}/\mu\text{s}$, then about 14 mm or 28% of the rod will be affected, so 72% or $M_R = 5.6 \text{ g}$ will remain. This estimate is low since M_R is observed to be closer to 6 g . Perhaps plug breakup reduces the interaction time with less mass loss. For $\dot{S}_0 = 1.5 \text{ mm}/\mu\text{s}$ we have $(4.2 - 1.4) = 2.8\mu\text{s}$ for the time, and at $3.5 \text{ mm}/\mu\text{s}$, about 10 mm or 20% of the rod will be lost so 80% will remain or $M_R = .8(7.78 \text{ g}) \approx 6.25 \text{ g}$, in agreement with observation. In these estimates we have assumed a lower deformation wave speed resulting from impact on a thinner target. We have no evidence for this, but it is not unreasonable.

Admittedly, our method of estimating residual mass is crude. However, before attempting a more elaborate model, we should first determine experimentally that this is indeed the way in which most mass is lost when such a rod perforates such plates. Much better statistical observations of plug and rod over a wider range of striking speed would be helpful. A more elaborate model is premature in the absence of such information.

It is encouraging that we can calculate the curves in Fig. 4.42 while using a single value of μ_0 , the same as we would use for a semi-infinite target, a single value of $T = .35 T_0$, in agreement with observations, and reasonable values of (A/A_0) , in fact, about the same values as for a semi-infinite target in the case of the thicker plate ($T_0 > 2D_0$, $T \sim D_0$). Correct values of target hardness and target and projectile density and geometry were, of course, also used. However, we would need a greater variety of observations in order to eliminate alternate explanations. As mentioned above, one such alternate explanation might be to have μ_0 vary with impact speed. For example, if $T = T_0 = 6.35 \text{ mm}$ in Eq (4.43), then $\mu_0 = (7.8 - M_R)/6.35$ must be 0.5 g/mm for $\dot{S}_0 = .7 \text{ mm}/\mu\text{s}$, 0.27 g/mm for $\dot{S}_0 = 1.0 \text{ mm}/\mu\text{s}$ and 0.24 g/mm for $\dot{S}_0 = 1.5 \text{ mm}/\mu\text{s}$. The flattening factor would also have to be different under this assumption that the original target thickness

should be used in Eq (4.43) and not some fraction of it. Since μ_o is three or four times larger than in our previous explanation, then $\bar{c} = c - I_o \mu_o^2$ will be negative, but not so negative as to make F negative in Eq (2.17) and lead to the unphysical prediction of acceleration rather than deceleration. There is no mathematical difficulty or basic physical objection to this explanation. However, it does not seem to fit as well into the complete picture of penetration we are trying to construct. Only experiment can decide this question. Until more information is available, we will not elaborate on such alternative explanations.

The uppermost curves in Figs. 4.45 and 4.46 are the same as the upper curves in Figs. 4.42 and 4.43. The lowest curves in Figs. 4.45 and 4.46 were also reported by Herr and Grabarek for a smaller 1.94 g,

$L_o/D_o = 32 \text{ mm}/3.2 \text{ mm} = 10$ rod of the same steel attacking the same 6.35 mm thick plate. Intermediate curves are for a 3.89 g, $L_o/D_o = 40 \text{ mm}/4 \text{ mm} = 10$ rod. The number of data points is minimal, but at least the observed trends agree with expectations. The ballistic limit reported for the 3.89 g rod seems a bit high and distorts the shape of the curve in Fig. 4.45 compared to the other two curves. As has been mentioned, ballistic limits are notoriously difficult to determine and require a large number of experiments in order to find a satisfactory average value.

Herr and Grabarek report that the plug driven out of the target by the 1.94 g rod was smaller than that driven out by the 7.78 g rod. In particular, it was thinner, with thickness about $0.4 T_o$, which implies $T = 0.6 T_o = 0.6 (6.35 \text{ mm}) = 3.81 \text{ mm}$ in the present case. By the usual procedure we find $\mu_o = .052 \text{ g/mm}$ for this rod and $M_R/M_o = 0.90$ from Eq (4.43). Since $A_o = .08 \text{ cm}^2$, $a_o = .0288 \text{ g mm}/\mu\text{s}^2$, $c_o = .0314 \text{ g/mm}$, $I_o = 7.96 \text{ mm/g}$ and $k = 1.41$. Then for $\dot{S}_o = 0.9 \text{ mm}/\mu\text{s}$, the reported ballistic limit, and $A/A_o = 4.2$, we find

$$\dot{S}_R = \sqrt{[(1.476)^2 + (.9)^2] (.9)^{1/.332} - (1.476)^2} = 0 \quad (4.49)$$

Similarly if $(A/A_o) = 3$ for $\dot{S}_o = 1.2 \text{ mm}/\mu\text{s}$,

$$\dot{S}_R = \sqrt{[(1.537)^2 + (1.2)^2] (.9)^{1/.505} - (1.537)^2} = .85 \text{ mm}/\mu\text{s} \quad (4.50)$$

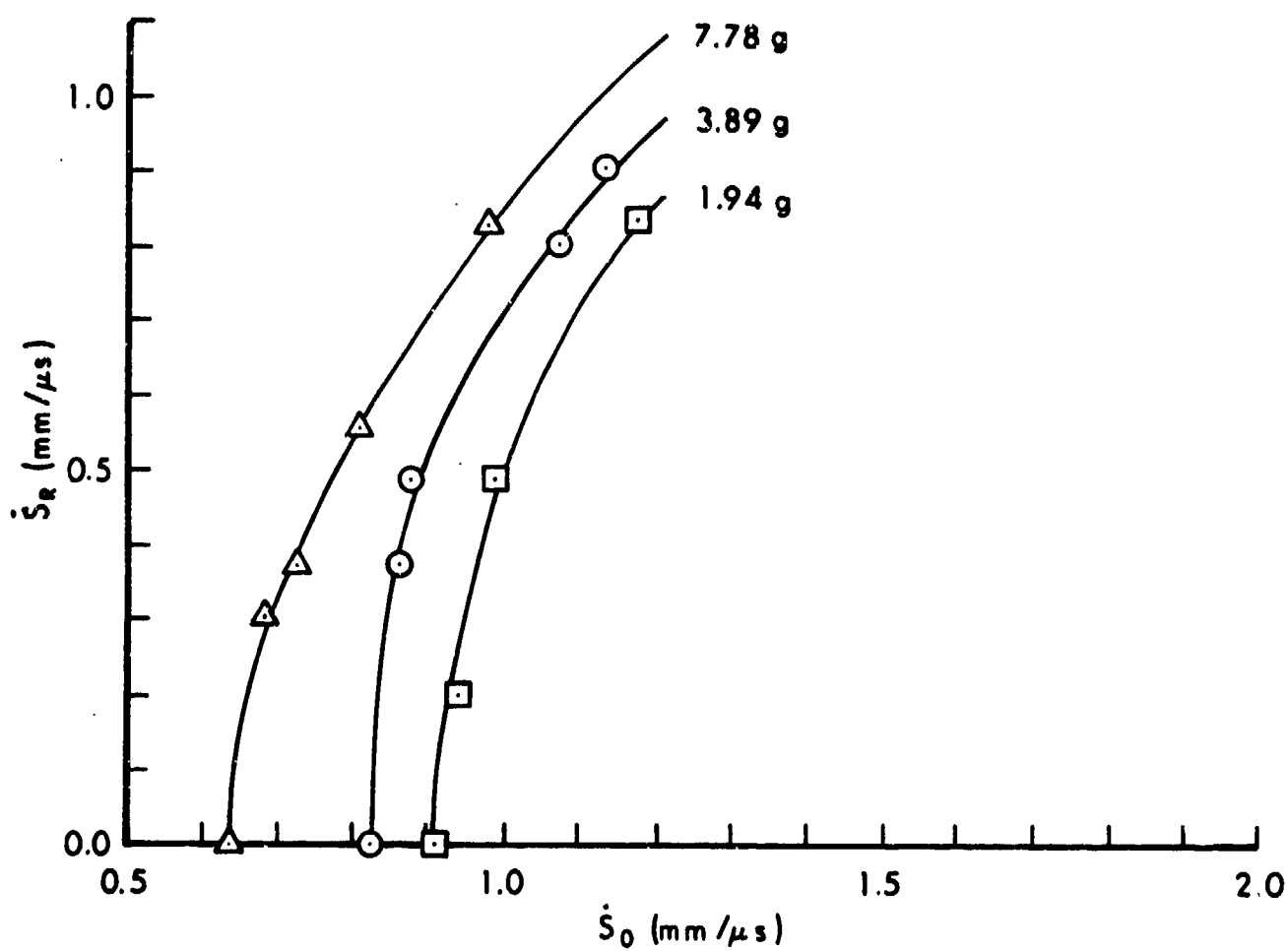


Fig. 4.45. Residual speed of $L_0/D_0 = 10$ steel rods of three masses perforating a 6.35mm armor steel plate.

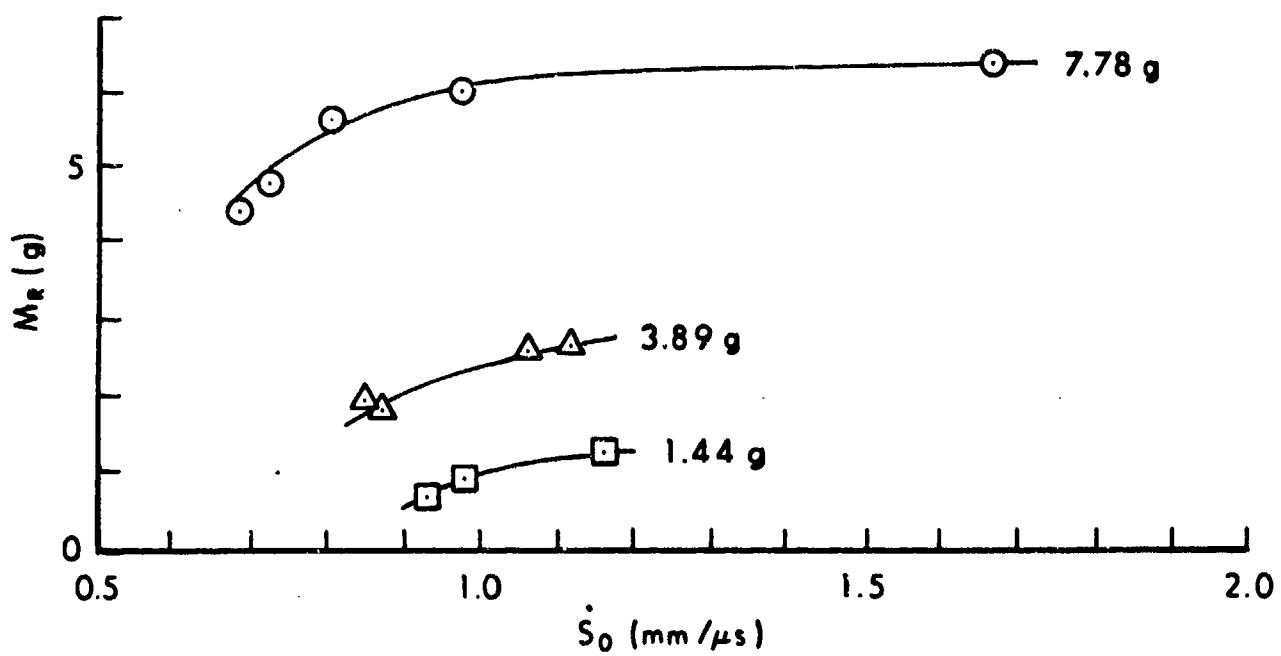


Fig. 4.46. Residual masses of $L_0/D_0 = 10$ steel rods of three masses after perforating a 6.35mm armor steel plate.

with intermediate values for intermediate striking speeds. We note that the values of (A/A_0) being used here are slightly smaller than those marked 6.35 mm in Fig. 4.44. It is difficult to say that this difference is real in view of the experimental and theoretical uncertainties involved. Perhaps there should be a single (A/A_0) curve for geometrically similar rods versus the same target plate.

In order to estimate the residual mass of the 1.94 g rod in Fig. 4.46 we note that about 10% or .19 g is lost before target failure. Near $\dot{S}_0 = 1 \text{ mm}/\mu\text{s}$, this occurs in about 3.8 μs . If the interaction time with the plug is about the same and the deformation wave speed is 3.5 mm/ μs as before, then about 13.3 mm (41%) or about .8 g is lost after target failure, for a total loss of .94 g. Thus the remaining mass should be nearly one gram. For $\dot{S}_0 = 1.2 \text{ mm}/\mu\text{s}$, .19 g is lost before failure in about 3.8 mm/1.2 mm/ μs = 3.17 μs . If this is also an estimate of the plug interaction time and the wave speed is unchanged, then about 11 mm or .67 g more is lost after failure for a total of .86 g lost, giving $M_R \approx 1.1 \text{ g}$. Both the experimental and calculated values are uncertain, but at least the values and trends agree approximately.

Herr and Grabarek also used aspect ratios of 5 and 20 as well as 10 for these rods versus these plates. There are indications in their data that crossovers may occur in both the residual speed and residual mass versus impact speed curves. In other words, a rod with a greater aspect ratio may have a higher ballistic limit and lose more mass just above the ballistic limit than a rod with the same mass but lower aspect ratio. However, well above the ballistic limit, the situation may reverse, with the longer rod having a greater residual speed and residual mass. The data is too sparse and inconsistent to say for sure. Consequently, we will not attempt a quantitative description here.

In an earlier report, Grabarek ^(4.35) carried out similar rod/plate experiments using rods which were softer ($\text{BHN} \approx 270 \text{ kg/mm}^2$) than the targets as well as rods harder than the target such as we have been examining. He found that the ballistic limit was higher and the mass loss greater for the softer rods, although these differences tended to disappear well above the ballistic limit. It is certainly possible to use somewhat different μ_0 and (A/A_0) values in our theory and reproduce these trends. However, nothing was reported about possible differences in plug thickness. It seems preferable to await better experimental information before presenting more calculations.

Lambert (4.36) has also given data for long steel rods perforating armor steel plates 25.4 mm thick. However, there are very few data points for particular cases and the speed range investigated was quite restricted. Where trends are evident at all, they agree with what we have already seen from the work of Herr and Grabarek.

2. Tungsten/Steel

Herr and Grabarek (4.34) also used tungsten alloy rods ($\rho_p = 17 \text{ g/cm}^3$, $\text{BHN} = 250 \text{ kg/mm}^2$) of various aspect ratios and masses against the same steel targets plates as above. The tungsten rods were softer than the targets yet were brittle enough that they usually emerged from the rear of the target broken into two or more pieces. In most cases there were not enough data points to give a positive indication of trends. In general there was more scatter for the smaller masses, thicker plates and greater aspect ratios. Figs. 4.47 and 4.48 are for the heaviest, shortest rod and thinnest plate used. In Fig. 4.47 we have plotted the reported ballistic limit, $\dot{S}_0 = .52 \text{ mm/us}$ and five residual speeds for the five impacts in which the projectile was reported to emerge in one piece. When the projectile emerged broken, different residual speeds were reported for the different pieces. In one case, these speeds were almost a factor of two different, while in two other cases they were almost the same. In Fig. 4.48 we have plotted the unbroken residual masses as circles and the sums of the broken pieces as +'s. Below each + there is a B, indicating the mass of the bigger piece and an S, indicating the mass of the smaller piece. In one case these symbols are beside each other, since the pieces were of approximately equal size. A dashed line has also been drawn, indicating the possibility of a maximum residual mass. The existence of such a maximum rests on very slender evidence, namely, a single data point near $\dot{S}_0 = .75 \text{ mm/us}$. Without this point the dashed line would be approximately horizontal. Fig. 4.49 shows similar data for a 3.89 g rod which hints at the possible existence of a maximum. Again there is only a single unbroken projectile data point to support this possibility, aided by some broken projectile information. For longer aspect ratios (10 and 20) and the thicker target plate (for any mass or aspect ratio) there was no evidence of a maximum in M_R versus \dot{S}_0 . Instead the curves were flat or slightly rising, similar to Fig. 4.46 in some cases.

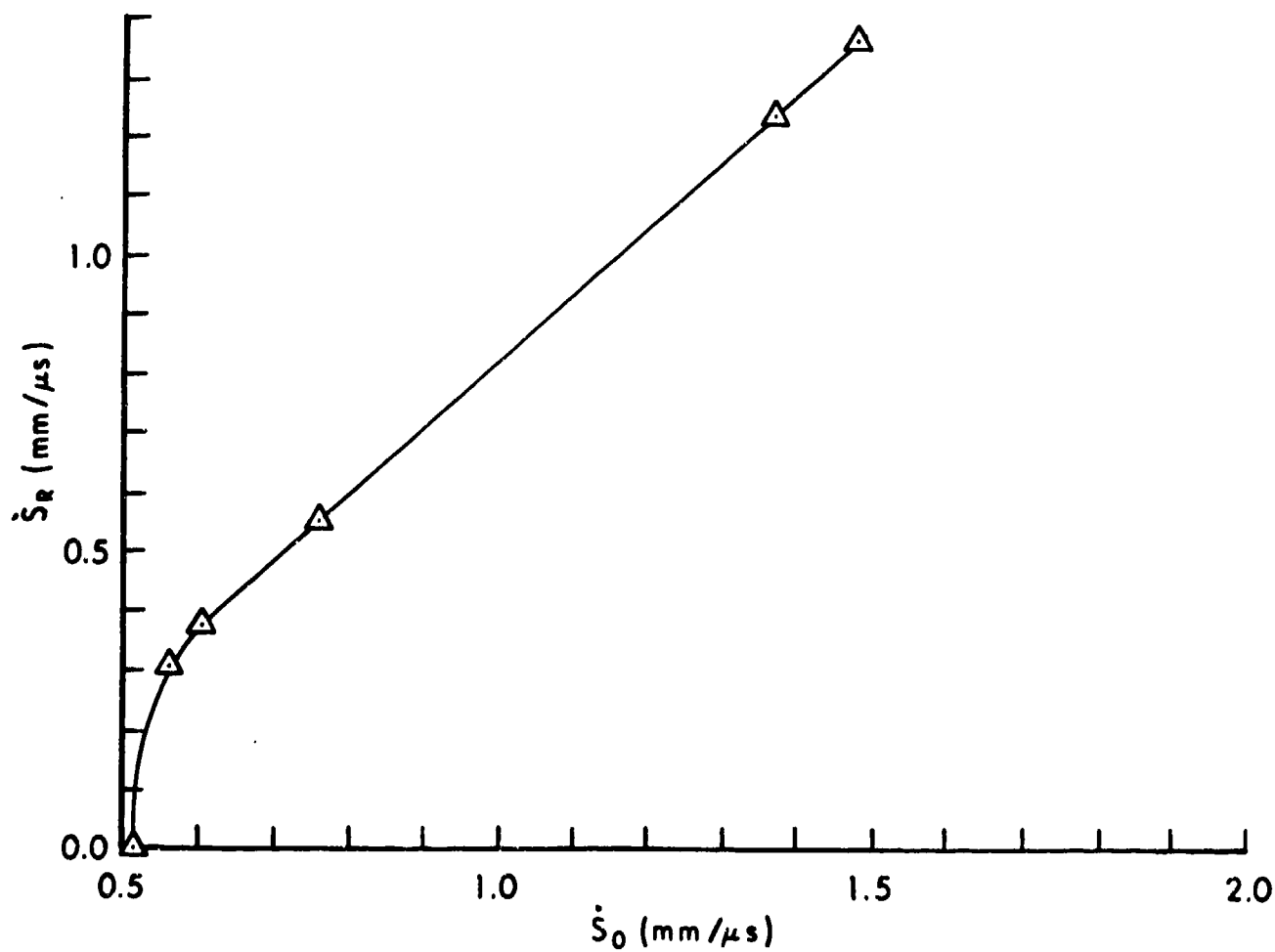


Fig. 4.47. Residual speed of 7.78g, $L_0/D_0 = 5$ tungsten rod after perforating a 6.35mm armor steel plate.

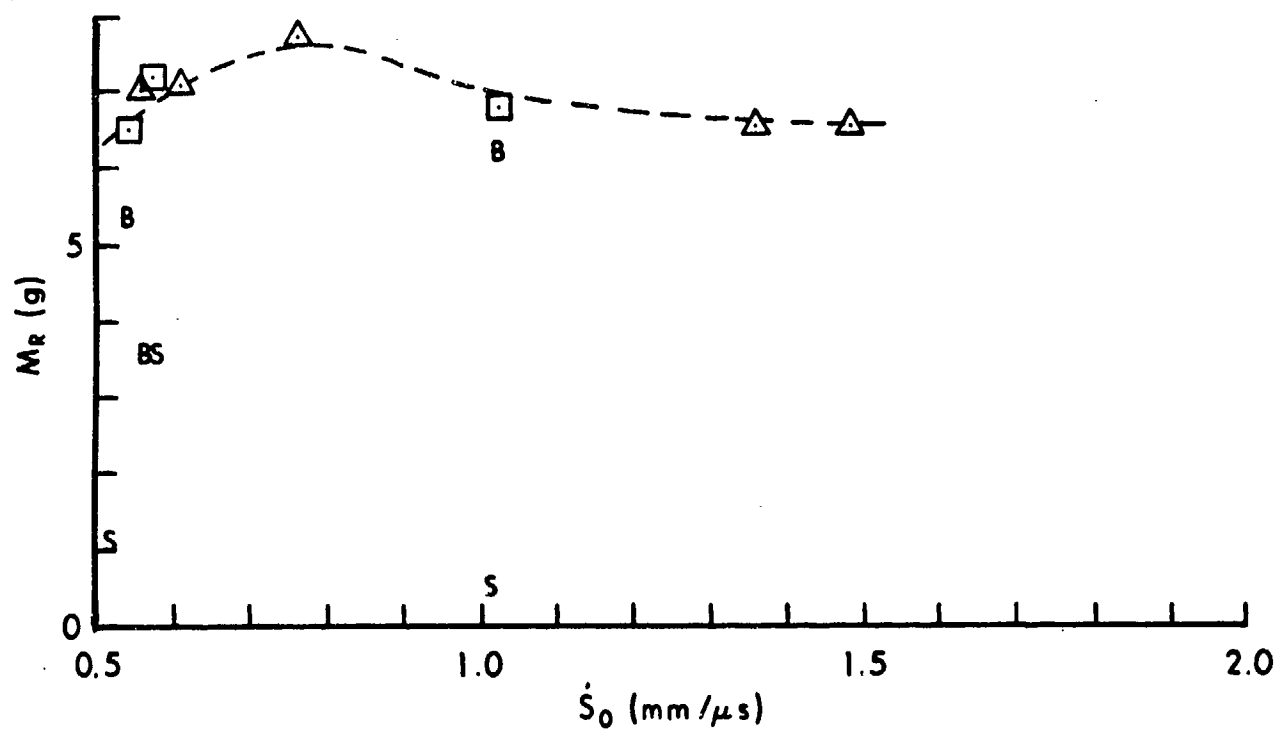


Fig. 4.48. Residual mass of 7.78g, $L_0/D_0 = 5$ tungsten rod after perforating a 6.35mm armor steel plate.

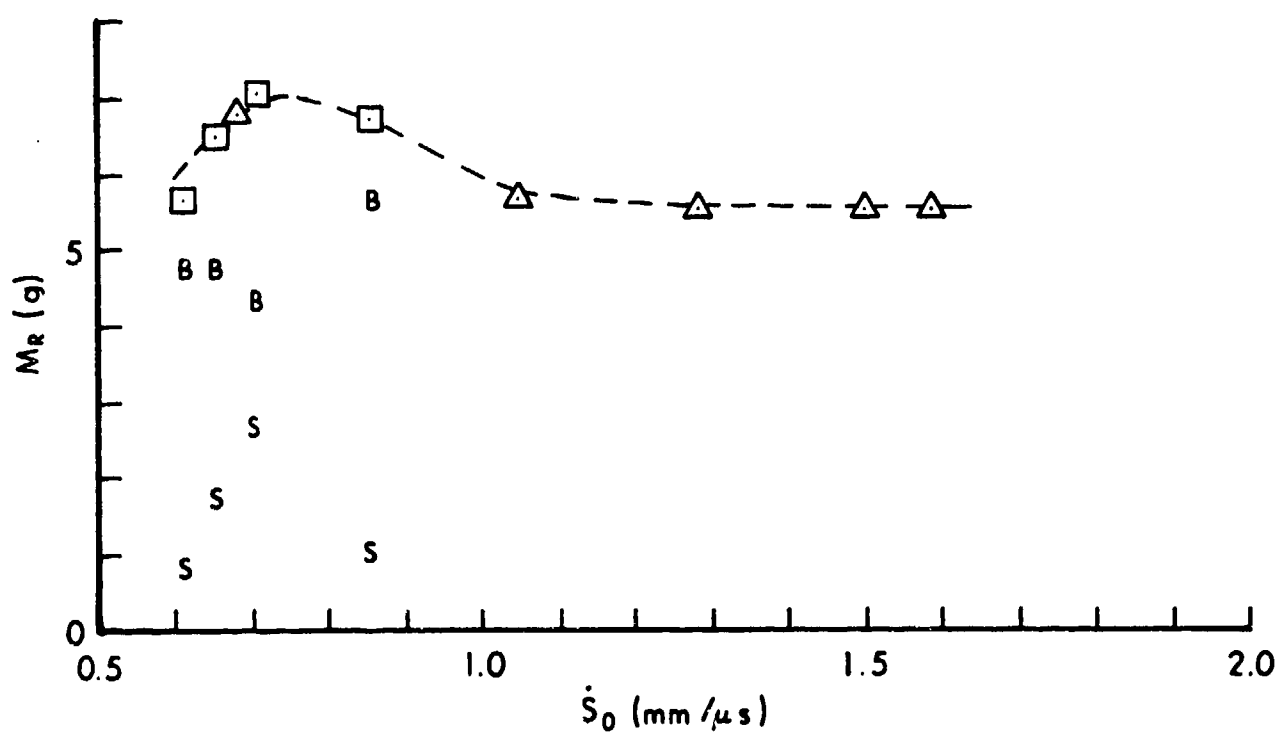


Fig. 4.49. Residual mass of 3.89g, $L_0/D_0 = 5$ tungsten rod after perforating a 6.35mm armor steel plate.

Let us speculate for a moment about a possible explanation for a maximum M_R , supposing that such a phenomenon exists. Our previous explanation for an increase in M_R as \dot{S}_0 increases just above the ballistic limit was a decrease in interaction time between the shocked rod nose and the plug after breakout. Herr and Grabarek's plug size measurements indicate that the plug breaks up and eventually shatters as impact speed increases, resulting in less mass being rubbed off the nose. The speed of identifiable plugs was generally the same as the projectile speed. The same explanation might apply to tungsten rods as well, except perhaps for short rods versus thin targets. In such cases the interference of shock waves might lead to nose shatter, similar to that encountered in semi-infinite targets. Here, however, instead of a decrease in penetration depth, we have an increase in mass loss over a certain impact speed range. If a short, dense, projectile has a lower shatter threshold than a less dense or longer one against a given target, then we might speculate about the possibility of a maximum occurring at a higher impact speed (say $\dot{S}_0 \sim 2 \text{ mm/s}$) in Figs. 4.43 or 4.46 (or similar figures for shorter rods). There is also a possibility of the onset of multiple scabbing and double plug interaction with the rod.

Finally, let us apply Eqs (4.42) and (4.43) to Fig. 4.47. We recall our estimates of μ_0 and (A/A_0) for Hohler and Stilp's ^(4.22) tungsten rods of various aspect ratios versus semi-infinite armor steel targets. Herr and Grabarek's rod in Fig. 4.47 is softer than theirs while the target is harder. In addition, the aspect ratio here is 5. For all these reasons we expect a somewhat larger erosion rate than we might estimate on the basis of mass per unit length alone. Here we will take $\mu_0 = .25 \text{ g/mm}$. We would also expect (A/A_0) to lie between the $L_0/D_0 = 1$ and $L_0/D_0 = 10$ curves in Fig. 4.33 for a semi-infinite target or a thick target. However, for a 6.35 mm target we expect (A/A_0) to be somewhat lower still. The flattening factor used in the present calculations is shown in Fig. 4.50 and meets these expectations. Since $I_0 = 1.47 \text{ mm/g}$, $a_0 = .072 \text{ g mm/ps}^2$, $c_0 = .17 \text{ g/mm}$, $k = 1.37$ and $\bar{c} = c - .092 \text{ g/mm}$, we can find ζ and ϵ . In addition $T = .35 (6.35 \text{ mm}) = 2.2 \text{ mm}$ as before, while $M_R/M_0 = .93$ by Eq (4.43). then we can calculate a curve in reasonable agreement with experiment,

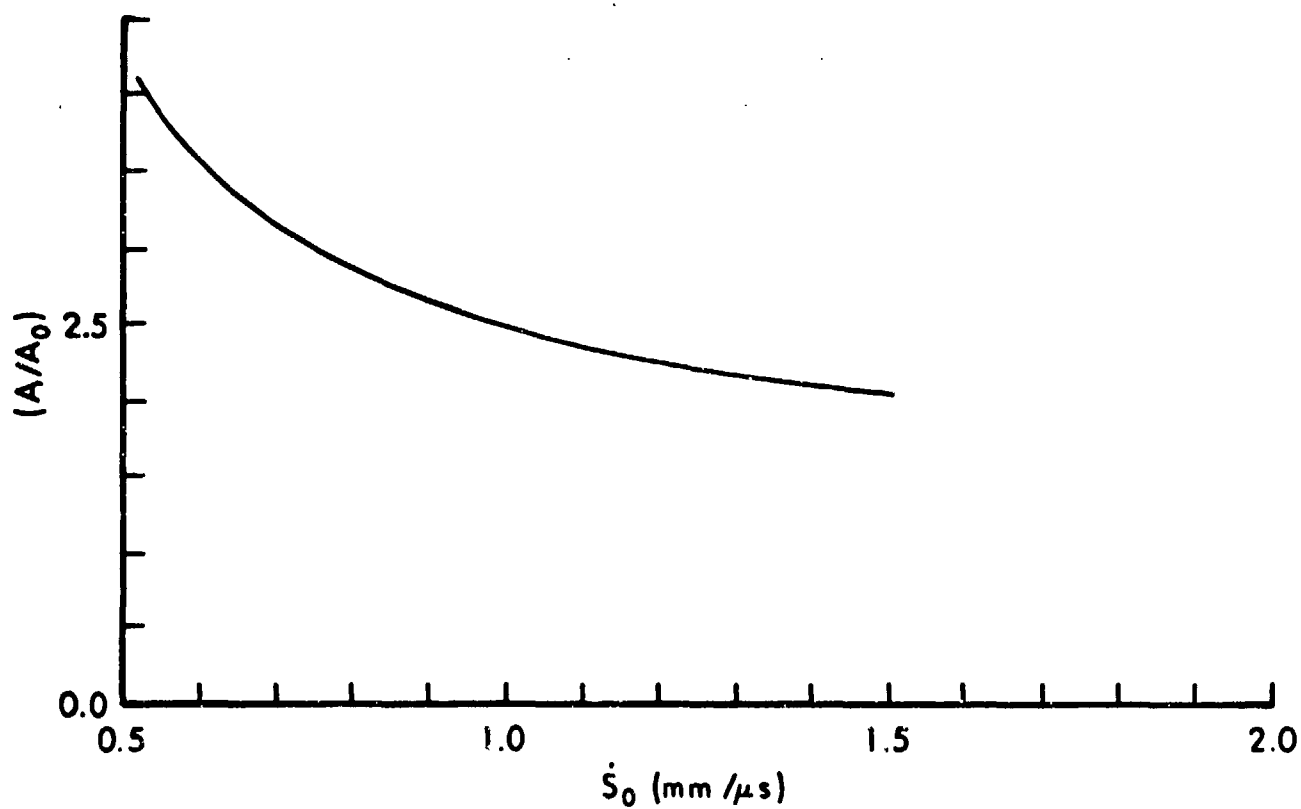


Fig. 4.50. Flattening factor for 7.7g, $L_0/D_0 = 5$ tungsten rod versus 6.35mm armor steel plate.

Hohler and co-workers (4.37) employed $L_0/D_0 = 10$ tungsten alloy rods versus steel target plates of various thicknesses and obtained residual speed and residual mass data quite comparable to that obtained by Herr and Grabarek. However, they only used two impact speeds for armor steel plates at zero degrees obliquity, so it is difficult to construct complete curves of the type we have been considering. They were more interested in determining a thickness ballistic limit rather than a velocity ballistic limit. Since they did not use an aspect ratio of 5, it is not surprising that they saw no evidence for a possible maximum in an M_R vs \dot{S}_0 curve. However, for $L_0/D_0 = 10$, they reported a smaller loss in rod length as the striking speed increased from about 1 mm/ μ s to 1.8 mm/ μ s. This agrees with an increase of residual mass with increasing \dot{S}_0 as found by Herr and Grabarek for high aspect ratio rods. A thickness ballistic limit is that value of P in Eq (2.20) which reduces P to zero for given \dot{S}_0 (and a given projectile/target combination).

V. SURVEY OF JET PENETRATION THEORIES

In an earlier report (1.14) we surveyed bullet penetration theories. Here we present a similar survey for jet penetration theories in order to compare older ideas with those being discussed in this report.

The first jet penetration theory seems to have been put forth in a report by Kistiakowsky and co-workers (5.1). Part of this report is devoted to their theory of jet formation according to which small fragments of steel from the liner of the hollow cavity in the explosive were guided by a gas Mach stem into a pencil-like jet. The rest of their report discusses a theory of how such a stream of explosive product gases and steel fragments might penetrate a metal target, usually also steel. Their model treats jet penetration into metal much like water-jet penetration into a mud bank. The head of the jet is "continuously annihilated, and the momentum contained there is transmitted to the steel which flows sideways..." Of course, mass is conserved and the jet material is deflected rather than annihilated. They took the length of jet removed from the stream per unit time to be equal to the difference between the velocity of the head of the jet, V , as determined from experiments in air or vacuum, and the velocity of penetration, U , as determined from the time it took to perforate plates of various thicknesses, with $U < V$. The wearing down of the head of the jet was responsible for the slowing of the jet during perforation. After perforation, they sometimes observed a speeding up of the jet once more. If ρ_p is the density of the jet penetrator and A is its cross-sectional area, then $\rho_p A$ is its mass per unit length and $\rho_p A (V-U)$ is an estimate of the mass lost per unit time during penetration. Since V is the velocity of the jet, then $\rho_p A (V-U)V$ is the momentum transferred per unit time from the jet stream to the target. Since the target also behaves like a fluid, its resistance is purely inertial and resembles that offered by the air to the flight of a metal fragment, namely, $C_D \rho_t A U^2$, where C_D is the drag coefficient, ρ_t is the target density and U is the speed of the fragment. If $C_D = 1$, and we equate the rate of momentum transfer to the resistive force,

$$\rho_p (V-U)V = \rho_t U^2 \quad (5.1)$$

Experimentally, they found $V = 6 \text{ mm}/\mu\text{s}$ and $U = 2.4 \text{ mm}/\mu\text{s} = .4V$ for steel ($\rho_t = 7.85 \text{ g/cm}^3$) as well as $V = 2.1 \text{ mm}/\mu\text{s} = .35V$ for lead ($\rho_t = 11.3 \text{ g/cm}^3$). Both of these sets of values are compatible with $\rho_p = 2.1 \text{ g/cm}^3$, much less than the density of the steel liner used, but consistent with their picture of a jet stream composed of steel fragments carried along by gaseous explosive products. They commented that this was probably fortuitous, but expressed satisfaction that the penetration speeds were of the right order of magnitude and in the correct order, higher for steel than for lead. Consequently, the penetration depth into steel should be greater than into lead, because lead has a higher density. Unfortunately, the opposite was observed; namely, greater penetration into lead than into steel. This apparently is the origin of the division into primary and secondary phases of penetration.

"Since the velocity of the jet is, of course, greater than the velocity of penetration, after penetrating through a certain thickness of steel, the jet will have been all used up. The penetration during this phase will be referred to as the primary penetration. Since, when this occurs, the steel in the target has some forward momentum, plastic flow forward probably continues until the forces have been reduced to about the elastic limit, and this will deepen the hole somewhat (referred to as secondary penetration). It is believed that the depth of secondary penetration is rather small in steel, because of its high tensile strength. However, for a very soft metal, such as lead, the second part of the process might result in a considerable increase in the depth of the hole." (5.2)

These authors explicitly referred to their theory as an "hypothesis." They went on to speculate further about the anomalous penetration into lead:

"However, in the case of lead, the secondary penetration must be large. The total depth of penetration is appreciably greater than for steel, although, due to its greater density, the depth of primary penetration should be less. No calculations have been made, but the facts are not surprising, on account of the very low tensile strength of lead. No penetration at all can occur if the momentum per unit length of the jet is not great enough to exceed the elastic limit of the target materials. It may be that for lead the slow tail of the jet is effective and for steel not." (5.3)

Near the end of their paper, the authors reported an attempt to verify their model of the jet as a stream of gas carrying metal fragments.

Experiments were done with liners made from steel filings cemented together. Fine carborundum and other fragmented materials were also used. Such liners were inferior in their penetration performance to solid liners of similar materials. Instead of questioning their model, they speculated that an assortment of particle sizes might be required to simulate the action of a jet instead of the single size used.

About a year later, Hill and co-workers ^(5.4) referred to the work of Kistiakowsky and co-workers in building their own model of jet penetration. They also referred to a model developed by Bethe ^(5.5). They let V be the velocity of the jet and U be the penetration velocity as before, and introduced the length of the jet, ℓ . They also introduced a Gallilean transformation from the stationary laboratory coordinate frame to coordinates with origin at the bottom of the crater being formed in the target, moving at the constant speed, U . The pressure exerted by the jet at the stagnation point at the bottom of the hole is $.5\rho_p (V-U)^2$, provided the material is incompressible. This pressure is balanced by that exerted by the target material moving at speed, U , namely, $.5\rho_t U^2$. If we equate these two expressions, we find

$$\rho_p (V-U)^2 = \rho_t U^2 \quad (5.2)$$

Moreover, if ℓ is the constant length of the jet and $(V-U)$ is its constant speed, then the time it acts on the target will be $\ell/(V-U)$. If we multiply this time by the penetration speed U , we should obtain the depth of penetration

$$P = \ell U / (V-U) = \ell \sqrt{\rho_p / \rho_t} \quad (5.3)$$

as we see by using Eq (5.2). The author's commented that this expresses an "interesting conclusion that the depth of penetration is independent of the velocity of the jet, and depends only on its length and density." The right side of Eq (5.3) is now called the hydrodynamic limit, as we have seen, since it neglects strength, viscosity and compressibility. For compressible targets

like rubber or paraffin, they took the pressure to be $p = K(\rho/\rho_t - 1)$, where K is the target compressibility and $\rho > \rho_t$ is its compressed density. Then $dp = (K/\rho_t) d\rho$, and $\int dp/\rho$ becomes

$$(K/\rho_t) \int_{\rho_t}^{\rho} d\rho/\rho = (K/\rho_t) \ln(\rho/\rho_t) = (K/\rho_t) \ln(1 + p/K). \quad (5.4)$$

If we equate this expression to $.5U^2$, we find

$$p = K \{ \exp [(.5\rho_t U^2)/K] - 1 \} \approx (.5\rho_t U^2) [1 + (.5\rho_t U^2)/(2K)] \quad (5.5)$$

if $(.5\rho_t U^2) \ll K$. For steel targets they found this pressure correction to be negligible, although it might not be negligible for a lead target. Even if it were included for a lead target, it would not help to explain the observed greater penetration into lead than into steel, which contradicts Eq (5.3). In fact, it would make matters worse, since ρ_t in Eq (5.3) would be multiplied by a factor somewhat greater than unity.

If we divide Eq (5.2) by $\rho_p v^2$, we find

$$U = V/[1 + \sqrt{\rho_t/\rho_p}] \quad (5.6)$$

If we assume that a steel jet has the same density as the conical liner from which it was formed, then $U = .5V$ for a steel target and $.45V$ for a lead target. This compares with $U = .4V$ for steel and $U = .35V$ for lead reported by Kistiakowsky and co-workers. In general, the experimental precision available at the time was not great enough to say for certain that V was greater for one target or another when the speeds were this close. The approximate agreement between Eq (5.6) and experiment was considered to be encouraging. If a low value such as one-third the steel liner density, namely, $\rho_p = 2.6 \text{ g/cm}^3$, is used in Eq (5.6), then $U = .37V$ for a steel target, while $U = .33V$ for lead, in close agreement with the values reported by Kistiakowsky and co-workers.

Because of this agreement. Hill, Mott and Pack went on to modify their theory to take into account the possibility that the jet was composed of a stream of explosive product gases, carrying steel liner fragments. They

reasoned that such a low-density fragment jet, where the metal occupies only a small fraction of the volume, might exert a mean pressure considerably larger than originally proposed. When a moving body collides with a stationary body and is just brought to permanent rest, it has transferred all of its momentum. However, if the stationary body is massive enough, the incident body will reflect elastically with its incident speed. In this case the momentum transfer is twice the incident momentum, since the stationary body gains as much reaction momentum while accelerating the incident body as it does in bringing it to momentary rest. Since the jet/target collision is never quite elastic, even for a jet of low density, they modified their expression for the mean pressure exerted by the jet to $\lambda^2 [.5 \rho_p (V-U)^2]$, where $1 < \lambda^2 < 2$. When this expression is equated to the target reaction pressure, namely, $.5 \rho_t U^2$, we find

$$P = 2\lambda \sqrt{\rho_p / \rho_t} \quad (5.7)$$

and

$$U = V / [1 + \sqrt{\rho_t / \rho_p} / \lambda] \quad (5.8)$$

instead of Eqs (5.3) and (5.6). The authors expressed the opinion that the factor, λ , should apply to most jet densities, except those with densities so low that penetration by individual fragments would have to be considered.

They also pointed out that their use of $(V-U)$ instead of V as a multiplier to convert the mass loss rate, $\rho_p A(V-U)$, into a momentum loss rate, giving Eq (5.2) instead of Eq (5.1), agreed better with the model of a low density jet being turned back rather than coming to rest during penetration. It also agreed with their steady-state pressure balance theory.

Finally, these authors noted that after a high-speed penetration was over, the average cross-sectional area of the target crater, A_t , is larger than the area, A , of the penetrator (rod or jet). This allows eroded penetrator material to turn back without interfering with incoming material. Following the suggestion of Kistiakowsky and co-workers, they also introduced a drag coefficient, C_D . Then the reaction pressure exerted by the target becomes

$C_D [.5 \rho_t A_t U^2]$. If we equate this to the pressure exerted by the jet, namely, $\lambda^2 [.5 \rho_p A (V-U)^2]$, we find

$$P = \lambda \sqrt{(\rho_p / \rho_t)} [A / (C_D A_t)] \quad (5.9)$$

and

$$U = V / [1 + \sqrt{\rho_t / \rho_p} / (\lambda \sqrt{A / (C_D A_t)})] \quad (5.10)$$

where $A_t > A$ and $C_D \geq 1$ is unknown. By assuming that Eqs (5.7) and (5.8) are correct, implying that $A / (C_D A_t) = 1$, it should be possible to measure A / A_t and so find C_D . They went on to note that the mechanism of penetration by a jet must be similar to that by a bullet in the shatter region of velocities, since in both cases the hole has an area greater than the cylinder of metal making it, because the shattered metal must flow out again. This led them to suggest that the total volume of hole excavated should be proportional to the kinetic energy of all the jet fragments, an idea which has been often used since then.

A short while later, these same authors published another report ^(5.6) in which they discussed penetration by projectiles as well as by jets. Following Bethe ^(5.5), they used the U^2 term in the Poncelet force to account for a change in projectile penetration behavior at high speeds where a constant target strength force was no longer sufficient. Consideration was also given to Taylor's ^(5.7) modification of Bethe's hole enlargement theory. Hill, Mott and Pack went on to note that the phenomenon of projectile shatter above a critical striking speed shows that the force acting on the nose of the projectile must increase with increasing velocity, as indicated by Poncelet's velocity-dependent term.

They modified their previous discussion of jet penetration by adding a constant target strength term, σ , to the target reaction pressure to obtain $(.5 \rho_t U^2 + \sigma)$, a Poncelet form. Now, if this is equated to the pressure of the jet head, $.5 \lambda^2 \rho_p (V-U)^2$, we find

$$.5 \lambda^2 \rho_p (V-U)^2 = .5 \rho_t U^2 + \sigma \quad (5.11)$$

where σ is a sum of elastic and plastic terms as proposed by Bethe (5.5), namely,

$$\sigma = (Y/\sqrt{3}) \{1 + \ln [\sqrt{3}E/(2Y [1 + \nu])]\} \quad (5.12)$$

where Y is the yield stress, E is Young's modulus of elasticity and ν is Poisson's ratio. For ductile materials they agreed with Bethe's estimate that σ should be three or four times the yield stress. We recall Tabor's estimate (1.18) of three times this stress. Now we find

$$P = \rho U/(V-U) \approx \lambda \sqrt{\rho_p/\rho_t} \{1 - \sigma/[\lambda^2 \rho_p (V-U)^2]\} \quad (5.13)$$

and

$$V = U + \sqrt{(\rho_t U^2 + 2\sigma)/(\lambda^2 \rho_p)} \quad (5.14)$$

instead of Eqs (5.7) and (5.8) to which they reduce if $\sigma \rightarrow 0$. Here they have chosen the positive sign of the square root in Eq (5.14) and have dropped consideration of $\sqrt{A/(C_D A_t)}$ in agreement with their idea that this factor must be equal to unity. Now Eq (5.13) gives them a way of explaining why penetration into lead is greater than into steel in spite of its greater density, provided $\sigma \approx 0$ for lead but is not negligible compared to the jet pressure in the case of steel. However, as they noted, the entire theory breaks down if the correction term in Eq (5.13) approaches unity. For steel the correction factor would have to be greater than 0.2 to account for the observed relative penetration depths into steel and lead.

They also noted that the idea of the jet density being much less than that of the liner was a subject "on which there has been considerable speculation, but no real evidence." (5.8) Because of this they attempted to compare Eq (5.8) with some experimental results on copper and aluminum targets, without success. They speculated that this might be due to the large scatter in the experimental measurements.

Finally, they used Eq (5.13) to describe penetration of a steel jet into a steel target, using $\sigma = 5.5Y$, not too far from their expected value of three

or four times Y . Their comment, however, was very cautious: "This result can only be considered fortuitous; but it does point to σ being of the order of magnitude predicted." (5.9)

Kistiakowski and co-workers (5.1) were also cautious about their theory, referring to it as "A rough calculation of the rate at which momentum is delivered to the plate by the jet..." (5.10), too qualitative to make predictions. Before continuing our review of the literature, let us comment on some of the reasons why both the American and British groups were so cautious. They knew that V , the jet tip speed before impact, was greater than the speed of the rear of the jet or any portion between. Consequently, their V was some sort of average velocity for the whole jet. They also knew that measurements of the penetration speed, U , depended not only on the material used for the target, but also on the thickness of the plate. So again, U is an average value for some typical plate thickness. The inconstancy of V and U is shown in Fig. 5.1 taken from DiPersio and co-workers who made such measurements about fifteen years later (5.11). Electrical contacts were placed between one-inch thick steel plates in a "semi-infinite" stack. The jet tip velocity, V , was taken to be the distance from the jet "origin" to the front of a given plate divided by the time it took to traverse this distance. The penetration velocity, U , was taken to be the thickness of a given plate divided by the time it took to perforate this plate. Both V and U obviously decline in time by a factor of four or more. Although the early British and American groups probably did not know the magnitude of these changes, they were aware that their assumption about the constancy of V and U was a rough approximation. They also knew that the length of the jet was not constant either. Its initial length depended on the standoff, or distance between the cone base and the target face. In addition, it had to be stretching since the tip moved faster than the rear. And finally, although there was no direct evidence, it was unlikely that a stretching, eroding jet should have a constant length. Again, the length, l , was known to be an effective or average value. There were no time-dependent measurements available, so a theory involving differential equations was probably considered to be of little use. Apparently these early theorists decided on a formulation which involved only the average values which were available from the experiments of their day.

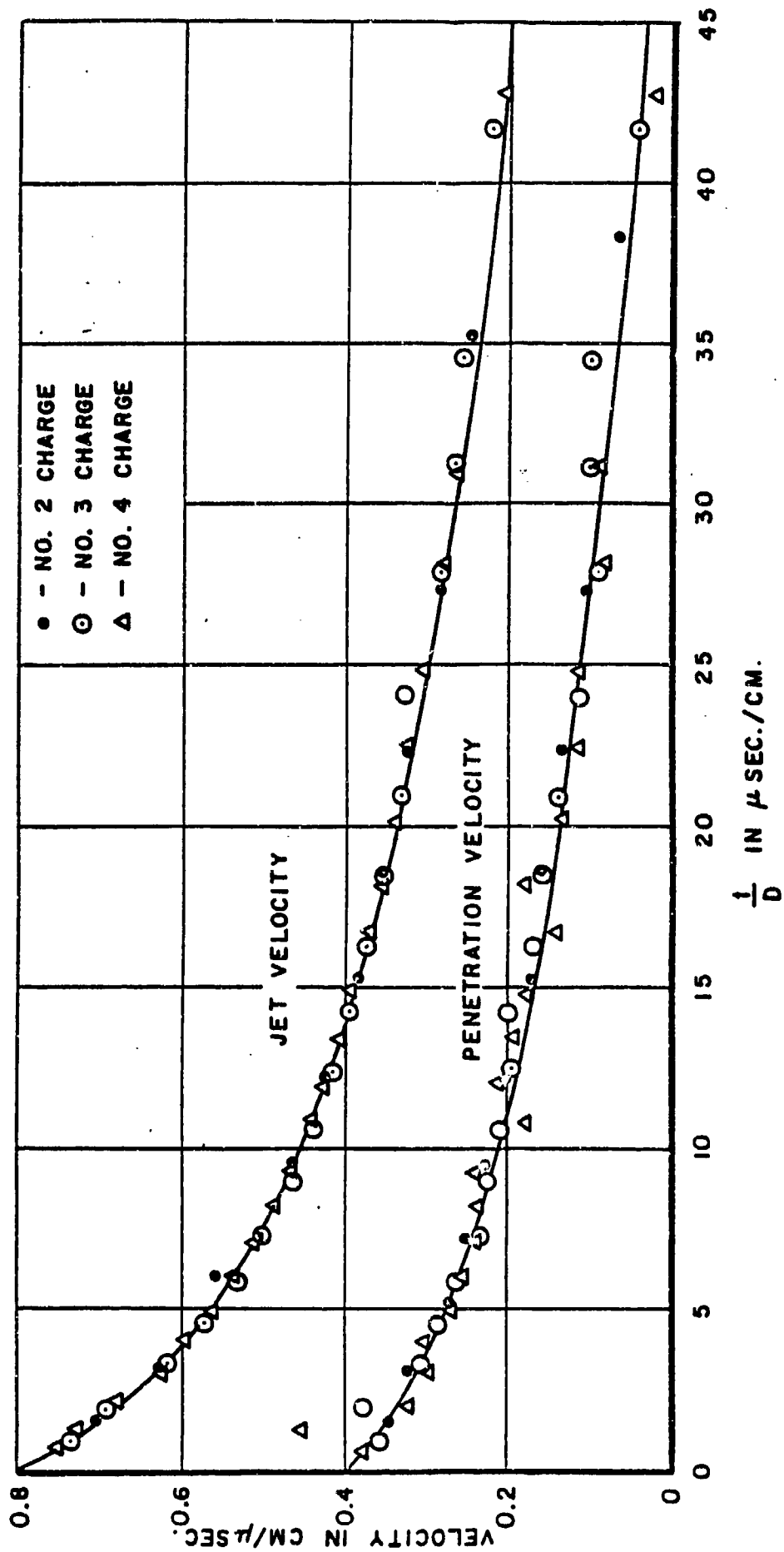


Fig. 5.1 Penetration and jet velocity vs. time.

The early theorists were aware that their choices of $(V-U)$ to estimate mass loss and $(V-U)V$ or $(V-U)(V-U)$ to approximate momentum transfer or pressure were somewhat arbitrary. Although they did not discuss other alternatives, they could have used V and V^2 instead. For example, they might have written $.5\rho_p V^2$ for the average energy per unit volume of the incident jet and $.5\rho_t U^2$ for the average energy of the yielding target material, and equated these values to obtain U/V . In this model, the time of action of the jet would be ℓ/V , so the penetration depth should be U times this, or

$$P = \ell U/V = \ell \sqrt{\rho_p/\rho_t} \quad (5.15)$$

which is the same as Eq (5.3). Here $U = V \sqrt{\rho_p/\rho_t}$ instead of Eq (5.6). However, for given ρ_p , this also predicts smaller U in lead than in steel, as reported. To obtain $U = .4V$ for steel, ρ_p would have to be 1.25 g/cm^3 instead of 2.6 g/cm^3 , as they used. Then $U = .33V$ for lead, giving agreement within the precision of their experimental information. In addition, if they had wanted to use a differential expression for loss of jet length instead of a difference between two velocities, they could have written $.5\rho_p \dot{\ell}^2$ for the average energy per unit volume lost by the jet and $.5\rho_t \dot{P}^2$ (where $\dot{P} = U$) for the average energy per unit volume acquired by the target. Since these two quantities should be equal, we obtain

$$\dot{P} = \sqrt{\rho_p/\rho_t} \dot{\ell} \quad (5.16)$$

This equation can be integrated with the initial condition that the penetration depth is zero when the length consumed is zero, to obtain Eq (5.15).

Now let us resume our review.

About the same time, flash X-ray techniques were being applied to the study of jet formation from the explosive collapse of a hollow conical liner. Seely and Clark (5.12) followed the collapse process and the formation of jet and slug as a function of time. Some of their pictures were included at the end of an article published six years later (5.13). In commenting on one of

their pictures they concluded that the jet diameter (from a cone with a one inch base diameter) was about 0.5 mm. "Thus within this diameter there must be almost solid iron in order to register so definitely on the film." (5.14) Birkhoff (5.15) used their pictures to dismiss jet formation theories which employed focusing, spalling, or shock wave explanations. Instead, he interpreted their evidence in terms of the usual hydrodynamical theory of jets (5.16) which implied a re-direction of the liner mass without change in density. In England, Tuck (5.17) was carrying out experiments very similar to those of Seely and Clark and interpreting his own results much as Birkhoff was doing. This theory was further refined by Taylor (5.18). This report also appears in the collection by Batchelor (5.19). Tuck also considered the idea that the jet density was significantly lower than the liner density. He admitted that the liner might be broken into very fine pieces. "If the fragmentation is so fine that no gaps exist between the particles into which flow could take place, then, hydrodynamically speaking, the system can be treated as a fluid." (5.20) Tuck went on to note the appearance of a periodicity about 1 cm in length in the jet after formation, which signalled break-up into a train of particles, all about the same size. "It is tempting to explain the break-up of the jet in terms of a tension arising out of this velocity gradient. But there seems no evidence that the jet is a continuous rod capable of supporting a tension and the indications are rather the reverse since a graininess is already visible before the main breakup has developed, and a general impression of cloudiness is given even earlier." (5.21) Thus Tuck was not as definite about the density of the jet as Seely and Clark were.

Still later, Pugh (5.22) discussed ideas very similar to those above. However, he tried to account for the fact that the jet tip speed was almost 8 mm/ μ s while the rear moved much more slowly at about 2 mm/ μ s. He assumed a linear decline in V from tip to rear and extrapolated the trajectories of selected jet elements backward in time. Since these trajectories crossed in a relatively small region of his space-time plot, he chose the center of this region as his coordinate origin, and suggested that one might think of all elements of the jet as issuing simultaneously from the same point in space but travelling at quite different speeds. This point has come to be called the "virtual origin" of the jet. (One might call this the little-bang theory of a

jet's origin by analogy with the big-bang theory of the origin of the universe.) If Z and t are the distance and time a jet element has travelled since its birth, then, its velocity is $V = Z/t$. If $\gamma = \sqrt{(\rho_t/A)/(\rho_p/A_t)}$ with $C_D = \lambda = 1$ in Eq (5.10), then

$$U = Z = (Z/t)/[1 + \gamma] \quad (5.17)$$

In this report Pugh considered ρ_p and A_t to vary in time, so γ was not constant and Eq (5.17) could not be easily integrated. He assumed that ρ_p varied inversely with time (lateral spreading of the particles composing the jet). He also assumed that the crater area increased quadratically with Z . Since this led to unreasonable conclusions, he temporarily abandoned this approach.

In a second report with Fireman (5.23) Pugh noted receipt of the two reports by Hill, Mott and Pack referenced above. He also decided to assume γ constant in Eq (5.17), which can then be integrated to obtain

$$Z = Z_0 (t/t_0)^{1/(1+\gamma)} = Z_0 + P \quad (5.18)$$

where Z_0 is the distance traversed by the tip when penetration starts at time t_0 , that is, the distance from the virtual origin to the front face of the target, a distance about a cone height, H , greater than the standoff distance, S . The second form in Eq (5.18) is obtained by adding the depth P at any time t , with $P = 0$ for $t = t_0$. If γ were equal to unity, then Eq (5.18) would be parabolic. In this model the penetration at any time increases linearly with Z_0 , which in turn is equal to the standoff plus a constant, $(S + H)$. In this way Pugh and Fireman were able to give an approximate explanation for the observed increase in P with increasing standoff. Later, a similar treatment was given by Abrahamson and Goodier (5.24). However, these authors assumed that Z_0 varied in time and could not integrate their expression analytically.

To account for the fact that penetration decreases at large standoffs, Pugh and Fireman assumed a linear increase in jet radius and therefore a quadratic increase in jet area, A , with increasing standoff, due to spreading of the jet particles. This led to a series expression for P which was not

easily joined to Eq (5.18), which was valid for short standoffs only.

In a third report ^(5.25) Pugh and Fireman derived another series expression for penetration versus standoff at large standoff. However, these results were also unsatisfactory.

Birkhoff ^(5.26) also tried to modify the theory of Hill, Mott and Pack to include the effects of standoff. He took the jet density, ρ_p , to be inversely proportional to the jet length, l , which in turn he assumed to increase linearly with standoff, S . Thus

$$P = l\sqrt{\rho_p/\rho_t} \sim \sqrt{l/\rho_t} \sim \sqrt{(a + bS)/\rho_t} \quad (5.19)$$

which gives a nonlinear increase in P with S . However, there is no maximum P at finite standoff, predicted by Eq (5.19), so it too applies only at short standoff. Here $P = P_E$, the final penetration depth when $t = t_E$ in Eq (5.18). Thus $P_E \sim (S + H)$ in Eq (5.18) while $P_E \sim \sqrt{a + bS}$ in Eq (5.19) which is closer to what is observed.

After World War II, Birkhoff, MacDougall, Pugh and Taylor ^(5.27) described their hydrodynamic theories of jet formation and penetration. Here we are interested in the latter. They began by saying that, "To a first approximation the strengths and viscosities of target materials can be neglected and the problem can be treated by hydrodynamics." Initially, they consider a continuous jet and explicitly assume three constants, length, l , speed, V , and penetration speed, U . Since the speed, U , is constant, a Gallilean transformation to the stagnation point at the crater bottom is permitted. In this coordinate system, steady-state conditions hold, so Bernoulli's theorem applies. Consequently, Eq (5.2) can be written. If the jet length were effectively infinite (as it is in the case of water from a hose) then the penetration would also be infinite. However, the finite length, l , leads to an end of the motion when the jet is used up at time $l/(V-U)$. As before, multiplication by U leads to Eq (5.3), according to which P is independent of speed. These authors comment that this surprising result might be correct if one imagines that a faster jet is used up in a time which is just small enough that the same penetration is produced. As they point out once more, if this is true, it can only be so for speeds and pressures large

enough to justify neglect of target strength. The results of later workers, shown in Figs 3.16 and 4.28 for example, make us wonder what such speeds might be. These results are for projectiles. However, we will see similar results of the importance of target strength for jet penetration in the next chapter.

For a jet composed of dispersed particles these authors adopted Eq (5.7) with λ under the square root sign, a practice introduced by Hill, Mott and Pack in their second paper. Of course, it makes no difference whether we let λ vary between 1 and $\sqrt{2}$ or let $\sqrt{\lambda}$ vary between 1 and $\sqrt{2}$, that is, λ vary between 1 and 2.

In the next section of their paper Birkhoff and co-workers mention the fact that neither the jet velocity, V , nor its length, ℓ , are constant. Since the tip moves four times faster than the rear (8 mm/ μ s versus 2 mm/ μ s for example), then each successive element of the jet strikes the bottom of the crater at a lower speed. One can of course speak of an average speed, $V = (8+2)/2 = 5$ mm/ μ s, but the variation from tip to rear is so large, that one should really consider V to vary with time during the penetration. These authors explicitly assumed that the jet density and the (incompressible) target density were constant in time. Consequently, U in Eq (5.10) must vary with time, so they wrote

$$P = \int U \, dt \quad (5.20)$$

However, they did not know how U varied in time, so they wrote

$$P = \ell J / \sqrt{\rho_t} \quad (5.21)$$

where " J is a kind of average value of the quantity $\sqrt{\lambda \rho_p}$ during the process of penetration," and ℓ is explicitly called an "effective length." The effective length was then assumed to have a linear dependence on standoff, while the jet density was assumed to decrease quadratically with standoff because of radial spreading. This led to formulas for short and long standoff with adjustment of the parameters to insure joining of the curves.

They concluded their paper by comparing Eq (5.10) with experimental data for a variety of targets. In spite of scatter in the data, there seemed to be general agreement.

In view of the large difference in velocity between the tip and rear of the jet, we should notice that there is a basic defect in the theory which has been proposed. If V is to be treated as an average value over the length of the jet, then V varies with time as the jet gets used up. Near the beginning of a penetration by a fully-formed jet, the average speed might be about 5 mm/ μ s as we have mentioned. However, this average value declines toward 2 mm/ μ s as the jet is consumed. Without averaging, the jet speed declines by a factor of four. With averaging over its length, its speed declines by a factor of 2.5 in this example. Either way, the dependence of V on t is significant. If ρ_p and ρ_t are constant in Eq (5.10) and V varies in time, then U must vary in time if this equation means anything. We recall Fig. 5.1. However, if U varies significantly in time, then a Gallilean coordinate transformation to a stagnation point moving at constant speed is not possible. Instead, a coordinate system with origin at the stagnation point is a decelerating system. Consequently, there is no steady state and Bernoulli's theorem does not apply.

It is unfair to criticize the authors of a theory for not adjusting their ideas to accomodate facts they were only dimly aware of. Nor is this being done. However, it is incumbent on us to devise new theories, when new facts make the need apparent.

Several years later, Pack and Evans (5.28) undertook an explanation of two deviations from the density law, Eq (5.3), which had by this time been firmly established. One was the difference between a (smaller) penetration into armor steel than into mild steel, which they explained on the basis of Eq (5.13). The other was the fact that for the 80°, 35 mm base diameter mild steel cone device they used, the 83 mm penetration into lead was about 25% larger than the 66.5 mm depth they observed in mild steel. They noted that the slug which follows the jet can become trapped part-way down the crater in a hard steel target. Since lead target craters were much wider, they supposed that the slug could find its way to the crater bottom and deepen the hole further. In addition, target "afterflow" was expected to be significant in lead and these two factors together might account for the additional depth (83 - 56) \sim 27 mm. They did not recover such slugs from their targets, nor

did they give an estimate of their expected mass and speed. The evidence they present is indirect and not convincing.

In later years, various workers used modified versions of Eq (5.11) to explain their observations. We will review some of these ideas in what follows.

Eichelberger (5.29) adopted Eq (5.11), but he used the symbol γ instead of λ^2 and took σ to be the difference between the target and jet strengths, namely, $\sigma = \sigma_t - \sigma_p$. Moreover, his constant γ , which he called a statistical breakup factor, was given quite a different meaning from that originally assigned to λ^2 . By this time improvements in flash X-ray photography had advanced to the point where everyone was convinced that the jet density was for all practical purposes equal to the liner density during formation and stretching. In fact, even after breakup due to stretching, the jet fragments, which continued to follow each other, retained their original density. In other words, the original idea which led to λ^2 , namely, the jet consisting of steel fragments dispersed in a column of explosive product gas, had to be abandoned. We will see more about this in the next chapter. Eichelberger wanted his γ to include any changes in the mode of momentum transfer which might occur, as well as separation of the jet fragments after breakup and any waver that might be present due to imperfections in charge or liner. For short standoffs he found $\gamma = 1$ and ρ_p equal to the density of his steel liner. For sufficiently long standoffs when most of the penetration was done by a jet which was already broken into a train of fragments, he found $\gamma < 1$, with no change in ρ_p , and γ continuing to decline as the standoff was increased. He concluded that the Hill-Mott-Pack mechanism for a low density jet did not apply and that λ was always equal to unity. If σ were unimportant, then, following the general scheme of an effective length acting for a finite time, we would have

$$P = \ell \sqrt{\gamma \rho_p} \rho_t \quad (5.22)$$

In qualitative agreement with observations, this equation says that P will decrease when the standoff becomes large enough that γ declines below unity once the jet is fragmented and the fragments become misaligned. This is quite different from Eq (5.7) which says that penetration will increase if a jet

consisting of steel fragments dispersed in a gas stream becomes sufficiently dispersed.

Eichelberger also tried different values for σ_t and σ_p in order to see whether experimental trends could be described. He found, for example, that he could use the experimental yield strength for a hard steel target, but had to use three times the experimental strength in the case of an aluminum target. He went on to express surprise that a steady-state hydrodynamic theory could do even as well as it did when applied to a "violently time-dependent phenomenon." Of course some of this could be explained by the large experimental uncertainties which were involved with attempts to verify the theory. Some of these have been described by Eichelberger and co-workers (5.30). This is also brought out by variations found in different laboratories. For example, Singh (5.31) repeated Eichelberger's tests and found that he needed σ_t values seven times the measured values of either steel or aluminum targets in order to obtain agreement between theory and experiment.

Cook (5.32) attempted to generalize Eq (5.11) further by adding to σ three terms to account for target compression, heating, and shock wave dissipation. Such terms depend on the impact speed range involved and so complicate the theory considerably in an unknown way. Conditions for impact explosions were also discussed. Cook seems to be the first author to write the solution of Eq (5.11) for U in terms of V instead of for V in terms of U as in Eq (5.14). Since Eq (5.11) is quadratic in either V or U, it is no more difficult to solve for one than the other. If we choose the negative sign for the square root, we find

$$U = V [1 - \sqrt{\Delta + 2 \sigma \Delta (1-\Delta) / (\rho_t V^2)}] / (1-\Delta) \quad (5.23)$$

where $\Delta = \rho_t / (\lambda^2 \rho_p)$. Cook cited Eichelberger in letting $\lambda = 1$ and used the symbol ϕ for σ plus correction terms. He also noted the solution in the case $\Delta = 1$, $\rho_t = \rho_p = \rho$, to be

$$U = .5V [1 - 2\sigma / (\rho V^2)] \quad (5.24)$$

as well as corresponding expressions for $P = \rho U / (V-U)$.

Allen and Rogers (5.33) repeated Eqs (5.23) and (5.24) and used the phrase "modified Bernoulli's equation" to describe Eq (5.11). Since the jet length, ℓ , which was supposed to be constant is not, these authors decided to apply the hydrodynamic theory to a rod which at least has a known length to begin with. As they pointed out, accurate experimental verification of the theory had not been reported previously. They introduced an average value for σ or ϕ for all metals and reported approximate agreement with their experiments with wire rods made from magnesium, aluminum, tin, copper, lead and gold striking aluminum targets at speeds up to almost 3 mm/ μ s. An exception was found when the rod density was much larger than the target density as in the case of gold.

Alekseevski (5.34) also applied the steady-state hydrodynamic theory to rods. He proposed using

$$\dot{\ell} = V - U = V - \dot{P} \quad (5.25)$$

for the magnitude of the change in rod length with time. In addition he adopted Eq (5.11) with $\lambda = 1$, but assumed that both V and U decreased in time in such a way that Eq (5.11) continued to be true. He went on to caution the reader that there is a minimum speed below which the model does not apply. This is obvious from Eq (5.11) with $\sigma \neq 0$. Clearly U and V cannot vanish and the motion can only terminate by the rod vanishing while still moving at a finite speed. He used an approximate solution for U in terms of V instead of Eq (5.23) and integrated his equations with numerical techniques, assuming that

$$dV/dt = - (\sigma_p / \sigma_p) / (\ell_0 - \ell) \quad (5.26)$$

Unfortunately, he did not point out that variable V and U are not compatible with the steady-state required by the theory. At least Hill, Mott and Pack were consistent in assuming constant V and U .

Tate (5.35) also adopted Eq (5.11) with $\sigma = \sigma_t - \sigma_p$ with $d\ell/dt = (U-V) < 0$ and $dV/dt = - (\sigma_p / \sigma_p) / \ell$. Unlike Alekseevski, he used Eq (5.23) instead of an approximation, and integrated numerically except in a few

special cases. In a footnote, Tate points out that one cannot really use Bernoulli's equation to describe an unsteady process. However, he assumes that V and U are approximately constant during most of the penetration process. For example, he uses his theory to describe penetration by aluminum rods striking a polyethylene target at $1.6 \text{ mm}/\mu\text{s}$, at least until their speed has declined to about $0.6 \text{ mm}/\mu\text{s}$, beyond which "the theory does not apply." Since he was forced to use different values for the strength of the same polyethylene target (one four times the other) when attacked by two different strengths of aluminum rod, he recognized that "the theory is not adequate in this case." He also rationalized that for targets made of the same material as the rod, we should expect the target strength to be greater "because of the inertia of the surrounding material." We have already referenced a subsequent article by Tate (4.19) in which he extended the ideas of this paper in an attempt to describe situations in which rods were not completely consumed at the end of a penetration. For rods much stronger than a target, he assumed cessation of erosion together with a Poncelet form for the opposing target force. The additional penetration could be added to that achieved during erosion. He also discussed how numerical integration of his previous equations could lead to a maximum in a plot of penetration depth versus impact speed with the penetration decreasing and "tending ultimately to the hydrodynamic limit." We have already seen that this is not true, at least in the cases of steel/aluminum and aluminum/lead cited by Tate and refuted by Perez (4.6). Perez restricted his own use of Eq (5.23) to speeds greater than $2.0 \text{ mm}/\mu\text{s}$.

Now let us return to a review of theories of penetration by jets rather than by rods.

Since it was well established by 1960 that neither V nor U remained constant during the penetration of a semi-infinite target, Allison and Vitali (5.36) followed the ideas of Pugh (5.22) and Pugh and Fireman (5.23) as expressed in Eq (5.18), at least for continuous jets. For penetration by jets after break-up, they assumed hydrodynamic theory to hold for each jet particle and added the total of these contributions to the penetration produced by the jet before break-up. They found that equally good results could be obtained by using the continuous jet theory for the entire penetration, provided they introduced a cutoff velocity, V_{MIN} , instead of a fixed finite length, l .

The following year, DiPersio and Simon (5.37) extended the method of Allison and Vitali to include a discussion of standoff at least on the rising portion of the penetration-standoff curve. A year later, DiPersio, Simon and Merendino (5.38) introduced U_{MIN} instead of V_{MIN} as a cut-off for penetration, and extended their discussion of standoff to the declining portion of the penetration-standoff curve. Still later, Merendino and Vitali (5.39) showed experimentally that high strength aluminum targets are more efficient on a weight basis than high strength steel in reducing jet penetration. This violated the classical density law even when modified to include target strength. The authors explained such behavior in terms of jet fragmentation together with properties of aluminum not yet identified.

In 1977, Walters and Majerus (5.40) proposed a penetration model which included target strength and viscosity as well as inertia. A general formulation was given by Walters (5.41) and a two-dimensional Eulerian formulation suitable for numerical integration was given by both authors shortly after (5.42). In this model three regions in a penetrator were distinguished and radial as well as axial flow was treated. Somewhat different formulations were given for jets and for projectiles. Walters (5.43) also wrote a report on the role of viscosity in jet formation, pointing out that Russian workers usually included viscosity in their theories. Measurements of solid viscosity both here and abroad were also discussed. Finally, Walters and Majerus (5.44) extended their model to include jet break-up by using an effective average jet density lower than the liner density. This they estimated by averaging the density of the jet fragments in the train (equal to the liner density) and the negligible density of the air gaps between these fragments.

The theory of Walters and Majerus seems to be the first attempt since World War II to go beyond a steady-state or "quasi-steady-state" pressure balance in calculating penetration. They use second order differential equations and include a linear velocity decrease in the case of a jet. However, they retain the form $(V-U)$ for the jet speed somewhere near its tip and attempt to define the region over which V is reduced to U . They do not treat addition of mass to the rear of a jet which begins penetration before it is fully formed, and discuss only mass loss at the front. Their model is

simpler than many visco-plastic codes in use, but complicated enough to require fairly elaborate calculations by machine.

More recently, measurements by Haugstad (5.45) and Haugstad and Dullum (5.46) have stimulated renewed interest in compressibility effects, at least for certain target materials like some modern plastics. For example, Flis and Chou (5.47) have developed a model to describe such effects.

VI. AN EXAMPLE OF A JET PENETRATOR

A. Device Characteristics

A shaped charge device consisting of a 42° conical copper liner with base diameter a bit larger than 80 mm, collapsed by composition B explosive has often been referred to as a standard of comparison. Since there is so much data available for this device, we will use it as our example. Fig. 6.1 is a drawing of a central section through this device.

Let H be the height of the cone and X be the axial distance from its apex downward. As the detonation wave sweeps over the cone from its apex to its base, the amount of metal per unit axial distance which is accelerated toward the axis increases for such a hollow cone with uniform wall thickness. This is because the mass of each elementary ring of metal lying between evenly spaced planes perpendicular to the axis increases as we approach the base. Meanwhile, the amount of explosive per unit axial distance decreases, approaching zero at the base of the cone. Consequently, the launch speed, or final axial speed attained by the metal after explosive acceleration, decreases as we approach the base, since the ratio of explosive mass to metal mass decreases.

The rate of mass addition to the rear of the jet can be written as $\dot{M}_R = m(t) V(t)$, where $m(t)$, the mass per unit axial distance being moved, is an increasing function of time, and $V(t)$, its final axial velocity, is a decreasing function of time. Consequently, \dot{M}_R tends to be independent of time.

Although time-dependent measurements of $m(t)$ and $V(t)$ or their product have not been made inside a collapsing cone, indirect estimates of $m(X)$ and $V(X)$ have been made. For early steel cones, Pugh has made such estimates (6.1). For a copper cone of the type we are describing, Allison and Vitali have presented similar results (6.2). The base diameter of their cone was slightly larger and their explosive was unconfined instead of having a thin aluminum case as in Fig. 7.1. However, these are minor differences for our purpose. More recently, Harrison (6.3-4) has compared computational estimates with the experimental estimates made by Allison and Vitali. He found substantial agreement with their results for the nonlinear decline of $V(X)$ with increasing X . His values for the cumulative jet mass M_j were larger than theirs and had a slope, dM_j/dX , which increased more slowly with X , but

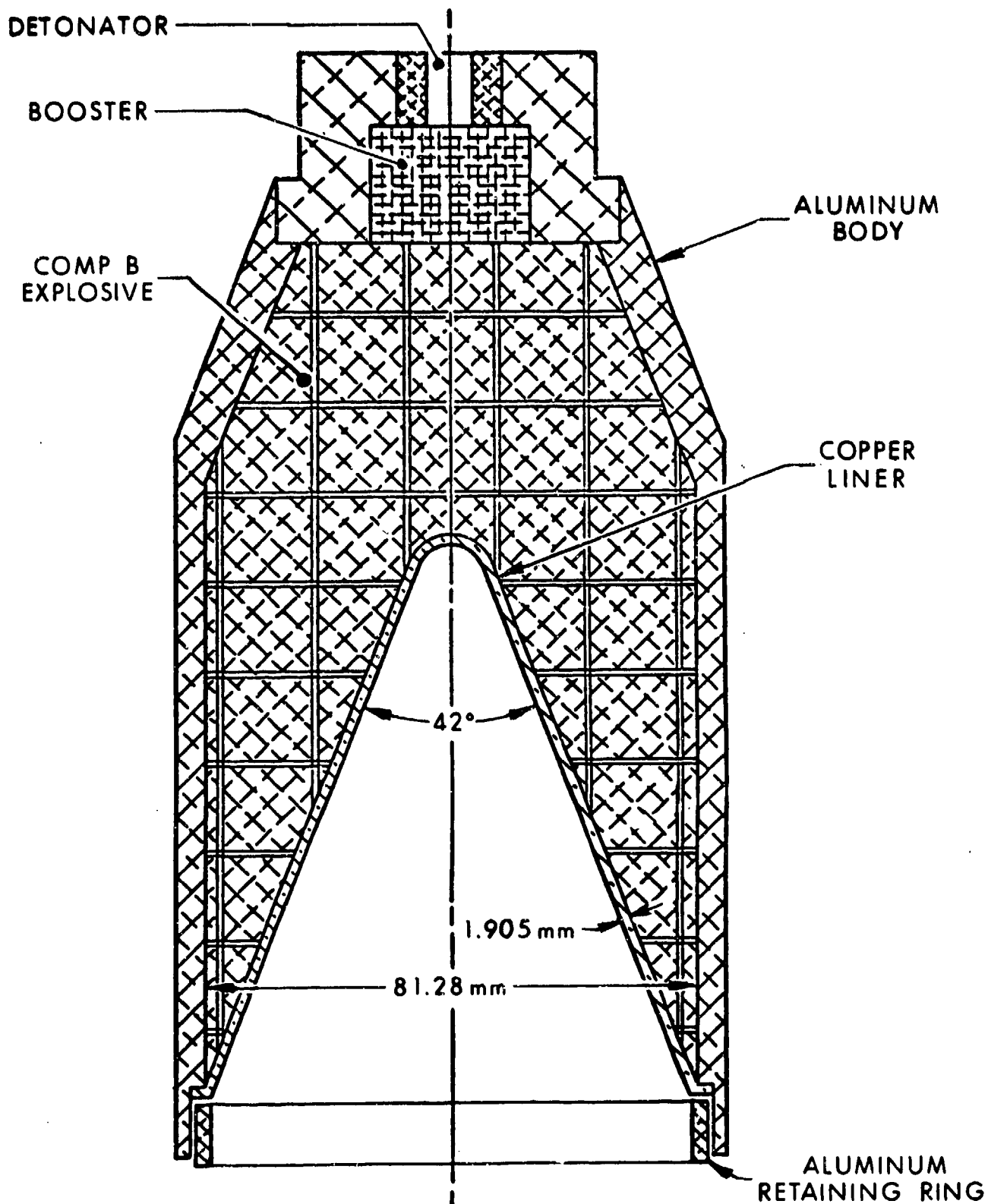


Fig. 6.1. BRL Precision Shaped Charge (81.28mm).

followed the same general trend. Even more recently, Simmons ^(6.5) used a computer program, HEMP, based on a Lagrangian formulation, to study the same problem and compared his results with those of previous computational estimates using a computer program, BRLSC, based on an Eulerian Formulation, as well as with radiographic experiments. His calculations were carried out only for the first 80% of the liner collapse, since computer run times became excessive. He used the theory of Birkhoff et al., ^(5.15) for the remainder, in spite of the fact that his code calculations showed a velocity gradient while this theory assumes it is zero.

The results of Allison and Vitali ^(6.2) are based on experiment but are inferences obtained by using the theory of Birkhoff et al. ^(5.15). The radiographic experiments cited by Simmons are more direct experimental evidence for liner and jet element position versus time, but say nothing about mass. All of the calculations and experiments involve approximations and uncertainties. However, there is general agreement between them, which enables us to estimate the slope, $dM_j/dX = m(X)$, the velocity, $dX/dt = V(X)$, and so the formation rate, $\dot{M}_R = m(X) V(X)$. The result is $\dot{M}_R = 2 \text{ g}/\mu\text{s}$, a value which is substantially constant over the time of jet formation, although it is a bit lower initially and a bit higher toward the end. We also find that the jet tip begins to form on the axis near $X = 40 \text{ mm}$, moving nearly $8 \text{ mm}/\mu\text{s}$, so it should reach the cone base ($X = 120 \text{ mm}$) in about $10 \mu\text{s}$.

According to the estimates cited above, both dM_j/dX and $V = dX/dt$ are nonlinear functions of X inside the cone. However, outside the cone radiographic measurements have established that V varies linearly with distance along the jet length, decreasing from tip to rear ^(6.6 - 6.7). If ρ_p is the jet penetrator density and r is its radius at any point along its length, then $\dot{M}_R = \rho_p (\pi r^2) V$ is an expression for the rate at which mass is added to the rear of the jet during its formation. At any instant in time during jet formation, we can write $V = V_0 + \lambda X$ where V_0 is the constant speed of a particular jet element and λ is a constant. Consequently,

$$\pi r^2 = (\dot{M}_R / \rho_p) / (V_0 + \lambda X) \quad (6.1)$$

Since ρ_p is the constant (liner) density, one consequence of \dot{M}_R being approximately constant is an inverse variation of r with position along the

length of the jet. This decrease from rear to front agrees qualitatively with observations of jet taper like the examples shown in Fig. 6.2 at three different times ^(6.8). The jet shown in Fig. 6.2 was produced by a 45° copper cone of somewhat larger base diameter and wall thickness than that in Fig. 6.1. In addition, the composition B explosive was confined by a steel rather than an aluminum case, and a spitback tube was used at the apex rather than the rounded shape in Fig. 6.1. This last feature is responsible for the tip shape which is a more distinctive bulb than that produced by the device in Fig. 6.1. Otherwise, the main jet features including jet taper are the same. These pictures were selected since they are one of the best examples available in the open literature. About one-fourth of the jet has formed in the bottom picture of Fig. 6.2, while it is almost fully formed in the middle picture. The stretching (and thinning down) which occurs after jet formation is especially clear from a comparison of the middle and top pictures. A conical flare at the rear of the jet as well as the presence of fragmented material between this flare and the slug to follow (not yet visible) are not counted as part of the jet in our description.

When the jet material has stretched to its breaking point, it begins to neck down and separate into fragments. This occurs first near the tip where the jet is thinnest and later toward the rear, when it has thinned down sufficiently. Radiographic estimates of the times involved have been discussed by Chou and co-workers ^(6.9 - 6.10). Part of the uncertainty in such time measurements comes from the difficulty of observing the separation of the pointed ends of jet fragments using radiographs. The time estimated for the beginning of jet breakup is 80 to 100μs after the detonation wave passes the cone apex. If we take the mean value of 90μs and add 10μs (5μs for the wave to reach the portion of the cone which forms the jet tip and 5μs more for this material to be accelerated and form the tip on the axis), we have an estimate for the time at which fragmentation begins, namely $t_2 = 100\mu\text{s}$ from the beginning of jet formation on the axis. Chou and co-workers also estimate that fragmentation is complete in about 150μs.

The report by DiPersio and co-workers ^(6.7) cited above gives data for three sizes of 42° copper cone liners driven by steel-cased composition-B

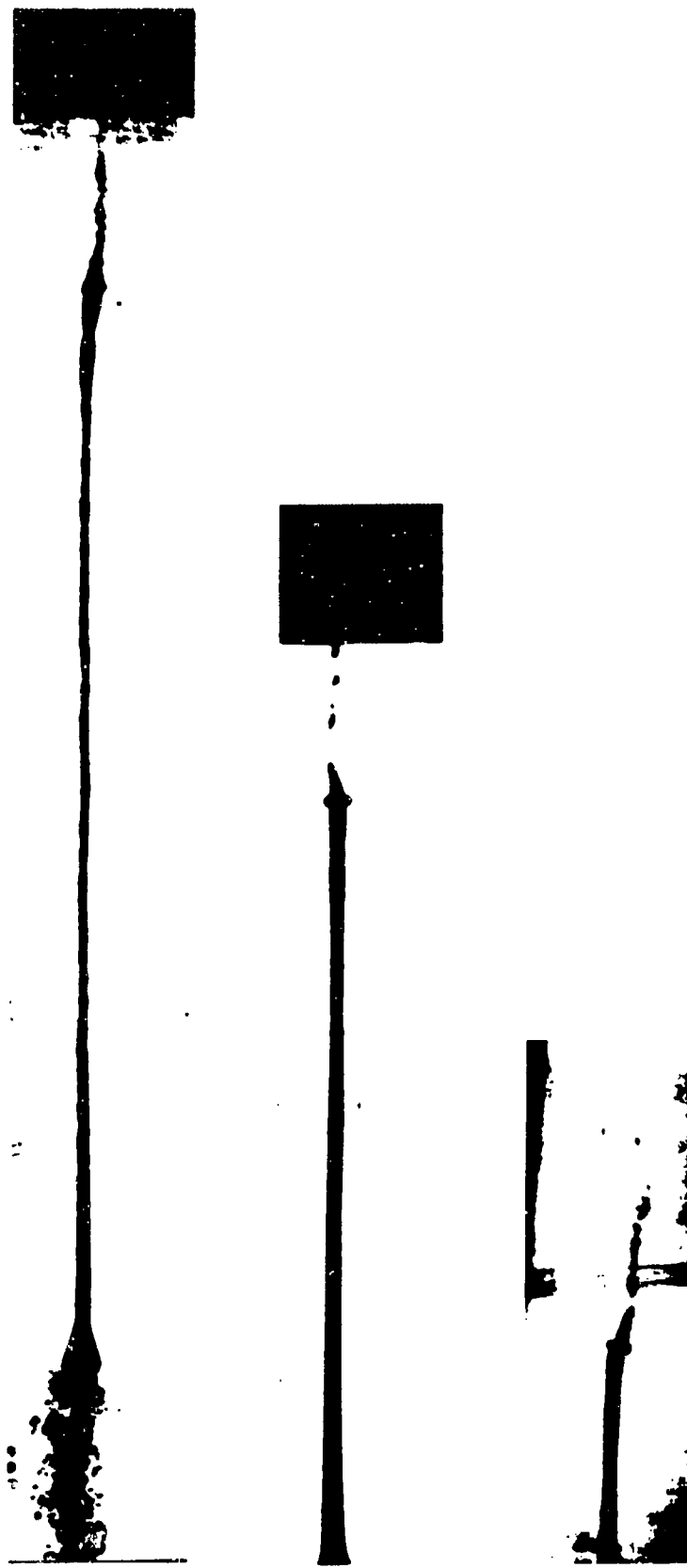


Fig. 6.2. Photographs of a Continuous Jet at Three Times.

explosive, all with rounded apices as in Fig. 6.1. The base diameters were 27 mm, 72 mm, and 96 mm, so the latter two cases bracket our example. They found that the jets from such precision-made devices break into about 50 roughly equal-size fragments, which continue to travel at their original speed without noticeable change in shape, orientation or alignment. This is true for at least 300 μ s, as judged from radiography of particulated jets extended over 240 cm (30CD) ^(6.11). Only the space between these fragments grows with time. DiPersio and co-workers measured the mean diameter of each fragment as well as the sum of their lengths. Then they calculated the volume of jet material by assuming it was a right circular cylinder with this diameter and length and calculated its mass by multiplying this volume by 8.9 g/cm³, the density of copper. If we interpolate their results to obtain the estimates we need for the 81 mm device we are interested in here, we find that the fragments (idealized as right circular cylinders) are each about 1.43 cm long and 0.4 cm in diameter (or .12 cm² cross-sectional area) with a mass of 1.6 g, giving a total jet mass of about 80 g. The actual mean fragment length is closer to 1.5 cm and might be approximated as the major axis of an ellipsoid.

If the jet mass is 80 g and the formation rate is $\dot{M}_R = 2$ g/ μ s, then the time to form the jet is $t_1 = 40 \mu$ s from time zero when the tip first begins to form on the axis near $X = 40$ mm, moving at about 8 mm/ μ s. It takes about 10 μ s for the tip to reach the plane of the cone base, and after 30 μ s more the tip is located about 240 mm beyond the cone base near $X = 360$ mm. At this time ($t = t_1 = 40 \mu$ s) the rear of the jet has just formed near the cone base. Thus, if the standoff distance, S , that is, the distance from the plane of the cone base to the target face, is set equal to 240 mm or 3CD (Cone Diameters), $S = L_0$, the fully-formed jet length at the start of penetration. At time $t_2 = 100 \mu$ s when jet breakup begins, the unimpeded tip will have travelled another 60 μ s or 480 mm and will be located about 240 + 480 = 720 mm beyond the original plane of the cone base. If the rear is moving at, say, 1.2 mm/ μ s, it will be located about 72 mm beyond this plane. Consequently, the jet length at time t_2 is about 648 mm when breakup begins. In other words it has stretched about 408 mm since formation was completed. If $S = 720$ mm (9CD), then penetration starts as breakup begins. Since breakup is complete in about

50 μ s, a much shorter time than the penetration time in semi-infinite targets of interest, then the entire penetration is accomplished by a train of jet fragments. For larger standoffs, the average distance between fragments is greater and the more opportunity they have to become mis-aligned. For smaller standoffs, only part of the penetration will be accomplished by a fragmented jet. This is true even for zero standoff, if the total penetration time is greater than 100 μ s. If t_0 is the time at which penetration begins, and $10 < t_0 < t_1 = 40\mu\text{s}$ ($0 < S < 240 \text{ mm} = 3\text{CD}$), then part of the penetration is accomplished during jet formation. If $t_1 < t_0 < t_2 = 100\mu\text{s}$ ($240 < S < 720 \text{ mm}$), then penetration begins after jet formation is complete ($M_0 = 80 \text{ g}$). Part of the penetration is accomplished by a continuous, stretching jet, while the rest is accomplished by a fragmented jet. For $t_0 > t_2$ ($S > 9\text{CD}$) as already mentioned, a train of jet fragments does the penetrating.

All of the above numbers are approximate although they are based on the best available information. There is no point in attempting to refine them, until better experimental information is available.

Fig. 6.3 is the penetration/standoff curve for this shaped-charge device versus a semi-infinite stack of armor steel plates each 25.4 mm thick. At each of six standoff values a vertical line is shown which connects the highest and lowest values observed, together with a circle indicating the average value. As can be seen, even with a precision device, the experimental uncertainty is considerable, varying from 5 - 10% for $S < 6\text{CD}$ to about 50% near $S = 20\text{CD}$. Generally speaking, the uncertainty is larger the greater the standoff. A notable feature of this curve is the occurrence of a penetration maximum near $S = 6\text{CD}$. This can be interpreted as follows. As S increases from zero, the jet mass when penetration begins grows from $M_0 = 20 \text{ g}$ (for $S = 0$) to $M_0 = 80 \text{ g}$ (for $S = 3\text{CD}$). Understandably, a greater initial mass as well as a greater initial aspect ratio leads to greater penetration. For $3 < S < 6\text{CD}$, no more mass is added, but the initial aspect ratio continues to increase because of stretching. Consequently, the penetration continues to increase. However, a larger portion of the penetration is accomplished by a fragmented jet which counteracts the effect of the increased initial aspect ratio, and the penetration increases more gradually. For S near 6CD most of

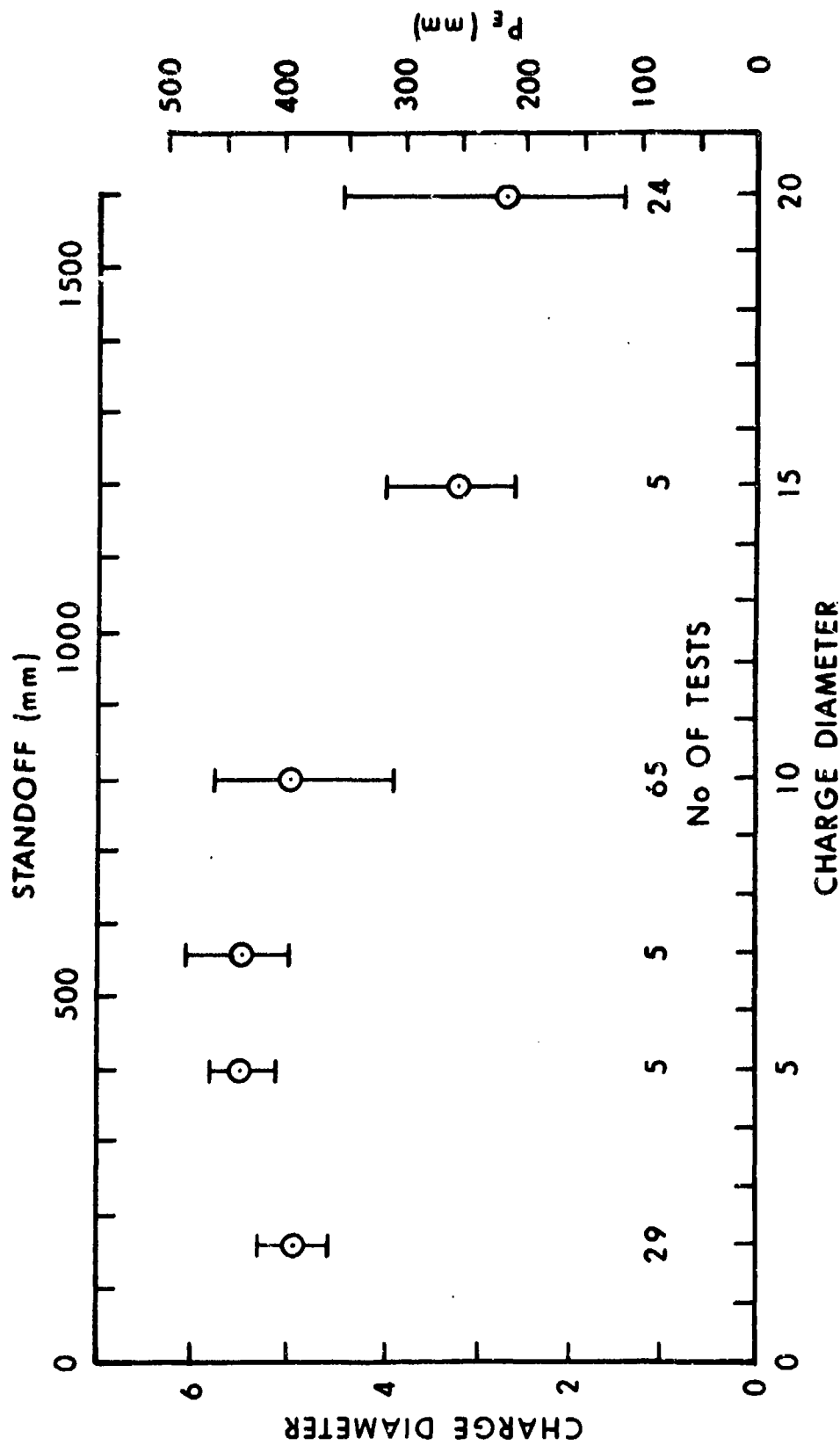


Fig. 6.3. Penetration depth versus standoff for 81mm precision shaped charge against a semi-infinite stack of armor plates.

the penetration is accomplished by a fragmented jet, and for $S \geq 9CD$ all of it is. At greater standoffs the jet is not only fragmented before penetration begins, but the jet particles also have time to become more and more misaligned, leading to lower penetration. The greater spread in the observed penetration at large standoffs also corresponds to this greater misalignment.

B. Penetration by a Train of Rods

1. Experimental Data

a. Rods with Identical Striking Speeds

The fact that a significant portion or even all of the penetration by a jet is accomplished by a train of fragments has stimulated a number of experiments over the years, using a train of identical rods all striking at the same speed. Since the number of rods used has always been quite small and since their speeds are identical, such trains do not simulate a jet which might have 50 fragments with the first and last fragment striking speeds differing by a factor of four or more. If a jet simulation is intended, then it must be for a small section of the train. Of course, a jet simulation need not be intended, since the question of the relative penetrating power of a single rod and the same rod divided into spaced sections can stand on its own merits.

One might conjecture that a series of well-aligned, zero-yaw rods could penetrate deeper than a single rod of the same diameter, material, total length and striking speed. In the case of a single long rod the rear is soon slowed by its connection to the front, long before it has a chance to act on the target directly. If we divide this rod into equal parts and separate them by enough space initially that a following rod strikes the target soon after the preceding rod has been consumed, then the second rod should penetrate as much as the first since it has not been slowed down before acting on the target. If we believe that target "afterflow" is a factor, then we might try to time the arrival of the next rod to take advantage of this movement.

There are some difficulties with this conjecture. First, a deformed residual mass is left in the bottom of the crater, so the next rod must first perforate this mass before acting on the target. This might be especially important if we segment the original rod into sections with $L_0/D_0 = 1$ for which the erosion rate seems to be zero. If the target and projectile are both soft enough to allow a rod to spread out in a thin layer, this problem may not be severe. However, a hard target may confine the residual rod mass enough to offer a significant obstacle to the next rod. Such effects could be cumulative, eventually preventing the last rod in a long train from ever reaching the crater bottom. Second, if we divide the original long rod into a number of equal segments of the same diameter, both the mass and the aspect ratio of the segments will be less than that of the original rod. As we have seen, smaller mass and aspect ratio both favor smaller penetration. Finally, there is no convincing evidence that "afterflow" is a significant factor in targets of interest.

In summary, there may be cases in which penetration is improved or degraded if we divide a long rod into equal segments. The fact that jet penetration is degraded after breakup, as implied by a decrease in penetration at large standoff, does not give us the answer for the case of a short train of well-aligned rods all striking at the same speed.

Christman and Gehring ^(6.12) seem to have been the first authors to report on the penetration ability of such "tandem" rods. They fired 2024-T3 aluminum rods at 4 mm/ μ s into 1100-0 aluminum targets. A single rod with $L_0/D_0 = 19.05 \text{ mm}/3.175 \text{ mm} = 6$ penetrated 27 mm, a single rod with $L_0/D_0 = 9.525 \text{ mm}/3.175 \text{ mm} = 3$ penetrated 15.7 mm, more than half the first value. Two such $L_0/D_0 = 3$ rods fired at the same spot a long time apart gave a total penetration of 28 mm, about the same as the $L_0/D_0 = 6$ rod. "Tandem" $L_0/D_0 = 3$ rods spaced about 3 mm and 10 mm apart, and so striking about 1 μ s and 2.5 μ s apart, give total penetrations of about 20 mm and 23 mm respectively, both considerably less than the 27 mm or 28 mm values above. However, the interpretation of these results is very difficult because of the large yaw and misalignments which were involved.

Perez and Giraud ^(6.13) used a long steel rod and a hard aluminum target in a reverse ballistics mode with an impact speed of 2 mm/ μ s. As they

divided their rod they found a decrease in penetration with increasing number of rod segments. Increasing the spacing between their rod segments had no effect on this result, which they attributed to blockage of one rod by the residual mass of the preceding rod. They compared their own results with those of Chou et al (6.14 to 6.16). These authors shot short bullets made of lead, copper-jacketed lead or tin at about 1 mm/ μ s, mostly into lead targets (although other soft target materials were also considered). They tried cases in which the masses of their two bullets were the same as well as cases in which the first bullet was larger (longer) or smaller (shorter) than the second. A 10 μ s delay between the two bullets seemed to give some increase in penetration over no delay, at least in some cases. However, delays of 30 to 100 μ s gave worse penetration. Two bullets fired minutes apart did the best of all. They attributed their results to partial occlusion of the first crater by flowing target and projectile material, which impeded the second bullet.

About the same time, Moore (6.17) used steel versus steel and claimed a large increase in penetration due to rod division. He compared trains of two or three rods with zero separation to a single rod on the basis of something he called the "diameter of an equivalent cylinder," that is, a cylinder of the same volume but with an aspect ratio of one. This method of comparison is misleading, since it artificially penalizes the original long rod by forcing it to have an incorrect aspect ratio. The same procedure also artificially penalizes a two-rod train compared to a three-rod train. It is not believable that one can make a better penetrator by simple division without spacing. Perhaps his comparison of a two-rod group to itself with different spacings between the rods has some validity, if the reported differences were outside of experimental error (not discussed). The same might be true of his three-rod group. However, only data normalized in terms of the "diameter of an equivalent cylinder" was reported so it is impossible to recover the original data with which one might make an evaluation.

b. A Train of Jet Fragments

The approximation that the fragments in such a train are alike in size and shape is probably good enough for most practical purposes. However, if we

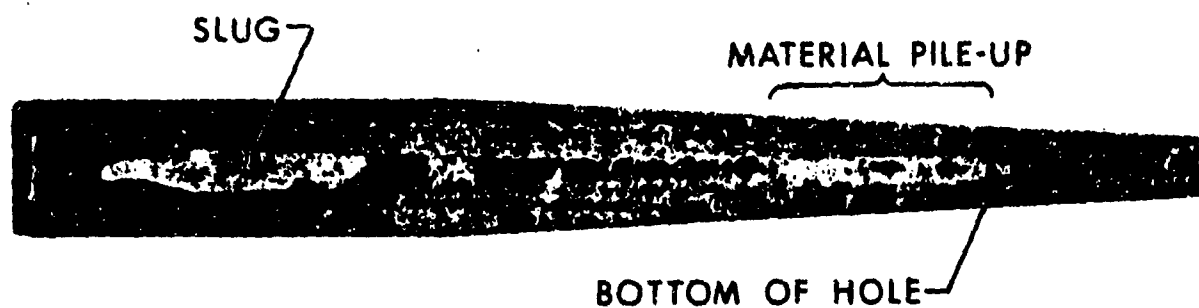


Fig. 6.4. Photograph of a Sectioned Armor Target after Penetration by a Precision 3.3 inch charge. Jet-target material has plugged bottom of hole. Slug is wedged in armor at the top.

wish to consider a train of 50 fragments or even a significant fraction of such a train, we cannot ignore the factor of four decrease in striking speed which exists in such a train.

Simon and DiPersio (6.18) used solid billets of armor steel or aluminum as targets for such a jet. They were able to radiograph the jet during penetration of the aluminum billets by making them slender enough. However, they had to section the steel billets lengthwise in order to study the results of a penetration. In all cases large amounts of copper from the jet were found in the craters. For at least one steel target the slug was also found wedged near the top of the crater as shown in Fig. 6.4. The buildup of copper in the crater was found to increase as the standoff was increased from $S = 4$ to $S = 12$ to $S = 16CD$. This increase could be associated with the transition from a case in which only part of the penetration was by a fragmented jet to cases in which all of the penetration was by such a jet, whose fragments had more time to become misoriented and misaligned as the standoff increased. Blockage and interference effects were cumulative and a point was reached where many of the fragments from the rear of the jet never reached the bottom of the crater. They chose to describe their observations in terms of a cutoff velocity, which they interpreted as the speed of the slowest fragment which was still able to deepen the crater. Fragments which had speeds slower than this merely penetrated copper and added to the buildup.

In an earlier report (6.19) these authors contrasted the accumulation of copper in the crater made in a truly solid target with the absence of such an accumulation in a target consisting of a stack of plates. In the latter case "this jet material is forced out between the target plates and can be seen on the plate surfaces." Unfortunately, we don't have much quantitative information on possible differences in depth of penetration in a stack of plates compared to penetration in a truly solid target. It seems likely that the thickness of the plates used in a stack should have some influence on the escape of eroded material with consequent reduction in interference and possible increase in penetration. In the extreme case of a single plate which qualifies as semi-infinite, it is clear that escape is minimized and interference maximized. Perhaps the reverse is true if a large number of very thin plates is used in a "semi-infinite" stack.

Radiographic evidence and soft copper rod recovery experiments indicate that there can be room for a straight, continuous jet to move down the center of a tube of eroded jet material without being impeded, at least in most metal targets (see Figs. 4.2 and 4.3). However, this is probably not true after jet breakup. Even slight misalignments of the jet fragments could lead to contact with the material coating the cavity wall. In addition, once a series of fragments begins to strike, it generates a series of interrupted and probably irregular short tubes rather than the continuous tube generated by a continuous jet. The combination of such effects can be cumulative and lead to so much interference and material pile-up that the last jet particles never reach the bottom of the cavity in a truly solid target. This effect should decrease in a stack of plates and may even disappear if the plates are thin enough.

2. Models of Penetration by a Fragment Train

Rinehart (6.20) proposed a simple method of describing penetration by a fragment train. He assumed that each fragment makes a spherical crater of diameter, P_i , and volume $(\pi/6) P_i^3 = f_o^{-1} (.5 M_i V_i^2)$, where f_o is an empirical constant. Here he adopted the suggestion by Hill, Mott and Pack (5.4) that the crater volume should be proportioned to the kinetic energy of a penetrator of mass M_i and speed V_i . If we solve this relation for P_i and sum the contributions of each fragment, the total penetration depth is

$$P_E = (6f_o^{-1}/\pi)^{1/3} \sum_{i=1}^N (.5 M_i V_i^2)^{1/3} \quad (6.2)$$

where $N = 50$ for the jet we are considering while $M_i = 1.6g$ for all i . If we assume that all the fragments have the same (average) speed, $V_i = 5 \text{ mm}/\mu\text{s}$, then $f_o = [2/(9\pi)] (g \text{ mm}/\mu\text{s}^2)/\text{mm}^2$ gives P_E close to 400 mm. This is nearly equal to the maximum of the curve in Fig. 6.3. To describe the whole curve, f_o must somehow depend on standoff.

Alexander and Finnegan (6.21) considered penetration by a cluster of spheres which were not necessarily aligned and did a dimensional analysis to describe the net "invasion depth." At the same symposium, Golesworthy (6.22), Held

(6.23), and Szendrei (6.24) all proposed models to describe the crater made by a train of jet fragments. The following year, Held (6.25) expanded his discussion to include the effect of transverse velocity such as might be imposed in a fly-over, shoot-down mode of attack.

About the same time, Segletes (6.26) proposed a similar model to describe crater formation by a train of jet fragments. He used measured values of the velocity components of each jet fragment in a train to calculate the observed hole profiles. By superimposing ellipsoidal craters produced by individual fragments he was able to reproduce experimental observations. For example, Fig. 6.5 shows his hole profile calculations (two orthogonal views) for a well-aligned train at a standoff of 23CD. Fig. 6.6 shows orthogonal views for a badly aligned train at 38CD standoff. One view shows the production of a dual crater, one branch slightly less than 1CD deep, the other slightly more. Segletes' method requires measurements on individual fragments and does not include a statistical generalization to describe the expected performance of a batch of devices all nominally the same. He chose to base his estimate of penetration by each fragment on the wave refraction theory of Fitzgerald (6.27). In this theory, Fitzgerald attempts to apply quantum mechanics to macroscopic deformation theory, an effort which has not gained wide acceptance. Of course, there is no need to choose such a basis, since a simple assumption of an ellipsoidal shape would suffice. More recently, Segletes (6.28) expanded his model to include the effect of a superimposed transverse velocity resulting from a fly-over attack mode.

In this report we will only be concerned with penetrations by trains of jet fragments which have no superimposed transverse velocity component. We assume that all the fragments are alike and idealize them as right circular cylinders with $L_o/D_o \approx 14 \text{ mm}/4 \text{ mm} = 3.5$ and $M_o = 1.6 \text{ g}$. If we assume that the erosion rate is such that $c = 0$, we can use Eq (2.27). The argument of the exponential in this equation becomes

$$(1 + .5\sqrt{\rho_t/\rho_p}) [\sqrt{\rho_p \rho_t}/6] (\dot{S}_o/k)^2/Y_t \sim 2.2 \times 10^{-3} (\dot{S}_o/1.5)^2/Y_t \quad (6.3)$$

when we use $u_o = (\mu_o)_{MAX}$. The approximate form holds for $\rho_t \sim \rho_p = 8.9 \times 10^{-3} \text{ g/mm}^3$. Our fragment speeds vary from $S_o \sim 7.5 \text{ mm}/\mu\text{s}$ to

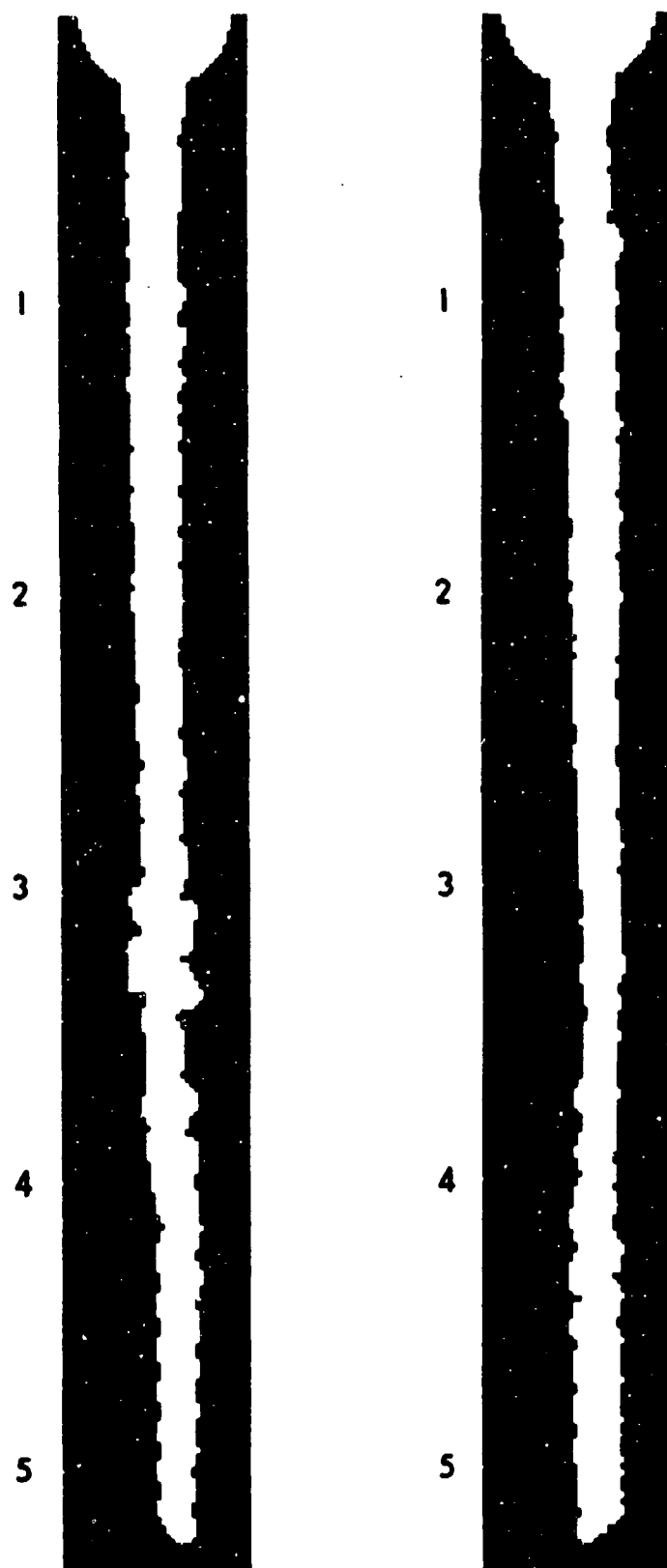


Fig. 6.5. PENJET Predictions of Hole Profile for Round 2937 at 23CD Standoff. Penetration in Cone Diameters.

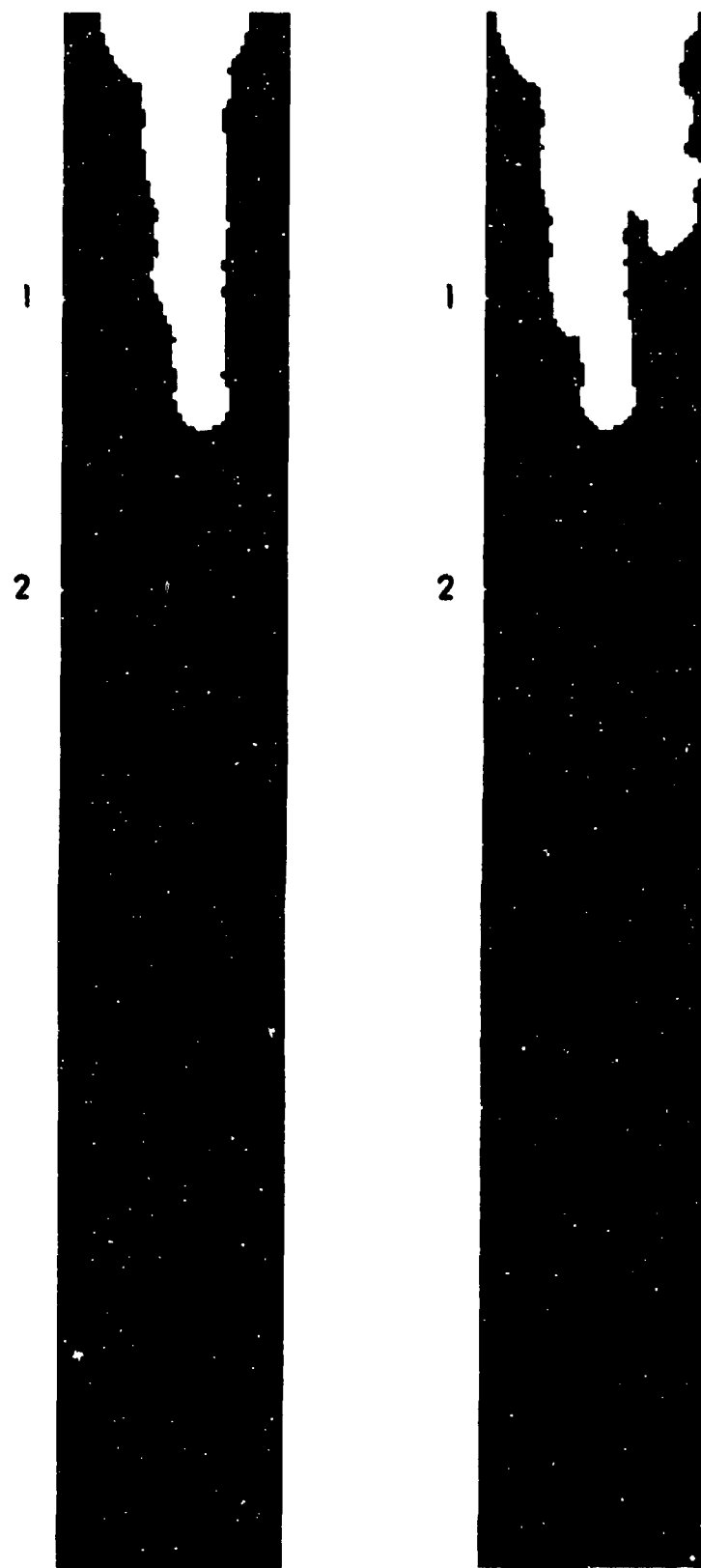


Fig. 6.6 Orthogonal Views of Projected Hole Profile of Round 2331 at 38CD Standoff as Predicted by PENJET. Penetration in Cone Diameters.

$S_0 \sim 1.5 \text{ mm}/\mu\text{s}$, so Eq (6.3) varies from $.055/Y_t$ to $.002/Y_t$. For an armor steel target $Y_t \sim .001 \text{ (g mm}/\mu\text{s}^2\text{)}/\text{mm}^2$, so the exponential correction factor is negligible for most of the (faster) fragments which penetrate about $L_0/\sqrt{A/A_0} \sim 10 \text{ mm}$ if $A/A_0 \sim 2$. However, for a slow fragment the correction factor is about 0.1 so it penetrates about 9 mm. For a weak target like lead, Y_t is 100 times smaller, so the correction factor will be negligible for every fragment in the train. In general, we will find smaller erosion rates, so $c > 0$ and Eq (2.22) must be used instead of Eq (2.27).

We should be able to add the penetrations by each fragment if (1) they are well-aligned, (2) there is no interference with the incoming fragments by the mass flow, and (3) each fragment is completely eroded before the next one strikes. The first two conditions tend to hold shortly after jet breakup, although the third condition may not be true at this time. The opposite tends to be true long after jet breakup and for the slower fragments. Unless there is an air gap about equal to the length of a fragment between successive fragments, we expect the nose of a following fragment to strike the rear of the one in front of it before it has been eroded. The problem is quite complicated and cannot be treated in the context of a one-dimensional model of the type we are discussing. Even a three-dimensional treatment should be statistical, since we want to describe the performance expected from a typical sample taken from a batch of devices. Here we will content ourselves with a temporary expedient, namely, the use of an empirical efficiency factor, applicable for standoff $S \geq 10\text{CD}$:

$$E = 2 \exp (-.0693 S) \quad (6.4)$$

with $E = 1$ for $S \leq 10\text{CD}$. The form chosen for Eq (6.4) is geared to the standoff curve in Fig. 6.3 for the jet we are considering versus a stack of armor steel plates and is not meant to apply to other situations. The choice of $E = 1$ for small standoffs implies that whatever part of a penetration is accomplished by a fragment train is close to the additive ideal. The exponential decrease is meant to approximate the behavior at large standoff in Fig. 6.3. We note that for $S \sim 65\text{CD}$, $E \sim .02$ so the penetration by a very inefficient train of 50 fragments is equivalent to that of a single

representative fragment. At very large standoffs fragment dispersion increases and the likelihood of two fragments striking the same spot decreases. However, such a purely empirical formula like Eq (6.4) cannot be expected to give correct quantitative predictions for extreme cases.

C. Calculational Aids

In order to apply the theory described by Eqs (2.42) to (2.83) above, we must estimate a number of parameters.

For a given standoff, S , we need to know the time, t_0 , when penetration begins, taking as our zero time the moment the jet tip is formed on the axis. We can let

$$t_0 = 10 + S/8 \quad (6.5)$$

since it takes about $10\mu s$ for the tip to reach the cone base if it travels at $8 \text{ mm}/\mu s$. Thus, if $S = 240 \text{ mm} \sim 3CD$, $t_0 = 40\mu s = t_1$, and the jet has just finished forming as penetration starts. The jet mass initially is

$$M_0 = \dot{M}_R t_0 = 2(10 + S/8) \quad (6.6)$$

since $\dot{M}_R = 2 \text{ g}/\mu s$. Of course $M_0 = 80 \text{ g}$ for $t_0 \geq t_1$. The jet length when penetration begins might be estimated from

$$L_0 = 60 + 3S/4 \quad (6.7)$$

Thus for $S = 0$, $L_0 = 60 \text{ mm}$, about half the cone height in agreement with radiographs of a collapsing cone taken as the jet tip reaches the plane of the base. For $S = 240 \text{ mm} = 3CD$, $L_0 = S$, which should be the fully-formed jet length at $t = 40\mu s$. For $S = 720 \text{ mm} = 9CD$, $L_0 = 600 \text{ mm} = 7.5CD$. This should be the fully-stretched jet length at $t = 100\mu s$. Since the jet has stretched 360 mm in about $50\mu s$, the stretching rate $L = 360 \text{ mm}/50s = 7.2 \text{ mm}/\mu s$.

If we divide Eq (6.6) by Eq (6.7) with 6 factored out, we find $M_0/L_0 = 1/3 \text{ g/mm}$ for any start time during jet formation. Since the space

average initial cross-sectional area is defined as $A_0 = (M_0/L_0)/\rho_p$, then $A_0 = .375 \text{ cm}^2$ for $0 < S \leq 240 \text{ mm}$. Since the mass stretching rate in Eq (1.27) is $\dot{u} = \rho_p L |\dot{A}_0|$, the constancy of A_0 implies $\dot{u} = 0$. However, for larger standoffs, $M_0 = 80 \text{ g}$, so

$$A_0 = 80 \text{ g}/(\rho_p L_0) \approx 15/(10 + S/8) \text{ cm}^2 \quad (6.8)$$

by Eq (6.7). Thus, for $S = 720 \text{ mm}$, $t_0 = 100\mu\text{s}$, and $A_0 = .15 \text{ cm}^2$ by Eq. (6.8). For $S = 1,120 \text{ mm}$, $t_0 = 150\mu\text{s}$, $A_0 = .10 \text{ cm}^2$. This is close to the value $A_0 = .12 \text{ cm}^2$ which we estimated above for a jet fragment idealized as a right circular cylinder.

We are making two kinds of approximation. One is the use of approximate numerical values such as $8 \text{ mm}/\mu\text{s}$ for the tip speed (instead of $7.6 \text{ mm}/\mu\text{s}$) and 80 mm for the cone diameter (instead of 81.28 mm as in Fig. 6.1). More accurate values could be used without complicating the theory. However, these values are good enough for our purpose. We are also using another kind of approximation in order to avoid unmanageable complications in our theory. For example, we are using an average area, A_0 , which does not change in time. For a stretching jet, $A_0 \neq 0$, a fact which we account for by the factor \dot{u} . If we let A_0 be a function of time, then we would not be able to integrate Eq (2.45) so simply. Since A_0 does not change greatly for most calculations of practical interest, and since we do not know what function of time to use, we have avoided this unnecessary complication. We are interested in the jet area just behind the mushroom cap, which is always smaller than A_0 , the average over the jet length. We estimated $A_0 = .375 \text{ cm}^2$ for $S < 3CD$, so the area of interest will be smaller, probably less than $.3 \text{ cm}^2$. The tip of our jet is bulbous, so taking $A_0 = .3 \text{ cm}^2$, a bit on the high side, should tend to compensate for neglecting to treat the tip separately. When the jet is fully stretched, A_0 is near $.15 \text{ cm}^2$, about half its value during formation.

For calculational purposes, during a given time period, we will take the time average value of the area of interest to be equal to the average of A_0 at the beginning and end of the period as estimated from Eqs. (6.5) and (6.8). For example, if the period extends from $40\mu\text{s}$ to $100\mu\text{s}$, we find $A_0 = .3 \text{ cm}^2$ at $40\mu\text{s}$, the value we assumed for jet formation, and $A_0 = .15 \text{ cm}^2$ at $100\mu\text{s}$. This

gives an average A_0 of $.225 \text{ cm}^2$. If the period extends from $40 \mu\text{s}$ to $70 \mu\text{s}$ ($S = 480 \text{ mm}$ from Eq (6.5)), the average A_0 is $.5 (.3 + .21) = .255 \text{ cm}^2$, and so on. For penetration during jet formation, A_0 is the same at the beginning and end of any period, so the average value is $A_0 = .3 \text{ cm}^2$.

We recall that $\dot{m} = \rho_p L |\dot{A}_0| = \rho_p \dot{L} A_0$ when no mass is being added. Here $\rho_p = 8.9 \text{ g/cm}^3$ and $\dot{L} = .72 \text{ cm}/\mu\text{s}$ as mentioned above. Once we have found A_0 for the particular time period we are considering, we can calculate \dot{m} .

In order to estimate the erosion rate, μ_0 , we recall section f of Chapter IV. There we saw rates for a high aspect ratio $L_0/D_0 = 60 \text{ mm}/3 \text{ mm} = 20$ copper rod of cross-section $A_0 = .0706 \text{ cm}^2$, at least at low speeds. Since we are assuming that μ_0 is independent of speed, we can use our previous method to estimate erosion rates for our copper jet. For example, we found $\mu_0 = .055 \text{ g/mm}$ for the rod versus a steel target. If we multiply this value by $(A_0/.0706)$, where A_0 is the jet area, we can estimate μ_0 for the jet. Since the jet has a higher aspect ratio than the rod, we expect a slightly lower erosion rate. For example, for $A_0 = .3 \text{ cm}^2$, we estimate $\mu_0 = .2 \text{ g/mm}$ for the forming jet versus steel. Similarly, we can use the rod values of $.032 \text{ g/mm}$ versus aluminum and $.059 \text{ g/mm}$ versus copper, multiplied by suitable factors. For a jet fragment with an aspect ratio of 3.5, we expect a higher value than we would find from using the rate for an $L_0/D_0 = 20$ rod, as explained above. For example, instead of about $.1 \text{ g/mm}$ for $A_0 = .12 \text{ cm}^2$, we might expect $\mu_0 = .15 \text{ g/mm}$ for a jet fragment versus steel. Thus, against a steel target our estimates for μ_0 will be $\leq .2 \text{ g/mm}$, depending on the stage of penetration. If all 80 g of jet were eroded at the rate of $.2 \text{ g/mm}$, this would require 400 mm of penetration. If lower rates applied to part of the penetration, we expect somewhat greater penetration, in agreement with the curve in Fig. 6.3 for mid-range standoff values.

D. Penetration/Standoff for Armor Steel

1. Standoff $\approx 2CD$

Merendino and Vitali (6.29) obtained the penetration/time curve in Fig. 6.7 for $S = 2CD$. They reported a final penetration depth, $P_E = 397 \text{ mm}$,

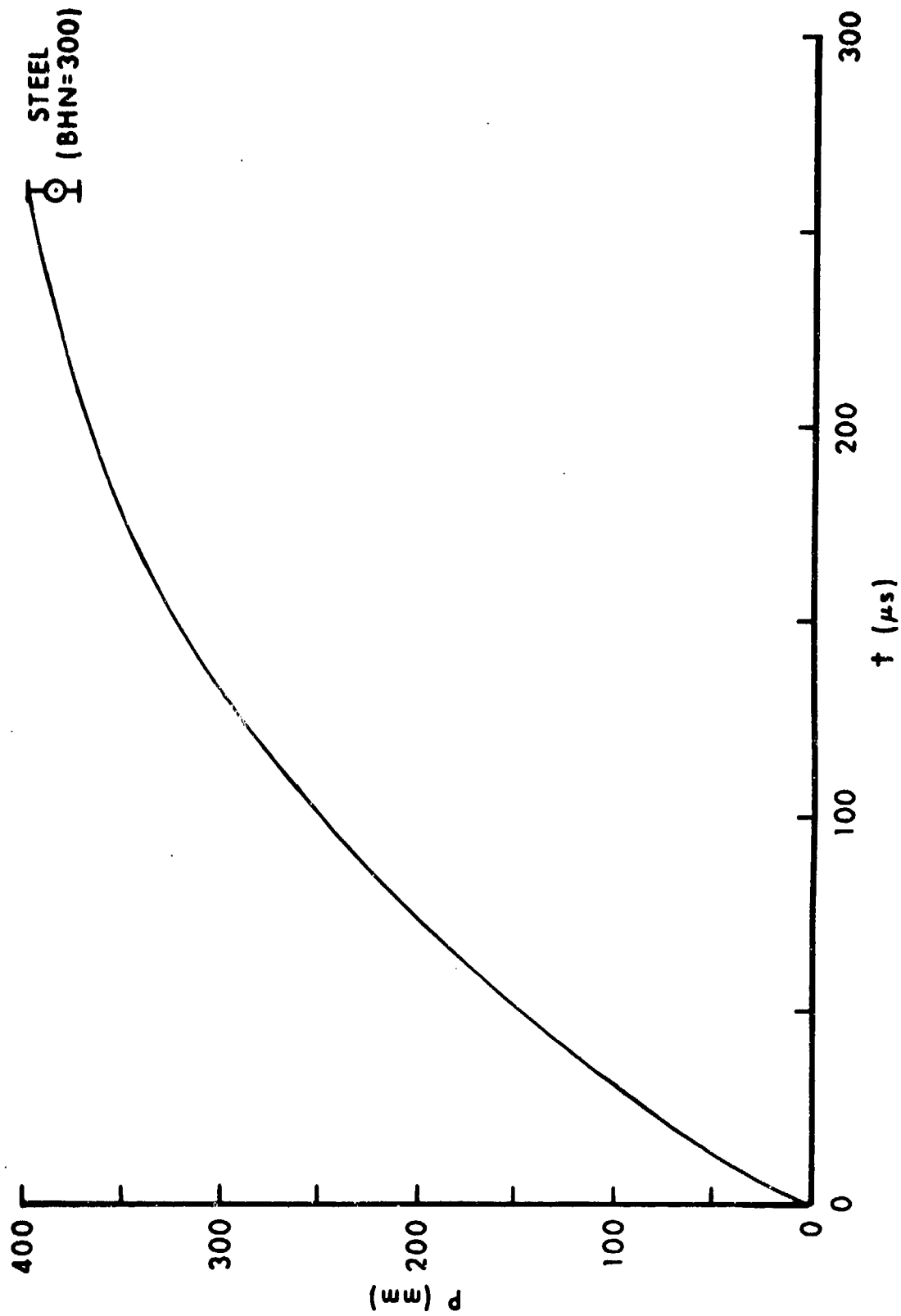


Fig. 6.7. Jet versus armor steel (BHN = 300) at 2CD Standoff.

reached 250 μ s after the start of penetration. In four such tests, the maximum penetration was 399 mm, the minimum was 374 mm and the average was 386 mm, also shown in the figure. We see that these values are representative of the 29 values averaged in Fig. 6.3. The armor steel target plates had BHN = 300 kg/mm².

a. $t_0 \leq t \leq t_1$

If we use $S = 160$ mm in Eq (6.5), we find $t_0 = 30\mu$ s. With this value we find $M_0 = 60$ g from Eq (6.6), and $L_0 = 180$ mm from Eq (6.7). We also take $A_0 = .3$ cm², since $S < 240$ mm. This first stage of the penetration only lasts 10 μ s, since jet formation is complete when $t = 40\mu$ s.

As explained above, we estimate $\mu_0 = .2$ g/mm during formation. In addition, $I_0 = 1.87$ mm/g, $k = 1.44$ and $P_0 = 5.6$ mm/ μ s. The penetration speed drops rapidly at first, then decreases more slowly. The average value of the slope in Fig. 6.7 during this period is about 4 mm/ μ s. Consequently, the average time rate of erosion is $\dot{M}_F = (.2 \text{ g/mm})(4 \text{ mm}/\mu\text{s}) = .8$ g/ μ s in Eq (2.42). If we did not have prior knowledge as in Fig. 6.7, we could iterate the entire calculation until a self-consistent average value emerged. Since the mass addition rate at the rear has been estimated to be $\dot{M}_R = 2$ g/ μ s, then $\dot{M}_0 = 2 - .8 = 1.2$ g/ μ s in Eq (2.42). Then $M_1 = 60 + 1.2(40 - 30) = 72$ g at the end of this stage of the penetration from Eq (2.43).

For high-speed penetration by rods we have learned to estimate a flattening factor of $A/A_0 = 2$. For an armor steel target we find $a_0 = .081$ g mm/ μ s² and so $a = .162$ g mm/ μ s², since $A_0 = .3$ cm². Similarly $c = .236$ g/mm. Since $\dot{\mu} = 0$ during formation as explained above, Eq (2.46) gives $a = .162 - (1.87)(1.2)(1.2 + 4) = -11.5$ g mm/ μ s². From Eq (2.47) with $b = 0$, we find $b_F = 4$ g/ μ s. Then $\Delta_F = -26.9$ (g/ μ s)² < 0 with $\sqrt{-\Delta_F} = 5.18$ g/ μ s, so Eqs (2.57) to (2.61) apply. We find $\gamma^+ = (-4 + 5.18)/.472 = 2.5$ mm/ μ s and $\gamma^- = -4 - 5.18)/.472 = -19.5$ mm/ μ s. In addition, $\dot{\mu}_0 = \dot{M}_0/\sqrt{-\Delta_F} = 1.2/5.18 = .23$. From Eq (2.59), $G_0 = (5.6 - 2.5)/(5.6 + 19.5) = .12$, and $G_1 = .12[1 + 1.2/60(40 - 30)]^{-1/.23} = .05$. From Eq (2.57) we find the

speed at time t_1 to be $\dot{P}_1 = [2.5 + 19.5 (.05)] / (1 - .05) = 3.7 \text{ mm}/\mu\text{s}$. In order to find the penetration depth, P_1 , from Eq (2.58), we must evaluate two special integrals:

$$B_1(\epsilon_F) = B_1(.23) = \int_{.05}^{.12} [x^{-.23}/(1-x)] dx$$

$$= .07 [.174 (2.063 + 1.858) + .326 (1.969 + 1.894)] = .14 \quad (6.9)$$

$$B_1(1 + \epsilon_F) = B_1(1.23) = \int_{.05}^{.12} [x^{-1.23}/(1-x)] dx$$

$$= .07 [.174 (37.57 + 16.14) + .326 (26.94 + 19.55)] = 1.72 \quad (6.10)$$

using the four-point Gauss Method. Then Eq (2.58) gives

$$P_1 = (60/5.18)(.05)^{.23} [2.5 (1.72) + 19.5 (.14)] = 41 \text{ mm} \quad (6.11)$$

which agrees closely with Fig. 6.7 after 10 μs of penetration.

$$b. \quad \underline{t_1 \leq t \leq t_2}$$

Since $t_1 = 40\mu\text{s}$ and $t_2 = 100\mu\text{s}$ with $t_0 = 30\mu\text{s}$, we are considering the time period from 10 μs after penetration begins to 70 μs after penetration begins. The initial values for this stage of the penetration are the final values of the previous stage, namely, $M_1 = 72 \text{ g}$, $\dot{P}_1 = 3.7 \text{ mm}/\mu\text{s}$ and $P_1 = 41 \text{ mm}$. We can subdivide this 60 μs time period into as many intervals as we like, using the final values of one interval as the initial values of the next. As an illustration, we will treat the entire period as a single interval. As discussed above, the time-average value of the length-average area is $A_0 = .225 \text{ cm}^2$. From this we estimate $\mu_0 = .18 \text{ g/mm}$, $I_0 = 2.5 \text{ mm/g}$ and $k = 1.45$. With $(A/A_0) = 2$, we find $a = .12 \text{ g mm}/\mu\text{s}^2$ and $c = .18 \text{ g/mm}$. In addition, $\dot{\mu} = (8.9 \text{ g/cm}^3)(.72 \text{ cm}/\mu\text{s})(.225 \text{ cm}^2) = 1.44 \text{ g}/\mu\text{s}$. From Eq (2.65) with $b = 0$, we find $\bar{b} = .58 \text{ g}/\mu\text{s}$ and from Eq (2.66), $\bar{c} = .11 \text{ g/mm}$. From Eq (2.67) $\Delta = -.284 (\text{g}/\mu\text{s})^2$ and $\sqrt{-\Delta} = .53 \text{ g}/\mu\text{s}$, so Eqs (2.76) to (2.80) apply. Moreover, $\bar{e} = .18/.11 = 1.64$ so $\bar{e}k^2 = 1.15$. Since $\beta^- = .58/.53 = 1.09$, we

have $\beta^-(\bar{\epsilon}k/2) = 1.25$. From Eq (2.78) we find

$$\gamma^+ = (-.58 + .53)/.22 = -.23 \text{ mm}/\mu\text{s} \text{ and } \gamma^- = (-.58 - .53)/.22 = -5.05 \text{ mm}/\mu\text{s}.$$

Also $G_1 = (3.7 + .23)/(3.7 + 5.05) = .45$, and from Eq (2.64)

$$F_1 = .12 + .58 (3.7) + .11 (3.7)^2 = .12 + 2.15 + 1.5 + 3.77 \text{ g mm}/\mu\text{s}^2. \text{ Then from Eqs (2.79) and (2.80) we find}$$

$$D^- = [(100 - 40)/(1.45 \times 72)] (3.77)^{1.15} (.45)^{-1.25} = 7.4$$

$$= \int_{\dot{P}_2}^{3.7} (.12 + .58x + .11x^2)^{.15} [(x + .23)/(x + 5.05)]^{-1.25} dx \quad (6.12)$$

From this equation we find $\dot{P}_2 = 1.8 \text{ mm}/\mu\text{s}$, since

$$D^- = 1.9 [.174 (4.666 + 3.374) + .326 (4.095 + 3.621)] = 7.4 \quad (6.13)$$

Now we can use this value of \dot{P}_2 to find $F_2 = .12 + .58 (1.8) + .11 (1.8)^2 = .12 + 1.04 + .36 = 1.52 \text{ g mm}/\mu\text{s}^2$ and $G_2 = (1.8 + .23)/(1.8 + 5.05) = .296$.

Then Eq (2.76) gives

$$P_2 = 41 + (72/.18) \left\{ 1 - \left(\frac{1.52}{3.77} \right)^{1.15} \left(\frac{.45}{.296} \right)^{1.25} \right\}$$

$$= 41 + 162 = 203 \text{ mm} \quad (6.14)$$

close to the value in Fig. 6.7 after 70 μs of penetration. From Eq (2.62) we find $M_2 = 72 - .18 (203 - 41) = 72 - 29 = 43 \text{ g}$. Thus $80 - 43 = 37 \text{ g}$ of jet have been used during the first two stages of penetration.

$$c. \quad \underline{t_2 \leq t \leq t_E}$$

Experimentally, the entire penetration took about 250 μs , so $t_E = 280 \mu\text{s}$ when we add 30 μs , counting from our zero time. Since $t_2 = 100 \mu\text{s}$, this last stage of the penetration takes about 180 μs compared to 70 μs for the first two stages combined, which accomplished about half the total penetration with an expenditure of slightly less than half the mass. Since each fragment on average is 1.6 g, it takes over 2.5 times longer for $43/1.6 = 27$ fragments to

accomplish the other half of the penetration, even though this is an almost ideal train with an efficiency of $E = 1$. This is because the striking speeds range from a high of $\dot{P}_2 = 1.8 \text{ mm}/\mu\text{s}$ to a low of about $1.2 \text{ mm}/\mu\text{s}$ as measured by Majerus and Walters (6.30).

As explained above, our estimate for the erosion rate of these jet fragments versus a steel target is $\mu_0 = .15 \text{ g/mm}$. Since the striking speeds are all below $2 \text{ mm}/\mu\text{s}$, we expect the flattening factor, (A/A_0) , to be greater than 2. We recall from Fig. 4.39 that for an $L_0/D_0 = 20$ copper rod versus steel for $1.2 < \dot{S}_0 < 1.8 \text{ mm}/\mu\text{s}$, the flattening factor was about 5. However, for a lower aspect ratio like 3.5, we expect a lower value for (A/A_0) . Let $(A/A_0) = 2.5$ for these jet fragments as an average value. With these assumptions and $A_0 = .12 \text{ cm}^2$, we find $a = .08 \text{ g mm}/\mu\text{s}^2$ and $c = .12 \text{ g/mm}$. In addition $I_0 = 4.68 \text{ mm/g}$ and $k = 1.7$. From Eq (2.18), $\bar{c} = .015 \text{ g/mm}$, so Eq (2.22) becomes

$$P_1 = (1.6/.15) \left\{ 1 - [1 + .06 \left(\frac{\dot{S}_{01}}{c_1} \right)^2]^{-8.5} \right\} \quad (6.15)$$

since $\bar{c}/(ak^2) = .06 (\mu\text{s/mm})^2$, while $\mu_0 k/(2\bar{c}) = 8.5$. From Eq (2.15), we have

$$M_1 = 1.6 - .15P_1 \quad (6.16)$$

with $i = 1$ to 27. The speed difference between the first and last fragments is $.6 \text{ mm}/\mu\text{s}$ so the drop in speed between one fragment and the next is $.6/26 = .023 \text{ mm}/\mu\text{s}$. Table 6.1 gives the striking speed, \dot{S}_{01} , of each fragment in the train, assuming that there are no collisions or interference, followed by the penetration produced by that fragment, P_1 and the residual mass, M_1 . For a stack of plates of this type, we are assuming that all residual mass escapes between the plates. The cumulative penetration and cumulative residual mass are also given in the last two columns of the table. Three decimal places are retained to minimize errors of a purely numerical type. This does not imply that the calculation is anywhere near this accurate. The total cumulative penetration by the fragment train is 188 mm. If we add this to the 203 mm produced by the continuous part of the jet, we find a total overall penetration of 391 mm. This is slightly less than the reported high

Table 6.1

Fragment	\bar{S}_0	P_1	M_1	$\Sigma_1 P_1$	$\Sigma_1 M_1$
1	1.800	8.313	.353	8.313	.353
2	1.777	8.228	.366	16.541	.719
3	1.754	8.142	.379	24.683	1.098
4	1.731	8.053	.392	32.736	1.490
5	1.708	7.961	.406	40.697	1.896
6	1.685	7.868	.420	48.565	2.316
7	1.662	7.772	.434	56.337	2.750
8	1.639	7.674	.449	64.011	3.199
9	1.616	7.574	.464	71.585	3.663
10	1.593	7.471	.479	79.056	4.142
11	1.570	7.366	.495	86.422	4.637
12	1.547	7.259	.511	93.681	5.148
13	1.524	7.150	.528	100.831	5.676
14	1.501	7.038	.544	107.869	6.220
15	1.478	6.925	.561	114.794	6.781
16	1.455	6.809	.579	121.603	7.360
17	1.432	6.691	.596	128.294	7.956
18	1.409	6.571	.614	134.865	8.570
19	1.386	6.448	.633	141.313	9.203
20	1.363	6.324	.651	147.637	9.854
21	1.340	6.198	.670	153.835	10.524
22	1.317	6.071	.689	159.906	11.213
23	1.294	5.941	.709	165.847	11.922
24	1.271	5.810	.729	171.657	12.651
25	1.248	5.677	.748	177.334	13.399
26	1.225	5.542	.769	182.876	14.168
27	1.202	5.407	.789	188.346	14.957

of 399 mm and somewhat more than the reported low of 374 mm, but not far from the average experimental value of 386 mm. We may simplify the calculation by taking the average of 8.313 mm and 5.407 mm, namely, 6.56 mm, and multiplying by 27 fragments to get 185 mm. This plus 203 mm gives 388 mm, even closer to the experimental average.

We see from Table 6.1 that almost half of the last fragment mass remains after it is brought to rest, while the total cumulative residual mass is about 15 g, almost 35% of the 43 g mass of the fragment train. If the target had been a solid billet instead of a stack of plates, we would expect interference and a lower penetration with a lot of residual mass in the crater.

2. Standoff = 6CD

Unfortunately, we do not have any time-dependent experimental data at this standoff. The only information we have is a final penetration depth of about 440 ± 40 mm from Fig. 6.3. Since $S = 480$ mm, $t_0 = 70\mu s > t_1$ by Eq (6.5), so the jet is completely formed ($M_0 = 80$ g) and partially stretched when the penetration begins.

$$a. \quad \underline{t_0 \leq t \leq t_2}$$

Since $t_2 = 100\mu s$ in our coordinate system, this first stage of the penetration lasts for $30\mu s$. The initial area at $t = 70\mu s$ is $.214 \text{ cm}^2$ from Eq (6.8), and is $.15 \text{ cm}^2$ at t_2 so the average area over the time of the first stage is $A_0 = .18 \text{ cm}^2$. This gives $\mu_0 = .14 \text{ g/mm}$. We also find $\dot{\mu} = 1.15 \text{ g}/\mu s$, $I_0 = 3.12 \text{ mm/g}$, $k = 1.44$, $\dot{P}_0 = 5 \text{ mm}/\mu s$, $a = .1 \text{ g mm}/\mu s^2$ and $C = .14 \text{ g/mm}$ with $(A/A_0) = 2$. Then $\bar{b} = .44 \text{ g}/\mu s$, $\bar{c} = .04 \text{ g/mm}$ and $\Delta = -.178$ so $\sqrt{-\Delta} = .42$. We have $\bar{e} = 3.5$, $\bar{e}k/2 = 2.52$, $\beta^- = 1.05$ and $\beta^- (\bar{e}k/2) = 2.65$, $\gamma^+ = -.25$, $\gamma^- = -10.75$, $G_0 = .36$ and $F_0 = 3.8 \text{ g mm}/\mu s^2$. Then

$$\begin{aligned} D^- &= \frac{(100-70)}{1.44(80)} (3.8)^{2.52} (.36)^{-2.65} = 112.7 \\ &= \int_{\dot{P}_2}^{5.6} (.1 + .44x + .04x^2)^{1.52} [(x + .25)/(x + 10.75)]^{-2.65} dx \quad (6.17) \end{aligned}$$

from which we find $\dot{P}_2 = 4.6 \text{ mm}/\mu\text{s}$.

$$D^- = 1/.174 (111.1 + 116.3) + .326 (12.5 + 114.5) = 113.6 \quad (6.18)$$

Then $G_2 = .316$ and $F_2 = 2.97 \text{ g mm}/\mu\text{s}^2$, so

$$\begin{aligned} P_2 &= \left(\frac{80}{.14} \right) \left\{ 1 - \left(\frac{2.97}{3.8} \right)^{2.52} \left(\frac{.36}{.316} \right)^{2.65} \right\} \\ &= 571.4 \{ 1 - (.537)(1.413) \} = 138 \text{ mm} \end{aligned} \quad (6.19)$$

Without time-dependent information we have no check on this intermediate result. However, we note that the value in Eq (6.19) is about 38 mm larger than the depth after 30 μs in Fig. 6.7. From Eq (2.62) we find $M_2 = 80 - .14 (138) = 60.68 \text{ g}$ which becomes a train of 38 fragments.

$$b. \quad \underline{t_2 \leq t \leq t_E}$$

Eqs (6.15) and (6.16) should apply to this fragment train as well. Now, however, the first fragment strikes at 4.6 mm/ μs so $P_1 = 10.66 \text{ mm}$ by Eq (6.15) while $\dot{P}_{38} = 1.2 \text{ mm}/\mu\text{s}$ and $P_{38} = 5.4 \text{ mm}$ as for the last fragment in Table 6.1. The average penetration per fragment is thus 8.03 mm or 305 mm for 38 fragments. If we add 138 mm to this from the first stage we find 443 mm for the total penetration which is close to the average value observed.

3. Standoff = 10CD

Here the entire penetration is accomplished by a train of 50 fragments. If $\dot{S}_0 = 8 \text{ mm}/\mu\text{s}$ for the first fragment, then $P_1 = 10.67 \text{ mm}$, while P_{50} is still 5.4 mm for an average of 8.03 mm and a total of 402 mm. This is close to the average value of the 65 observations in Fig. 6.3.

4. Standoff = 20CD

For $S > 10\text{CD}$ we invoke our efficiency factor in Eq (6.4), namely, $E = .5$ for $S = 20\text{CD}$. The 50-fragment train would still penetrate 402 mm as

for $S = 10CD$ if $E = 1$. As it is, we calculate a total depth of 201 mm, which is close to the average of the 24 observations in Fig. 6.3.

E. Penetration into Steel and Aluminum Targets of Various Strengths

We are fortunate to have time-dependent experimental data for these targets for at least one standoff, namely, $S = 2CD$. In their report cited above (6.29) Merendino and Vitali also studied aluminum and steel targets with a range of hardness values, using the same techniques with stacked plates. Four selections from their data are shown in Fig. 6.8. Both steel targets offer greater resistance to penetration than either aluminum target. Moreover, for a given metal density, the greater the hardness, the lower the penetration. Clearly, a hydrodynamic theory which neglects target strength cannot explain such results. Once more the importance of including hardness for high speed penetrations is evident. The hardest aluminum target used in Fig. 6.8 did almost as well as the softest steel target, considering final penetration depth. In fact, we might expect a still harder aluminum to outperform a somewhat softer steel with $BHN < 100 \text{ kg/mm}^2$.

Another feature of these curves is the fact that, for given target density, they are almost indistinguishable early in the penetration versus a fast, continuous jet. However, at later times, after the jet has broken into a train of fragments, the curves are easily distinguished, especially for the less dense aluminum targets which differ in hardness by a factor of 6.8 instead of 3 as in the case of the steel targets.

1. Steel Targets

The lowest curve in Fig. 6.8 has already been calculated during our discussion of Fig. 6.7. We recall that at the beginning of the penetration of the steel target with $BHN = 300 \text{ kg/mm}^2$, $\bar{a}_F = a - I_O \dot{M}_O (\dot{M}_O + 2 \dot{M}_R) = .162 - (1.87)(1.2)(5.2) = -11.5 \text{ g mm}/\mu\text{s}^2$ while $b_F = 4 \text{ g}/\mu\text{s}$ and $c = .236 \text{ g/mm}$. For a steel target with $BHN = 100 \text{ kg/mm}^2$, the only factor which changes will

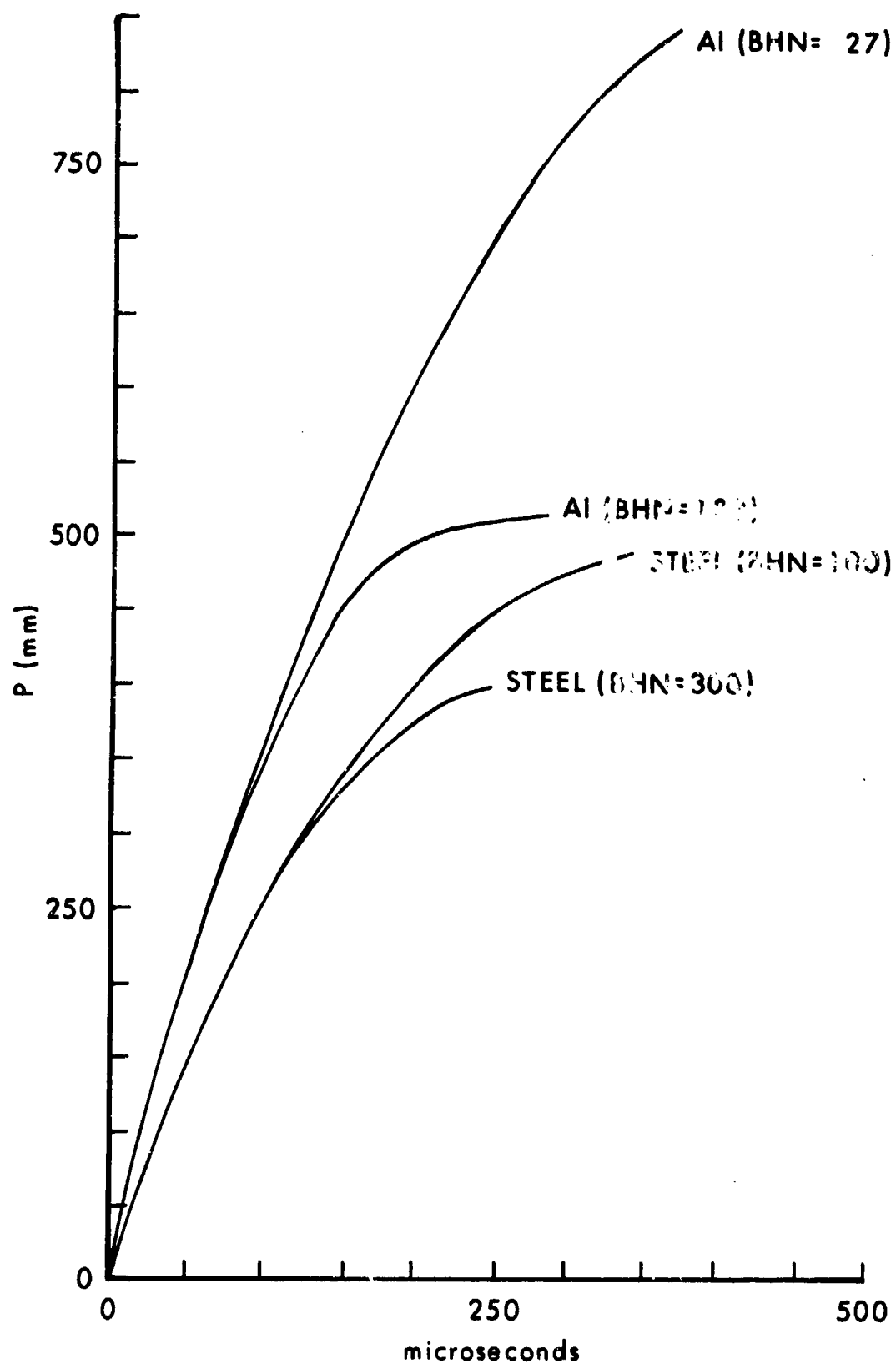


Fig. 6.8. Jet penetration versus time for four targets at 2CD standoff.

be a , which we expect to drop to $.162/3 = .054$ g mm/ μ s. Clearly this will give a negligible change in the opposing force, F , so the predicted penetration will be almost identical, in agreement with what is observed. Here we are making our usual assumption that the erosion rate is the same for two such targets of the same density. Similarly, we recall for the second stage of penetration that initially the force was $F_1 = .12 + 2.15 + 1.5 = 3.77$ g mm/ μ s², while at t_2 it was $F_2 = .12 + 1.04 + .36 = 1.52$ g mm/ μ s². Switching to $a = .12/3 = .04$ g mm/ μ s² for the softer steel target is a negligible change, and the curves are still indistinguishable in agreement with Fig. 6.8. However, during the last stage of the penetration by a train of 27 fragments, target hardness becomes important in the coefficient of \dot{S}_O^2 in Eq (6.22), namely $\bar{c}/(ak^2)$. Since a decreases by a factor of 3 for the soft steel target, Eq (6.15) becomes

$$P_i = 10.67 \{ 1 - [1 + .18(\dot{S}_{oi})^2]^{8.5} \} \quad (6.20)$$

although Eq (6.16) remains the same. Now we find $P_1 = 10.46$ mm instead of 8.3 mm as in Table 6.1. Similarly, $P_{27} = 9.17$ mm instead of 5.4 mm for an average of 9.82 mm and a total of 265 mm. If we add 203 mm to this from the first two stages of penetration by the still continuous jet, we find 468 mm, which is somewhat below the value shown in Fig. 6.8 which was a deeper than average penetration.

2. Aluminum Targets

$$a. \quad \underline{t_0 \leq t \leq t_1}$$

During the first 10 μ s of penetration we can estimate the erosion rate by multiplying .2 g/mm for a steel target by $\sqrt{2.7/7.83}$ as usual to obtain $\mu_O = 1.87$ mm/g as before so now $k = 1.22$ and $\dot{P}_O = 6.5$ mm/ μ s, larger than for steel. The average speed is about 5 mm/ μ s so $\dot{M}_p = (.12 \text{ g/mm})(5 \text{ mm}/\mu\text{s}) = .6 \text{ g}/\mu\text{s}$. Since $\dot{M}_R = 2 \text{ g}/\mu\text{s}$, $\dot{M}_O = 1.4 \text{ g}/\mu\text{s}$, so $M_1 = 60 + 1.4(10) = 74$ g. With $(A/A_O) = 2$, we find $a = .10$ g mm/ μ s² for the target with BHN = 183 kg/mm² and $a = .015$ g mm/ μ s² for the target with

BHN = 27 kg/mm². Of course $c = .081$ g/mm for either target. Then
 $\bar{a}_F = .1 - (1.87)(1.4)(1.4 + 4) = -14.0$ g mm/ μs^2 for the harder target and
 $\bar{a}_F = -14.085$ g mm/ μs^2 for the softer target. These values are practically
the same. Of course $\bar{b}_F = 4$ g/ μs and c are exactly the same for both targets,
so the curves will be indistinguishable as observed. Then $\sqrt{-\Delta_F} = 4.53$
approximately the same for both, giving $\gamma^+ = 3.27$ and $\gamma^- = -52.65$. Also
 $\bar{\epsilon}_F = 1.4/4.53 = .31$, and $G_0 = (6.5 - 3.27)/(6.5 + 52.65) = .055$, while
 $G_1 = .055 [1 + (1.4/60)(10)]^{-1/.31} = .028$, so
 $\dot{P}_1 = [3.27 + 52.65 (.028)]/(1 - .028) = 4.9$ mm/ μs . Next we find
 $B_1 (.31) = .076$ and $B_1 (1.31) = 1.921$, so
 $P_1 = (60/4.53)(.028)^{.31} [3.27 (1.921) + 52.65 (.076)] = 45$ mm in approximate
agreement with Fig. 6.8.

$$b. \quad t_1 \leq t \leq t_2$$

To start off the next 60 μs of penetration we have $M_1 = 74$ g,
 $\dot{P}_1 = 4.9$ mm/ μs and $P_1 = 45$ mm. Now $\mu_0 = .108$ g/mm and $I_0 = 2.44$ mm/g so
 $k = 1.26$. With $(A/A_0) = 2$, $a = .076$ g mm/ μs for the harder target and
 $a = .011$ g mm/ μs for the softer one, with $c = .108$ g/mm for both. Of course
 $\dot{\mu} = 1.23$ g/ μs as before, so $\bar{b} = (2.44)(.108)(1.23) = .324$ g/ μs and
 $\bar{c} = .108 - (2.44)(.108)^2 = .08$ g/mm. Then $\sqrt{-\Delta} = .285$ g/ μs for the harder
target and $\sqrt{-\Delta} = .266$ g/ μs for the softer. Moreover, $\bar{\epsilon} = 1.35$ and $\bar{\epsilon}k/2 = .85$
for both, but $\beta^- = 1.137$ and $\beta^- (\bar{\epsilon}k/2) = .966$ for the harder, while
 $\beta^- = 1.218$ and $\beta^- = 1.137$ and $\beta^- (\bar{\epsilon}k/2) = 1.035$ for the softer. Also
 $\gamma^+ = -.244$, $\gamma^- = -3.806$, $G_1 = .591$ and $F_1 = 3.58$ g mm/ μs^2 for the harder
target, while $\gamma^+ = -.362$ mm/ μs , $\gamma^- = -3.686$ mm/ μs , $G_1 = .613$ and
 $F_1 = 3.52$ g mm/ μs^2 for the softer. Since the resistive forces of the two
targets are slightly different, there will be a slight but observable
difference in penetration as in Fig. 6.8.

For the harder target we find

$$D^- = \frac{60}{1.26(74)} (3.58)^{.85} (.591)^{-.966} = 3.165$$

$$= \int_{\dot{P}_2}^{4.9} (.076 + .324x + .08x^2)^{-.15} [(x + .244)/(x + 3.806)]^{-.966} dx \quad (6.21)$$

and $\dot{P}_2 = 2.92 \text{ mm}/\mu\text{s}$ so $G_2 = .470$ and $F_2 = 1.704 \text{ g mm}/\mu\text{s}^2$, and

$$P_2 = 45 + \left(\frac{74}{.108}\right) \left\{ 1 - \left(\frac{1.704}{3.58}\right)^{.85} \left(\frac{.591}{.470}\right)^{.966} \right\}$$

$$= 45 + 685 \{ 1 - (.532)(1.248) \} = 45 + 230 = 275 \text{ mm} \quad (6.22)$$

so

$$M_2 = 74 - .108 (230) = 49.2 \text{ g} \quad (6.23)$$

For the softer target we find

$$D^- = \frac{60}{1.26(74)} (3.52)^{.85} (.613)^{-1.035} = 3.115$$

$$= \int_{\dot{P}_2}^{4.9} (.011 + .324x + .08x^2)^{-.15} [(x + .362)/(x + 3.688)]^{-1.035} dx \quad (6.24)$$

and $\dot{P}_2 = 2.95 \text{ mm}/\mu\text{s}$, so $G_2 = .499$ and $F_2 = 1.663 \text{ g mm}/\mu\text{s}^2$, so

$$P_2 = 45 + \left(\frac{74}{.108}\right) \left\{ 1 - \left(\frac{1.633}{3.52}\right)^{.85} \left(\frac{.613}{.499}\right)^{1.035} \right\}$$

$$= 45 + 685 \{ 1 - (.529)(1.237) \} = 45 + 237 = 282 \text{ mm} \quad (6.25)$$

$$\text{so } M_2 = 74 - .108 (237) = 48.4 \text{ g.} \quad (6.26)$$

Thus, when jet breakup begins, the crater in the softer target is about 7 mm deeper.

$$c. \quad \underline{t_2 \leq t \leq t_F}$$

For fragments versus a soft aluminum target let $(A/A_0) = 2.1$ and estimate $\mu_0 = .085 \text{ g/mm}$. Since $A_0 = .12 \text{ cm}^2$, we find $a = .006 \text{ g mm}/\mu\text{s}^2$ and $c = .034 \text{ g/mm}$, $I_0 = 4.68 \text{ mm/g}$ and $k = 1.4$, so $c = 0$ and Eq (2.26) becomes

$$P_1 = (1.6/.085) [1 - \exp(-5.06\dot{S}_0^2)] \quad (6.27)$$

since $\mu_0/(2ak) = 5.06 (\mu\text{s/mm})^2$. Thus, even for the slowest fragment, the exponential correction factor is negligible, and we have 18.8 mm of penetration by each of 30 fragments. The cumulative total for the train is 564 mm. If we add 282 mm from the continuous part of the jet, we find 846 mm, which is close to the final value in Fig. 6.8.

The harder aluminum target is 6.8 times harder, so we expect an increase in (A/A_0) as well as in a_0 . If $(A/A_0) = 3$, we find $a = .06 \text{ g mm}/\mu\text{s}^2$ and $c = .05 \text{ g/mm}$. If μ_0 is the same, then I_0 and k are the same so $\bar{c} = .016 \text{ g/mm}$ and Eq (2.22) is

$$P_1 = 18.8 \{1 - [1 + .425 \dot{S}_0^2]^{-1.19}\} \quad (6.28)$$

since $\bar{c}/(ak^2) = .425 (\mu\text{s/mm})^2$ and $\mu_0 k/(2c) = 1.19$. The first fragment strikes at about $\dot{P}_2 = 2.9 \text{ mm}/\mu\text{s}$ so $P_2 = 15.7 \text{ mm}$. The last fragment strikes at $1.2 \text{ mm}/\mu\text{s}$, so $P_{30} = 8.1 \text{ mm}$. The average value of 11.9 mm gives 357 mm for the train. When we add 275 mm from the continuous part of the jet, we find 632 mm which is much higher than the value near 500 mm shown in Fig. 6.8. Perhaps the harder target gives a higher erosion rate near $.15 \text{ g/mm}$ as well as a larger flattening factor near 6. These values would give something close to the observed penetration, but they are hard to justify. If we keep the more reasonable values used above, then we might consider using an efficiency factor of $E = .6$ which reduces penetration by the fragment train to about 215 mm. Adding 275 mm gives 490 mm, close to the observed value.

A justification for using an efficiency factor much less than unity might be based on observations by Merendino and Vitali (6.29). They used flash X-rays to observe jet penetration into a hard (6061) aluminum target billet at 4CD standoff, and concluded that the material eroded from the impact of each fragment did not flow smoothly along the crater wall. Instead, they observed a series of bulbous craters with partial closures between craters. This pinching off effect could well cause interference with incoming fragments and lead to reduced efficiency for the train. The rapid bending over of the hard aluminum curve in Fig. 6.8 suggests that such effects "cascade," producing a great deal of interference with the last fragments in the train. Unfortunately, these authors did not report flash X-ray observations for a

stack of plates as well as a solid billet. In addition they used 4CD instead of 2CD and a shaped charge device not as precisely constructed as that used for Fig. 6.8. In spite of these differences, this explanation seems to be plausible although difficult to quantify except in the ad hoc, purely empirical manner suggested above, namely, $E = .6$.

F. Lead Targets

One of the anomalies of early hydrodynamic theory was greater penetration into lead than into steel, contrary to the density law. When better measurement techniques became available, the discrepancy turned out not to be as large as was once thought, but real nonetheless. Feldman (6.30a) used a slightly larger (86 mm) version of the shaped charge device we are considering at 2.44CD standoff against semi-infinite stacks of plates 2.54 cm thick with break-foils between. Fig. 6.9 shows his curves for mild (1020) steel and lead. His mild steel curve lies slightly above that in Fig. 6.8, perhaps because of a slightly lower target strength (not reported). His curve for lead shows that its greater density does offer greater resistance to penetration by the continuous portion of the jet. However, penetration by the fragment train continues for a longer time in lead with even the slower fragments making a substantial contribution because of the very low strength of lead. Feldman gave similar data for aluminum and zinc as well. In his figure 4b, he reported crater areas for lead to a depth of 550 mm. For lead, these areas were much larger than for his other target materials at the original target surface but were only about 50% larger near the bottom. He did not offer "secondary penetration" as an explanation, nor did he attribute his results for lead to penetration by a slug. Feldman's curves were later reported, at least in part, by Majerus and co-workers (6.31).

Since the standoff used was 210 mm and this early version of the device we are describing had a tip speed closer to 7 mm/ μ s than 8 mm/ μ s, then the penetration began at $t_0 = 10 + 210/7 = 40\mu$ s, with this change in Eq (6.5). In other words, the penetration began just as jet formation ended, so $M_0 = 80$ g.

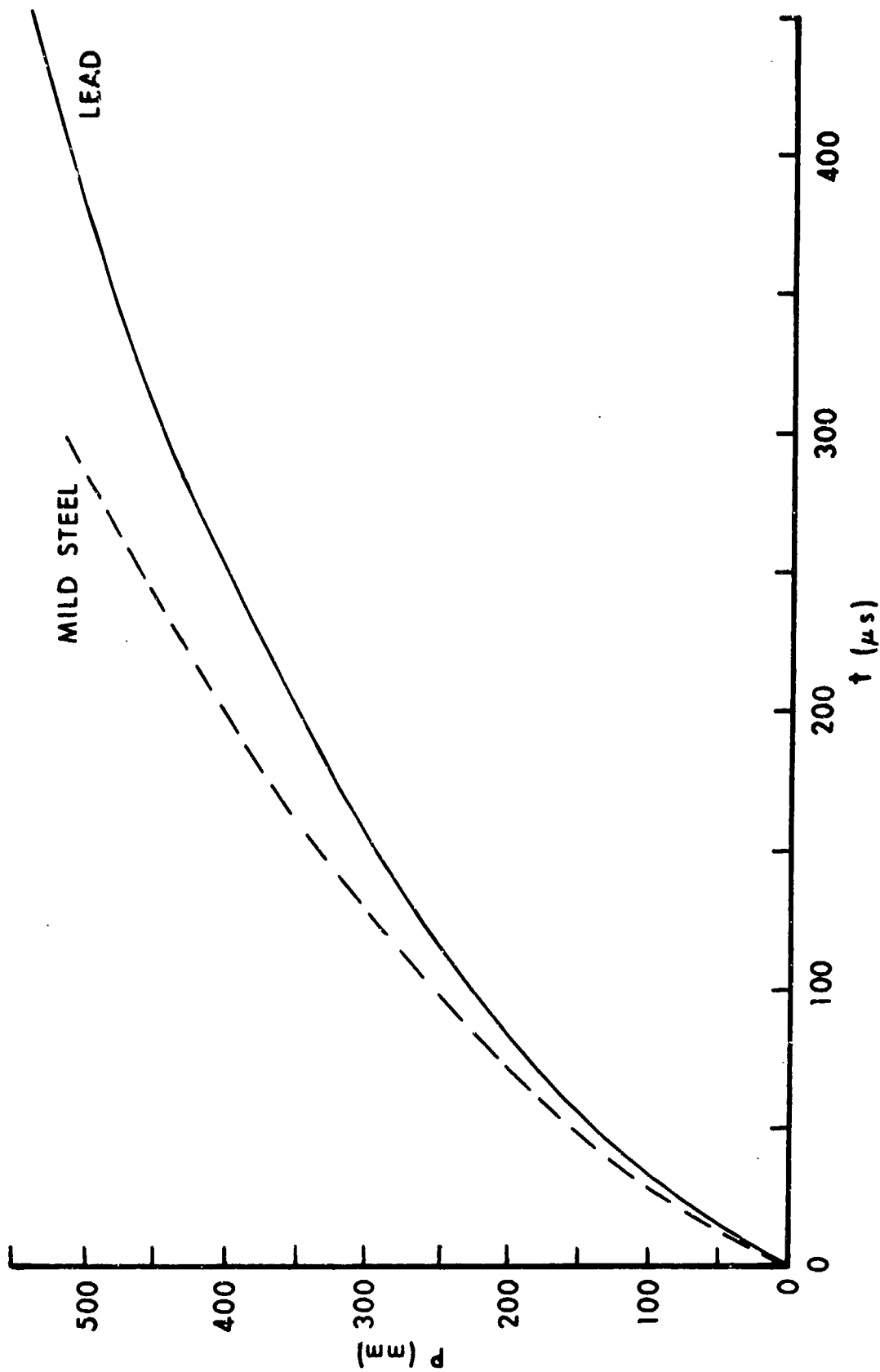


Fig. 6.9. Jet penetration into lead at 2.44CD.

$$1. \underline{t_0 \leq t \leq t_2}$$

During this same 60 μ s period we took the average area of the jet to be .225 cm² and the erosion rate in steel to be .18 g/mm. Let us multiply this latter value by $\sqrt{11.3/7.85}$ to obtain $\mu_0 = .22$ g/mm for lead. Of course $I_0 = 2.5$ mm/g as before, so $k = 1.55$ and $\dot{P}_0 = 7/1.55 = 4.5$ mm/ μ s. For lead with $A_0 = .225$ cm² and $(A/A_0) = 2$ we find $a = .0007$ g mm/ μ s² and $c = .254$ g/mm. We still have $\dot{\mu} = 1.44$ g/ μ s so $\bar{b} = I_0 \mu_0 \dot{\mu} = .79$ g/ μ s from Eq (2.65), and $\bar{c} = .133$ g/mm by Eq (2.66). Then $\Delta = -.62$ (g/ μ s)² and $\sqrt{-\Delta} = .79$ g/ μ s $\approx \bar{b}$ since a is so small. Again Eqs (2.76) to (2.80) apply with $\bar{e} = \mu_0 / \bar{c} = \frac{.22}{.133} = 1.65$, $\beta^- = \bar{b} / \sqrt{-\Delta} = 1$, and $\bar{e}k/2 = 1.28 = \beta^-(\bar{e}k/2)$. In addition, $\gamma^+ = 0$ and $\gamma^- = -5.9$ mm/ μ s, giving $G_0 = (4.5 - 0)/(4.5 + 5.9) = .43$ from Eq (2.77) and $F_0 = .0007 + 7.9 (4.5) + .133 (4.5)^2 = 6.25$ g mm/ μ s². Then

$$D = [(100 - 40)/(1.55 \times 80)](6.25/.43)^{1.28} = 14.9$$

$$= \int_{\dot{P}_2}^{4.5} (.0007 + .79x + .133x^2)^{.25} [x/(x + 5.9)]^{-1.28} dx \quad (6.29)$$

from which we find $\dot{P}_2 = 2.6$ mm/ μ s. Then

$$G_2 = (2.6 - 0)/(2.6 + 5.9) = .31 \text{ and}$$

$$F_2 = .0007 + .79 (2.6) + .133 (2.6)^2 = 2.95 \text{ g mm}/\mu\text{s}^2, \text{ so}$$

$$P_2 = (80/.22) \left\{ 1 - \left[\left(\frac{2.95}{6.25} \right) \left(\frac{.43}{.31} \right) \right]^{1.28} \right\} = 152 \text{ mm} \quad (6.30)$$

which is close to the value reported in Fig. 6.9 after 60 μ s of penetration.

$$2. \underline{t_2 \leq t \leq t_E}$$

The mass at the beginning of this second stage is $M_2 = 80 - .22 (152) = 46.5$ g which is divided into a train of 29 fragments which accomplish the majority of the penetration. We can estimate the erosion rate from that of the previous stage by recognizing that the area is now .12 cm² compared to .225 cm² before. Then $\mu_0 = (.12/.225)(.22 \text{ g/mm}) = .117$ g/mm. We use this procedure because of the

very low strength of lead. By a like procedure we find $a = .00036 \text{ g mm}/\mu\text{s}^2$ and $c = .138 \text{ g/mm}$. Since $I_0 = 4.68 \text{ mm/g}$ as before for this stage of the jet, we find $k = 1.55$ and $\bar{c} = .074 \text{ g/mm}$. Consequently, $\bar{c}/(ak^2) = 85.6 (\mu\text{s/mm})^2$ and $\mu_0 k/(2\bar{c}) = 1.23$, so Eq (2.22) becomes

$$P_1 = (1.6/.117)\{1 - [1 + 85.6\dot{S}_0^2]^{-1.23}\} \quad (6.31)$$

Clearly, even for the last fragment with $\dot{S}_0 = 1.2 \text{ mm}/\mu\text{s}$ the correction factor is negligible because of the low strength of lead, so each fragment penetrates $(1.6/.117) = 13.7 \text{ mm}$ for a total of 397 mm for the train. When we add 152 mm from the first stage, we find 549 mm, close to the observed value.

G. Finite Targets

There is very little data in the open literature on the perforation of plates by jets. Fig. 6.10 does however show residual jet speed measured after perforating various thicknesses of armor steel at a standoff of $2CD$ (6.31). The five data points are generally the average values from three or four experiments and lie on the straight line.

$$\dot{S}_R = 7.2 - .015 T \quad (6.32)$$

when the target thickness, T , is given in mm. The value $\dot{S}_R = 7.2 \text{ mm}/\mu\text{s}$ is somewhat less than the reported tip speed of $7.6 \text{ mm}/\mu\text{s}$ and the thickness $T = 480 \text{ mm}$ which reduces \dot{S}_R to zero in Eq (6.32) is somewhat more than the 400 mm penetration depth which was reported as the average for a semi-infinite stack of armor steel plates in Fig. 6.3. This is to be expected because of breakin and breakout effects which are important in the case of finite plates. In addition, measurements of \dot{S}_R were carried out sufficiently far behind the plates that the recovered jet element speed rather than the penetration speed is being observed. The thickness $T = 400 \text{ mm}$ reduces \dot{S}_R to $1.2 \text{ mm}/\mu\text{s}$ in Eq (6.32), which is the free-flight speed of the rear of the jet. The linear decrease in Fig. 6.10 corresponds to the linear decrease in speed along the

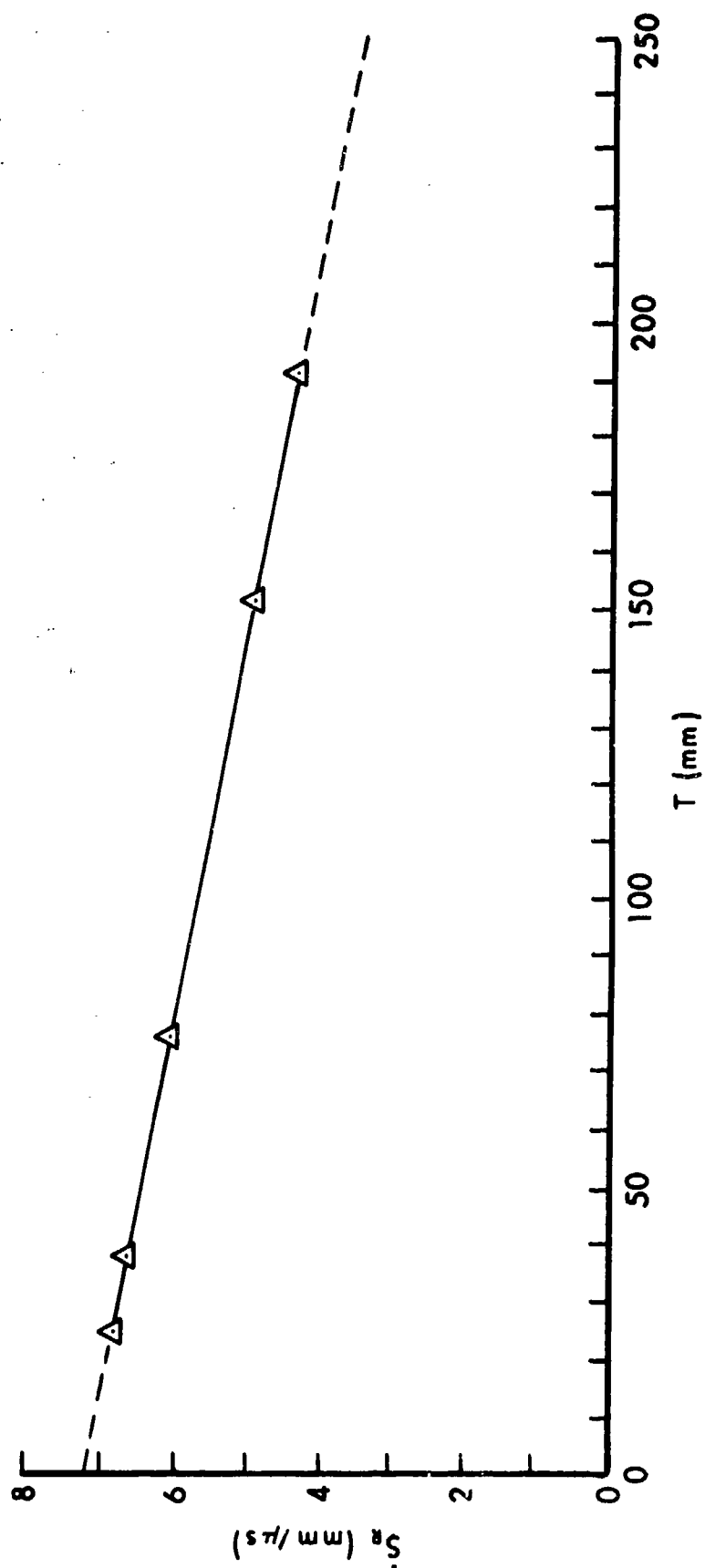


Fig. 6.10. Residual jet speed after penetrating various thicknesses of armor steel.

length of the jet. This implies that for finite plates with thickness less than 80% of the jet penetration in a semi-infinite stack of plates, we may estimate the residual speed 200 or more mm behind the plate to be the free-flight speed of the first jet element to emerge from the back of the plate.

We recall from Chapter IV, section C above that armor plates failed when rods penetrated only part way through. For example a 6.35 mm thick plate struck by a 7.78 g $L_0/D_0 = 10$ steel rod at about 1 mm/ μ s failed when $P = .35 T_0$. Similar information is not available for thicker plates struck by copper jets at 2CD at much higher speeds. Suppose, however, that we assumed that the plates used to gather the data in Fig. 6.10 failed when $P = T_0/3$. This means that $T_0 = 120$ mm corresponds to $P = 40$ mm. We recall that for a semi-infinite stack of armor steel plates we found $\dot{P} = 3.7$ mm/ μ s after about 40 mm penetration with $k = 1.44$. Then we expect $\dot{S}_R = 1.44 (3.7) = 5.32$ mm/ μ s, which is close to the value observed in Fig. 6.10 for $T_0 = 120$ mm.

Clearly we need more information on the penetration of finite plates of various thicknesses and materials before we can expect to obtain an adequate testing ground for a theory. We hope to pursue this matter in a later report.

SUMMARY AND CONCLUSION

We have derived a single equation and developed a self-consistent method for calculating the performance of all types of penetrators against finite or semi-infinite monolithic targets at zero degrees obliquity. Perhaps we have raised as many questions as we have answered. If this is true, then we have accomplished one of the main objectives of a theory, which is to stimulate thought and further experimentation. We have also presented a reasonably simple method of calculating such performance and have illustrated it with many examples. Future reports will extend this non-linear theory to targets with non-zero obliquity, as well as targets consisting of arrays of (possibly spaced) plates. The treatment will also be extended to glass and ceramic target materials when suitable data becomes available. At present, we do not really understand the mechanisms at work in such target materials.

The author wishes to thank William de Rosset and John Kineke of the Ballistic Research Laboratory for their many helpful discussions.

REFERENCES

- 1.1 Isaac Newton, The Mathematical Principles of Natural Philosophy (Cambridge, Trinity College, 1686), Definition II.
- 1.2 Euler, "Principles Généreaux du Movement des Fluides," Hist. de l'Acad. de Berlin, 1755.
- 1.3 H. Lamb, Hydrodynamics (Cambridge, The University press, 1879)
- 1.4 R. Courant and K. O. Friedrichs, Supersonic Flow and Shock Waves (New York, Interscience, 1948) p. 14.
- 1.5 F. Hunt, "Propagation of Sound in Fluids" in the American Institute of Physics Handbook (New York, McGraw-Hill, 1957).
- 1.6 G. K. Batchelor, An Introduction to Fluid Mechanics (Cambridge, The University Press, 1970) pp. 147 ff.
- 1.7 A. I. O. Zaid, A. El-Kalay and F. W. Travis, "An Examination of the Perforation of a Mild Steel Plate by a Flat-ended Cylindrical Projectile,) Int. J. Mech., Sci. 15, 129 (1973), Fig. 4.
- 1.8 A. L. Wingrove, "The Forces for Projectile Penetration of Aluminum," J. Phys. D:Appl. Phys, 5, 294 (1972).
- 1.9 J. M. Krafft, "Surface Friction in Ballistic Penetration," J. Appl. Phys. 26, 1248 (1956).
- 1.10 R. B. Pond, C. Mobley and C. M. Glass, "Energy Balances in Hypervelocity Penetration," Sixth Symposium on Hypervelocity Impact, Vol. 2, part 2, p 401.
- 1.11 D. E. Gault and E. D. Heitowit, "The Partition of Energy for Hypervelocity Impact Craters Formed in Rock", Sixth Symposium on Hypervelocity Impact, Vol. 2, part 2, p 419 (1963).
- 1.12 E. Schneider and A. J. Stilp, "Influence of Projectile Properties on the Partition of Energy during Hypervelocity Impact," Fifth International Symposium on Ballistics (1980).
- 1.13 A. E. Olshaker and R. L. Bjork, "Hydrodynamics Applied to Hypervelocity Impact II. The Role of Melting and Vaporization in Hypervelocity Impact," Fifth Symposium on Hypervelocity Impact Vol. 1, part 1, p 225 (1962).
- 1.14 J. Dehn, "The Particle Dynamics of Target Penetration," BRL TR 2188 (1979).
- 1.15 J. Dehn, "The Particle Dynamics of Penetration," Sixth International Symposium on Ballistics (1981), p. 315.
- 1.16 H. F. Olson, Dynamical Analogies (Princeton, D. Van Nostrand, 1958).

REFERENCES (CONT'D)

- 1.17 L. M. Milne - Thomson, Theoretical Hydrodynamics (New York, Macmillan, 1960) p 25.
- 1.18 D. Tabor, "A Simple Theory of Static and Dynamic Hardness," Proc. Roy. Soc. Lond. A192, 247 (1948).
- 1.19 D. Tabor, The Hardness of Metals (Oxford, the Clarendon Press, 1951).
- 1.20 H. Hencky, Z. Angew. Math. Mech. 3, 241 (1923).
- 1.21 Ishlinsky, J. Appl. Math. Mech. (USSR) 8, 233 (1944).
- 1.22 C. J. Osborn and R. L. Woodward, "The Effect of Penetrator Geometry on the Deformation of Ductile Metal Targets," in Strength of Metals and Alloys, Proceedings of the Sixth International Conference, Ed. by R. C. Gifkins (New York, Pergamon Press, 1983) Vol. 1, p. 467.
- 1.23 W. Goldsmith, Impact (London, Arnold, 1960), c. 4.
- 1.24 T. D. Riney and P. R. Chernoff, "Inertial, Viscous and Plastic Effects in High Speed Impact," Fifth Symposium on Hypervelocity Impact (1962) Vol. 1, part 1, p 135.
- 1.25 M. Zaid, "Penetration by Hypervelocity Particles," Ibid. p. 241.
- 1.26 P. C. Chou, "Visco-Plastic Flow Theory in Hypervelocity Perforation of Plates," Ibid., p. 307.
- 1.27 T. D. Riney, "Visco-Plastic Solution of Hypervelocity Impact Cratering Phenomenon," Sixth Symposium on Hypervelocity Impact (1963) Vol. 2, part 1, p. 105.
- 1.28 S. W. Yuan and R. W. Courter, "An Investigation of Crater Formation by Hypervelocity Impact," Seventh Symposium on Hypervelocity Impact (1965) Vol. 3, p. 123.
- 1.29 N. Davids, R. Minnich and J. Sliney, "A Penetration Method for Determining Impact Yield Strength," Ibid., p. 261.
- 1.30 R. G. Thomson and E. T. Kruszewski, "Effect of Target Material Yield Strength on Hypervelocity Perforation and Ballistic Limit," Ibid., Vol. 5, p. 273.
- 1.31 W. P. Walters, "Influence of Material Viscosity on the Theory of Shaped-Charge Jet Formation," BRL MR 2941 (1979).
- 1.32 J. N. Majerius and W. P. Walters, "A Predictive Penetration Model Utilizing an Effective Flow Viscosity of the Interaction Region," Sixth International Symposium on Ballistics, p. 290 (1981).
- 1.33 Sir William Thomson (Lord Kelvin) and Peter Guthrie Tait, Principles of Mechanics and Dynamics, Part II (New York, Dover, 1962) p. 303, re-publication of Treatise on Natural Philosophy (Cambridge, the University Press, 1879).

REFERENCES (CONT'D)

- 1.34 J. Clerk Maxwell, "On the Dynamical Theory of Gases," Phil. Trans. Roy. Soc. Lond. 157, 49 (1867), esp. p. 52.
- 1.35 K. F. Herzfeld and T. A. Litovitz, Absorption and Dispersion of Ultrasonic Waves (New York, Academic Press, 1959).
- 1.36 H. Hencky, Ann. der Physik 2, book 6 (5), 42 (1929).
- 1.37 N. A. de Bruyne, "Note on Viscous and Plastic Flow," Proc. Phys. Soc. Lond. 53, 251 (1941).
- 1.38 E. N. da C. Andrade, Nature 125, 580 (1930).
- 1.39 C. Zener, Elasticity and Anelasticity of Metals (Chicago, University of Chicago Press, 1948), esp. p. 150.
- 1.40 T. S. Ke, "Experimental Evidence of the Viscous Behavior of Grain Boundaries in Metals," Phys. Rev. 71, 533 (1947).
- 1.41 T. S. Ke, "Anelastic Properties of Iron," Amer. Inst. of Mining and Metallurgical Engineers, Tech. Publ. 2370 (1948), esp. p. 22.
- 1.42 T. S. Ke, "A Grain Boundary Model and the Mechanism of Viscous Intercrystalline Slip," J. Appl. Phys, 20, 274 (1949).
- 1.43 T. S. Ke, "Anomalous Internal Friction Associated with the Precipitation of Copper in cold-worked Al-Cu Alloys," Phys, Rev. 78, 420 (1950).
- 1.44 A. S. Krausz and H. Eyring, Deformation Kinetics (New York, Wiley, 1975), esp. pp. 37-43.
- 1.45 J. Frenkel, Kinetic Theory of Liquids (New York, Dover, 1955) c. 4, Eq (11) and footnotes on pp 195-6. Also note his discussion on p. 224.
- 1.46 J. Frenkel, Ibid., p. 190.
- 1.47 R. H. Goddard, Rockets (New York, American Rocket Society, 1946), first published by the Smithsonian Institution in its Miscellaneous Collections as two reports, the first in Vol. 71, No. 2 (1919), and the second in Vol. 95, No. 3 (1936).
- 1.48 H. Goldstein, Classical Mechanics (Cambridge, MA, Addison-Wesley, 1953) pp 1-2.
- 1.49 J. Morgan, Introduction to University Physics (Boston, Allyn and Bacon, 1963) Vol. 1, pp 57-9.
- 1.50 S. W. McCuskey, An Introduction to Advanced Dynamics (Reading, MA, Addison-Wesley, 1959), p 144.
- 1.51 P. Y. Chanteret and F. Jamet, "Quasi non-stretching Hypervelocity Jets," Proceedings of the Eighth International Symposium on Ballistics (1984), p VI-15.

REFERENCES (CONT'D)

- 2.1 I. Prigogine, From Being to Becoming, Time and Complexity in the Physical Sciences (New York, Freeman, 1980).
- 2.2 H. A. Bethe, "Attempt of a Theory of Armor Penetration," Frankford Arsenal R 492 (1941), p. 40.
- 2.3 Handbook of Mathematical Functions, Ed. by M. Abramowitz and I. A. Stegun, National Bureau of Standards Applied Mathematics Series, No. 55 (Washington, D.C., U.S. Government Printing Office, 1964), p. 505, paragraph 13.2.6 with $Z=0$, $a=1/2$ and $(b-a) = \epsilon$ in their notation.
- 2.4 I. S. Gradshteyn and I. M. Ryzhik, Table of Integrals, Series and Products (New York, Academic Press, 1980) p 197.
- 3.1 K. Weimann, "Die Endballistische Wirkung von Stahlkugeln auf Stahlplatten verschiedener Festigkeiten," Arbeitsgruppe fur Ballistische Forschung (ABF), Weil am Rhein, V (1/75 (1975)).
- 3.2 K. Weimann, "Eindringing von Stahlkugeln in Dural Al Cu Mg 1F40," ABF E 3/74 (1974).
- 3.3 J. Zook, W. Slack and B. Izdebski, "Ricochet and Penetration of Steel Spheres Impacting Aluminum Targets," Ballistic Research Laboratory, BRL MR 3243 (1983), p. 20.
- 3.4 C. J. Maiden, J. Charest and H. P. Tardif, "An Investigation of Spalling and Crater Formation by Hypervelocity Projectiles," Fourth Hypervelocity Impact Symposium (HIS), v. 3, paper 38.
- 3.5 F. Smith, W. A. Clayden, C. R. Wall and D. F. T. Winter, "Hypervelocity Launchers and Hypervelocity Impact Experiments at ARDE, Fort Halstead," Fifth HIS, v. 1, Pt. 2, p 475.
- 3.6 R. B. Pond and C. M. Glass, "Metallurgical Observations and Energy Partitioning," Chapter 8 in High-velocity Impact Phenomena, Ed. by R. Kinslow (New York, Academic Press, 1970).
- 3.7 J. S. Rinehart and J. Pearson, Behavior of Metals under Impulsive Loads (Cleveland, the American Society of Metals, 1954).
- 3.8 J. S. Rinehart, On Fractures Caused by Explosions and Impacts (Golden, Colorado, Colorado School of Mines, 1960).
- 3.9 J. S. Rinehart, Stress Transients in Solids (Santa Fe, N.M., Hyperdynamics, 1975).
- 3.10 Shock Waves and High-strain-rate Phenomena in Metals, Ed. by M. A. Meyers and L. E. Murr, (New York, Plenum Press, 1981).
- 3.11 Shock Waves in Condensed Matter - 1981, Ed. by W. J. Nellis, L. Seaman and R. A. Graham, American Institute of Physics (AIP) Conference Proceedings No. 78 (New York, AIP, 1982).

REFERENCES (CONT'D)

- 3.12 J. Dehn, "Probability Formulas for Describing Fragment Size Distributions," BRL TR 2332 (1981).
- 3.13 J. Dehn, Ref. 1.14 above, "The Particle Dynamics of Target Penetration," BRL TR 2188 (1979), esp. section 8.
- 3.14 J. Dehn, "Terminal Effectiveness, Vulnerability Methodology and Fragmentation Warhead Optimization.I.," BRL TR 2234 (1980), Appendix II.
- 3.15 A. Charters, "High-speed Impact," Scientific American, Oct. 1960, p. 128.
- 3.16 See reference 1.31 in chapter one above.
- 3.17 H. Seff, "Splitterwirkung gegen harte Ziele," ABF E 7/74 (1974).
- 3.18 E. P. Palmer, R. W. Grow, D. K. Johnson and G. H. Turner, "Cratering: Experiment and Theory," Fourth HIS, v. 1, paper 13.
- 3.19 Ordnance Engineering, v. 2, Book 2, Ballistics (West Point, U. S. Military Academy, 1968), p. 22-16.
- 3.20 W. W. Atkins, "Hypervelocity Penetration Studies," Third HIS, v. 1, p. 199.
- 3.21 W. W. Atkins, "Hypervelocity Penetration Studies," Fourth HIS, v. 1, paper 11 (1960).
- 3.22 E. H. Goodman and C. D. Liles, "Particle-Solid Impact Phenomena," Sixth HIS, v. 2, part 2, p. 543.
- 3.23 O. E. Engel, "Hypervelocity Cratering Data and a Crater-depth Model for the Regime of Partial Fluidity," Sixth HIS, v. 2, part 2, p. 337.
- 3.24 S. M. Halperson "Some Phenomena Associated with Impacts into Aluminum," Sixth HIS, v. 2, part 2, p 525.
- 3.25 S. M. Halperson, "Comparisons between Hydrodynamic Theory and Impact Experiments," Seventh HIS, v. 5. p. 235.
- 3.26 S. M. Halperson and W. W. Atkins, "Observations of Hypervelocity Impact," Fifth HIS, v. 2, part 2, p 497.
- 3.27 N. R. Sorensen, "Systematic Investigation of Crater Formation in Metals," Seventh HIS, v. 6, p. 281 (1965).
- 3.28 C. E. Mobley, Jr. and R. B. Pond, "Energy Balances for Hypervelocity Targets," Seventh HIS, v. 5, p. 73 (esp. p. 96).
- 3.29 J. M. Walsh and W. E. Johnson, "On the Theory of Hypervelocity Impact," Seventh HIS, v. 2, p. 1 (esp. p. 47).

REFERENCES (CONT'D)

- 3.30 J. H. Kineke and L. G. Richards, "Influence of Target Strength on Hypervelocity Crater Formation in Aluminum," Sixth HIS, v. 2, part 2, p. 513 (1963).
- 3.31 Reference (1.1), p. 282).
- 3.32 Reference (3.3), p. 15).
- 3.33 J. S. Rinehart, "Some Quantitative Data Bearing on the Scabbing of Metals under Explosive Attack," J. Appl. Phys. 22, 555 (1951).
- 3.34 J. S. Rinehart, "Scabbing of Metals under Explosive Attack: Multiple Scabbing," J. Appl. Phys. 23, 1229 (1952).
- 3.35 H. Senf and K. Weimann, "Die Wirkung von Stahlkugeln auf Dural-Einzeln und Viele Platten," ABF V 6/73 (1973).
- 3.36 M. E. Backman and W. Goldsmith, "The Mechanics of Penetration of Projectiles into Targets," Int. J. Eng. Sci. 16, 1 (1978), p. 10.
- 3.37 M. E. Backman and S. A. Finnegan, "A Phenomenological Investigation of the Impact of Compact Projectiles against Plates at Speeds up to 3km/s," Eighth ISB, VIII-13 (1984).
- 3.38 J. Liss, W. Goldsmith and J. M. Kelly, "A Phenomenological Penetration Model of Plates," Int. J. of Impact Eng. 1 (4), 321 (1983).
- 3.39 J. Liss and W. Goldsmith, "Plate Perforation Phenomena due to Normal Impact by Blunt Cylinders," Int. J. of Impact Eng. 2 (1), 37 (1984).
- 3.40 B. Landkof and W. Goldsmith, "Petalling of Thin, Metallic Plates during Penetration by Cylindro-conical Projectiles," Int. J. of Solids and Structures (in press).
- 3.41 N. Levy and W. Goldsmith, "Normal Impact and Perforation of Thin Plates by Hemispherically-tipped Projectiles.I. Analytical Considerations," Int. J. of Impact Eng. 2, 209 (1984).
- 3.42 N. Levy and W. Goldsmith, "Normal Impact and Perforation of Thin Plates by Hemispherically-tipped Projectiles.II. Experimental Results," Int. J. of Impact Eng. 2, 299 (1984).
- 3.43 A. J. Ricchiazzi and C. J. Brown, "Penetration Equations for Tungsten Fragments," Second ISB, (1976).
- 4.1 V. Hohler and A. J. Stilp, "Penetration of Steel and High Density Rods in Semi-infinite Steel Targets," Third ISB, paper H3 (1977).
- 4.2 G. Weihrauch and H. F. Lehr, "Experimental Studies on Terminal Ballistics of Kinetic Energy Projectiles," Third ISB, paper H2 (1977).

REFERENCES (CONT'D)

- 4.3 G. Weihrauch, "Das Verhalten von Kupferstiften beim Auftreffen auf verschiedene Werkstoffe mit Geschwindigkeiten zwischen 50 m/s und 1.650 m/s," Doctoral Dissertation, University of Karlsruhe, FRG (1971) Fig. 4.33, p. 135.
- 4.4 Reference (4.3), Figs. 4.6 and 4.6b, p. 95.
- 4.5 H. Margenau and G. Murphy, The Mathematics of Physics and Chemistry (Princeton, Van Nostrand, 1956).
- 4.6 E. Perez, "Étude Experimentale et Théorique de la Pénétration de Sables Métalliques Semi-infinies par des Projectiles Métalliques de Grand Allongement et de Vitesse Supérieure à 2,000 m/s," Sciences et Techniques de L'Armement 56 (1), 11 (1982).
- 4.7 E. Perez, "A Theory for Armor Penetration by Hypervelocity Long Rods," Fourth ISB (1978).
- 4.8 E. Perez and R. Haensel, "Investigation of the Penetration of Slender Rods in Thick Metal Targets," Second ISB (1976).
- 4.9 Reference 4.6, Fig. 48, p. 64.
- 4.10 Reference 4.6, Figs. 49a and 49b, pp. 65 and 66.
- 4.11 Reference 4.6, Fig. 40, p. 53.
- 4.12 Reference 4.6, Fig. 74c, p. 113.
- 4.13 Reference 4.6, Fig. 21, p. 40.
- 4.14 Reference 4.6, Fig. 61, p. 82.
- 4.15 Reference 4.6, Fig. 22, p. 40.
- 4.16 Reference 4.6, Fig. 28, p. 44.
- 4.17 Reference 4.6, Fig. 37, p. 50.
- 4.18 Reference 4.6, Fig. 62, p. 83.
- 4.19 A. Tate, "Further Results in the Theory of Long Rod Penetration," J. Mech. Phys. Solids 17, 141 (1969).
- 4.20 LASL Ephemex Data, 2 vols., Ed. by C. Mader, T. Neal and R. Dick (Berkeley, University of California Press, 1980).
- 4.21 H. Winick and S. Donach, Editors, Synchrotron Radiation Research (N.Y., Plenum, 1980).
- 4.22 V. Hohler and A. Stimp, "Influence of the Length-to-Diameter Ratio in the Range from 1 to 32 on the Penetration Performance of Two Projectiles," 8th ISB, p. IB-13.

REFERENCES (CONT'D)

- 4.23 D. Christman, A. Wenzel and J. Gehring, "Penetration Mechanisms of High Velocity Rods," Seventh HIS, V. 6, p. 169 (1965).
- 4.24 A. Tate, K. Green, P. Chamberlain and R. Baker, "Model Scale Experiments on Long Rod Penetration," Fourth ISB (1978).
- 4.25 Reference (4.23), p. 192.
- 4.26 Reference (4.23), p. 180.
- 4.27 A. Merendino, J. M. Regan and S. Kronman, "A Method of Obtaining a Massive Hypervelocity Pellet from a Shaped Charge Jet," BRL MR 1508 (1963).
- 4.28 A. B. Wenzel and J. W. Gehring, "Techniques for Launching 0.01 to 25 Gram Discrete Projectiles at Velocities up to 54,100 ft/s," Fourth Hypervelocity Techniques Symposium, p. 379 (1965).
- 4.29 V. Hohler and A. J. Stilp, "Study of the Penetration Behavior of Rods for a Wide Range of Target Densities," Fifth ISB (1980).
- 4.30 G. F. Silsby, "Penetration of Semi-infinite Steel Targets by Tungsten Long Rods at 1.3 to 2.5 km/s," Eighth ISB, TB-31 (1984).
- 4.30a Reference 4.3, pp. 44-5, Figs. 3.10 to 3.20.
- 4.31 Reference 4.3, p. 58, Fig. 3.35 to 3.40.
- 4.32 Reference 4.3, pp. 123-4, Tables 4.4 and 4.5, as well as, pp. 113, 116, and 119, Figs. 4.18, 4.20 and 4.25.
- 4.33 Reference 4.3, p. 130.
- 4.34 L. Herr and C. Grabarek, "Ballistic Performance and Beyond Armor Data for Rods Impacting Steel Armor Plates," BRL MR 2575 (1976).
- 4.35 C. L. Grabarek, "Penetration of Armor by Steel and High Density Penetrators," BRL MR 2134 (1971).
- 4.36 J. P. Lambert, "The Terminal Ballistics of Certain 65 Gram Long Rod Penetrators Impacting Steel Armor Plate," BRL TR 2072 (1978).
- 4.37 V. Hohler, E. Schneider, A. J. Stilp and R. Tham, "Length- and Velocity-Reduction of High Density Rods Perforating Mild Steel and Armor Steel Plates," Fourth ISB (1978).
- 5.1 G. B. Kistiakowsky, D. P. MacDougall and G. H. Messerly, "The Mechanism of Action of Cavity Charges," Office of Scientific Research and Development, OSRD 1338 (15 Mar 1943).
- 5.2 Reference 5.1, p. 17.

REFERENCES (CONT'D)

- 5.3 Reference 5.1, p. 18.
- 5.4 R. Hill, N. F. Mott and D. C. Pack, "Penetration by Munroe Jets," Ministry of Supply, Advisory Council, A.C. 5756, Jan. 1944.
- 5.5 H. A. Bethe, "Attempt of a Theory of Armor Penetration," Frankford Arsenal, 23 May 1941.
- 5.6 R. Hill, N. F. Mott and D. C. Pack, "Penetration of Armour by High Velocity Projectiles and Munroe Jets," A.C. 6024, Mar. 1944.
- 5.7 G. I. Taylor, "Notes on Bethe's Theory of Armour Penetration. I. Static Penetration," R.C. 279, and "II. Enlargement of a Hole in a Flat Sheet at High Speeds," R.C. 280.
- 5.8 Reference 5.6, p. 9.
- 5.9 Reference 5.6, p. 11.
- 5.10 Abstract by D. P. MacDougall entitled "The Action of Cavity Charges" and appended to reference 5.1.
- 5.11 R. DiPersio, J. Simon and T. H. Martin, "A Study of Jets from Scaled Conical Shaped Charge Liners," BRL MR 1298 (1960).
- 5.12 L. B. Seely and J. C. Clark, "High Speed Radiographic Studies of Controlled Fragmentation," BRL R 368, June 1943.
- 5.13 J. C. Clark, "Flash Radiography Applied to Ordnance Problems," J. Appl. Phys. 20, 363 (1949).
- 5.14 Reference 5.12, p. 17.
- 5.15 G. Birkhoff, "Mathematical Jet Theory of Lined Hollow Charges," BRL R 370, June 1943.
- 5.16 L. M. Milne-Thompson, Theoretical Hydrodynamics (London, 1938), chapter XI, section 43.
- 5.17 J. L. Tuck, "Studies of Shaped Charges by Flash Radiography," A.C. 4130, June 1943.
- 5.18 G. I. Taylor, "A Formulation of Mr. Tuck's Conception of Munroe Jets," A.C. 3734 (1943).
- 5.19 The Scientific Papers of Sir Geoffrey Ingram Taylor, Ed. by G. K. Batchelor (Cambridge, The University Press, 1963), vol. 3, p. 358.
- 5.20 Reference 5.17, pp. 4-5.
- 5.21 Reference 5.17, p. 5.

REFERENCES (CONT'D)

- 5.22 E. M. Pugh, "A Theory of Target Penetration of Jets," OSRD 3752, May 1944.
- 5.23 E. M. Pugh and E. L. Fireman, "Fundamentals of Jet Penetration," OSRD 4357, Nov. 1944.
- 5.24 G. R. Abrahamson and J. N. Goodier, "Penetration by Shaped Charge Jets of Nonuniform Velocity," J. Appl. Phys. 34 (1), 195 (1963).
- 5.25 E. M. Pugh and E. L. Fireman, "Fundamentals of Jet Penetration" OSRD 5462e, 15 Aug 1945.
- 5.26 G. Birkhoff, "Remarks on the Hill-Mott-Pack Theory of Penetration by Munroe Jets," BRL R 497 (1944).
- 5.27 G. Birkhoff, D. P. MacDougall, E. M. Pugh and G. I. Taylor, "Explosives with Lined Cavities," J. Appl. Phys. 19, 563 (1948).
- 5.28 D. C. Pack and W. M. Evans, "Penetration by High-Velocity ('Munroe') Jets: I and II," Proc. Phys. Soc. Lond., 64B, 298 and 303 (1951).
- 5.29 R. J. Eichelberger, "Experimental Test of the Theory of Penetration by Metallic Jets," J. Appl. Phys. 27, 63 (1956).
- 5.30 G. M. Bryan, R. J. Eichelberger, D. MacDonald and P. E. Zigman, "Application of Radioactive Tracers to the Study of Shaped Charge Phenomena," J. Appl. Phys. 28, 1152 (1959).
- 5.31 S. Singh, "Penetration by High-Speed Metallic Jets," Proc. Phys. Soc. Lond. 70B, 867 (1957).
- 5.32 M. A. Cook, "Mechanism of Cratering in Ultra-High Velocity Impact," J. Appl. Phys. 30, 725 (1959).
- 5.33 W. A. Allen and J. W. Rogers, "Penetration of a Rod into a Semi-infinite Target," J. Franklin Inst. 272, 275 (1961).
- 5.34 V. P. Alekseevski, "Penetration of a Rod into a Target at High Velocity," Combustion, Explosion and Shock Waves 2, (2), 99 (1966).
- 5.35 A. Tate, "A Theory for the Deceleration of Long Rods after Impact," J. Mech. Phys. Solids 15, 387 (1967).
- 5.36 F. E. Allison and R. Vitali, "A New Method of Computing Penetration Variables for Shaped Charge Jets," BRL R 1184 (1963).
- 5.37 R. DiPersio and J. Simon, "The Penetration-Standoff Relation for Idealized Shaped-Charge Jets," BRL R 1542 (1964).
- 5.38 R. DiPersio, J. Simon and A. Merendino, "Penetration of Shaped-Charge Jets into Metallic Targets," BRL R 1296 (1965).

REFERENCES (CONT'D)

- 5.39 A. Merendino and R. Vitali, "The Penetration of Shaped-Charge Jets into Steel and Aluminum Targets of Various Strengths," BRL MR 1932 (1968).
- 5.40 W. P. Walters and J. N. Majerus, "Hypervelocity Impact Models for Hole Growth and Geometry," Third Vulnerability/Survivability Symposium, American Defense Preparedness Association, 1977.
- 5.41 W. P. Walters, "Axially Symmetric Incompressible Shaped Charge Jets," BRL TR 2045 (1978).
- 5.42 W. P. Walters and J. N. Majerus, "Impact Models for Penetration and Hole Growth," BRL TR 2069 (1978).
- 5.43 W. P. Walters, "Influence of Material Viscosity on the Theory of Shaped-Charge Jet Formation," BRL MR 2941 (1979).
- 5.44 W. P. Walters and J. N. Majerus, "Shaped-Charge Penetration Model," BRL TR 2184 (1979).
- 5.45 B. S. Haugstad, "Compressibility Effects in Shaped Charge Jet Penetration," J. Appl. Phys. 52 (3), 1243 (1981).
- 5.46 B. S. Haugstad and O. S. Dullum, "Finite Compressibility in Shaped Charge Jet and Long Rod Penetration - The Effect of Shocks," J. Appl. Phys. 52 (8), 5066 (1981).
- 5.47 W. J. Flis and P. C. Chou, "Penetration of Compressible Materials by Shaped-Charge Jets," Seventh ISB, P. 617 (1983).
- 6.1 E. M. Pugh, "A Theory of Lined Hollow Charges," pp. 11-42 in "Transactions of a Symposium on Shaped Charges," BRL R 837 (1952).
- 6.2 F. E. Allison and R. Vitali, "An Application of the Jet Formation Theory to a 105 MM Shaped Charge," BRL R 1165 (1962).
- 6.3 J. T. Harrison, "BASC, An Analytical Code for Calculating Shaped Charge Properties," Sixth ISB (1981), p. 253.
- 6.4 J. T. Harrison, "Improved Analytical Shaped Charge Code: BASC," BRL TR 2300 (1981).
- 6.5 B. M. Simmons, "A Study of Shaped-Charge Collapse and Jet Formation using the HEMP Code and a Comparison with Experimental Observations," BRL MR 3417 (1984).
- 6.6 J. E. Shaw, "Liner Performance" in "Critical Review of Shaped Charge Information," BRL R 905 (1954), pp. 45-102.
- 6.7 R. DiPersio, J. Simon and T. H. Martin, "A Study of Jets from Scaled Conical Shaped Charge Liners," BRL MR 1298 (1960).

REFERENCES (CONT'D)

- 6.8 J. J. Paszek, B. G. Taylor and J. L. Squier, "Low-Voltage Flash Radiography" in "Transactions of a Symposium on Shaped Charges," BRL R 837 (1951), p. 125.
- 6.9 P. C. Chou and J. Carleone, "Calculation of Shaped Charge Jet Strain, Radius and Breakup Time," BRL CR 246 (1975).
- 6.10 P. C. Chou, J. Carleone, C. A. Tanzio and R. D. Cicarelli, "Shaped Charge Jet Breakup Studies using Radiograph Measurement and Surface Instability Calculations," BRL CR 337 (1977).
- 6.11 W. P. Walters and J. N. Majerus, "Shaped Charge Penetration Model, Part I: Monolithic Penetration and Comparison with Experimental Data," BRL TR 2184 (1979), p. 12.
- 6.12 D. R. Christman and J. W. Gehring, "Penetration Mechanisms and High-Velocity Projectiles," General Motors, GM TR 65-50 (1965), App. F.
- 6.13 E. Perez and M. Giraud, "Simulation Experimentale de la Penetration d'une Cible par un Jet Fragmenté de Charge Creuse," Fifth ISB (1980), Supplement.
- 6.14 P. C. Chou and R. H. Toland, "Experimental Study of Multiple Interior Impacts," Experimental Mechanics, p. 201, June 1977.
- 6.15 P. C. Chou, M. Minnick and L. Gause, "Experimental Study of Multiple Interior Impacts," BRL CR 199 (1975).
- 6.16 R. H. Toland, P. C. Chou and D. Leidel, "Interior Sequential Impact and Cylindrical Waves by Exploding Wire," BRL CR 264 (1975).
- 6.17 J. D. Moore, "Spaced Projectile Study," Potomac Research, Inc., Task 3 of Contract N 00173-78-M-H-331 (1978).
- 6.18 J. Simon and R. DiPersio, "Experimental Verification of Standoff Effects on Shaped Charge Jet Cutoff in Solid Targets," BRL MR 1976 (1969).
- 6.19 R. DiPersio, J. Simon and A. B. Merendino, "Penetration of Shaped Charge Jets into Metallic Targets," BRL R 1296 (1965), pp. 41-2.
- 6.20 J. S. Rinehart, "Multiple-Fragment-Impact Effects in Shaped Charge Penetration" in Transactions of a Symposium on Shaped Charges, BRL R 837 (1951).
- 6.21 M. D. Alexander and S. A. Finnegan, "A Model for Multiple Fragment Interactions in 3-D Targets," Seventh ISB, p. 295 (1983).
- 6.22 R. C. Golesworthy, "The Effect of Transverse Velocity on Shaped Charge Performance," Seventh ISB, p. 257 (1983).
- 6.23 M. Held, "Characterizing Shaped Charge Performance by Standoff Behavior," Seventh ISB, p. 331 (1983).

REFERENCES (CONT'D)

- 6.24 T. Szendrei, "Analytical Model of Crater Formation by Jet Impact and Its Application to Calculation of Penetration Curves and Hole Profiles," Seventh ISB, p. 575 (1983).
- 6.25 M. Held, "Transverse Shaped Charges," Eighth ISB, p. VII-39 (1984).
- 6.26 S. Segletes, "Drift Velocity Computations for Shaped-Charge Jets," BRL MR 3306 (1983).
- 6.27 E. Fitzgerald, Particle Waves and Deformation in Crystalline Solids (N.Y., Interscience, 1966).
- 6.28 S. Segletes, "A Model of the Effects of Transverse Velocity on the Penetration of a Shaped-Charge Jet," BRL MR 3409 (1984).
- 6.29 A. B. Merendino and R. Vitali, "The Penetration of Shaped Charge Jets into Steel and Aluminum Targets of Various Strengths," BRL MR 1932 (1968).
- 6.30 Reference 1.32, p. 294.
- 6.30a J. B. Feldman, Jr., "Volume-Energy Relation from Shaped Charge Jet Penetrations," Third HIS, vol. 1, p. 215 (1959).
- 6.31 J. N. Majerus, W. P. Walters and G. F. Neitzel, "Impact Models for Penetration and Hole Growth," Fourth ISB (1978), figures 5A to 5D.
- 6.31a Reference 1.32, p. 297.

APPENDIX

Mass/Speed Tradeoffs

For KE weapons, should we invest more in mass or in speed? An answer to this question can be given by a recent model.

If our bullet does not erode, its penetration depth in a semi-infinite target can be described by

$$P_E = .5(M_O/c) \ln [1+(\dot{S}_O/\alpha)^2] \quad (2.11)$$

where α , the inflection point in a P_E versus \dot{S}_O curve, depends only on target strength and density. The constant c depends on target density and projectile presented area. If we fix this area and vary the projectile mass, M_O , by varying its density and/or length, then the depth at embedment, P_E , is a function only of striking mass, M_O , and striking speed, \dot{S}_O . Then

$$\partial P_E / \partial M_O = (.5/c) \ln [1+(\dot{S}_O/\alpha)^2] \quad (a)$$

and

$$\partial P_E / \partial \dot{S}_O = (M_O/\alpha) \dot{S}_O / [1+(\dot{S}_O/\alpha)^2] \quad (b)$$

Clearly $P_E(\dot{M}_O, \dot{S}_O)$ has no maximum for finite, positive values of the mass and speed. Here the constant, α , depends on target strength and projectile presented area which we have assumed constant. Clearly P_E and its derivatives depend on both target and projectile characteristics.

We want to compare the rates (a) and (b) and to do this, we must specify the parameters and express both rates in the same units. The latter may be achieved in two ways: either multiply (a) by M_O/\dot{S}_O or multiply (b) by \dot{S}_O/M_O . Let us adopt the second procedure and use an example with $a=c=1$ so $\alpha=\sqrt{a/c}=1$. Then we can construct the following table:

\dot{S}_O	0	1	2	3	5	∞	mm/ μ s
(a) $.5 \ln(1+\dot{S}_O^2)$	0	.35	.8	1.15	1.63	∞	mm/g
(\dot{S}_O/M_O)(b) $\dot{S}_O^2/(1+\dot{S}_O^2)$	0	.5	.8	.9	.95	1.0	mm/g

In this case, it is more advantageous to increase \dot{S}_O below 2 mm/ μ s, but more advantageous to increase M_O for $\dot{S}_O > 2$ mm/ μ s. The crossover speed where both

rates are equal depends on the target strength and density. A general expression may be found by equating (a) and (\dot{S}_0/M_0) (b) to obtain

$$[1+(\dot{S}_0/\alpha)^2] \ln [1+(\dot{S}_0/\alpha)^2] = 2(\dot{S}_0/\alpha)^2 \quad (c)$$

which for given α may be solved for the crossover speed, \dot{S}_0 .

The model has been shown to hold at least up to $\dot{S}_0 = 10.0$ mm/ μ s. Obviously, it does not hold for very much higher speeds when melting and vaporization become important.

If our bullet erodes, then

$$P_E = (M_0/\mu_0) \{1 - [1+(\dot{S}_0/\zeta)^2]^{-\epsilon}\} \quad (2.22)$$

where μ_0 is a constant erosion rate in g/mm. Here ϵ is a dimensionless erosion rate, $\epsilon = (\mu_0 k)/(2\bar{c})$, where k also depends on μ_0 as well as the projectile density and presented area. \bar{c} is related to c and also involves μ_0 as well as the projectile density and area. The parameter ζ is similar to α in Eq (2.11) and is $\zeta = k\sqrt{a/\bar{c}}$. For $\mu_0 \rightarrow 0$, $\epsilon \rightarrow 0$, $k \rightarrow 1$, $\bar{c} \rightarrow c$ and $\zeta \rightarrow \alpha$. It is easy to show that Eq (2.22) reduces to Eq (2.11) in this limit. It can also be shown that in most cases of interest we can take ζ and ϵ as well as μ_0 be approximately constant for a given projectile/target combination. Then we can find the rates

$$\partial P_E / \partial M_0 = (1/\mu_0) \{1 - [1+(\dot{S}_0/\zeta)^2]^{-\epsilon}\} \quad (d)$$

and

$$\partial P_E / \partial \dot{S}_0 = [M_0/(ak)] \dot{S}_0 / [1+(\dot{S}_0/\zeta)^2]^{1+\epsilon} \quad (e)$$

Again we see that $P_E(M_0, \dot{S}_0)$ has no maximum for finite, positive values of mass and speed.

Let us consider an example for which $\mu_0 = 4.7$ g/mm, $\zeta = 1.1$ mm/ μ s, $\epsilon = 1$, $a = 2$, and $k = 1.25$. Then we can construct the following table:

\dot{S}_0	0	1	2	3	5	∞ mm/ μ s
(d)	0	.1	.16	.19	.20	.21 mm/g
(\dot{S}_0/M_0) (e)	0	.12	.09	.06	.02	0 mm/g

Again the rate of increase of P_E with M_0 continues to grow as \dot{S}_0 increases (without limit). However, in this case it increases very little above $\dot{S}_0 = 3 \text{ mm}/\mu\text{s}$. The comparable rate of increase of P_E with \dot{S}_0 reaches a maximum near the inflection point and decreases thereafter. A plot of P_E versus M_0 for any \dot{S}_0 above $3 \text{ mm}/\mu\text{s}$ will be approximately a straight line with slope $0.2 \text{ mm}/\text{g}$. A plot of P_E versus \dot{S}_0 for given M_0 will be an almost horizontal line above $\dot{S}_0 = 3 \text{ mm}/\mu\text{s}$. This approach to a maximum $P_E = M_0/\mu_0$ is characteristic of erosive penetrations. Of course, the particular maximum can be increased by increasing M_0 (or reducing μ_0). A general expression for the crossover speed can be obtained by equating (A.4) and (\dot{S}_0/M_0) (A.5) to obtain

$$[1 + (\dot{S}_0/\zeta)^2] \{ [1 + (\dot{S}_0/\zeta)^2]^\varepsilon - 1 \} = 2\varepsilon (\dot{S}_0/\zeta)^2 \quad (f)$$

which for given ζ may be solved for \dot{S}_0 . When $\varepsilon = 1$, we have $\dot{S}_0 = \zeta$ in Eq (f).

The above analysis enables us to answer the question in the first paragraph. It is always advantageous to increase both mass and speed versus a semi-infinite target. For speeds below the inflection point (below 1 or $2 \text{ mm}/\mu\text{s}$), it can be more advantageous to increase the striking speed. For higher speeds, it is always more advantageous to increase the projectile mass.

This conclusion holds for semi-infinite targets. The same may not be true for complicated targets with more open structures.

DISTRIBUTION LIST

<u>No. of Copies</u>	<u>Organization</u>	<u>No. of Copies</u>	<u>Organization</u>
1	Boeing Aerospace Company ATTN: E. Wilhelm 8C-61 Seattle, WA 98124	1	USA Materials Technology Laboratory ATTN: J. Mescall Watertown, MA 02172
1	University of California Dept. of Mechanical Engineering ATTN: W. Goldsmith Berkeley, CA 94720	1	Naval Weapons Center ATTN: M. Backman China Lake, CA 93555
1	University of California Los Alamos National Laboratory ATTN: R. Karpp Los Alamos, NM 87544	1	Sandia National Laboratory ATTN: W. Herrmann Albuquerque, NM 87115
1	University of California Lawrence Livermore Laboratory ATTN: M. Wilkens Livermore, CA 94550	1	Defense Advanced Research Projects Agency ATTN: T. Hafer 1400 Wilson Blvd. Alexandria, VA 22209
1	University of Dayton Research Institute ATTN: S. Bless Dayton, OH 45469	1	Pacifica Technology ATTN: R. Bjork Box 148 Del Mar, CA 92014
1	University of Denver Research Institute ATTN: R. Recht 2390 S. University Blvd. Denver, CO 80208	1	Battelle-Columbus Laboratories ATTN: Technical Library 505 King Ave. Columbus, OH 43201
1	Southwest Research Institute ATTN: C. Anderson 8500 Culebra Rd. San Antonio, TX 78228	1	Dyna East Corporation ATTN: P. C. Chou 3432 Market Street Philadelphia, PA 19104-2588
1	Computer Code Consultants ATTN: W. Johnson 1680 Camino Redondo Los Alamos, NM 87544	1	Villanova University ATTN: J. N. Majerus Villanova, PA 19085
1	Honeywell, Inc. ATTN: G. Johnson 5121 Winnetka Ave. New Hope, Minn. 55428	1	Aerojet Ordnance Corporation ATTN: J. Carleone 2521 Michelle Drive Tustin, CA 92680
1	Strategic Defense Command ATTN: S. Brockway P.O. Box 1500 Huntsville, AL 35807	1	Physics International Company ATTN: R. Rerus P.O. Box 1004 Wadsworth, OH 44281-0904

DISTRIBUTION LIST

<u>No. of Copies</u>	<u>Organization</u>	<u>No. of Copies</u>	<u>Organization</u>
1	System, Science and Software ATTN: R. Sedgwick P.O. Box 1620 La Jolla, CA 92037	1	Ford Aerospace, Aeronautics ATTN: D. A. Rodriguez Ford Road Newport Beach, CA 92660
1	General Dynamics ATTN: E. LaRocca P.O. Box 2507 Pamona, CA 91769	1	Louisiana Tech University ATTN: E. Callens, Jr. Dept. of Mech. Eng. Ruston, LA 71272
1	California Research and Technology ATTN: R. E. Brown 11875 Dublin Blvd. Dublin, CA 94568	1	Mississippi State University ATTN: J. Brown Drawer One Mississippi State, MS 39762
1	Michigan Technology University ATTN: W. W. Predebon Houghton, MI 49931		
1	Science Applications International Corp. ATTN: N. Banks 626 Towne Center Drive Suite 206 Joppatowne, MD 21085		
1	U.S. Naval Research Laboratory Code 8320.6 ATTN: J. Baker Washington, D.C. 20375-5000		
1	LTV Aerospace and Defense Co. ATTN: G. R. Hough P.O. Box 225907 Dallas, TX 75265		
1	Lockhead Engineering, Inc. ATTN: K. J. Draper 2400 NASA Rd 1, C23 Houston, TX 77058-3711		
1	Stress Engineering Services, Inc. ATTN: J. R. Fowler 13800 Westfair East Drive Houston, TX 77041		

DISTRIBUTION LIST

<u>No. of Copies</u>	<u>Organization</u>	<u>No. of Copies</u>	<u>Organization</u>
12	Administrator Defense Technical Info Center ATTN: DTIC-DDA Cameron Station Alexandria, VA 22304-6145	1	Director US Army Air Mobility Research and Development Laboratory Ames Research Center Moffett Field, CA 94035
1	HQDA (DAMA-ART-M) Washington, DC 20310	1	Commander US Army Communications- Electronics Command ATTN: AMSEL-ED Fort Monmouth, NJ 07703
1	Commander US Army Materiel Command ATTN: AMCDRA-ST 5001 Eisenhower Avenue Alexandria, VA 22333-0001	1	Commander ERADCOM Technical Library ATTN: DELSD-L (Reports Section) Fort Monmouth, NJ 07703-5301
1	Commander Armament R&D Center US Army AMCCOM ATTN: SMCAR-TSS Dover, NJ 07801	1	Commander US Army Missile Command Research, Development and Engineering Center ATTN: AMSMI-RD Redstone Arsenal, AL 35898
1	Commander Armament R&D Center US Army AMCCOM ATTN: SMCAR-TDC Dover, NJ 07801	1	Director US Army Missile & Space Intelligence Center ATTN: AIAMS-YDL Redstone Arsenal AL 35898-5500
1	Director Benet Weapons Laboratory Armament R&D Center US Army AMCCOM ATTN: SMCAR-LCB-TL Watervliet, NY 12189	1	Commander US Army Tank-Automotive Cmd ATTN: AMSTA-TSL Warren, MI 48397-5000
1	Commander US Army Armament, Munitions and Chemical Command ATTN: SMCAR-ESP-L Rock Island, IL 61299	1	Director US Army TRADOC Systems Analysis Activity ATTN: ATAA-SL White Sands Missile Range NM 88002
1	Commander US Army Aviation Research and Development Command ATTN: AMSAV-E 4300 Goodfellow Blvd St. Louis, MO 63120	1	Commandant US Army Infantry School ATTN: ATSH-CD-CSO-OR Fort Benning, GA 31905

DISTRIBUTION LIST

<u>No. of Copies</u>	<u>Organization</u>	<u>No. of Copies</u>	<u>Organization</u>
1	Commander US Army Development and Employment Agency ATTN: MODE-TED-SAB Fort Lewis, WA 98433		<u>ABERDEFN PROVING GROUND</u> Dir, USAMSAA ATTN: AMXSY-D AMXSY-MP (H. Cohen)
1	AFWL/SUL Kirtland AFB, NM 87117		Cdr, USATECOM ATTN: AMSTE-TO-F
1	AFATL/DLODL Eglin AFB, FL 32542-5000		Cdr, CRDC, AMCCOM ATTN: SMCCR-RSP-A SMCCR-MU SMCCR-SPS-IL
10	Central Intelligence Agency Office of Central Reference Dissemination Branch Room GE-47 HQS Washington, DC 20502		

DISTRIBUTION LIST

Internal Distribution

Terminal Ballistics Division, BRL

W. Gillich
W. de Rosset
A. Dietrich
G. Moss
R. Frey
W. Bruchey
G. Hauver
T. Wright
A. Finnerty
J. Polk

G. Filbey
D. Puckett
E. Murray
W. Gooch
T. Havel
D. Hansen
H. Meyer
R. Carroll
F. Harris
G. Gentle
P. Cianelli
L. Herr
A. Copland
K. Kimsey
J. Pollock

B. Ringers
L. Magness
J. Zook

H. Jonas
J. Zukas
K. Frank
G. Silsby
A. Kurian
J. Kineke
M. Lampson
J. Paszek
P. Baker
W. Walters
F. Grace
D. Silvia
R. Meissner
S. Segletes
S. Golaski
F. Malinoski
J. Barb
N. Huffington
J. Harrison
P. Simmers
G. Randers-Pehrson